Comparison of Microanalysis using Energy-Dispersive X-ray Spectroscopy and Electron Energy Loss Spectroscopy

by James H. Paterson

submitted for the degree of Doctor of Philosophy in the University of Glasgow.

February 1988

ProQuest Number: 10997895

ProQuest 10997895

"I forget what kind of books you write."

"Science Fiction!"

from

37°2 IN THE MORNING

directed by JEAN-JACQUES BEINEIX

Declaration

This thesis has been written solely by myself and details the research which I have carried out in the Department of Physics and Astronomy at the University of Glasgow. The work described is my own, except where otherwise stated. Some of the results from this work have been presented in the following papers :-

"A Single-Stage Process for Quantifying Electron Energy Loss Spectra", J D Steele, J M Titchmarsh, J N Chapman and J H Paterson (1985), Ultramicroscopy **17**, 273.

"The Separation of Characteristic Signals from Complex EELS Spectra", J N Chapman, J D Steele, J H Paterson and J M Titchmarsh (1985), in EMAG 85, Inst. Phys. Conf. Ser. 78 (ed. G J Tatlock), 177.

"Measurements of K-shell/L-Shell Ionisation Cross Section Ratios Using a Windowless X-ray Detector", J H Paterson, J N Chapman and J M Titchmarsh (1986), in Electron Microscopy 1986 (eds. T Imura, S Maruse and T Suzuki, Japanese Society of Electron Microscopy), p 567.

"Investigation of Cross Section Models for X-ray Production by Electrons of Kinetic Energy of 80-200keV", J H Paterson, W A P Nicholson, J N Chapman and R H Geiss (1987), in Proc. Pacific Regional Workshop on Analytical Electron Microscopy.

"Cross Sections for Elemental Analysis in EDX", J H Paterson, J N Chapman, W A P Nicholson and J M Titchmarsh (1987), in EMAG 87, Inst. Phys. Conf. Ser. 90 (ed. L M Brown), 177.

This thesis has not been submitted in any previous application for a degree.

Contents

References

Acknowledgements

I would like to thank all those who have helped me to carry out the work presented in this thesis. I must thank in particular my academic supervisor, Dr. J.N. Chapman, for his guidance and encouragement in all aspects of this work. Thanks also to Professor R.P.Ferrier for provision of the research facilities within the Solid State Physics Group in the Department of Physics and Astronomy. I would also like to thank my industrial supervisor, Dr. J.M. Titchmarsh, for many useful discussions and for the opportunity to make use of the VG HB501 scanning transmission electron microscope at AERE Harwell.

I am grateful to Dr. W.A.P. Nicholson for discussions on EDX analysis in particular, and for providing the data described in chapters 4 and 5 from the JEOL 2000FX transmission electron microscope at IBM's Almaden Research Center. I must also thank Drs. P.A.Crozier and J.D. Steele for useful discussions, and in the case of the former for providing the EELS data from second phase carbides described in chapter 8. Thanks also to Miss M. Low and Mrs M. Waterston for stencilling a number of the diagrams in this thesis.

Finally, I would like to thank the Science and Engineering Research Council and AERE Harwell for the provision of a CASE award.

Summary

The work presented in this thesis is concerned with the development and comparison of two techniques for microanalysis in the electron microscope. These are energy-dispersive x-ray spectroscopy (EDX) and electron energy loss spectroscopy (EELS). Particular emphasis has been placed on light element analysis, as these elements have become accessible to EDX analysis with the recent advent of windowless x-ray detectors.

The interest here is confined to analysis without recourse to standard specimens of known composition. Standardless analysis requires a theoretical knowedge of the processes which give rise to the various features in both types of spectrum. Chapter 2 outlines the formalism of the relevant basic theory, and describes how expressions are obtained for the cross sections relevant to inelastic scattering of electrons by interactions with inner-shell electrons in the specimen, and to the x-ray production which is associated with such scattering. The signals in EELS and EDX spectra which arise due to inner shell scattering occur at energy losses and photon energies respectively which are characteristic of the atoms in the specimen. Other processes, which contribute to non-characteristic backgrounds in both cases, are described briefly.

The work for this thesis was carried out using three microscopes: two similar scanning transmission electron microscopes (STEMs), one of which was equipped with a windowless x-ray detector, and one transmission electron microscope (TEM). Chapter 3 gives a description of one of the STEMs, and goes on to outline the differences between the two STEMs. The TEM is then briefly described. The remainder of the chapter discusses the detectors and spectral acquisition systems fitted to each microscope.

The results obtained on EDX are presented in chapters 4, 5 and 6. Chapter 4 starts by discussing general EDX analysis techniques, and then goes on to detail a series on measurements of the ratios of characteristic signals to the local background in the EDX spectrum. The results obtained using all three

microscopes are then used as the basis of a parameterisation of the ionisation cross section for the K-shell. The parameterisation allows the prediction of this quantity within an accuracy of ~20% over a range of elements with $14 < Z < 50$, and a range of accelerating voltages from 80keV to 200keV. Chapter 5 details the investigation of L-shell ionisation cross sections. This involved measuring the ratio of the K-shell/L-shell cross sections over a wide range of elements, and using the results of the previous chapter to deduce the L-shell cross sections. These measurements required the detector efficiency to be carefully considered over the entire energy range of an EDX spectrum. The accuracy with which the L-shell cross sections could be determined was limited by uncertainties in the values in the literature for the relevant fluorescence yields. Nevertheless, the results generally suggested that the model used for the K-shell may be applied also to the L-shell. Chapter 6 gives the results of the analyses of a number of compounds of light elements, and shows that many difficulties exist in the determination of quantitative information on these elemnts by EDX.

EELS analysis procedures are discussed in chapter 7. Conventional procedures, and an alternative technique proposed by Steele et al. (1985), are detailed. The latter approach involves the inclusion in the function which is fitted to the spectrum of a scaled theoretical cross section. Fitting may then be carried out both before and after the characteristic edge onset. This removes the need for the background to be extrapolated beneath the edge, as conventional background fitting requires. Results of the application of the new procedure are given in chapter 8. Firstly, it is used to re-analyse EELS data which had previously been analysed conventionally. These data were recorded simultaneously with equivalent EDX data. The results showed that the use of the new technique leads to some improvement in the correlation between concentration ratios determined using EELS and EDX. A second analysis, of TiB_2 and CrB_2 failed to produce any conclusive results.

Finally, chapter 9 discusses the implications of the results obtained in this work, and suggests some ways in which the accuracy of each of the two techniques might be improved.

Table of frequently used symbols

General

c	velocity of light = $2.998 \times 10^8 ms^{-1}$
h	Planck's constant = $6.626 \times 10^{-34} Js$
$\hbar$	$h/2\pi = 1.055 \times 10^{-34} Js$
m_0	rest mass of electron = $9.109 \times 10^{-31} kg$
e	charge on an electron = $1.602 \times 10^{-19} C$
a_0	Bohr radius = $h^2/m_0 e^2 = 5.292 \times 10^{-11} m$
R	Rydberg energy = $m_0 e^4/h^2 = 13.606 eV$
v	velocity of an electron
β	v/c *(see also under "Symbols specific to EELS")*
T	kinetic energy of an electron = $1/2 m_0 v^2$
K	momentum transfer in a collision
T_0	accelerating voltage in microscope
Z	atomic number
A	atomic weight
N_0	Avogadro's number = $6.022 \times 10^{23} mol^{-1}$
ρ	density of a material

Symbols specific to EDX

ω_x	fluorescence yield for a shell or sub-shell x
s	K-shell partition function = $K_\alpha/K_\alpha + K_\beta$
I_x	binding energy for a shell or sub-shell x
U_x	overvoltage = T_0/I_x
$h\nu$	x-ray photon energy
$\mu/\rho_X(h\nu)$	mass absorption coefficient for photons of energy $h\nu$ in element X
σ_i	total ionisation cross section
σ_c	characteristic x-ray production cross section/sr

$\sigma_b(h\nu,\Omega)dh\nu$	bremsstrahlung cross section
σ''	reduced bremsstrahlung cross section
θ	x-ray detector take-off angle (defined with respect to the incident beam direction)
$\epsilon(h\nu)$	efficiency of an x-ray detector for photons of energy $h\nu$
k_{ab}	Cliff-Lorimer k-factor for the conversion of the ratio of characteristic counts for two elements a and b to the corresponding concentration ratio
P	total number of counts in a characteristic peak
B	number of background counts in a 20eV channel below the characteristic peak
P/B	peak to background ratio, given by the ratio of P and B as defined separately above
b_x, c_x	Bethe parameters for the shell or sub-shell x
$b_x(Z), c_x(Z)$	Bethe parameters for the shell or sub-shell x and atomic number Z
Q_{KL}^t	theoretical value of K_α/L-shell x-ray production cross section ratio
Q_{KL}^e	experimentally measured value of K_α/L-shell x-ray production cross section ratio

Symbols specific to EELS

ΔE or E	energy loss
α	probe convergence semi-angle
β	spectrometer collection semi-angle
β^*	effective spectrometer collection semi-angle in which account is taken of the effect of a convergent probe
$d\sigma_n(\Delta E,\beta)/d(\Delta E)$ or $\sigma(E)$	energy-differential cross section for scattering into an angle β
$\sigma(\delta,\beta)$	partial cross section for scattering into an angle β integrated over a range of energy loss δ
B(E)	background in the EELS spectrum at energy loss E

constrained fitting parameters-

k	cross section scaling factor

A, Γ parameters defining the background shape $AE^{-\Gamma}$

χ_1^2, χ_2^2 values returned by a chi-squared test on a background shape in the pre-edge and post-edge fitting regions respectively

χ^2 the sum of χ_1^2 and χ_2^2, used as a criterion for selecting the best background shape

o_a cross section alignment offset

o_c convergence offset

Chapter 1

Introduction

$\mathbf{A}$ number of techniques have been used in the electron microscope for the extraction of quantitive information on the chemical composition of materials (see Goodhew and Castle,1983, or Venables, 1981 for a review). Two widely used techniques are energy dispersive x-ray spectroscopy (EDX, although sometimes referred to in the literature as EDS) and electron energy loss spectroscopy (EELS). Each of these has its own particular advantages and limitations as compared to the other. Until recently, the main drawback of EDX was that solid state detectors could not be used to detect any signals from elements with $Z<11$. The reason for this lay in the need to protect the detector crystal from contaminants present in column of the typical electron microscope. To this end, a conventional x-ray detector has a Be window, typically $\sim 10\mu m$ thick, between the crystal and the column, and hence between the crystal and the specimen. This window strongly absorbs low energy x-rays. In the past few years, improvements in the performance of microscope vacuum systems have allowed the installation of detectors without such a protective window. This has opened up the range of elements with $5<Z<11$ to analysis by EDX. Elements in this range are easily accessible to EELS analysis. The aim of the work presented in this thesis is to assess the accuracy of analysis obtainable with each technique generally, and in particular to compare their performances for these light elements.

EDX analysis involves the deduction of information about a specimen from the x-rays produced by the interactions of the electron beam of the microscope with the atoms of the specimen. Microanalysis using x-rays became a standard analysis technique following the introduction of the energy-dispersive solid state detector in the early 1970's. These offered a number of advantages over the wavelength-dispersive detectors which had been used previously (see for example Duncumb,1968), the most important of which was the compatibility of the solid state detectors with standard electron optics. The main disadvantage lay in the need for the protection for the crystal by a Be window as described above. The configuration of these detectors also made them prone to the detection

of radiation from sources other than the area of interest on the specimen. The performance of the combination of microscope and detector in this respect has improved considerably in recent years. Steps required to bring about such an improvement in a typical microscope have been described by Nicholson et al. (1977).

As mentioned above, detectors are now available without Be windows. The window is either replaced with an ultra-thin window made from, for example, parylene (UTW detector), or omitted completely (windowless detector). A considerable amount of work has been published in the last few years showing that elements as light as B can now be detected by EDX, and that C and heavier elements can be detected routinely. This body of work has indicated that problems for the quantitative analysis of light elements will arise due to uncertainty in the detection efficiency for low energy photons, and in some cases because of overlap between peaks, which can occur in the low energy region if many elements are present. For a review of the state of windowless EDX, see, for example, Goodhew,(1985). The operation of the solid state EDX detector is described in more detail in chapter 3.

Most of the information in the EDX spectrum is contained in the characteristic signals arising from interaction of the electron beam with inner shell electrons in the specimen. The interest in this thesis is generally confined to thin specimens, where "thin" means <1000Å. In this case, the ratio of the characteristic signals from a pair of elements is approximately proportional to the ratio of the concentrations of the elements in the area of specimen illuminated by the electron beam. This is the basis of the EDX ratio technique described by Cliff and Lorimer(1975). The constant of proportionality here may be determined either by reference to standard specimens of known composition, or by calculation from first principles (Goldstein and Williams, 1977). The latter approach offers the possibility of easy applicability in a wider range of situations than the former, and is the approach on which this thesis concentrates. Theoretical considerations for the production of x-rays by interaction of electrons with atoms are outlined in chapter 2, and the applications to standardless EDX analysis are discussed in chapters 4, 5 and 6.

The EELS spectrum is obtained by passing the electrons which have been transmitted through the specimen into a spectrometer, in which a magnetic field disperses the electrons according to the amount of energy which they have lost

in interactions with the specimen. The information on the specimen composition is provided by those electrons which have been scattered by inner shell electrons in the specimen. EELS is less established as a microanalytical technique than EDX. The technique is subject to rather stringent limitations on the thickness of specimens from which meaningful results may be obtained, much more so than EDX. Until recently, the serial nature of EELS spectrum acquisition dictated that experiments were generally rather time consuming. Parallel detection systems for EELS have now been developed (eg. Egerton, 1984a) which offer the potential to remove the latter drawback. No such system was available for this work. This was not considered to compromise the validity of any conclusions regarding the usefulness of EELS, since the advantage of parallel detection lies in experimental practicality, rather than offering any fundamental extension to the applicability of the technique as is the case for the windowless detector in EDX. Theoretical considerations for EELS are discussed in chapter 2, while the nature of the EELS spectrum is described in chapter 7. The extra complexity of the EELS spectrum which is discussed in those chapters makes the use of standard specimens in EELS less practicable than in EDX, and the standardless approach is followed by most workers.

EELS and EDX have existed side by side as microanalytical techniques because of the complementary nature of the ranges of elements over which they are most applicable. Typical EDX systems respond to x-rays of energy up to 40keV. The lower limit of the useful energy range is ~1keV for a Be window detector. This range includes signals corresponding to transitions to the K-shell for a wide range of elements, ie $11<Z<60$. For $Z>~30$, the L-shell signal is detected, and the M-and higher order shell signals can be detected for heavier elements still. With the Be window detector, no signal from the lightest elements is detected. The range of energy loss measured by an EELS spectrometer is typically 0-2keV. This places a far greater limitation on the signals which are detected. Electrons which have lost energy by ionisation of the K-shell may be detected for target atoms with $Z<14$. In principle L-shell signals can be detected for elements with $Z<40$. Higher order shell signals lie in the relevant energy window over similarly limited ranges of Z. In practice, the range of signals available in EDX allows many analyses to be carried out by consideration of signals from the K-shell only. In EELS, on the other hand, this is possible only when the analysis involves light elements alone. In many cases, measurement of concentration ratios requires comparison of signals from different shells. It will be shown in chapter 2 that theoretical calculations of the cross sections for

the processes relevant to EELS are most reliable for the K-shell. The need to consider higher order shells can therefore introduce substantial uncertainties into the results of many EELS analyses. The advent of the windowless x-ray detector has resulted in EELS no longer being alone in its ability to detect light elements. This raises the question of whether the advantages of EDX can be extended to this region, hence making it an undeniably superior microanalytical technique overall. The qualification should be made that the discussion here is restricted to the ability of each technique to measure elemental concentrations. The EELS spectrum contains much information about a specimen which is not contained in the EDX spectrum, regarding among others specimen thickness and a number of solid state effects (Egerton, 1984b). EELS existed for many years as a technique for studying band structure (for example Burge and Misell 1968), before being recognised as a microanalysis technique in the early 1970's.

The approach taken in this work was to consider the factors which affect the accuracy of each of the two techniques, and examine ways in which improvements may be introduced. In the case of EDX, where characteristic signals may be extracted from the background with relative ease, the main source of error is in the determination of factors for the conversion of count ratios to concentration ratios. Outwith the light element region, the component part of this factor which is least well known is the ionisation cross section. The values generally used are based on empirical parameterisations derived from experimental data. Preliminary work on EDX involved carrying out such a parameterisation for the K-shell over a range of conditions which had not been available to previous workers. These results appear in chapter 4.

Measurements of ionisation cross sections had previously been made successfully for the K-shell. Comparison of K-shell and L-shell signals in the same spectra offers the possibility of deducing corresponding information for the L-shell. This observation lead to measurements being made to obtain reliable values for K/L-shell count ratios (see chapter 5). These ratios were then converted to the corresponding cross section ratios, and some success was achieved in fitting the deduced L-shell ionisation cross sections to theory. The results obtained in chapters 4 and 5 were applied to light element analysis in the work described in chapter 6. Three compounds of known chemical composition were analysed in order to assess the accuracy with which the elemental concentrations could be determined by EDX. In one of these cases, NiO, the knowledge of the Ni K_α/L ratio gained from the work described in chapter 5

was useful in that absorption within the specimen of the O K signal for a particular spectrum could be detected by examination of the Ni K_α/L ratio in that spectrum. In general, it was found that light element analysis by EDX is subject to very considerable errors.

Problems in EELS are particularly associated with extraction of the characteristic signals from the background, and with uncertainties in the theoretical cross sections required. The background in the EELS spectrum varies rapidly with energy loss, and the signal to background ratio is always small compared to the equivalent quantity in the EDX spectrum. A characteristic signal extends over a large range of energy loss, and so some form of extrapolation is generally used to deduce the shape of the background in order to allow extraction of the characteristic signal. The work on EELS in this thesis is concerned with investigation of an alternative background fitting technique, originally proposed by Steele et al.(1985), in which a theoretical cross section shape is incorporated into the function which is fitted to the spectrum, thus allowing fitting on both sides of the signal onset. Chapter 7 describes general EELS analysis procedures, and goes on to describe the use of the new procedure. The results of two analyses are given in chapter 8. The first of these used data previously analysed by Crozier et al.(1983, 1984). The signals considered were from the L-shell only. These data had been analysed by conventional EELS procedures, and by EDX, in order to assess the degree of correlation between the two techniques in a particular case. The EELS data have been re-analysed using the new procedure, which is shown to yield some improvement in correlation with the EDX results. Following Crozier et al., cross sections calculated according to the two most widely used models were incorporated, in order to ascertain whether either of these is clearly superior to the other. These models are discussed in chapter 2. In this case, the two models were applied with a comparable degree of success. The second analysis involved comparison of K-shell and L-shell signals. TiB_2 and CrB_2 specimens were subjected to EELS analysis using the new fitting technique. The results obtained were not sufficiently conclusive to give any useful indication of the success of the technique.

The final chapter discusses the implications of the results presented in the preceding chapters, and concludes that while EDX now shows some promise for light element analysis, its accuracy in this range is not sufficiently high for EELS to be superceded for this purpose.

Chapter 2

Theoretical considerations for EELS and EDX

2.1 Introduction

The work presented in this thesis is largely concerned with the extraction of quantitative information from EELS and EDX spectra. In order to relate the information contained in a spectrum to the elemental composition of the specimen it is necessary to have some knowledge of the probabilities of the scattering events taking place which give rise to the characteristic signals in the spectrum. As stated in chapter 1, one area of interest in this work lies in carrying out analyses without recourse to standard specimens. It is necessary to calculate the relevant probabilities theoretically. The characteristic signals which are of interest arise due to inelastic collisions of the monoenergetic incident electrons with the atoms in specimens which are generally thin. The probability of such a collision is usually expressed as a cross section σ, defined by

$$N = \sigma \, n \, I \qquad\qquad (2.1)$$

where N is the number of scattering events, n is the number of scatterers per unit area and I is the number of incident electrons. This chapter outlines the development of theoretical expressions for the cross sections relevant for EELS and EDX

The chapter starts by describing the Bethe theory (Bethe, 1930) for inelastic scattering of fast electrons. Whether an incident electron is considered fast or slow depends on its velocity relative to the orbital velocity of the atomic electron involved in the scattering process. In this work the incident electron energy was always $\geq 80 \text{keV}$. These electrons can be considered fast for most elements. Any inaccuracy introduced by this assumption will manifest itself increasingly for heavier elements. This theory leads to the Bethe differential cross section, which applies to the case of an electron being scattered into a

small element of solid angle $d\omega$, and losing an amount of energy ΔE. The following sections go on to discuss in turn the derivation from this of the cross sections which are of use for EELS and EDX. The appropriate cross section for EELS, discussed in section 2.3, is that which is integrated over a cone of half angle β, corresponding to the spectrometer collection angle as described in chapter 3. The cross section is also integrated over a range of energy loss δ. The result is known as a partial cross section. Evaluation of the cross section requires a form to be assumed for the relevant initial and final quantum mechanical wave functions. Two approaches are described here: the semi-analytic hydrogenic model and the numerical Hartree-Slater model.

For EDX, the fate of the electron subsequent to scattering is of no interest. The appropriate cross section is the total ionisation cross section. Section 2.4 briefly discusses the general process of x-ray production. Section 2.5 goes on to describe the derivation of the Bethe form for the ionisation cross section. This is a simple approximate functional form, dependent on two parameters for which values can be obtained by fitting to suitable experimental data. Determination of the Bethe parameters will be discussed in chapter 6.

The final two sections in this chapter describe some non-characteristic signals which contribute to EELS and EDX spectra. The scattering cross sections discussed up to this point are based on the assumption that the electron is scattered once only. They also assume that the scatterer is an isolated atom. In EELS, however, the effects of plural inelastic scattering by valence electrons and plasmon excitation can become important for all but the thinnest specimens. These effects can result in loss of visibility of the characteristic signals, and so place a limitation on the applicability of EELS. This process is described, together with a brief discussion of solid state effects, in section 2.6. In the EDX spectrum, there is a continuous background due to non-characteristic bremsstrahlung. This effect results from the incident electron making a transition between two states of the continuum in the field of the atom. The models which are available for bremsstrahlung cross sections are described in section 2.7.

2.2 Fast electron scattering from atomic inner shells

The Bethe theory is the most frequently used approach to the description of scattering of charged particles by atomic inner shells. This theory has been reviewed by Inokuti (1971). The general approach and the major results given in that work are outlined here. The incident electron is assumed to be non-relativistic, but sufficiently fast that the atom can be regarded as a sudden and small perturbation to it. This assumption permits the use of the Born approximation (Mott and Massey, 1965). No account is taken of exchange effects which may arise due to the indistinguishability of the interacting incident and atomic electrons. These effects are only important if the incident electron loses a significant fraction of its energy. This situation would be inconsistent with the previous assumption.

The incident electron has rest mass m_0, velocity v and charge $-e$, and collides with a stationary atom with atomic number Z in a state with energy E_0. The electron is scattered into an element of solid angle $d\omega$ centred about a direction (θ, ϕ) with respect to the beam direction. As a result the atom makes a transition to an energy state E_n. The electron loses energy $\Delta E = E_n - E_0$. The cross section for this process, differential in solid angle and energy loss, is $d\sigma_n$. The geometry of the collision is shown in figure 2.1. The momentum of the electron before and after the collision is given by $\hbar \underline{k}$ and $\hbar \underline{k}_n$ respectively. The momentum transferred to the atom is given by $\hbar \underline{K}$. Figure 2.1 also illustrates the momentum representation of the collision, and shows the range of possible values of $\underline{k}_n$ for particular values of momentum transfer magnitude K and ΔE.

$d\sigma_n$ is generally independent of ϕ. This can be because the atoms are oriented randomly or because the initial state is spatially symmetric. There can therfore be many transitions, corresponding to different directions for K, for which E_n is identical. $d\sigma_n$ can therefore be redefined as the cross section for a transition to any state of energy E_n involving a momentum transfer of hK. $d\sigma_n$ is now a function of the scalar variable K rather than θ. Use of the first Born approximation leads to the result

$$d\sigma_n = \frac{4\pi N_e m_0 e^4}{\hbar^4} \cdot \frac{1}{k^2 K^4} \left| \epsilon_n(K) \right|^2 d(K^2) \qquad (2.2)$$

$$d\Omega = 2\sin\theta \ d\theta$$

$$K = k + k' - 2kk'\cos\theta$$

$$2KdK = 2kk'\sin\theta \ d\theta$$

$$\Rightarrow d\Omega = \frac{\pi \ d(K)}{kk'}$$
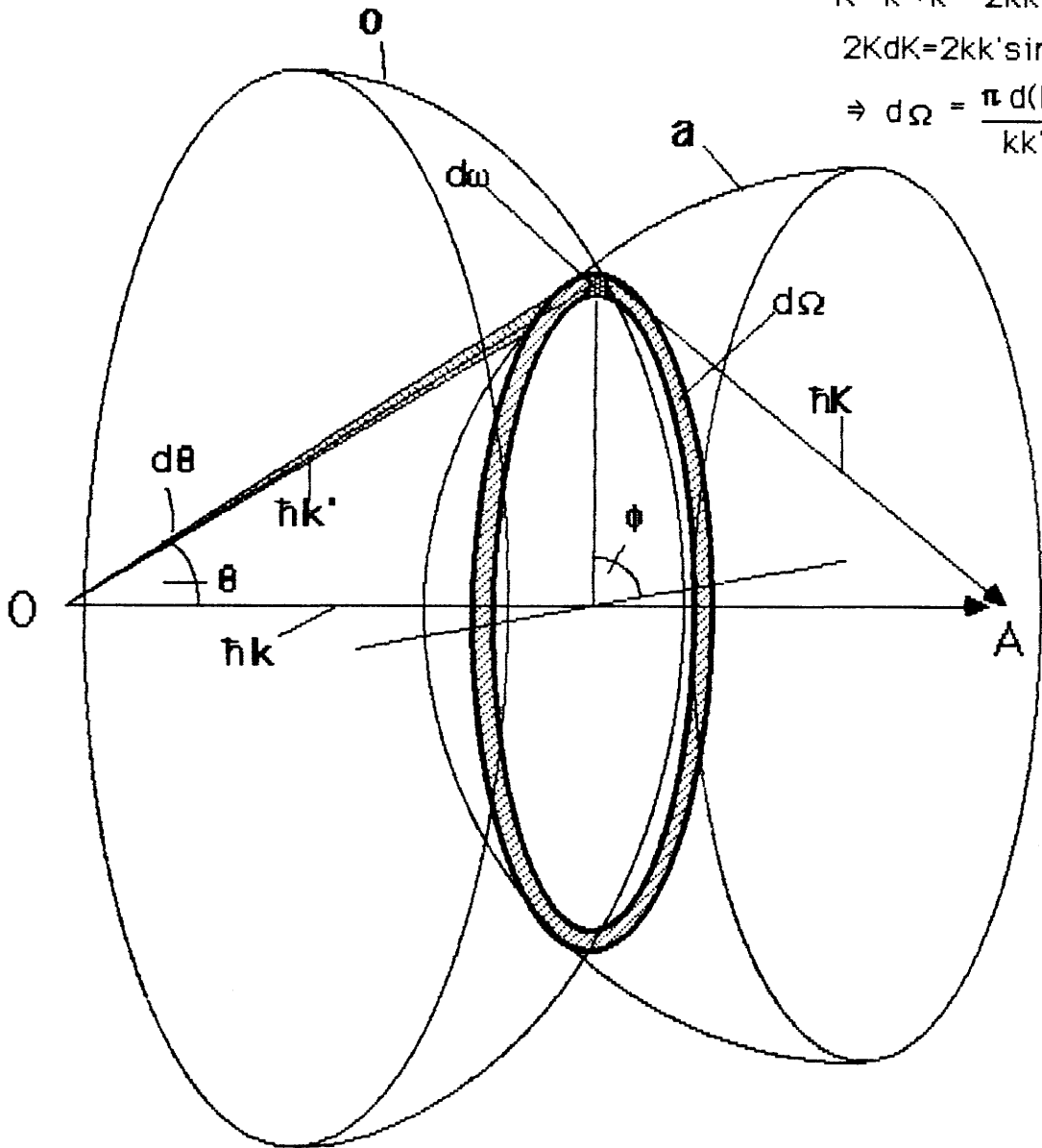
Figure 2.1

Scattering geometry and kinematics. Surface o is part of a sphere,
centred at O, on which the end point of the scattered electron
momentum vector, magnitude $\hbar k'$, must lie. Surface a is part
of a sphere centred at A, the end point of the incident electron
momentum vector, on which the end point of the momentum
transfer vector, magnitude $\hbar K$, must lie. The intersection of
these surfaces represents the locus of possible states for a
particular value of energy loss and momentum transfer. Due to
spatial symmetry, the cross section for all these states is
identical, and so it is a function of Ω rather than θ, and hence
of the scalar variable K.

where N_e is the number of electrons in the shell or sub-shell, and $\varepsilon_n(K)$ is an atomic matrix element

$$\varepsilon_n(K) = \langle n| \sum_{j=1}^{N} \exp(iKr_j) |o\rangle \qquad \textbf{(2.3)}$$

r_j is the coordinate of the jth atomic electron. Equation 2.2 can be considered to consist of two factors of different natures. The inelastic scattering form factor $|\varepsilon_n(K)|^2$ reflects the dynamics of the atom. The remaining terms are concerned with the incident electron only, and are equivalent to the Rutherford cross section for the scattering of an electron by a free and initially stationary electron (Rutherford, 1911). In atomic physics it is common to use the generalised oscillator strength (GOS) $f_n(K)$ instead of $\varepsilon_n(K)$. The GOS is given by

$$f_n(K) = \frac{\Delta E}{RKa_o} |\varepsilon_n(K)|^2 \qquad \textbf{(2.4)}$$

where R is the Rydberg energy, defined as

$$R = \frac{m_o e^4}{2\hbar^2}$$

and a_0 is the Bohr radius, defined as

$$a_o = \frac{\hbar^2}{m_o e^2}$$

It can be shown that $\lim_{K \to 0} f_n(K) = f_n$, where f_n is the dipole oscillator strength for the absorption of a photon of energy $\Delta E = hc/\lambda$ by the atom. The limit $K \to 0$ is approached for forward scattering at high velocities, in which case the scattering of fast particles follows a similar form to photoabsorption. Expressed in terms of the GOS, equation 2.2 becomes

$$d\sigma_n = \frac{4\pi a_o^2 N_e f_n(K)}{T/R \quad \Delta E/R} d(\ln(Ka_o)^2) \qquad \textbf{(2.5)}$$

where $T = 1/2\, m_0 v^2$.

2.3 Partial cross sections for EELS

In EELS analysis it is necessary to know the cross section for an electron losing energy ΔE and being scattered through all angles θ from 0 up to the spectrometer collection angle β. It is assumed that the incident electron can be described by a plane wave. Correction for the case of a convergent electron beam is discussed in chapter 3. Equation 2.5 expresses $d\sigma_n$ in terms of $(Ka_0)^2$. The relationship between $(Ka_0)^2$ and θ is derived from conservation of energy and momentum, and is given by

$$
(Ka_0)^2 = \frac{2T}{R}\left(1 - \frac{\Delta E}{2T} - \left[1 - \frac{\Delta E}{T}\right]^{\frac{1}{2}} \cos\theta\right) \tag{2.6}
$$

$\theta = 0$ corresponds to $(Ka_0)^2_{min}$, $\theta = \beta$ to $(Ka_0)^2_{max}$. The cross section, integrated over all possible values of $(Ka_0)^2$, is given by

$$
\frac{d\sigma_n(\beta)}{d(\Delta E)} = \frac{4\pi a_0^2 N_a}{T/R} \int_{(Ka_0)^2_{min}}^{(Ka_0)^2_{max}} \frac{df_n(K,\Delta E)}{d(\Delta E)} \frac{R}{\Delta E} \, d(\ln(Ka_0)^2) \tag{2.7}
$$

The energy dependence is stated explicitly in equation 2.7. The partial cross section, for an electron losing energy within the range ΔE to $\Delta E + \delta$ is then given by

$$
\sigma(\delta,\beta) = \int_{\Delta E}^{\Delta E + \delta} \frac{d\sigma_n(\beta)}{d(\Delta E)} \, d(\Delta E) \tag{2.8}
$$

In order to evaluate this expression it is necessary to know the form of the GOS. This requires knowledge of atomic wave functions. The model most commonly used is the semi-analytic hydrogenic model of Egerton (1979,1984c). In this model the wave functions are taken to be solutions of the Schrodinger equation in the presence of a Coulombic potential. The results are correct for atomic

hydrogen, for which the wave functions are known exactly. For other atoms the effective nuclear charge felt by an atomic electron is affected by the presence of other electrons, necessitating a screening correction (Zener, 1930). In the case of the K-shell, the predominant interaction takes place close to the nucleus, so the outer shell electrons do not greatly distort the inner shell wave functions. It is to be expected that the hydrogenic model will give less accurate results for the L and higher order shells. Using the hydrogenic model, analytic expressions can be obtained for the GOS. These have been given by Egerton (1979), who shows that evaluation of $d\sigma_n(\Delta E, \beta)/d(\Delta E)$ using these expressions gives to a good approximation

$$\frac{d\sigma_n(\Delta E, \beta)}{d(\Delta E)} \propto \Delta E^{-s} \qquad\qquad (2.9)$$

where s is constant over a limited range of ΔE, but depends on β.

A plot of the GOS as a function of ΔE and $(Ka_0)^2$ is known as the Bethe surface. Figure 2.2 shows the Bethe surface for the case of atomic hydrogen (after Inokuti, 1971). A slice through the surface parallel to the $\Delta E/R$ axis at low $\ln(Ka_0)^2$ approximates to the GOS for photoabsorption. Note that the surface should extend as a plateau as $\ln(Ka_0)^2 \to -\infty$. The figure shows clearly the Bethe ridge, in which the scattering is concentrated for large $\Delta E/R$. The partial cross section $\sigma(\delta, \beta)$ can be thought of as the area under the Bethe surface within the bounds $0 < \Delta E < \delta$ and $(Ka_0)^2_{min} < (Ka_0)^2 < (Ka_0)^2_{max}$. The form of the Bethe ridge illustrates that the angle at which the scattering is centred becomes larger as the energy loss increases. The size of the spectrometer collection angle can therefore have a large effect on the shape of the spectrum. If the angle is small then many of the electrons scattered with high energy loss will not be collected.

Egerton wrote Fortran programs SIGMAK and SIGMAL to evaluate the energy-differential and partial cross sections for the K and L-shells respectively. SIGMAL was found not to predict accurately the shape of the energy differential cross section for δ close to zero. It fails to account for the 'delayed maximum' shape found experimentally (Ahn and Krivanek, 1983). Egerton modified SIGMAL to include an energy dependent correction factor to give closer agreement with experimental EELS results and photoabsorption data. The
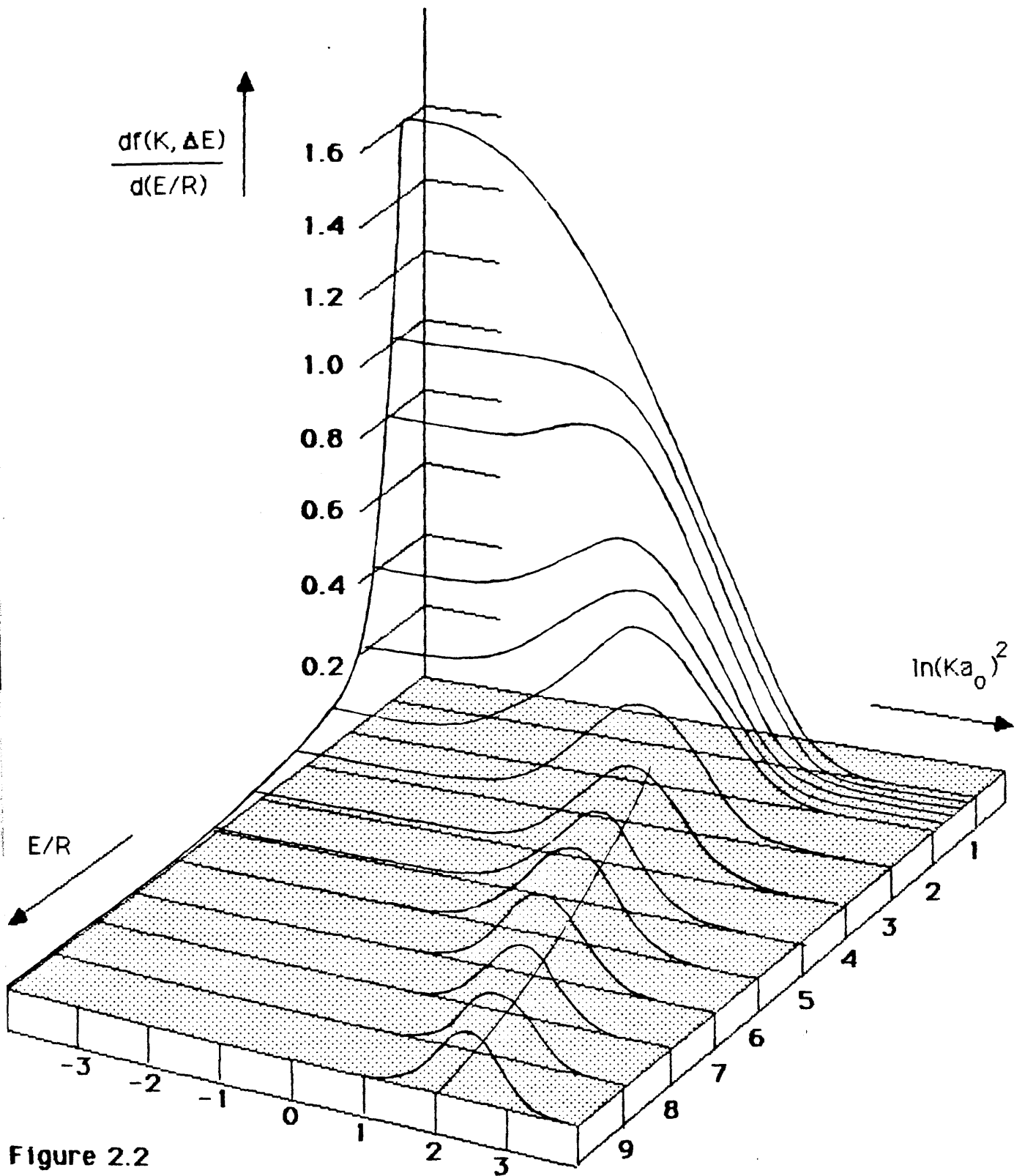
Figure 2.2

The Bethe surface for atomic hydrogen (after Inokuti, 1971). The curve on the base shows the position of the Bethe ridge..

resultant program was called SIGMALO. More recently (Egerton, 1984d), both SIGMAK and SIGMALO have been modified to take some account of relativistic effects by replacing $(Ka_0)^2{}_{max}$ with $(Ka_0)^2{}_{max}/(1-v^2/c^2)$. The modified programs are known as SIGMAKR and SIGMALR respectively. These last two programs have been used in the work described in this thesis.

The GOS has also been evaluated numerically using the Hartree-Slater model (Leapman et al, 1980 and Rez, 1984). In this model the potential is taken as a self-consistent central field. Leapman et al have compiled tables of the GOS as a function of K and ΔE for a limited range of elements. These can be used as data files for a program to calculate energy- differential and partial cross sections. A Fortran program INTG has been written for this purpose by Dr. P.A. Crozier, to run on an IBM mainframe. The program asks for β to be input, and then calculates the energy differential cross section at intervals of 5eV, 10eV or 15eV, the increment being specified in the data file. It then integrates over a user-specified energy range to give the required partial cross section.

Both models correctly predict the shape of the energy-differential cross section for the K-shell, and agree to within 10% (Egerton, 1984c). The differences between the predictions for the L-shell are generally greater, particularly when δ is small. These differences will be discussed in more detail in chapter 4.

2.4 X-ray production

There is a definite probability that the creation of a vacancy in an inner shell or sub-shell by ionisation will lead to the emission of an x-ray. The atom may de-excite by emitting either a photon or an Auger electron. The latter case corresponds to a radiationless transition taking place in which the available energy is used to release an outer-shell electron. The probabilities of these processes are expressed as the fluorescence yield ω for x-ray production and the Auger yield a for Auger electron production. These are related by the expression

$$\omega + a = 1 \qquad\qquad (2.10)$$

The situation is further complicated in the case of a shell which is split into a number of sub-shells (ie. any shell other than the K-shell) by the existence of radiationless Coster-Kronig transitions within the shell. These are discussed in chapter 7.

The energy of the emitted x-ray is equal to the difference between the energies of the initial and final states of the electron which makes the transition to fill the vacancy. For a given shell, there is a definite probability that a vacancy will be filled by a transition from each higher order sub-shell. Each possible transition leads to a line in the x-ray spectrum with a unique characteristic energy. Figure 2.3 shows the notation applied to each line which occurs due to transitions to the K and L-shells. The probability of a transition to a shell originating from a particular higher order shell is expressed as a partition function. The partition function s for the K-shell is given by

$$S = \frac{K_\alpha}{K_\alpha + K_\beta} \qquad (2.11)$$

where K_α is the number of transitions from the L-shell and K_β is the number of transitions from the M-shell. The probability of transitions to the K-shell from N and higher order shells is negligible. Values for ω and s will be discussed in chapters 6 and 7.

The cross section per unit solid angle σ_c for the production of an x-ray of a particular type is given by

$$\sigma_c = \frac{1}{4\pi} S \omega \sigma_i \qquad (2.12)$$

where σ_i is the total ionisation cross section. Derivation of an expression for σ_i is outlined in the next section.

2.5 Total ionisation cross sections for EDX-the Bethe form

For EDX analysis the appropriate cross section is the total ionisation cross section σ_i. This is obtained from equation 2.7 with $(K a_0)^2{}_{max}$ corresponding to
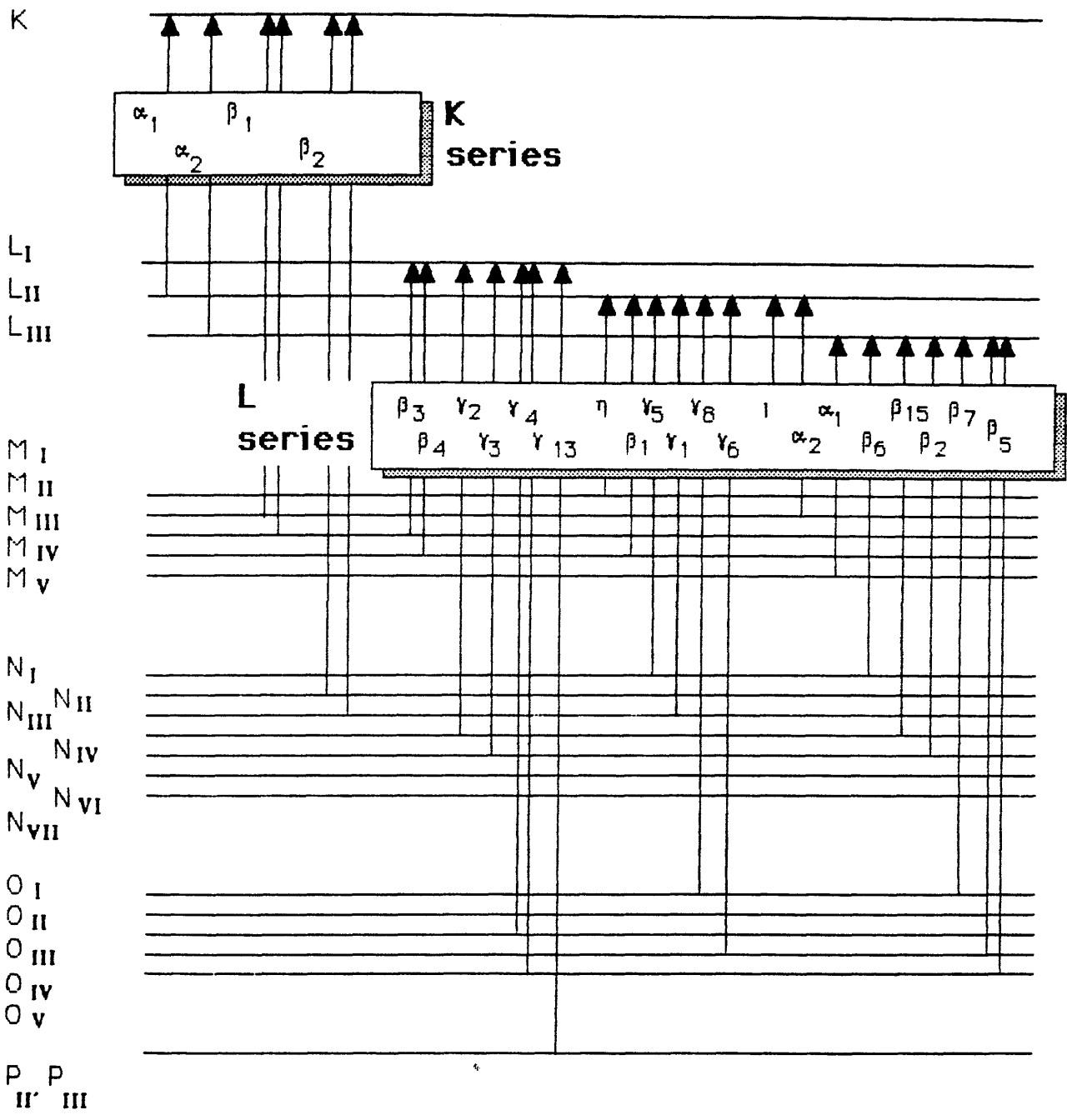
Figure 2.3

Nomenclature for x-ray lines arising from transitions to the K-shell and the L-shell from shells up to the P-shell.

the maximum kinematically allowed value of the momentum transfer, which occurs at $\theta=\pi$. The resultant energy differential cross section is then integrated over all energy transfers in the range $I_{shell} < \Delta E < T_0$, where I_{shell} is the binding energy of the shell or sub-shell of interest, and T_0 is the incident electron energy. This integration gives σ_i.

σ_i has been evaluated for a range of elements by Rez (1984) using the hydrogenic and Hartree-Slater models discussed in section 2.3. In principle it is possible to evaluate σ_i in this way for any element of interest, as is done in the case of partial cross sections for EELS. A more common approach for microanalysis is based on parameterisation of experimental cross section data. This is the approach considered in this thesis. A useful functional form on which to base such a parameterisation is the Bethe form (Bethe, 1930). The derivation of this form assumes that T is large. In this case an asymptotic approximation can be made in which the integral of equation 2.7 is replaced by the product of the optical GOS f_n and an average value of $\ln(K a_0)^2$. Bethe used hydrogenic wave functions to give

$$\sigma_i = \frac{2\pi e^4 N_e}{T I_n} b_n \ln \left[\frac{c_n T}{I_n} \right] \qquad (2.13)$$

The parameters b_n and c_n are determined in principle from the Bethe surface. Several sets of values of b_n and c_n have been published, and these have been reviewed by Steele (1987). The values in the literature are based on theoretical calculations and on fits to experimental data. The latter approach will be discussed further in chapter 6. Note that the Bethe form assumes hydrogenic wave functions, and so the comments in section 2.3 regarding the accuracy of that model for shells other than the K-shell apply here also. The case of the L-shell will be discussed in chapter 7.

The foregoing neglects relativistic effects. In order to extend the range of incident electron energies to which the model may be applied, a relativistic form of equation 2.13 is discussed by Inokuti (1971). The appropriate expression is

$$\sigma_i = \frac{2\pi e^4 N_e}{(\frac{1}{2}m_o v^2)I_n} b_n \left[\ln\left(\frac{c_n(\frac{1}{2}m_o v^2)}{I_n}\right) - \ln(1-\beta^2) - \beta^2 \right] \quad (2.14)$$

where $\beta = v/c$. The velocity dependence is stated explicitly in equation 2.15. It should be noted that the parameter $T = 1/2m_0v^2$ used in previous equations is not generally identical to the incident electron energy $T_0 = eV_0$, where V_0 is the accelerating voltage. For $T_0 = 100keV$, the difference is ~25%. Many workers, eg. Gray et al. (1983), replace T by T_0 when using the non-relativistic Bethe form. This substitution, while strictly incorrect, does not greatly affect the accuracy of the predicted cross sections since the results depend on empirical parameterisation. This is only true if the Bethe parameters used have been deduced using the same substitution. This approach is adopted in this work in order to allow direct comparison with the results of Gray et al. When considering the relativistic form, $1/2m_0v^2$ is used in place of T_0 to remain consistent with the results derived by Steele (1987) from the experimental data of Gray et al.

2.6 Other contributions to the EELS spectrum

Cross sections calculated according to the theory outlined in sections 2.2 and 2.3 are based on the assumption of single scattering by isolated atoms. Such theory cannot explain the aspects of EELS spectra which arise due to solid state effects in real specimens. In a solid the energy levels of each atom become broadened into bands. This leads to the existence of fine structure in the shape of the spectrum within the first 25eV above the ionisation threshold energy for each shell. This effect is known as energy loss near edge fine structure (ELNES). There is considerable uncertainty over the precise nature of this effect (eg. Colliex and Mory, 1984). Backscattering of the ejected electrons by neighbouring atoms can produce an interference effect leading to redistribution of the GOS over a longer energy range. This effect is known as extended energy loss fine structure (EXELFS).

The assumption of single scattering becomes increasingly invalid as the specimen thickness t increases. Plural inelastic scattering by valence electrons becomes important when t exceeds the mean free path λ for valence shell excitations. In metals or insulators with a small band gap, the incident electron

can lose ~25eV of energy by exciting an oscillation of the valence electrons. Such an oscillation is known as a volume plasmon. The probability of an electron being scattered n times by this mechanism in the specimen is given by the Poisson formula

$$P_n = \left(\frac{t}{\lambda}\right)^n \frac{\exp\left(\frac{-t}{\lambda}\right)}{n!} \qquad (2.15)$$

Clearly the single scattering approximation is most closely approached when $t \ll \lambda$, in which case the majority of incident electrons do not lose energy by plasmon excitation. For 100keV electrons, λ is generally in the range 500-1500Å. Colliex and Mory (1984) and Egerton (1984b) detail how calculated values of λ can be used to deduce specimen thickness from EELS spectra.

Chapter 4 discusses how the shape of the characteristic signals in the EELS spectrum is affected by solid state effects and plural scattering. The difficulties presented by these in quantitation by comparison of the spectrum with atomic cross sections is of particular interest.

2.7 The non-characteristic background in the EDX spectrum

Interaction with the nuclear field of the target atom can cause an incident electron to undergo a transition between two states in the continuum. This process results in the emission of a photon whose energy, in the range OeV to T_0, is not characteristic of the atom. This radiation is known as bremsstrahlung, and produces a continuous background beneath the characteristic peaks in the EDX spectrum. Theoretical treatments of bremsstrahlung production have been reviewed eleswhere by Robertson (1979). Two main approaches exist for the derivation of expressions for the bremsstrahlung cross section. The Sommerfeld theory (Sommerfeld, 1931), evaluated by Kirkpatrick and Weidmann (1945), gives the most widely used expression. It is not valid for high incident electron energies and high photon energies. Bethe-Heitler theory (Koch and Motz, 1959) is based on the Born approximation. It does not suffer from the restrictions which apply to the Sommerfeld theory. Its reliance on the Born approximation, however, dictates that it becomes less reliable for target atoms with high atomic number, and for

low incident electron energies. A modified Bethe-Heitler (MBH) theory incorporates a Coulomb correction based on the Elwert factor (Elwert, 1930) which reduces the seriousness of these restrictions. A screening correction is also included (Gluckstern and Hull, 1953), which should improve the accuracy of the model for low photon energies.

Chapman et al. (1983) compared the predictions of these theories with their experimental data. Photon energies in the range 3-30keV were considered, the lower limit being dictated purely by the rapid fall-off in detector efficiency for photons with energy lower than this value. They found that the MBH theory yielded the most satisfactory results. This conclusion is supported by comparison with the exact but incomplete calculations of Pratt et al.(1977). This comparison has been made for photon energies down to 0eV by Adam (1986). It appears that, over the range of interest in microanalysis using transmission or scanning transmission electron microscopes, MBH should be accurate to within 5%, and it is this theory which is adopted for the work presented in this thesis.

Some general properties of bremsstrahlung production are predicted by Kramers' law (Kramers,1923). Its cross section is approximately proportional to Z^2, $h\nu^{-1}$ and T_0^{-1}. Bremsstrahlung intensity therefore falls off monotonically with increasing photon energy. The Z^2 dependence suggests that the background in an EDX spectrum will be largely due to the heavier elements present. In view of these properties, it is often useful to define a reduced cross section σ'', which is related to the bremsstrahlung production cross section $\sigma_b(h\nu,\Omega)$, differential in energy and solid angle Ω, by

$$\sigma'' = \frac{T_0\, h\nu}{Z^2}\, \sigma_b(h\nu,\Omega) \qquad (2.16)$$

This definition removes the most significant dependence of the cross section on Z, $h\nu$ and T_0. The full MBH equation for σ'' is given in appendix A.

Finally, it should be noted that bremsstrahlung production is anisotropic. The maximum intensity occurs at an angle $\theta < 90°$ to the incident electron beam direction, and then falls off monotonically with increasing θ. This contrasts with the isotropic nature of characteristic x-ray emission.

17

Chapter 3

Instrumentation

3.1 Introduction

The experiments described in this thesis made use of three electron microscopes. Two of these were of the scanning transmission electron microscope (STEM) type: an extended VG HB5 STEM in the Department of Physics & Astronomy at Glasgow University; and a VG HB501 STEM at AERE Harwell. The third was a JEOL 2000FX transmission electron microscope (TEM) at the IBM Almaden Research Centre. This chapter separately describes each microscope together with its associated detectors and spectrum acquisition systems. This is followed by a description of the computer and software used in the analysis of data from all the microscopes.

3.2 The VG HB5 STEM (Glasgow University)

This section describes the HB5 STEM and the operatingconditions used in this work. Much of this applies also to the similar HB501 STEM, but there are several differences between the two instruments which will be pointed out in the next section. This type of microscope has been found to be highly suited to EDX microanalysis because of its low instrumental contribution to x-ray spectra. Figure 3.1 shows schematically the complete column of the HB5, illustrating the interrelation of the component parts. In the STEM lenses C1 and C2 here form a image of the electron source in the plane of the selected area aperture (SAA). The objective lens pre-specimen field transfers this image to a demagnified image of the source, or probe, on the specimen. The probe, can be scanned in a raster over an area of the specimen. Selected parts of the transmitted electron signal are then used to modulate the intensity on synchronously scanned monitors to form an image. The magnification of the STEM depends purely on the size of the specimen area scanned, the resolution available being dependent on the size of the probe. For microanalysis the probe can be held stationary at a point on the specimen, and electron or x-ray signals
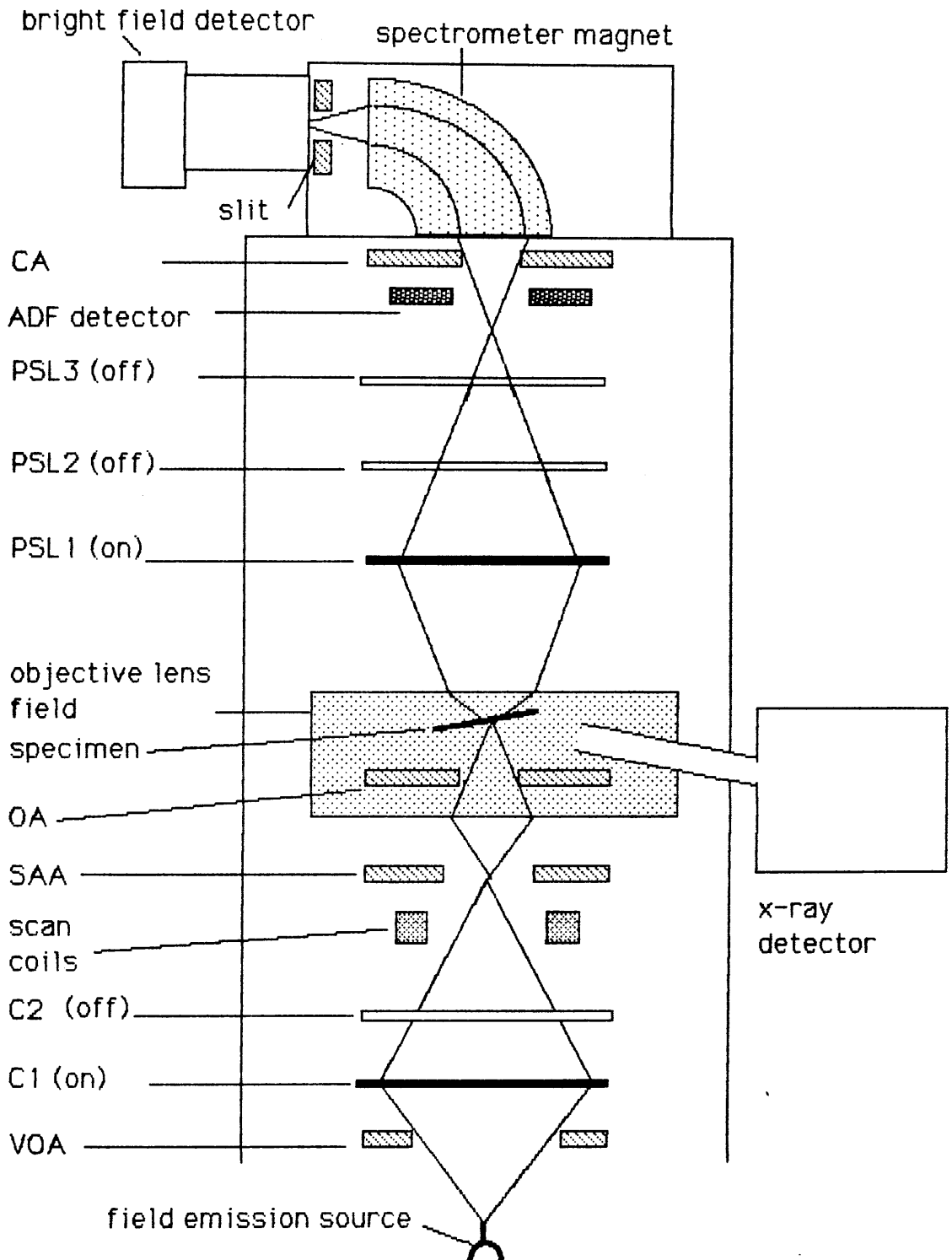
Figure 3.1. Schematic diagram of the extended VG HB5 STEM column, in a standard microanalysis mode using C1, objective and PSL1 lenses only.

from that point used to provide information on the local elemental composition.Details of the source and the various stages of the electron optics are described separately in this section. The HB5 was used for the collection of both EELS and EDX data. The electron and x-ray detection systems fitted to the HB5 are also described here.

3.2.1 The field emission source

Microanalysis with high spatial resolution has the conflicting requirements of small probe size and high count rates. The former is necessary to allow data to be recorded from very small areas of the specimen, while the latter is desirable so that data with good statistical accuracy can be recorded within a reasonably short time. The most suitable source type should maximise the current available within a given probe size. For small probes the field emission source, as described in detail by Crewe (1971), provides more current than a conventional thermionic source. Craven (1979) showed the relationship between probe diameter and current for the HB5, which is equipped with a cold field emisson source, and a thermionic source with a brightness of 5×10^{5} A cm^{-2} sr^{-2}. In the case of the HB5, the variation of probe diameter with current is affected by aberrations which limit the minimum probe diameter attainable to ~5Å. Its behaviour cannot be described by a simgle value of brightness. For larger probes, $>$~1μm, a thermionic source can provide more current than a field emission source.

A field emission gun requires more stringent operating conditions than a conventional source. A vacuum of ~10^{-10} torr is required for cold emission. In the HB5 the gun chamber is separated from the rest of the column, which has a vacuum of ~10^{-9} torr, by a differential pumping aperture. The tungsten tip is susceptible to the accumulation of contaminants. This leads to unstable emission, and can result in the destruction of the tip by vacuum arcing. It is normal practice to pass a high current through the tip for a short period at intervals of ~ 30 minutes during operation to remove contaminants and surface irregularities. This processes is called "flashing" the tip.

3.2.2 Pre-specimen optics

The HB5 has a double condenser lens system, which allows greater flexibility

in the probe forming conditions than a single lens. For microanalysis, however, the use of lens C1 alone allows a suitable probe to be defined. The excitation of C1 is usually set so that a focussed image of the source is formed in the same plane as the selected area aperture   . As the beam is scanned across the specimen in image mode, the SA A limits the part of the scan during which electrons are allowed to reach the specimen, and hence the area of the specimen illuminated. The convergence angle of the probe is limited by either the objective aperture (OA) or the virtual objective aperture (VOA). The convergence angles corresponding to each aperture size available have been calculated by Crozier (1985). The values used here are given in sections 3.2.4 and 3.2.5.

The HB5 has a Z-lift specimen stage. Focussing the probe on the specimen can therefore be done either by adjusting the objective lens excitation or by adjusting the specimen height. It is thus possible to have a standard objective excitation, and to focus using the Z-lift facility. This procedure ensures that the optical configuration of the column is always the same. If the specimen is tilted, then the Z setting is altered to maintain focus while moving between different areas of the specimen. This means, for example, that x-rays reaching the x-ray detector always emanate from the same point in space.

3.2.3 Post-specimen optics

The post-specimen optics have the task of ensuring that the angular distribution of the electrons transmitted through the specimen is matched to the physical sizes of the detectors in use. The Glasgow HB5 has been modified by the addition of three post-specimen lenses (PSLs), PSL1, PSL2 and PSL3. This modification allows the angular distribution of the electrons transmitted through the specimen to be easily matched to the size and shape of the detectors. In this work only the annular dark field (ADF) and bright field detectors were used, and only these are shown in figure 3.1.

The angular distribution of the electrons entering the electron spectrometer is limited by the collector aperture (CA). The collection angle is determined by the angular compression of the PSL or combination of PSLs in use. As for the probe convergence angle, the available values of collection angle have been measured by Crozier (1985). The values used in this work are given in section 3.2.4.

20

3.2.4 Operating conditions for EELS and the electron spectrometer

EELS spectra were always recorded with the probe stationary. Quantitation in EELS depends on knowledge of the collection angle β. It is desirable to select a PSL configuration which introduces as small a chromatic aberration as possible (Crozier, 1985). Chromatic effects can affect the resolution in the EELS spectrum (Craven and Buggy, 1981). For imaging, PSL3 was usually used on its own. This lens, in combination with a 500μm CA, defined a collection angle β=3.1mrad. This small collection angle gives rise to high contrast. For the collection of energy loss spectra, however, PSL1 only was always used in this work. In combination with the 500μm CA, this lens defined a collection angle β=27mrad. Before using this value of β in the calculation of partial cross sections it was necessary to consider the effect of the convergent probe. Joy et al.(1980) suggested the use of an effective collection angle β^* in which the effect of the convergence error has been incorporated. Calculations by Crozier (1985) showed that for β=27mrad β^* is close to β provided that $\alpha<\sim$15mrad. This was always the case here, and so no probe convergence corrections were necessary.

The PSLs form an image in the object plane of the electron spectrometer. The spectrometer on the HB5 is a VG Mk I sector magnet spectrometer. It collects electrons either to form the bright field image or to produce an energy loss spectrum. The spectrometer magnet deflects the incoming electrons fixed angle onto a variable width slit in front of the electron detector. The angle through which an electron is deflected depends on its energy, and so an energy loss spectrum is formed. Deflection coils allow this spectrum to be scanned across the slit and recorded serially. The spectrometer dispersion plane is at an angle to the plane of the slit, so it is not possible to focus the whole spectrum simultaneously. Usually the PSL excitation was adjusted so that a particular feature, such as the zero-loss peak or a characteristic edge, was in focus. The energy resolution is limited by aberrations. For this design of spectrometer, second order aberrations are most significant. These are proportional to the square of the spectrometer acceptance semi-angle (Egerton 1984b). As a result the resolution in the spectra was generally rather poor, especially since a large collection angle was chosen in the interests of maximising the collection efficiency and hence the count rate.

3.2.5 Operating conditions for EDX

The pre-specimen optics can be set up to satisfy two basic requirements in EDX :-

1. The intensity of x-rays emanating from the specimen should be such that the count rate at the detector is high enough that there are sufficient counts in the spectral region of interest to provide the required statistical accuracy without the spectrum taking an unreasonably long time to record. The count rate should not, however, be so high that the detector is saturated. The number of photons emitted depends on the current in the incident electron beam, which in turn depends on the probe convergence angle. This can be selected by making a suitable choice of OA or VOA.

2. The possibility of radiation reaching the detector from sources other than close to where the electron probe is centred should be minimised. The OA plane is in a position such that electrons scattered from the edge of the aperture can easily lead to the production and subsequent detection of such "stray" x-rays. It is preferable therefore to define the probe convergence angle by means of a VOA. EDX spectra are usually recorded with the beam stationary, or scanning over a very small area of the specimen. This means that the beam should not strike the edge of even the smallest SADA, which should not therfore give rise to any stray radiation. Such stray radiation emanating from the VOA will, however, generally not pass through the SADA, and is therefore prevented from contributing to the spectrum.

Taking these factors into consideration, EDX spectra were usually recorded with a 100um VOA, defining a probe semi-angle α = 11mrad, or a 50μm VOA, defining α = 5.5mrad. A 50μm SADA, the smallest available, was used as a "spray" aperture.

3.2.6 Electron detectors on the HB5

A photoelectric electron detector consists of a scintillator coupled via a light pipe to a photomultiplier tube. When an electron strikes the scintillator a burst

of photons is produced, some of which produce photoelectrons in the photomultiplier. This small current is then amplified in the photomultiplier tube. The resultant current pulse can be used modulate the signal sent to a cathode ray tube to produce an image. The HB5 has two such detectors. The ADF is in the form of an annulus, and detects electrons which have been scattered through angles larger than those which are collected by the spectrometer. The ADF detector is used to form a dark field image. The bright field detector is positioned so that it collects electrons which have passed through the spectrometer. This detector is used both for forming images and for collecting EELS spectra. The signals from it can be passed to the EELS acquisition system where they are counted.

3.2.7 The Si(Li) x-ray detector

The Si(Li) detector is common to all the microscopes used in this work. This section gives a general description of this type of detector, and then describes the installation found on the HB5. The installations on the other microscopes are described later.

A Si(Li) detector consists of a cooled piece of lithium drifted silicon crystal in between two electrodes with a bias of ~500V across them. A photon entering the crystal ionises a Si atom, causing the emission of a photoelectron. De-excitation of the Si ion causes either an Auger electron or a Si x-ray to be emitted. These x-rays are absorbed by similar mechanisms. Eventually all the energy of the incident photon is carried by photo and Auger electrons. These lose their energy by producing a cascade of electron- hole pairs. The electrons are drawn by the applied bias toward the n type Si of the back surface, the holes to the p type Si at the front surface. A pulse of current proportional to the incident photon energy is collected. The pulse is amplified and its height measured. The channel of a multi-channel analyser which represents the correponding photon energy is then incremented.

If the efficiency of the detector is unity for photons of a particular energy then all such photons will be detected. In practice this is not always the case. Low energy photons may be absorbed before they reach the crystal. In the case of conventional detectors, the crystal is separated from the microscope vacuum by a protective Be window with a typical thickness of ~10μm. Absorption in this

window is the most significant factor in limiting the detection efficiency for low energy photons. Below ~3keV the efficiency falls off rapidly with decreasing photon energy. No characteristic lines are detected for elements with Z<11. The efficiency at low energies is improved if the Be window is replaced with an ultra-thin window or removed altogether. Such detectors are known as UTW and windowless detectors respectively.

Whether or not the detector has a window there are two other sources of absorption which contribute to a lesser extent to the fall off in efficiency at low photon energies. Some absorption takes place in the Au contact at the front surface of the crystal. The Si of the detector crystal is generally not uniformly efficient in transferring the incident photon energy to a pulse of current at the electrodes. It is often assumed that there is a layer of completely inactive Si at the front surface of the crystal. In many calculations of detector efficiency this dead layer is considered to be an extra layer of absorber in front of the active part of the crystal. In fact this is an oversimplification. Rather than being absorbed without being detected at all, it appears that the incoming photon produces the expected cascade of charge, some of which is trapped without being detected. This phenomenon is known as incomplete charge collection (ICC). Adam (1985) discussed in detail several proposed mechanisms by which the charge carriers may be trapped. He concluded from consideration of experimental peak shapes that ICC is probably not a bulk crystal effect, but instead occurs within a layer at the crystal surface. The result of ICC in practice is to distort the peak shapes in the EDX spectrum from their ideal gaussian shape by distributing a proportion of the counts in the peak over a range of energies below the peak energy. This proportion is dependent on the mass absorption coefficient for photons with that energy in Si. Adam quantified this effect for the detector on the HB5.

High energy photons (>~20keV) may pass through the detector crystal without being absorbed at all. Clearly if this happens the photon is not detetcted. The higher the energy of a photon, the greater will be its penetration. The efficiency of the detector therefore falls off with increasing photon energy in a way which depends on the thickness of the crystal.

The detector fitted to the HB5 was a Link Systems Si(Li) detector, of the conventional Be window type. It was mounted at an angle of 100.5 degrees with

respect to the incident electron beam direction. This angle we define as the take-off angle θ. It should be noted that other definitions of take-off angle are sometimes used by other authors. θ is sometimes defined with respect to the horizontal specimen plane.

3.2.7 EELS acquisition on the HB5

EELS spectra from the HB5 are collected under the control of a Toltec minicomputer system. (This system also offered facilities for EDX and image acquisition, but these were not used in this work). The system is configured to act as a multichannel analyser. The spectrum display capability is based around a GEMs framestore. The computer controls the spectrometer scan coils described in section 3.2.4 to allow the data in channels of width usually 1ev to be acquired each for a preset period known as the dwell time. The spectrum is usually scanned from high to low energy losses to eliminate decay tailing effects in the scintillator after the zero-loss peak has passed across it.

The EELS spectrum has a very wide dynamic range, typically from ~10^{10} electrons/second in the zero-loss peak to ~10^2 electrons/second at high energy losses. The acquisition system on the HB5 relies on two different forms of counting: a pulse counter which allows single electrons to be counted, but saturates at the high count rates of the low-loss region; and an analogue counting system based on a voltage to frequency converter (VFC), which is not limited by saturation, but is rendered unsuitable for measuring low count rates by dark current. The spectra recorded on by these methods are referred to as the pulse and current spectra respectively. This acquisition system has been described in detail by Craven and Buggy (1984).

The acquisition software was supplied by Toltec. The EELS menu allows the user to set values for the acquisition parameters. The function of each parameter is described in detail by Crozier (1985). The specific values used in this work are listed in table 3.1. The software package contains basic spectrum display and manipulation routines. Several extra analysis and manipulation programs have been written at Glasgow University and incorporated into the Toltec software. Details of these are given in the description of EELS analysis procedures in chapter 4.

Beam voltage : **100keV**

Count limit : maximum number of counts in any channel, **10^6**

Channel width : **1eV**

Number of channels : **1024**

Start energy : energy loss of first channel in spectrum, **-100eV**

Zero loss offset : energy of undeflected beam, **546eV**

Rest energy : energy which passes through slit when spectrum is not being recorded, set to **2000eV** to avoid saturating scintillator.

Base dwell : dwell time for a channel, **10ms**

Pulse/current words : number of words in counter that the computer reads after each dwell time, **2**

Table 3.1. Values used in this work for the main parameters in the Toltec EELS acquisition menu.

3.2.9 EDX acquisition on the HB5

All x-ray spectra from the HB5 were acquired using a Link Systems 860 series computer. Spectrum acquisition took place under the control of a stand-alone operating system (SOS) analyser. This analyser stores spectra as numbered tracks on a floppy disk. The 860 can also acquire spectra using an analyser program running under the LDOS operating system. LDOS is based on the Data General Disk Operating System (DOS). An LDOS spectrum is stored as a disk file, in the form of a header block and a series of blocks of spectrum data, the contents of each channel being stored as an integer. The header block contains information about the spectrum such as its label, ev/channel, etc. These spectra can be read and manipulated by user-written software running under LDOS. The SOS analyser is more convenient to use for acquisition. It is, however, limited in the facilities which it offers for analysis. In practice, spectra were acquired using the SOS analyser, and converted to 860/LDOS format using a program supplied by Link.

3.2.10 Specimen cartridges

Two different types of specimen cartridge were used in the HB5. The base of the cartridge was the same in each case, to the standard VG design. The differences lay in the area in which the specimen was mounted. Figures 3.2(a) and (b) illustrate these differences. Figure 3.2(a) shows the standard VG Be double-tilt cartridge. The specimen can be tilted about two axes. The cartridge is loaded in an orientation such that tilting equal amounts about the X and Y axis causes the specimen to be tilted directly towards the x-ray detector. Adam (1986) considered that the large amount of bulk material in the vicinity of the specimen with this cartridge might result in a spurious contribution to the background in EDX spectra. Such a contribution would be difficult to detect since no characteristic lines from Be can be detected. The cartridge shown in figure 3.2(b) was designed and built at Glasgow University by Dr W.A.P. Nicholson and Dr P.F. Adam. It is based on a VG cartridge "blank". The specimen is held in place, at a fixed tilt of ~15 degrees towards the detector, by two Cu "ears". The design is such that the amount of bulk material surrounding the specimen is minimised, to give as small an EDX background contribution from the cartridge as possible. This cartridge is therefore known as the fixed low background cartridge.

ɐp in direction of x-ray
ɛtector
) allow clear x-ray path

specimen grid (3mm diameter)

circlip to hold specimen
in place

Y-tilt assembly

X-tilt assembly

tilt assembly
supports
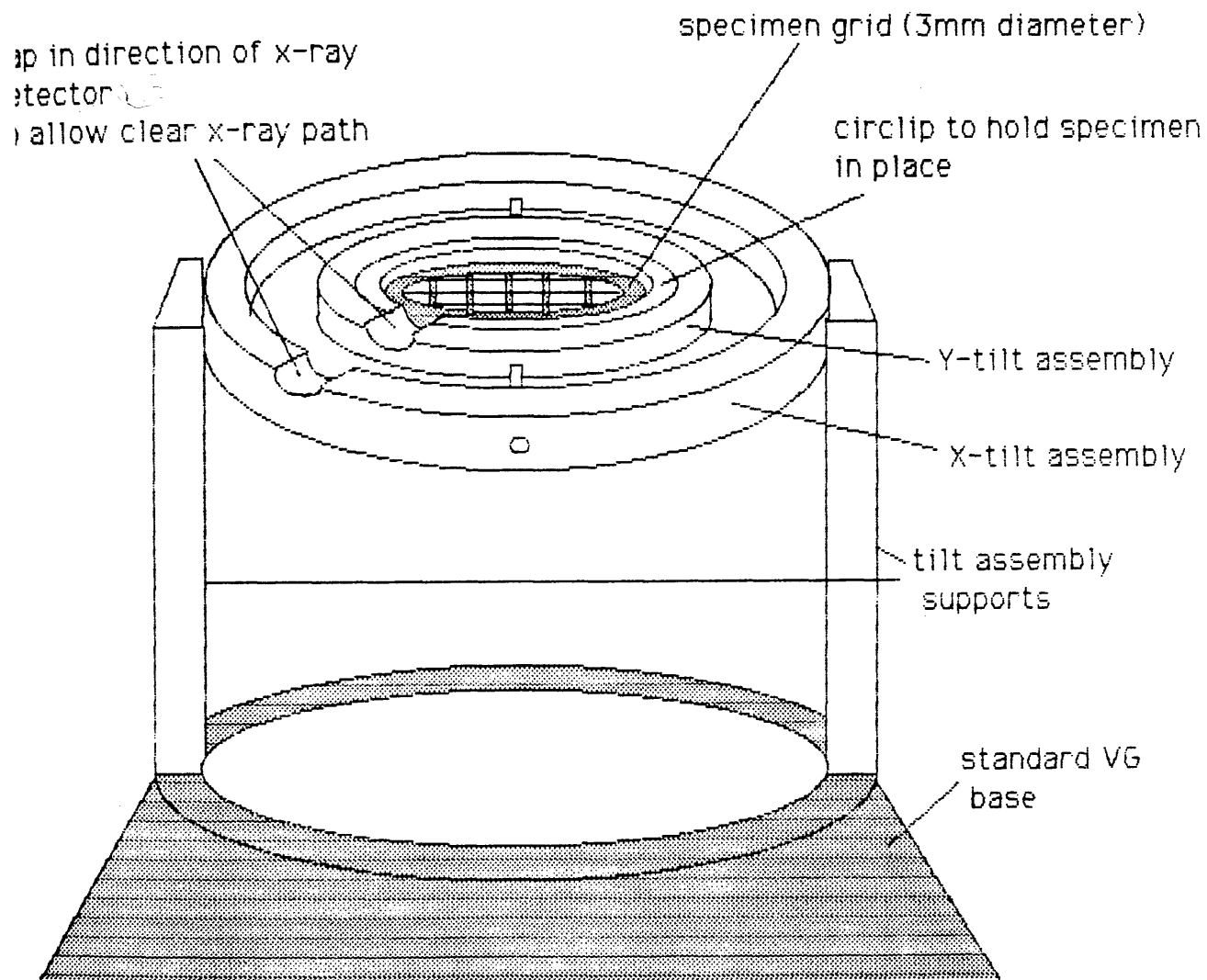
standard VG
base

Figure 3.2(a) Simplified illustration of standard VG double-
tilt cartridge specimen support assembly.
Tilt drive connections are not shown.

Cu "ears"   specimen grid (3mm diameter)

base
(slots into
standard VG
"blank")
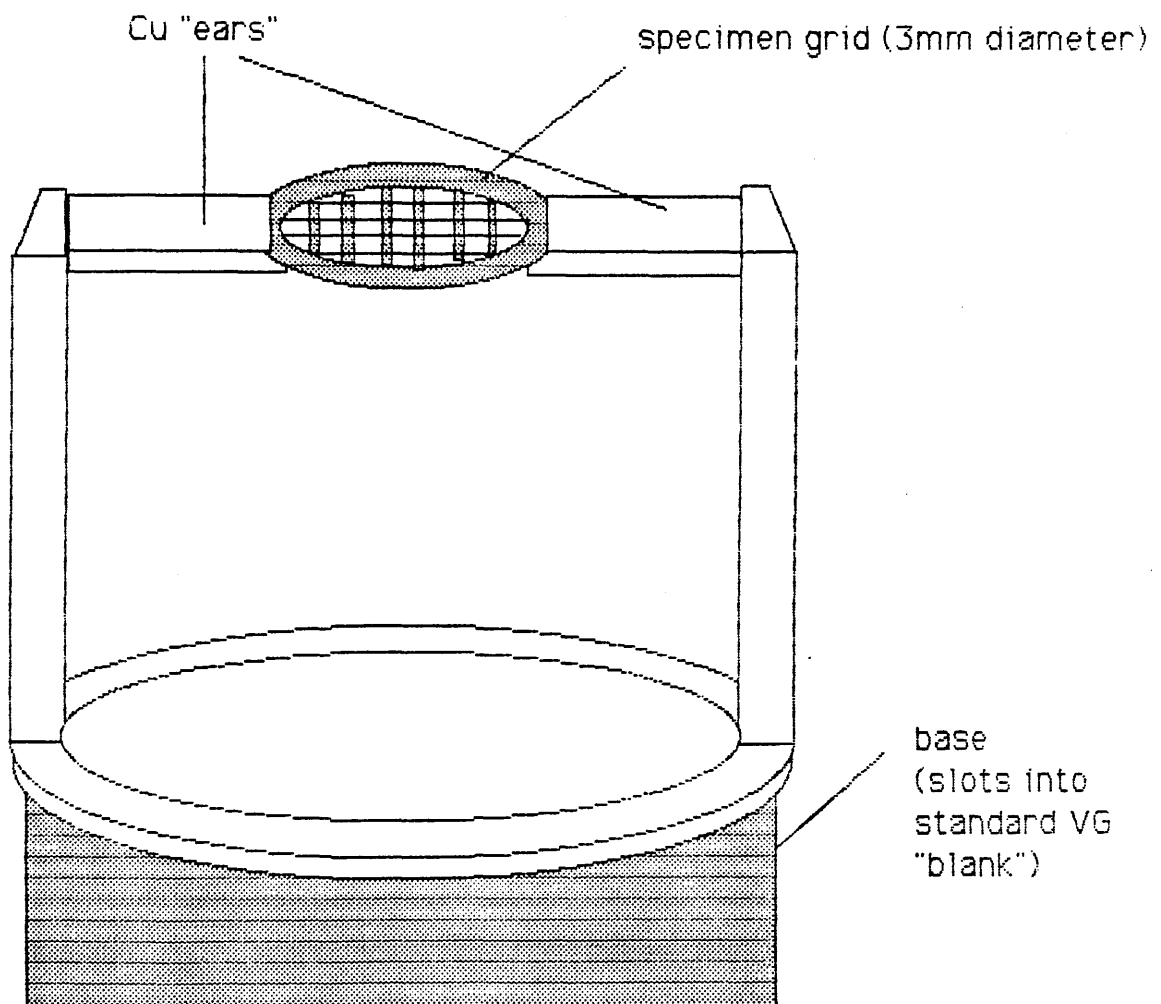
(b) Illustration of fixed tilt low-background holder
    for the VG HB5. The tilt assembly of the double-
    tilt cartridge is replaced by a simple arrangement
    of two thin Cu "ears", which results in there being
    much less bulk material in the vicinity of the
    specimen.

3.3 The VG HB501 STEM (AERE Harwell)

This microscope is similar in most respects to the HB5 which has already been described. There are, however, several differences, both on the microscopes and in the EDX acquisition facilities. These differences are detailed in this section. This instrument was not used to record any EELS data.

3.3.1 Differences between the HB501 and the HB5

The most obvious difference is that the HB501 does not have any post-specimen lenses. The angular compression produced by the objective lens post-specimen field is suitable for the formation of bright field and dark field images. This microscope is fitted with a VG mark II electron spectrometer. In this work the spectrometer was used only for the collection of bright field images. Dark field images were collected by an ADF detector as on the HB5.

The HB501 is not fitted with a Z-lift stage. The most important consequence of this was discovered when the fixed low background cartridge designed for the HB5 was used in this microscope. It appeared that the dimension of this cartridge in the Z direction was not equal to that of the standard VG design. The combination of specimen height and objective lens excitation variation gave a range of adjustment in the HB5 which allowed the probe to be suitably focussed on a specimen in this cartridge. To focus the probe of the HB501 when using this cartridge would require changing the excitation of C1 from the standard setting used for microanalysis. The SADA would no longer be in a position to act as a spray aperture. An increased instrumental contribution would therfore be expected, negating the purpose of using a low background holder. Two standard VG cartridges were used in the HB501. One of these was a Be double-tilt cartridge of similar design to that used in the HB5. The other was a single-tilt cartridge. This allowed a range of tilts from 0 degrees to ~60 degrees towards the x-ray detector.

The HB501 is fitted with an extra lens before the VOA, known as the gun lens. This lens focusses the electrons emanating from the source so that more of them reach the column, increasing the current in the probe.

3.3.2 EDX acquisition on the HB501

The vacuum in the column of a VG STEM is typically $\sim 10^{-9}$ torr. It is therefore possible to fit an x-ray detector with no Be window to protect the crystal. The advantages of using such a detector have been discussed in section 3.2.8. The HB501 is equipped with a Link Systems windowless detector, mounted at a take-off angle of 100.5 degrees to the incident electron beam. Spectra were acquired using a Link Systems AN10000 analyser. This system stores spectra as disk files on a Winchester disk drive. These can be transferred to floppy disks if required.

3.4 The JEOL 2000FX TEM (IBM Almaden Research Center)

A brief description only is given of this microscope since the experiments carried out using it were not performed by the author. Data from the JEOL TEM (EDX data only) were provided by Dr. W.A.P. Nicholson for detailed analysis. Section 3.2.1 discussed the advantages for microanalysis of using a FEG STEM when a small probe is required. This work did not, however, demand particularly high spatial resolution. As discussed in section 3.2.1, for relativley large probes the current provided by the conventional thermionic electron source with which this TEM is equipped could in fact be greater than that available with a field emission source.

The motivations for using these data were twofold. The 2000FX is a medium voltage electron microscope, allowing incident electron energies of up to 200keV. There were therefore data in a region of interest inaccessible using the VG STEMs, which which can only provide incident electron energies of 100keV. It was of particular interest to assess the extent to which relativistic effects could become important at such energies. In addition, this microscope was equipped with two x-ray detectors. Both of these were Kevex Be window detectors. One was mounted conventionally at a take-off angle of 90 degrees with respect to the incident beam direction. The second detector had a take off angle of 158 degrees. The configuration is illustrated in figure 3.3. Spectra were acquired using a Kevex 8000 system. There is considerable interest in high take-off angle detectors at present. They offer the possibility of minimising the path length through the specimen which x-rays must take before reaching the detector, without the need to tilt the specimen. It is clear from figure 3.3 that
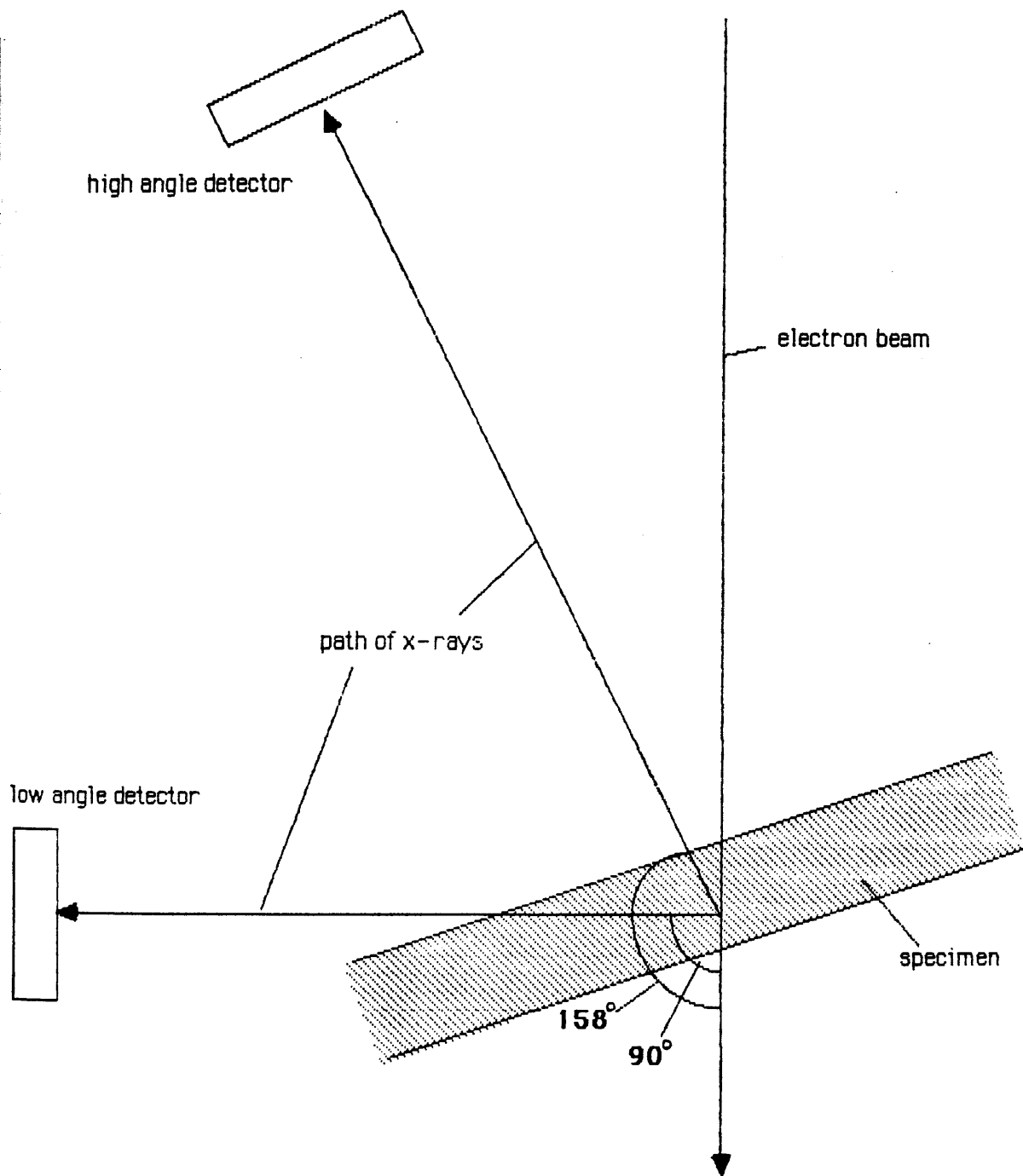
Figure 3.3 Schematic diagram of the configuration of the x-ray detectors on the JEOL 2000FX TEM. The specimen is shown tilted slightly. Clearly, the absorption path within the specimen for x-rays reaching the 158° detector is much smaller than that for the 90° detector.

the minimum possible absorption path for a 90 degree detector is longer than the absorption path for an untilted specimen in the case of a158 degree detector. Use of a high angle detector should therefore reduce the need for absorption corrections. In addition the anisotropic nature of bremsstrahlung emission implies that the non-characteristic background should be lower in spectra from a high angle detector than a low angle detector. This point is discussed in chapter 4.

The geometry of the objective lens region in most electron microscopes, including the 2000FX, presents difficulties in the installation of x-ray detectors at high take-off angles. The detector must "look" through a gap in the upper polepiece of the objective lens. It is not possible, therefore, to position the detector as close to the specimen as it is for a low angle detector. This has implications for the count rates which are achievable. A high angle detector is potentially in a position where it is more likely to detect spurious signal than a low angle detector. The effect of this in practice is illustrated by the results presented in chapter 4.

Specimens in the 2000FX were mounted in a side entry rod constructed entirely of titanium. Motivated by similar considerations to those which led to the design of the low background cartridge for the HB5, the design of the rod was such that the amount of bulk titanium in the vicinity of the specimen was minimised as much as possible.

3.5 EDX analysis software

The analysis which was carried out on the data in this work required specialised software not found in standard analysis packages. The software used was based on the ANALYSIS suite of programs written at Glasgow University by Dr P.F. Adam. These are described in detail and listed in his PhD Thesis (Adam, 1985). This package was written in FORTRAN to run under LDOS on the Link Systems 860 computer. The time-consuming nature of the analyses made it desirable to run the programs on a system which, unlike the 860, would not often be used for acquisition purposes. A system based around a Data General Nova 3 minicomputer was used. This system included spectrum display hardware and software such that it could emulate a Link Systems 290 analyser. It was not possible to incorporate any user-written software into the 290

analyser software. Consequently the spectra could not simultaneously be displayed and processed, it being necessary to quit from the user-written analysis program in order to display the processed spectra on the monitor, and vice versa The 290 analyser requires spectra to have a slightly different format from that required by the 860. It was decided to work with spectra always in 290 format, and to convert ANALYSIS to read spectra in this format. This conversion, which required new spectrum reading and writing routines, was carried out by Dr. W.A.P Nicholson. The resultant program, AN29, was run on the Nova 3 under Data General DOS. Some additional routines were written by myself and incorporated into AN29. Appendix B gives details of the facilities available using AN29, and describess the routines additional to those listed by Adam.

The spectra from the three microscopes were all stored in different formats by the various acquisition systems so that it was necessary to convert all the spectra to 290 format for analysis. Conversion between Link Systems formats was carried out using program LINKCON written by Dr. W.A.P. Nicholson and myself. This program allowed spectra to be converted to 290 format from 860/LDOS or AN10000 formats. Facilities for conversion of Kevex spectra to 860/LDOS format were provided by Dr. A.J. Garrat-Reed at Massachussetts Institute of Technology. These spectra could then be further converted to 290 format using LINKCON.

Appendix B gives details of the various Link Systems formats, and lists the conversion program LINKCON.

Chapter 4

X-ray analysis using K-shell signals

4.1 Introduction

This chapter describes the procedure by which the EDX spectrum can be used to obtain information about the elemental composition of a thin specimen. Firstly, the general form of the EDX spectrum is discussed, and the method of using characteristic signal ratios to deduce elemental concentration ratios introduced. Section 4.3 discusses methods of modelling the background in the spectrum, and describes the application of the theoretical model which is used throughout this work. This procedure allows the extraction of the numbers of photons detected which are characteristic of the elements in the specimen. Section 4.4 outlines two methods by which the factor relating this information to the concentration ratio is obtained. The method of using standard specimens of known composition is described briefly. An alternative approach involves calculation of the conversion factor from first principles. This requires knowledge of several atomic properties. The accuracy with which these are known is considered, particular attention being paid to the ionisation cross sections.

The remainder of the chapter is concerned with these cross sections. It is convenient to describe the ionisation cross section by a simple approximate functional form such as the Bethe model introduced in chapter 2. Previous results obtained using this model are briefly reviewed. Section 4.5 details experimental measurements made of ionisation cross sections using the JEOL 2000FX TEM described in chapter 3. These results were obtained by comparing the ratio of the counts in the characteristic peaks to the counts in the background beneath each peak with absolute bremsstrahlung cross sections calculated as described in section 4.3. The effect on these values of spurious contributions to the background is discussed. As an example the performances of the two detectors fitted to this microscope are discussed, and it is shown that the high-angle detector configuration is unsuitable for this work. Section 4.7 shows how the results from the low angle detector are fitted to the Bethe model.

Experimental values of cross sections determined using different microscopes should not differ. The final part of the chapter details an investigation of the invariability of the measured values. The data set of the previous section is expanded to include results from the two VG STEMs described in chapter 3. In conclusion, the likely accuracy and applicability of the cross sections predicted by the Bethe model is discussed.

4.2 The form of the EDX spectrum and the ratio technique

The x-rays which contribute to the EDX spectrum are produced by two different mechanisms, as described in chapter 2. An incident electron may ionise an atom in the specimen by causing an electron to be ejected from an inner shell. The vacancy can then be filled by a transition from a higher order shell, and a photon is emitted with energy $h\nu$ equal to the difference in energy between the two states involved. The value of $h\nu$ is characteristic of the atom, and so a peak appears in the spectrum at this energy. Interaction of the incident electron primarily with the nucleus produces bremsstrahlung, which is non-characteristic. Thus there is a continuous background in the spectrum, decreasing in size with increasing photon energy. The intensity of the bremsstrahlung due to a particular species of atom depends approximately on the square of the atomic number Z.

The information provided by the spectrum on the composition of the specimen is contained in the characteristic peaks. In this chapter, only the peaks arising from transitions to the K-shell are considered. The larger of the two significant K-shell peaks is the K_α peak. The number of characteristic K_α x-rays due to an element Z detected at its K_α characteristic energy $h\nu_Z$ is given by .

$$P = N_0 \, A^{-1} \, \rho x \, i \, t \, \varepsilon(h\nu_Z) \, S \, \omega_K \, \sigma_{iK} \, d\theta/4\pi \qquad (4.1)$$

where N_0 = Avogadro's number

A = atomic weight of the element

ρx = specimen mass thickness

i = incident beam current in electrons/sec

t = live time

$\varepsilon(h\nu_z)$ = detector efficiency at photon energy $h\nu_z$

s = partition function for K_α to total K-shell x-ray yield

ω_K = K-shell fluorescence yield

σ_{iK} = K-shell ionisation cross section

$d\theta$ = solid angle subtended by the x-ray detector

Usually the information required concerns the ratio of the number of atoms of two different elements in the irradiated area of the specimen. For two atomic species a and b, the ratio N_a/N_b of the numbers of atoms present is related to the ratio of peak intensities P_a/P_b by

$$\frac{N_a}{N_b} = \frac{\varepsilon_b(h\nu_b)\, s_b\, \omega_{Kb}\, \sigma_{iKb}}{\varepsilon_a(h\nu_a)\, s_a\, \omega_{Ka}\, \sigma_{iKa}} \cdot \frac{P_a}{P_b} \qquad (4.2)$$

i, t and $d\Omega$ are identical for both elements, and so cancel out when ratios are taken. Equation 4.2 can be simplified to

$$\frac{N_a}{N_b} = k_{ab} \frac{P_a}{P_b} \qquad (4.3)$$

where k_{ab} is a conversion factor for the pair of elements a and b, and is given by

$$k_{ab} = \frac{\varepsilon_b(h\nu_b)\, s_b\, \omega_{Kb}\, \sigma_{iKb}}{\varepsilon_a(h\nu_a)\, s_a\, \omega_{Ka}\, \sigma_{iKa}} \qquad (4.4)$$

Knowledge of this k factor for a pair of elements allows calculation of the relative atomic fractions from the ratio of the counts in their K_α characteristic peaks. (Cliff & Lorimer, 1975). The efficiency terms in equation 4.4 are not properties purely of the elements a and b. They are dependent on the detector, and so the k factor must always be determined for the particular detector which is being used.

4.3 Modelling the background in the EDX spectrum

The initial motivation for modelling the bremsstrahlung is the requirement to extract the characteristic signals from the background. For K_α peaks with energies in the region where the background is varying relatively slowly (>~3keV), several methods are available, none of which generally introduce significant errors in extracting the K_α counts. The simplest method involves interpolating a linear background between two points on either side of the peak. This is available on most commercial analysis software packages. More sophisticated methods involve fitting linear or quadratic backgrounds over energy windows on either side of the peak, or digitally filtering the spectrum. These methods are less applicable at lower energies, where the background is changing rapidly due to the fall off in detector efficiency. With a windowless detector, where the efficiency begins to fall off at a lower energy than for a Be window detector, further problems are encountered with significant peak overlap. It seems desirable therefore to have a model which describes the bremsstrahlung over as much of the energy range in the spectrum as possible. Such a model would have the further advantage of being able to indicate the presence of certain artefacts in the spectrum. These could include self-absorption effects and spurious contributions to the background from sources other than the area of specimen irradiated by the beam. In both cases a poor fit of the background to the theoretical bremsstrahlung would result.

Chapman et al. (1983) reviewed two different approximate theories for the calculation of bremsstrahlung cross sections and compared their predictions with the results of exact numerical calculations and with their experimental measurements. They concluded that a modified Bethe Heitler (MBH) model gives a good description of bremsstrahlung production in thin foils over the energy

range of interest in EDX. This model lends itself well to rapid computer evaluation, which allows bremsstrahlung spectra to be calculated easily for different combinations of Z, T_0 and detector take-off angle θ. The MBH equation is given in full in appendix A. This approach to background modelling is taken where possible throughout the work presented here. Corrections can be made to the background shapes thus produced to take into account the fall off in detector efficiency at both low and high photon energies. Adam (1986) and Steele et al. (1984) fitted corrected MBH backgrounds to experimental spectra from a Be window detector to determine values for nominal Be thickness and Si crystal thickness. The use of a theoretical model, in addition to predicting the shape of the background, also allows the prediction of absolute bremsstrahlung cross sections. Section 4.5 shows how this attribute can be used to deduce values for absolute characteristic cross sections.

4.4 Determination of k-factors

The most accurate method of determining k-factors is to measure their values using standard specimens of known composition. Where a k-factor has been measured for two elements for a particular microscope, its application will generally result in accurate results being obtained when analysing those elements with that instrument. However, as would be expected from the dicsussion in section 4.2, k factors measured on different microscopes often differ widely. Furthermore, detector performance is often found to vary with time, particularly in the case of windowless detectors (Goodhew, 1985). For accurate analysis, therefore, it is probably necessary to re-measure k-factors periodically.

In cases where suitable standards are not available, it is necessary to calculate the required k-factors from first principles using equation 4.4. The accuracy of this method depends on the accuracy with which the individual terms in equation 4.4 are known. The detector efficiencies must be determined for the particular detector being used. The accuracy of these values at the extremes of the energy range will depend on knowledge of the detector parameters described in chapter 3. Schreiber & Wims (1981) and Scofield(1974) have measured values for the partition function s. Langenberg & van Eck (1978) and Krause (1979) have listed values for K-shell fluorescence yields. Uncertainties in these values are significant only for light elements. Krause quotes uncertainties of ~10% at

Z=10 and ~40% at Z=5. The implications of this for light element analysis are discussed in chapter 6. A model commonly used to describe K-shell ionisation cross sections is the Bethe model introduced in chapter 3. σ_{iK} is given by

$$\sigma_{iK} = 4\pi e^4 b_K \ln \left(\frac{c_K T_0}{I_K} \right) / T_0 I_K \qquad (4.5)$$

The cross sections calculated using this model depend on the values used for the two Bethe parameters b_K and c_K. Powell (1976) derived a pair of values from best fits to experimental data. These values were obtained by considering ionisation of generally light elements by electrons of energies towards the low end of the range of interest in EDX. Gray et al. (1983) measured values for ionisation cross sections for a wide range of elements, with accelerating voltages ranging from 40 kV to 100kV. They suggested new values for the Bethe parameters to give the closest fit to the experimental data. The remainder of this chapter details experimental measurements made of x-ray production cross sections following the approach of Gray et al. with the aim of obtaining values for the Bethe parameters which would extend the applicability of the model to a wider range of accelerating voltages.

4.5 Experimental determination of x-ray production cross sections

Equation 4.1 shows the relation between the number of characteristic K_α x-rays detected and the corresponding ionisation cross section. Evaluation of this expression requires knowledge in particular of specimen mass thickness, total charge incident during acquisition, detector efficiency and the solid angle subtended by the detector. Considerable errors can arise in the measurement of these. The corresponding expression for the number of bremsstrahlung photons detected in time t within an energy window dhν centred at photon energy hν is

$$B = N_0 A^{-1} \rho x \; i \; t \; \epsilon(h\nu) \; \sigma_b(h\nu,\Omega) \; dh\nu \; d\Omega \qquad (4.6)$$

where $\sigma_b(h\nu,\Omega)$ is the bremsstrahlung cross section differential in $h\nu$ and Ω, and the remaining terms are as in equation 4.1. The cross section for the production of characteristic x-rays in a solid angle $d\Omega$, $\sigma_c \, d\Omega$ is given by

$$\sigma_c \, d\Omega = S \, \omega_K \, \sigma_{iK} \, d\Omega / 4\pi \qquad\qquad \textbf{(4.7)}$$

Combining equations 4.1, 4.6 and 4.7 gives

$$\frac{P}{B} = \frac{\sigma_c}{\sigma_b(h\nu, \Omega) \, dh\nu} \qquad\qquad \textbf{(4.8)}$$

Since the number of characteristic x-rays and the number of bremsstrahlung x-rays depend in exactly the same way on the factors listed above, the ratio P/B is independent of all of these. As discussed in section 4.3, the MBH theory can be used to calculate values for $\sigma_b(h\nu,\Omega)$ dhν. Thus experimental measurements of peak to background values P/B can be used to determine values for ionisation cross sections using equations 4.7 and 4.8. Gray et al. used this approach, defining P/B to be the ratio of the total number of counts in the K_α characteristic peak to the mean number of background counts in a single 20eV channel beneath the peak. This definition is the one used here.

Errors in measuring the size of the background are generally not highly significant in obtaining the number of counts in a characteristic peak. Any inaccuracy in measuring B will, however, lead to a corresponding inaccuracy in P/B. A possible source of error in the P/B measurements of Gray et al. lay in the necessity to subtract out significant instrumental contributions to the spectra. Since these measurements were made the analytical performance of electron microscopes has improved considerably. The results detailed in this section were obtained from spectra recorded by Dr. W.A.P. Nicholson using the JEOL 2000FX TEM described in chapter 3. As mentioned in that chapter, this microscope was equipped with two x-ray detectors with different values of take-off angle θ. There are theoretical advantages for P/B in using a high value of θ. The realisation of these is investigated in section 4.6. Initial analysis was

undertaken using spectra recorded on the 90 degree detector. Single element specimens were used to ensure that the bremsstrahlung was due as far as possible to the element under investigation in each case. Light elements, eg. C or O in the specimen could contribute to the backgrounds. Since the bremsstrahlung intensity varies approximately as Z^2, however, it was considered unlikely that such a contribution would have a significant effect for any of the elements studied here. The specimens were thin foils of Cr, Fe, Co, Cu, Mo and Ag. In order to minimise non specimen-related contributions, these were supported on single hole mounts of Cu or Ti, and mounted in the side-entry rod described in chapter 3. Where the specimen contained a formvar backing film, spectra were also recorded from the backing alone so that its contribution could be taken into account. In order to assess approximately the extent of the instrumental contribution, bulk spectra were recorded from the material of the grid on which each specimen was mounted. The accelerating voltage was increased in 20kV steps from 80kV to 200kV.

Where applicable, before any attempt was made to model the background for each spectrum the associated formvar spectrum, normalised by comparison of the number of electrons incident during acquisition, was subtracted from the total spectrum. A spectrum from Co, recorded at 120keV, and the normalised associated formvar spectrum are shown in figures 4.1(a) and 4.1(b)respectively.Figure 4.1(c) shows the resultant Co spectrum after subtraction of the formvar spectrum. This specimen was supported on a Cu single hole mount. Figure 4.1(d) shows bulk Cu and Ti spectra recorded on the same detector, also at 120keV. From the size of the Cu and Ti peaks in figure 4.1(c) it was estimated that the bulk contributions from the specimen mount added ~1.5% to the background in the relevant peak regions. Similar estimates suggested that the relevant bulk contribution was at most 2% for any of these spectra, and no bulk subtraction was done. However there was a large carbon block about 10mm above the specimen which could give rise to extraneous radiation with no characteristic lines detectable using the Be window detector. The extent of any contribution to the background from this is difficult to estimate. It would be expected that a large effect would lead to discrepancies between results from this microscope and the results described in section 4.8 from the VG STEMs.

An MBH background was calculated for each spectrum using program CROSS as described in appendix B, and fitted to the spectrum over several peak-free
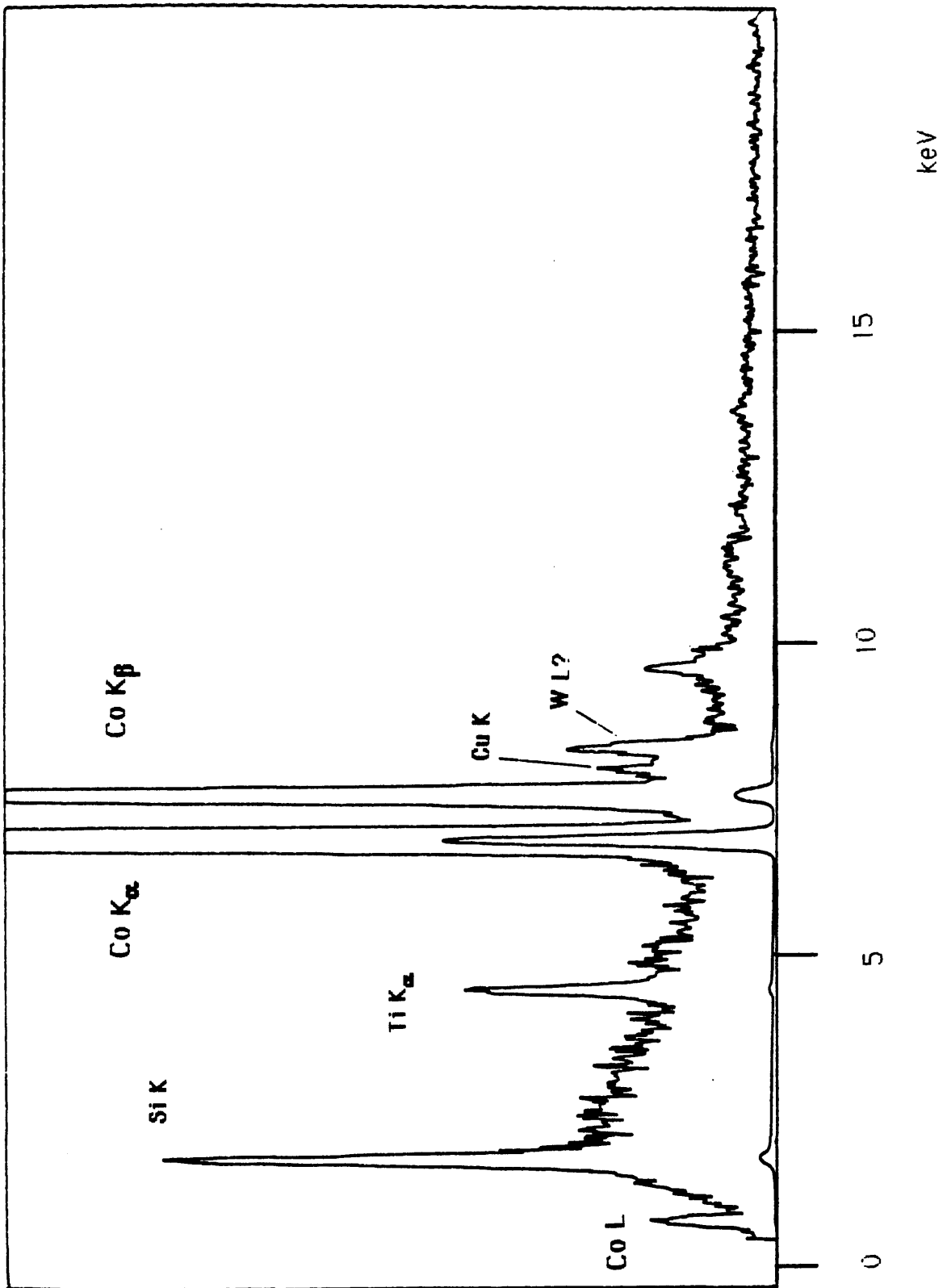
Figure 4.1 (a) Spectrum recorded from Co using the 90 detector on the JEOL TEM, with $T_0 = 120 keV$.
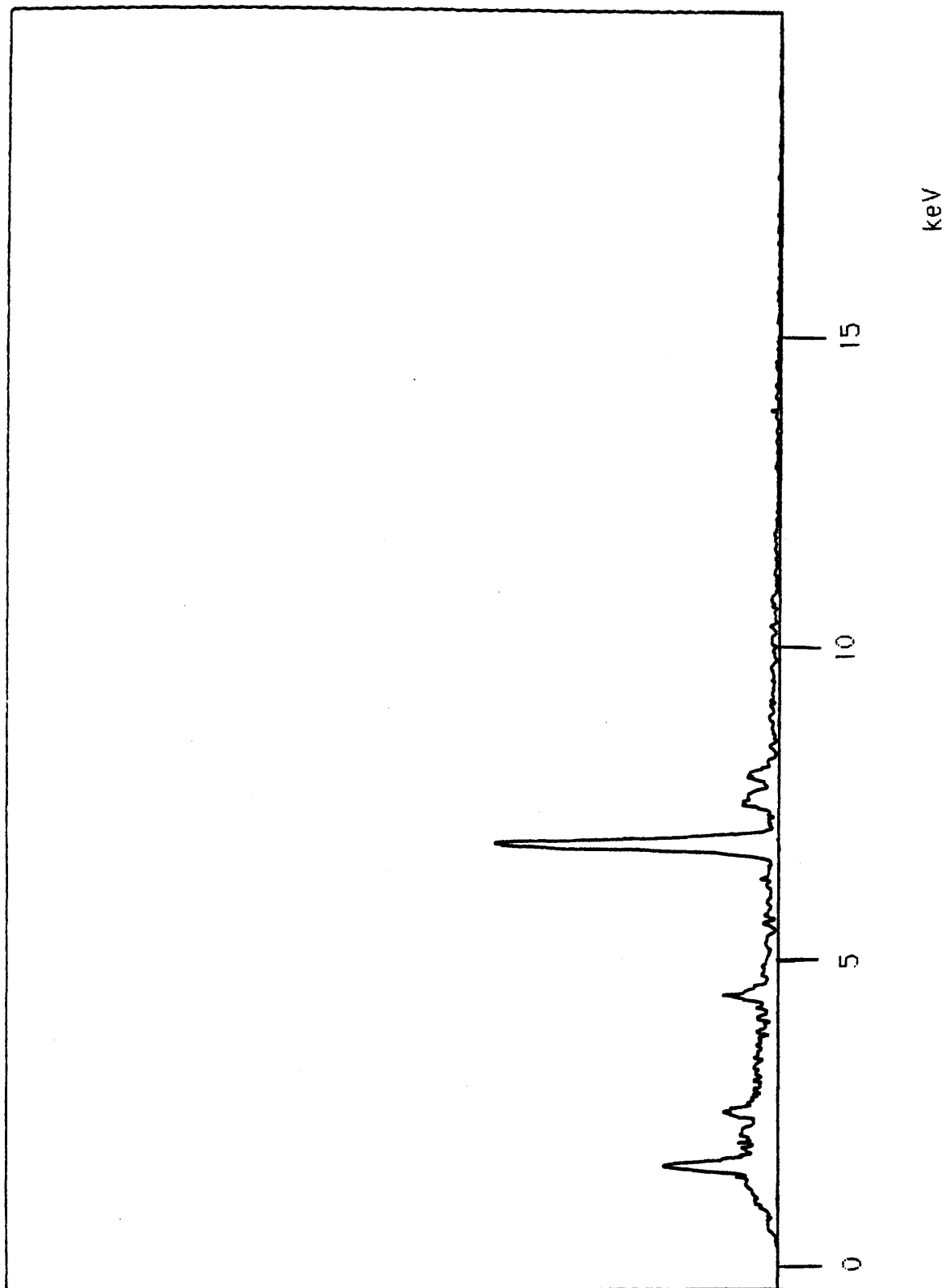
(b) Spectrum recorded from the formvar backing film of the same specimen, also at 120keV, and normalised to the spectrum in (a) by comparison of the number of electrons incident during acquisition.
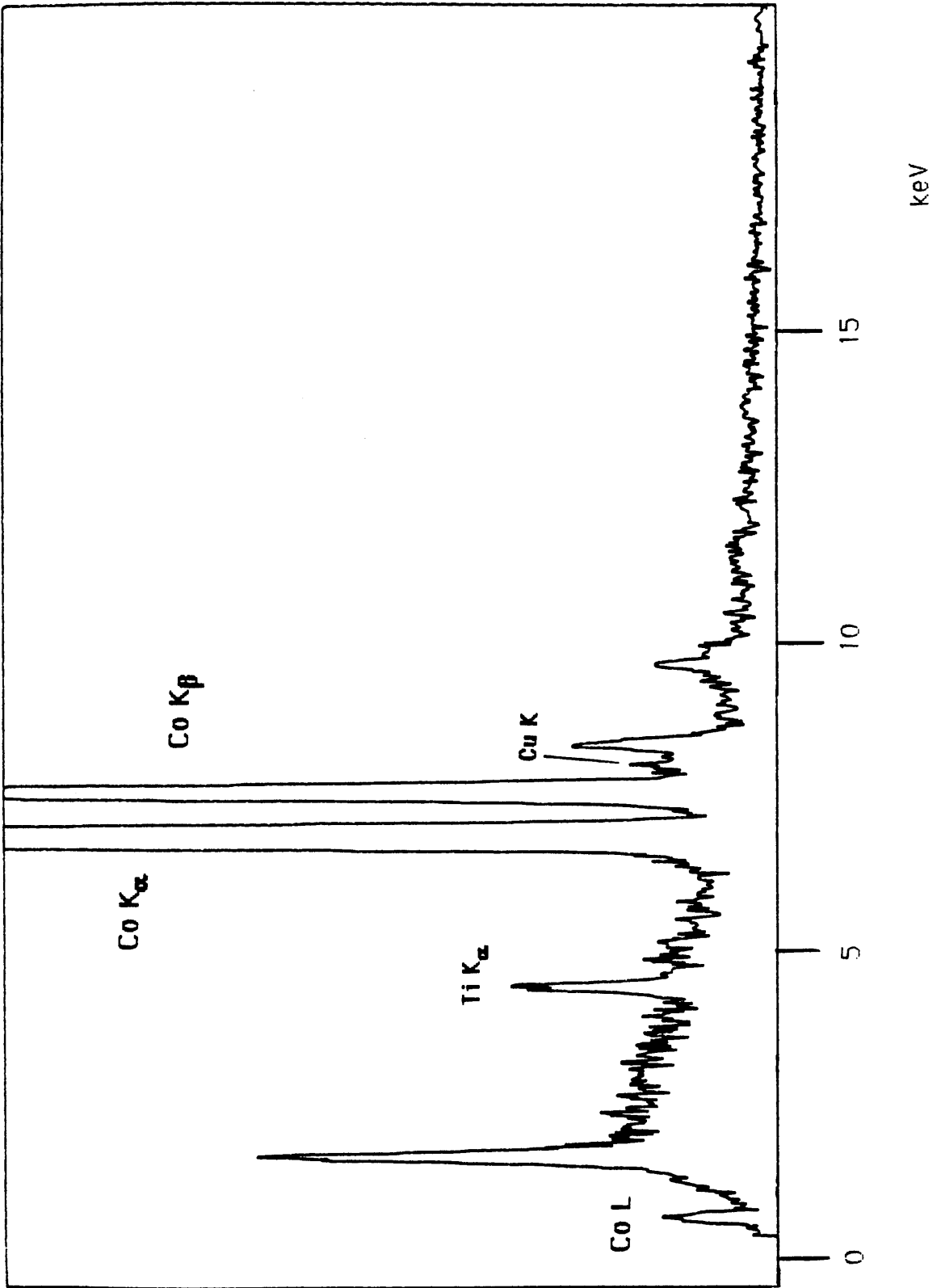
(c) The spectrum in (a) with the formvar contribution, represented by the spectrum in (b), subtracted.

Cu K$_\alpha$

Cu K$_\beta$

0　　　　　5　　　　　10　　　　　15

keV

Ti K$_\alpha$

Ti K$_\beta$

5　　　　　10　　　　　15

keV
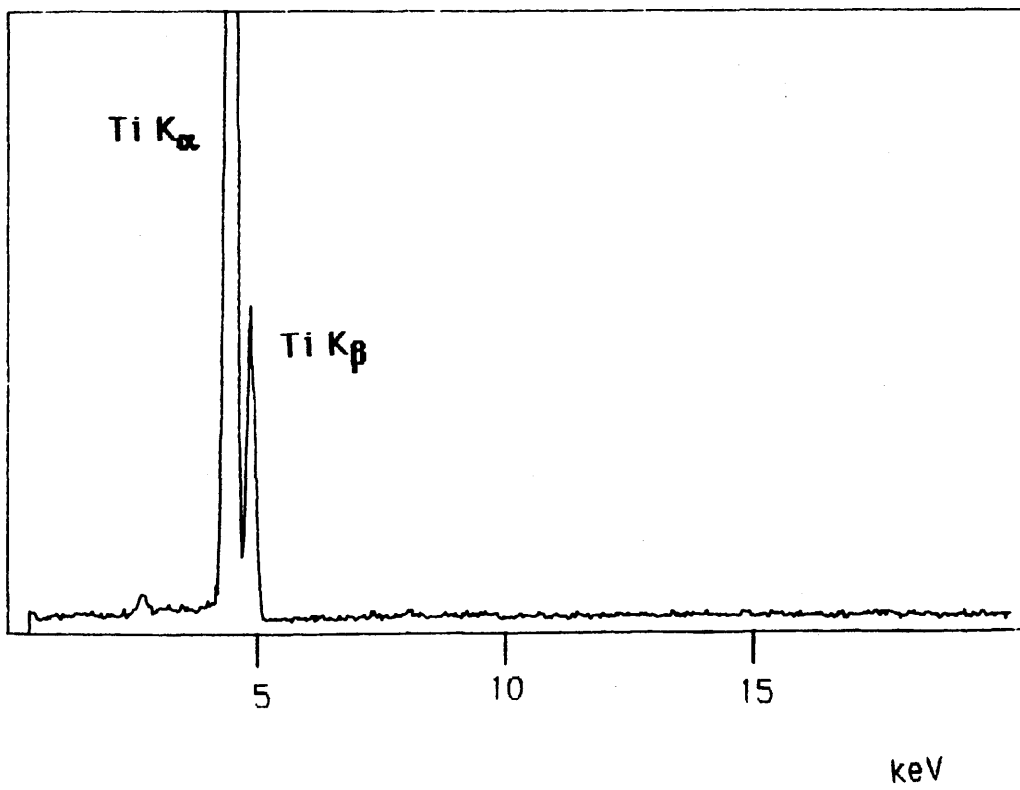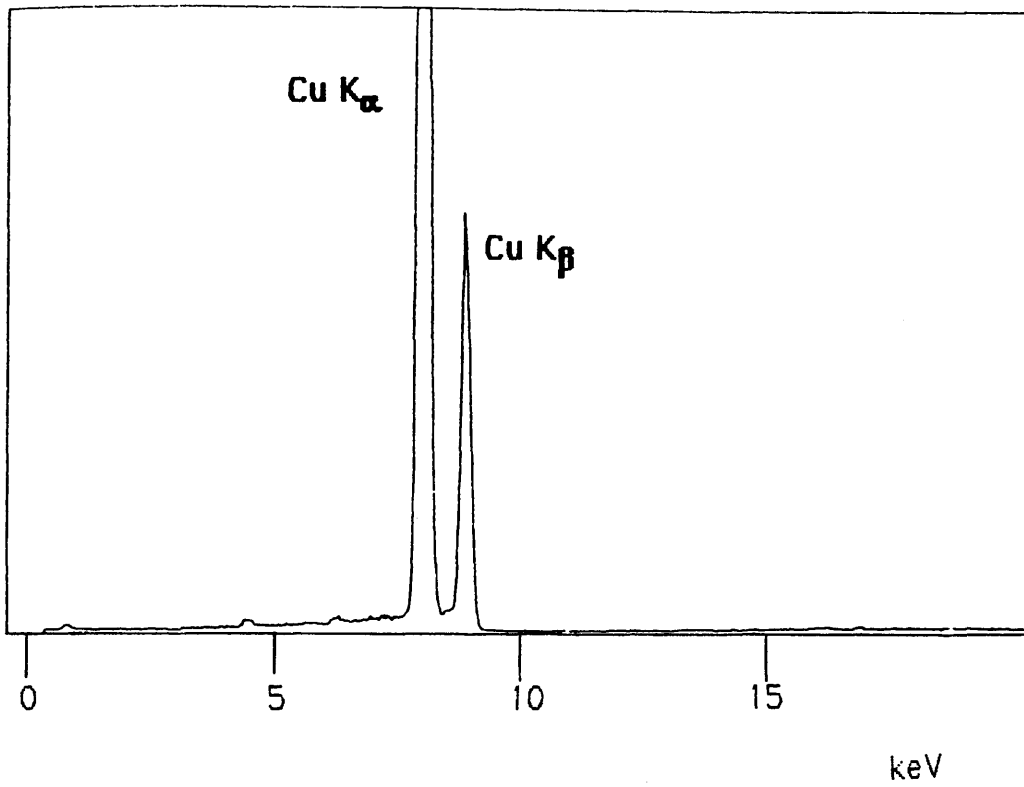
(d) Bulk Cu and Ti spectra recorded on the same microscope at 120keV.
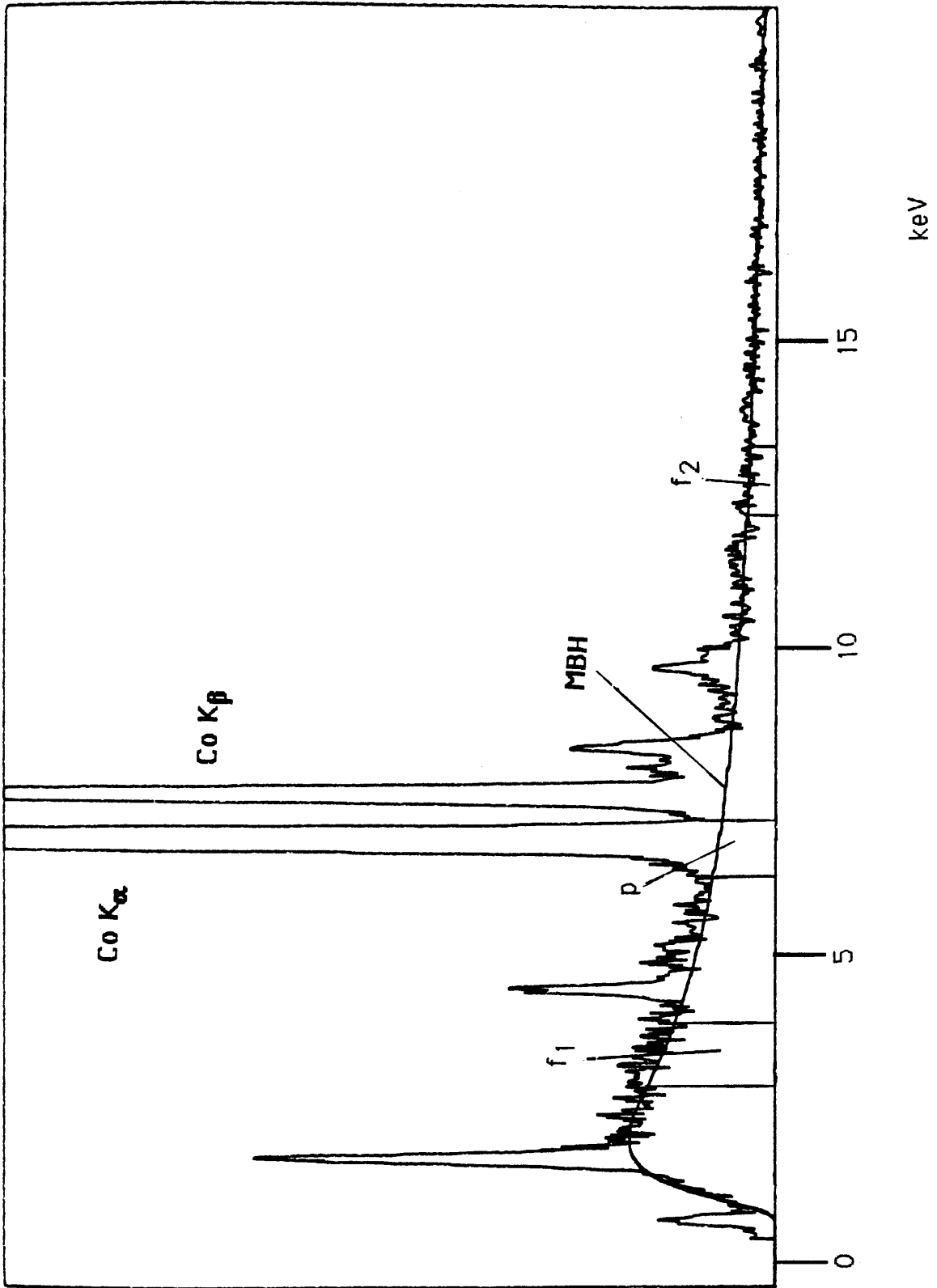
(e) The Co spectrum in (c), with a fitted MBH background.
The background fitting and peak regions are indicated.
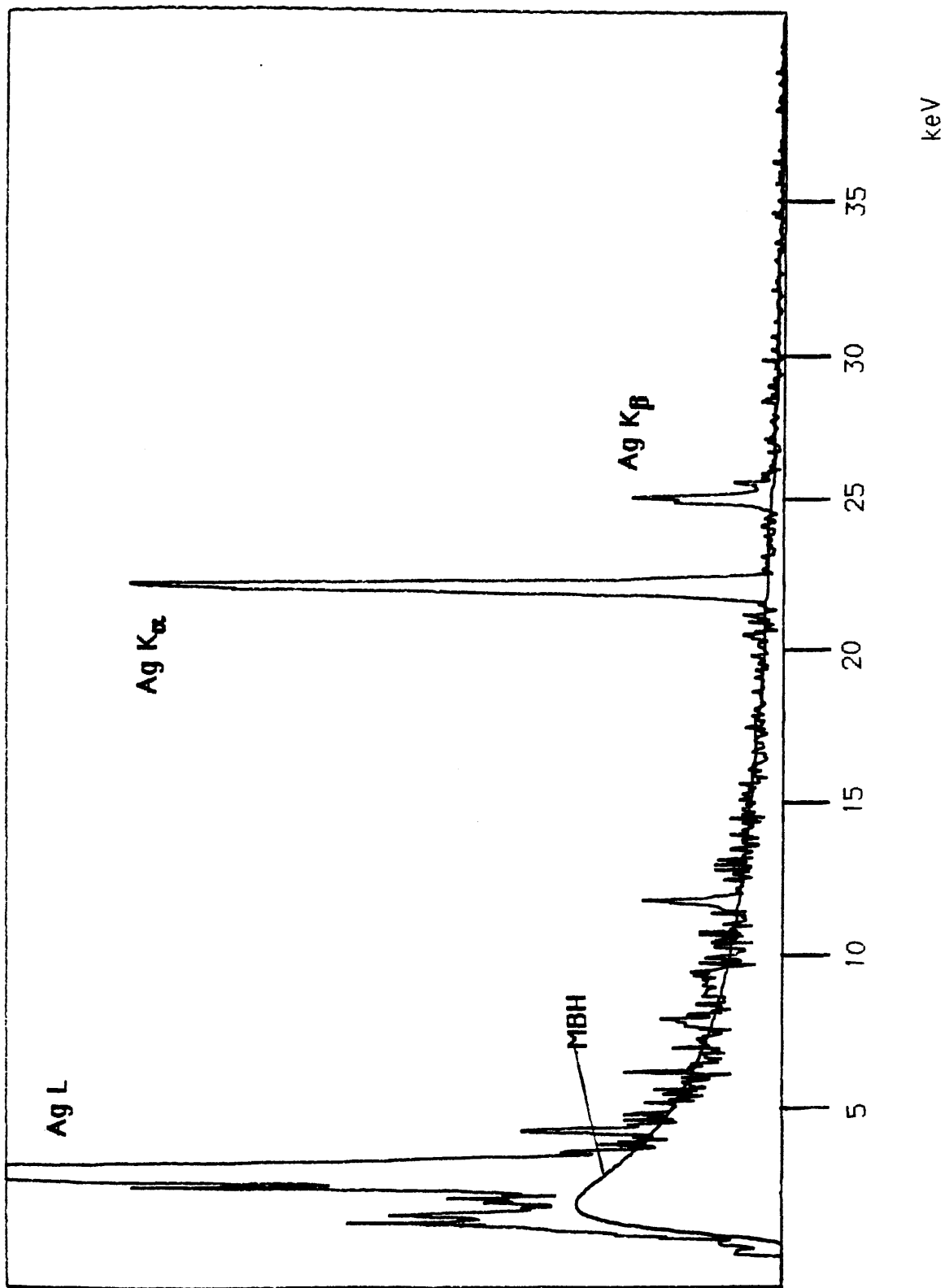
(f) A spectrum from Ag, recorded at 100keV on the same microscope, together with a fitted MBH background.
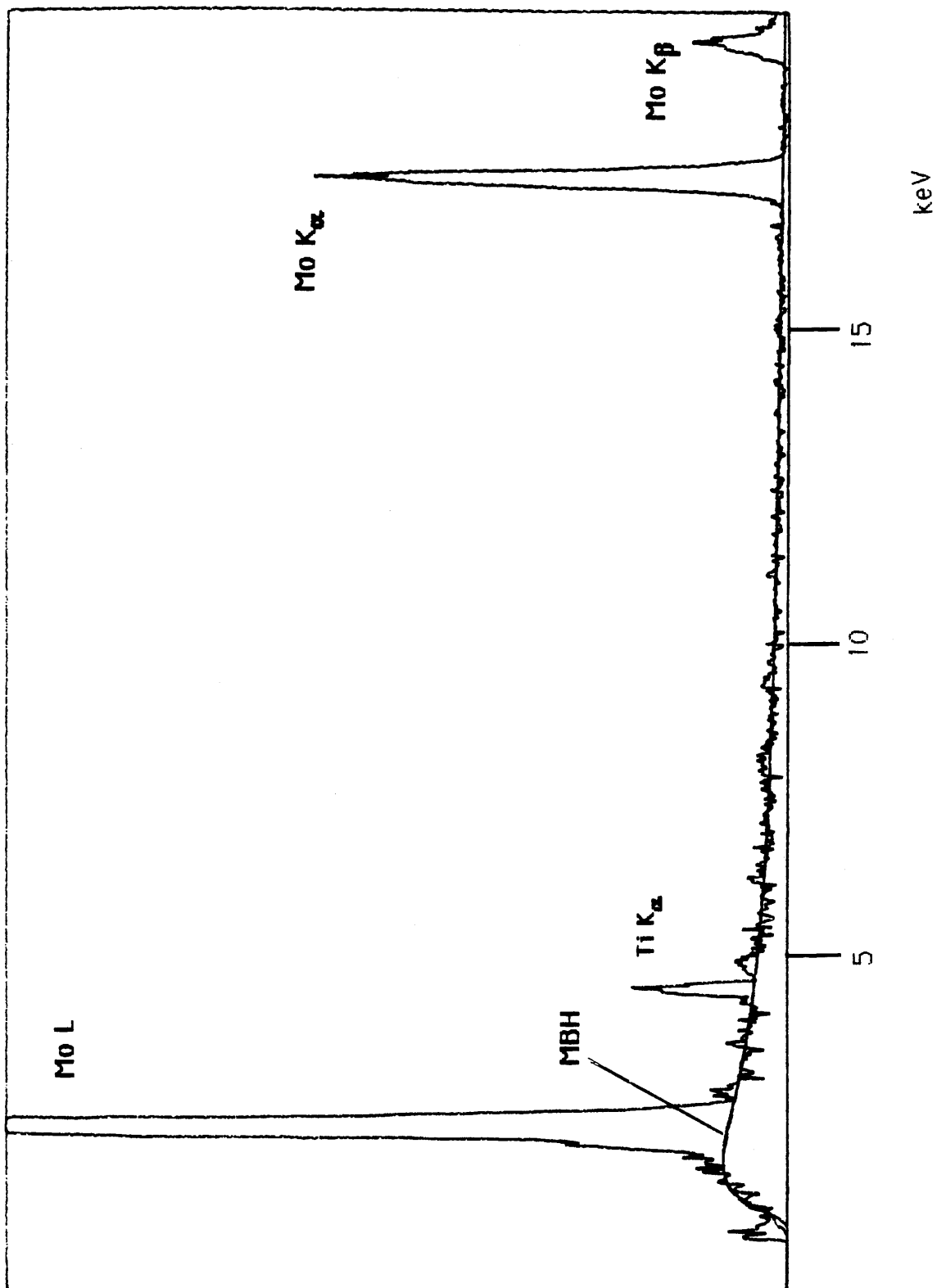
(g) Ag spectrum from Mo, recorded at 100keV on the same microscope, together with a fitted MBH background.
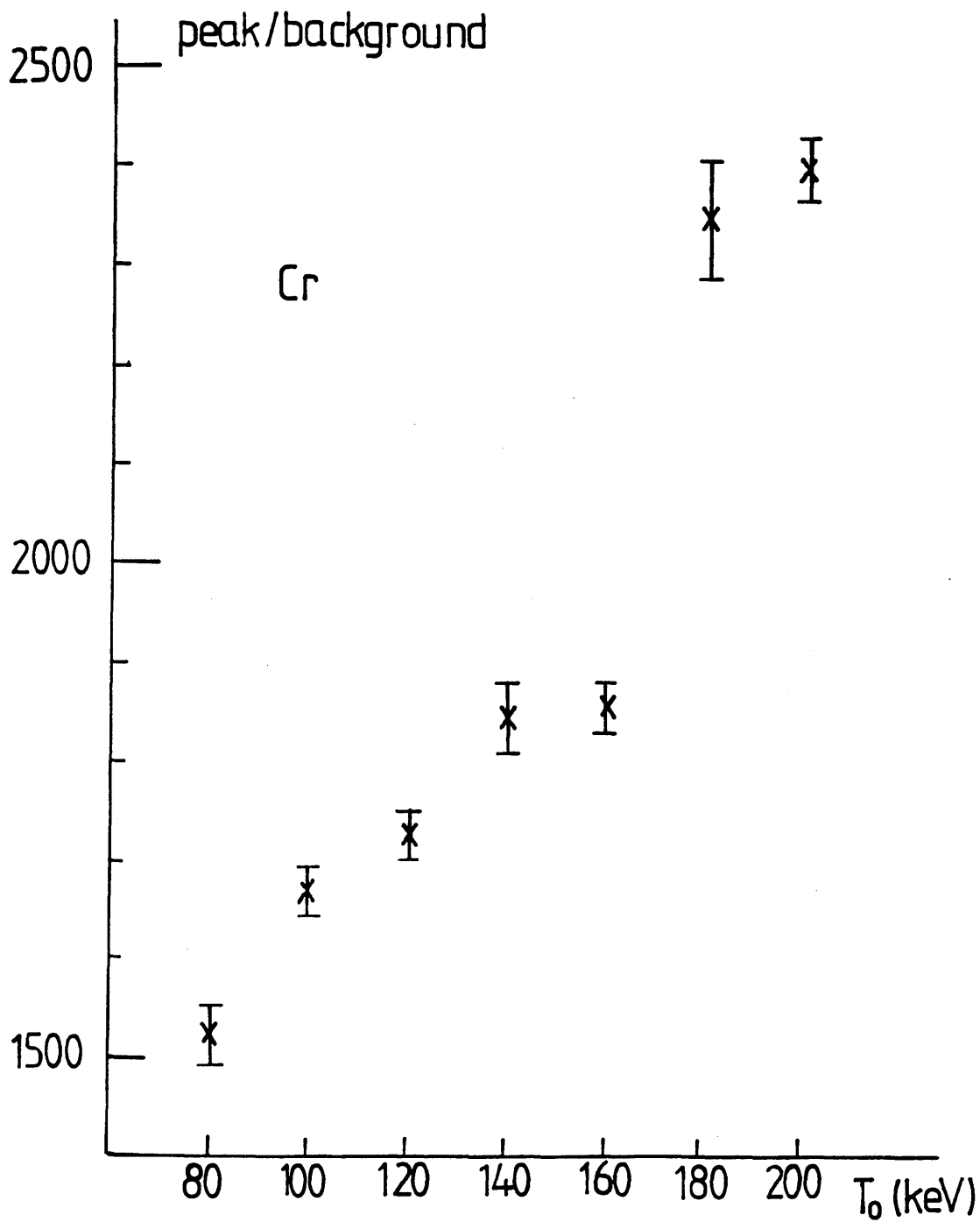
Figure 4.2   Peak to background ratio P/B vs. T_0 for individual elements, measured using the JEOL TEM.
(a) Cr (90° detector only)

peak/background

2000

1500

1000

Fe

80 100 120 140 160 180 200 T_0 (keV)

(b) Fe (90° detector only)

peak/background

2000

1500

1000

Co

⚪ 90° detector
◆ 158° detector

80   100   120   140   160   180   200 T_0 (keV)

(c) Co (90° and 158° detectors)

peak to background

⬦ 90° detector
⬦ 158° detector

Cu
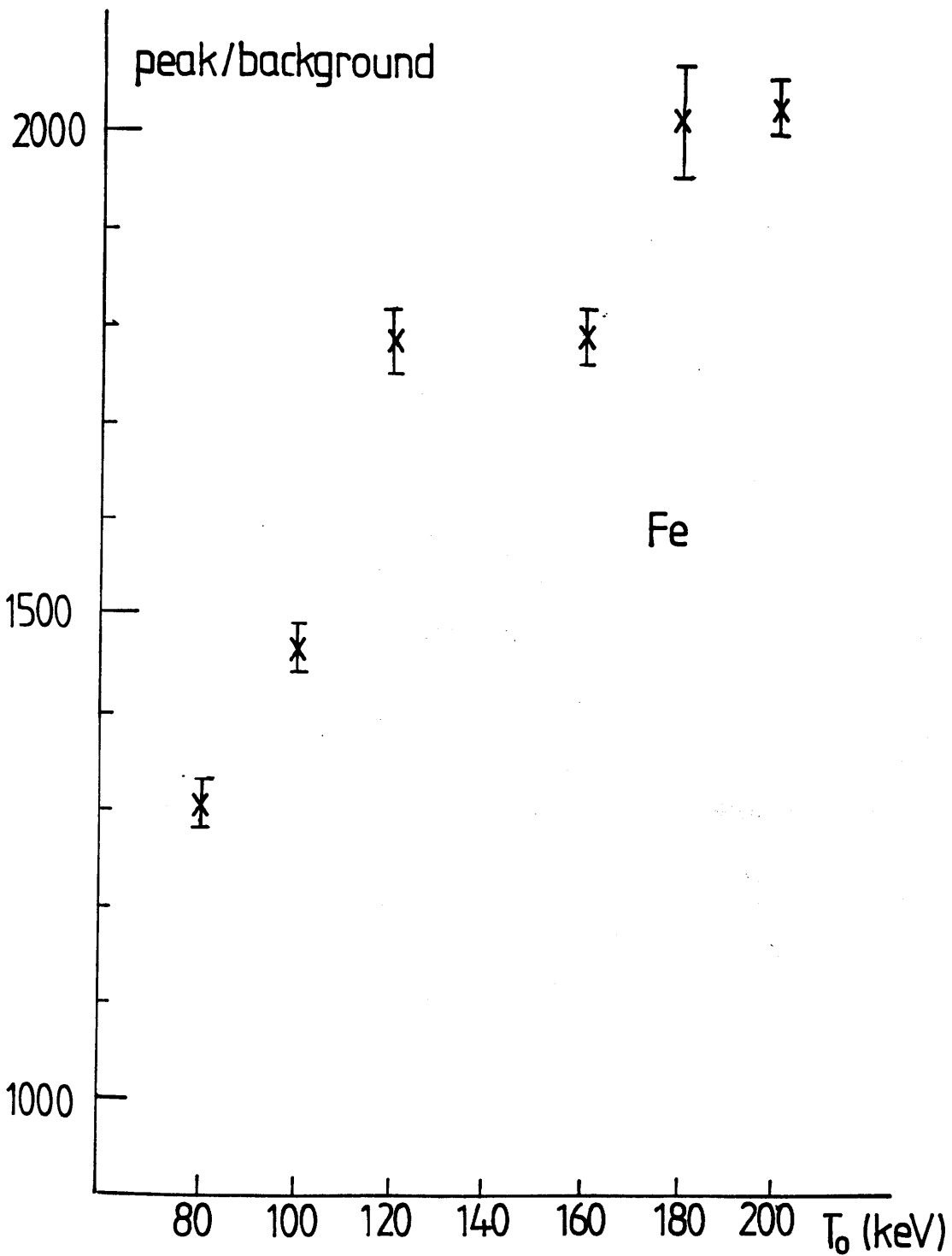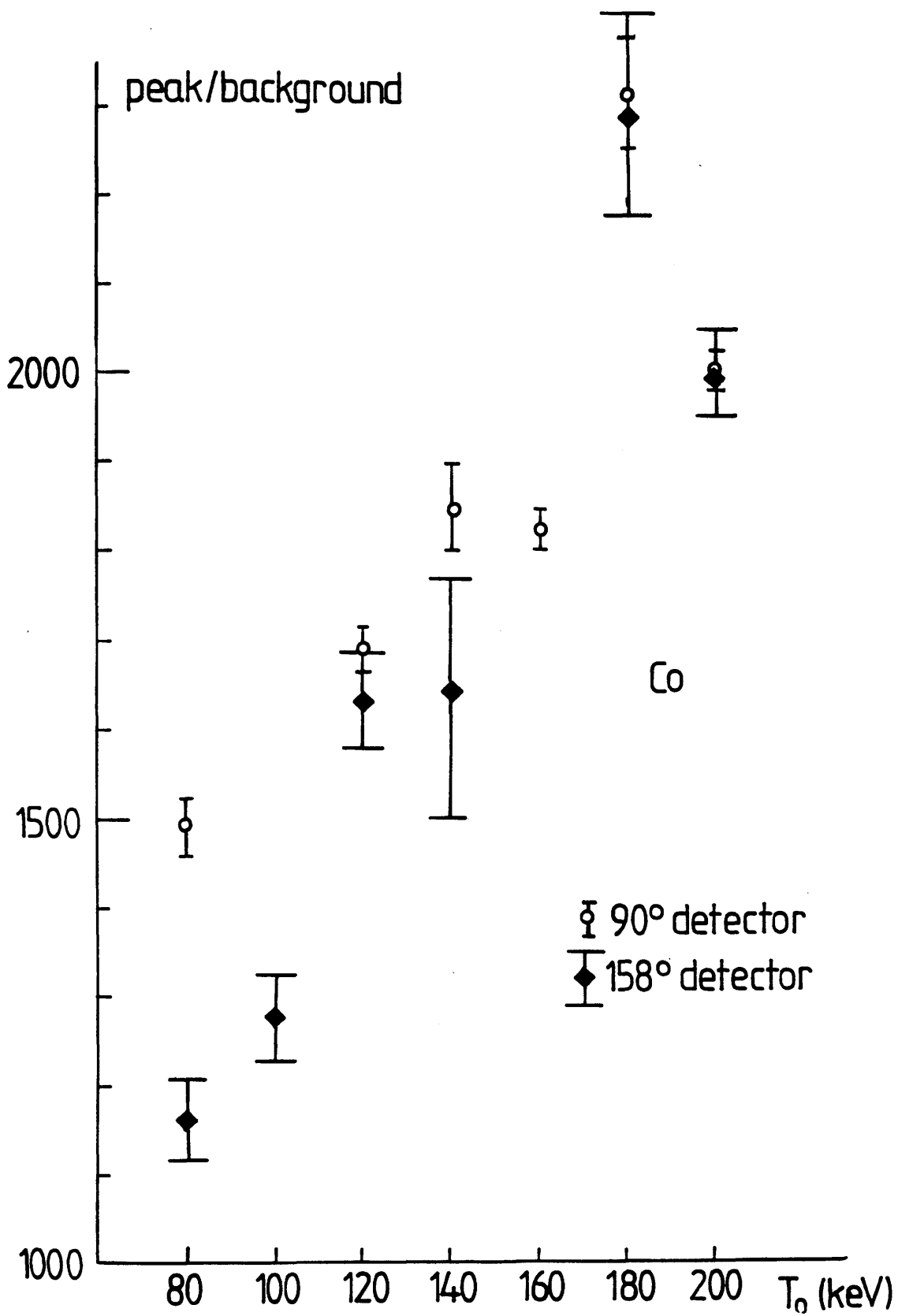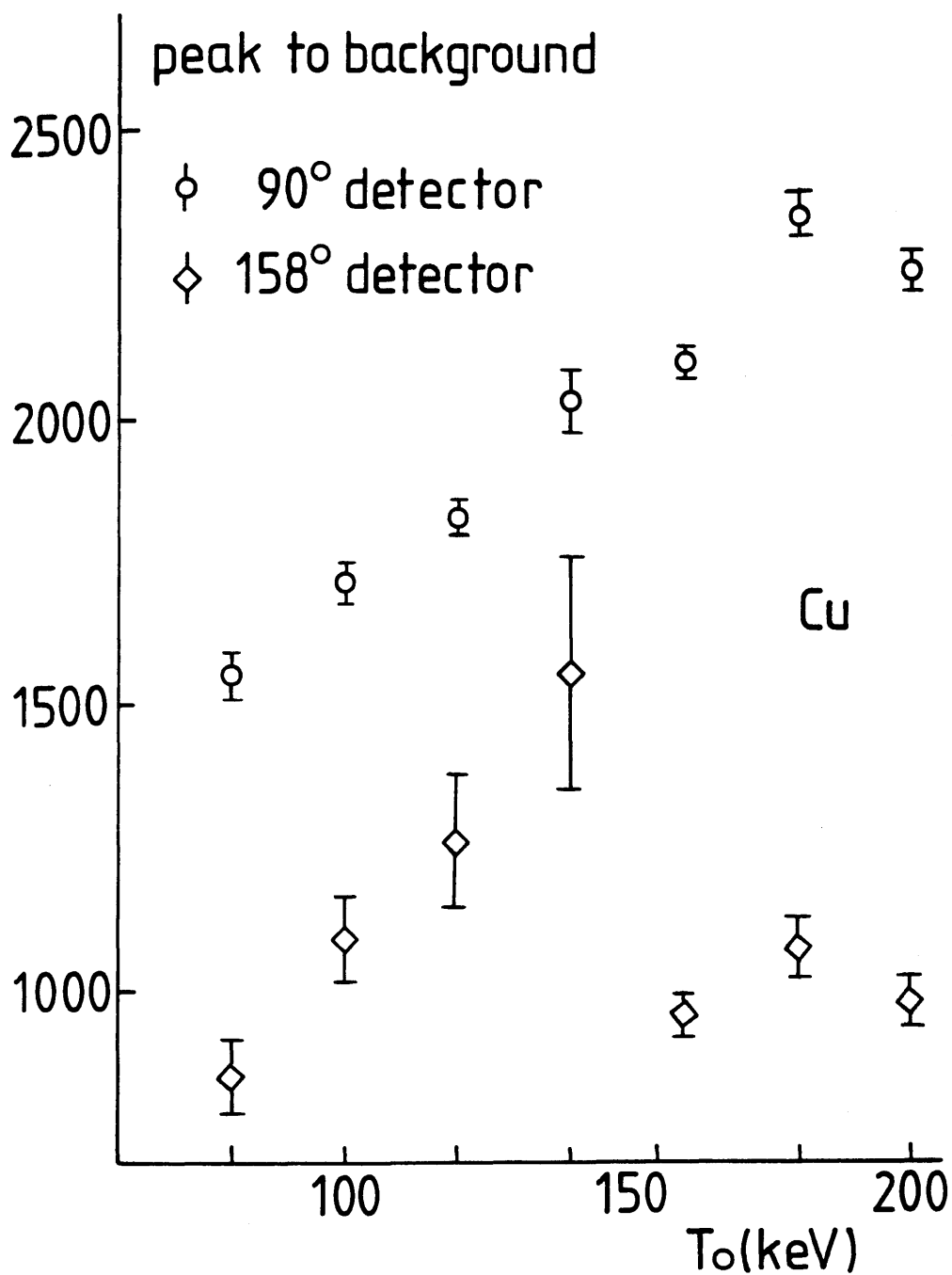
(d) Cu (90° and 158° detectors)
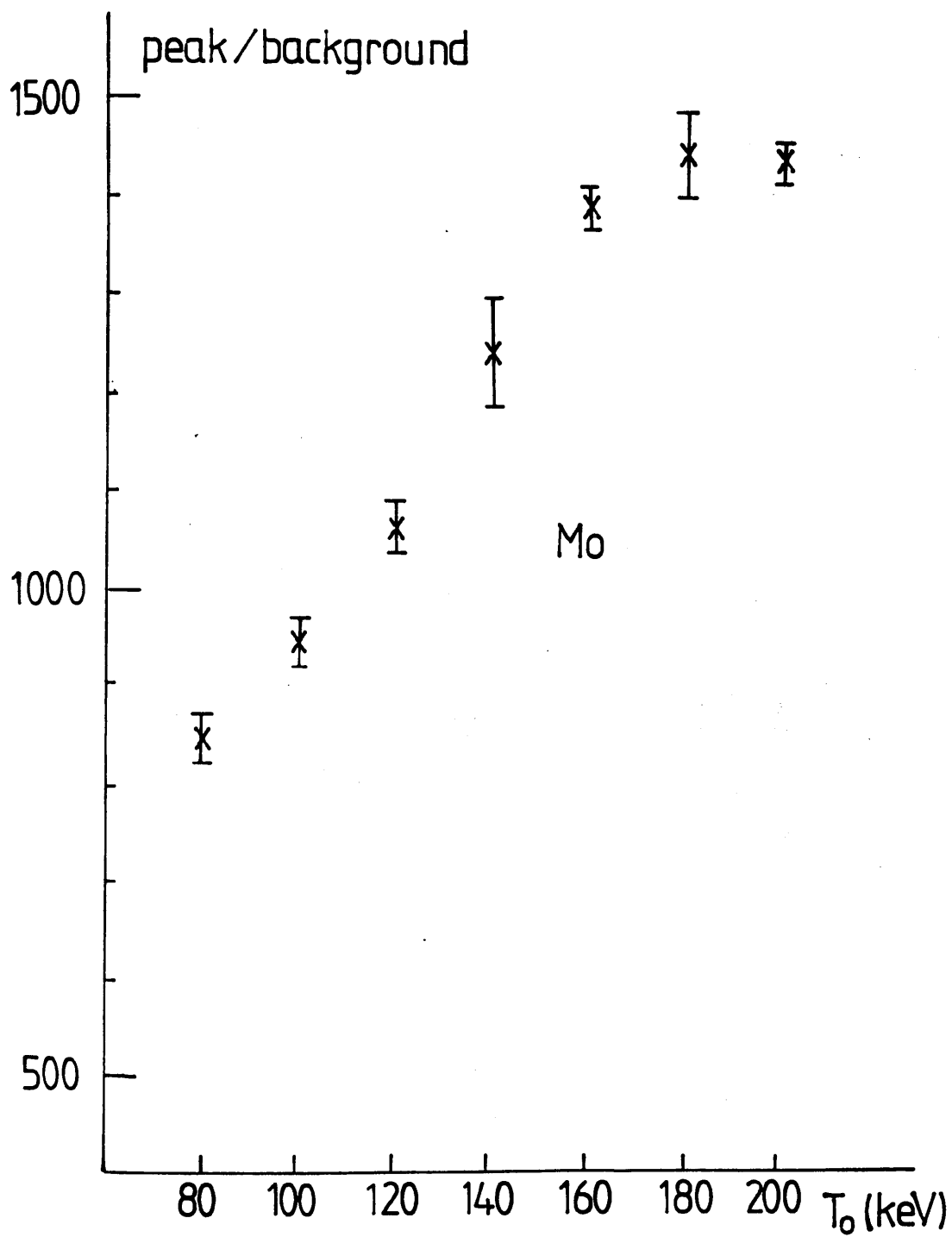
(e) Mo (90° detector only)
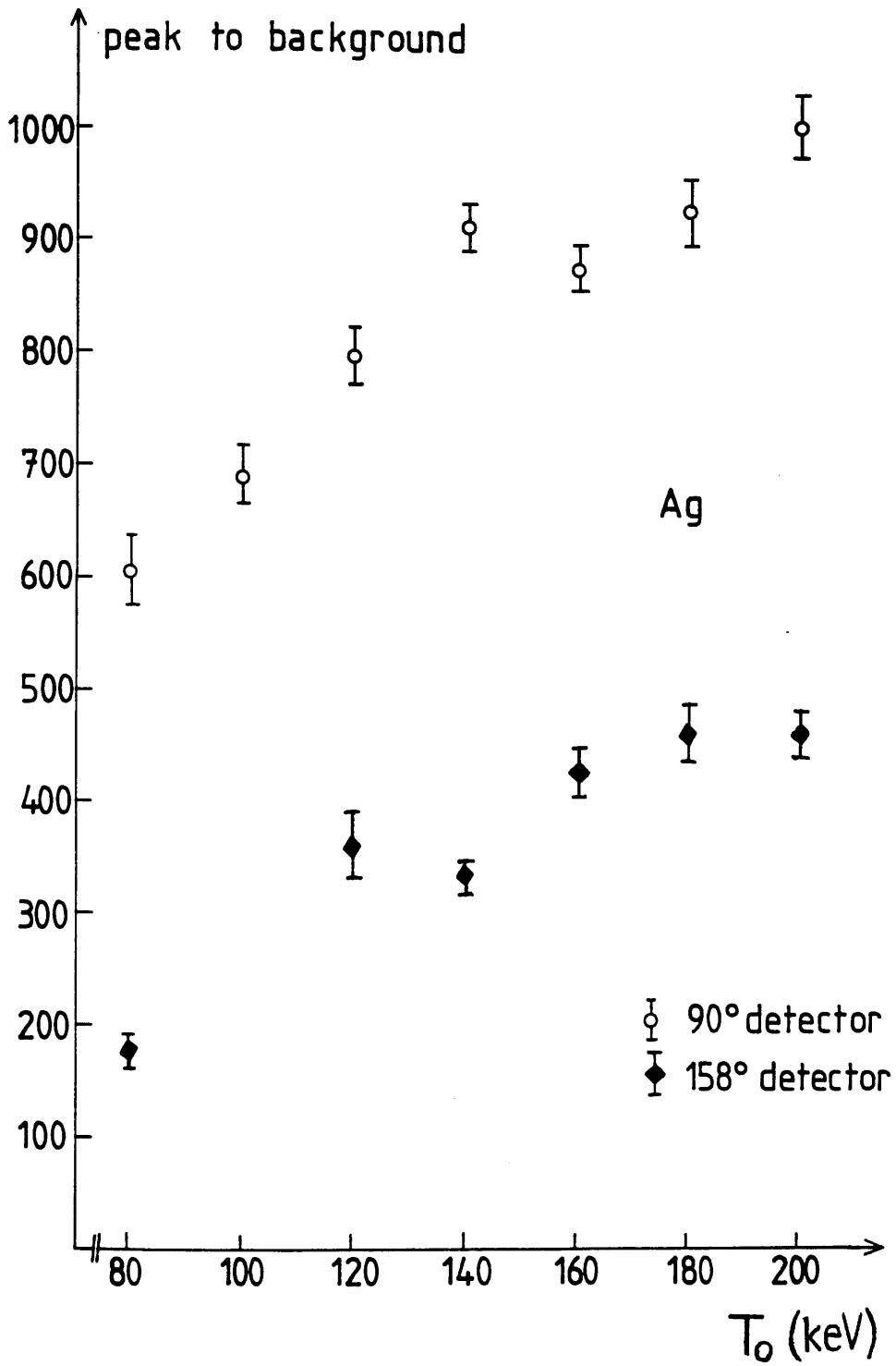
(f) Ag (90° and 158° detectors)

regions away from the extremes of the energy range. Figure 4.1(e) shows the same Co spectrum as figure 4.1(c), with its associated MBH background. background. The fitting regions f_i are indicated. The fit is good over the entire energy range of the spectrum. For the K_α lines of Mo and Ag the detector efficiency falls below unity due to the effect of finite crystal thickness. The efficiency of detection of photons which reach the active part of the crystal is given by

$$\varepsilon(h\nu) = 1 - \exp(-\mu/\rho_{Si}(h\nu)\ \rho_{Si}t_{Si}) \qquad \textbf{(4.9)}$$

where $\mu/\rho_{Si}(h\nu)$ is mass absorption coefficient for photons of energy hνin Si, ρ_{Si} is the density of Si and t_{Si} is the active thickness of the detector crystal. in the cases of Ag and Mo, regions were chosen at the high energy range of the spectra, and the experimental background was compared with MBH corrected for a range of values of crystal thickness using a chi-squared test. The values corresponding to the lowest chi-squared were 0.25cm for Ag and 0.19cm for Mo. Examples of spectra from Ag and Mo, are shown in figure 4.1(f) and 4.1(g) respectively. The MBH backgrounds shown were scaled over regions f_i, and corrected for the values of crystal thickness which yielded the best fit over regions h. The Mo spectrum was recorded over the range 0-20keV, compared with the 0-40keV range of the Ag spectrum. The efficiency up to 20keV remains >90%, and so the background fit in the Mo spectrum is relatively insensitive to the crystal thickness value used. The discrepancy between the two values obtained is therefore not significant. The low energy efficiency was also modelled for each element. Discussion of the results obtained is deferred until chapter 5 since none of the K_α peaks studied here are affected by this factor.

Windows were set on the K_α peaks, region p in figure 4.1(e), and the background counts and nett peak counts measured. The mean number of background counts per 20eV channel in region p and hence P/B were then calculated. Note that the statistical error on the background depends on the total number of counts in the fitting regions f_i, and so is small, typically of the order of a few percent, even if there are only a few counts per channel beneath the peak. Table 4.1 details one typical calculation of P/B to illustrate the general procedure. The values of P/B obtained are shown in figure 4.2 (a) to (f). The results generally show the expected trend of an increase in P/B with increasing T_0. For Cr and Co, however, the values corresponding to T_0=180keV, and

Cu, 100keV

Regions :- Background fitting regions f_i

f_1 3.10-3.90 keV
f_2 5.18-6.02 keV
f_3 11.00-12.00 keV

K_α peak region

p 7.52-8.44 keV
number of 20eV channels n = 46

Gross counts in K_α peak region P = 42510±206

(errors quoted are based on counting statistics only)

total counts in background fitting regions F = 4369±66

$$\frac{\Delta F}{F} = 0.015$$

counts in K_α background B_{peak} = 1109

$$\frac{\Delta B_{peak}}{B_{peak}} = \frac{\Delta F}{F}$$

∴ B_{peak} = 1109±17˙

B = B_{peak} / n = 24.1±0.4

∴ **P/B = 1717±28**

Table 4.1. Example of calculation of P/B, for spectrum
recorded from Cu at T_0=100keV.

T_0=200keV for Cr, appear to be inconsistent with the remaining data. Figure 4.3 shows the Co spectrum recorded at 200keV. No obvious artefact was observed in this spectrum which would explain this discrepancy. The weight of evidence from the rest of this data and all theoretical expectation suggest that these particular results are spurious, and they were not considered for the purposes of fitting the data to theory. The existence of such inconsistency with no apparent artefacts in the spectra must, however, give some cause for concern.

4.6 Results from the high take-off angle detector

MBH theory predicts that bremsstrahlung intensity falls off pronouncedly with increasing angle relative to the beam direction. Although the measurements of Chapman et al. (1983) were all made at θ=90 degrees, both of the approximate models studied in that work and the results of exact numerical calculations predict such a trend. Figure 4.4 shows values calculated using MBH for $\sigma_b(h\nu,\Omega)dh\nu$ from Ag over an increment of 20eV at the K_α line energy. T_0 is 200keV and θ varies from 90 degrees to 180 degrees. The implication of this is that the higher the take-off angle of a detector is, the better will be its performance, in that P/B values will be higher, since characteristic radiation is emitted isotropically. The JEOL 2000FX TEM used here is equipped with a high take-off angle detector mounted at 158 degrees to the beam direction. Figure 4.4 suggests that with T_0=200keV, the 158 degree detector should record a P/B value for Ag of the order of three times as great as that recorded on the 90 degree detector on the same microscope.

Spectra were recorded from the Co, Cu, and Ag specimens on the 158 degree detector to assess its performance. Figure 4.5 shows such a spectrum from Cu, together with the corresponding spectrum recorded on the 90 degree detector. These have been normalised so that the Cu K_α peaks are the same size. Clearly the 158 degree data does not fit to MBH over any reasonable energy range. The shape shown is typical of spectra recorded with the 158 degree detector. The background does not decrease significantly at photon energies above 10keV. This contradicts all expectations and suggests that there is a considerable amount of non specimen-related radiation contributing to the spectrum. The high angle detector is in a position such that it may collect a significant number of backscattered electrons if the collimation is inadequate. P/B values were obtained by fitting quadratic background curves over very limited energy
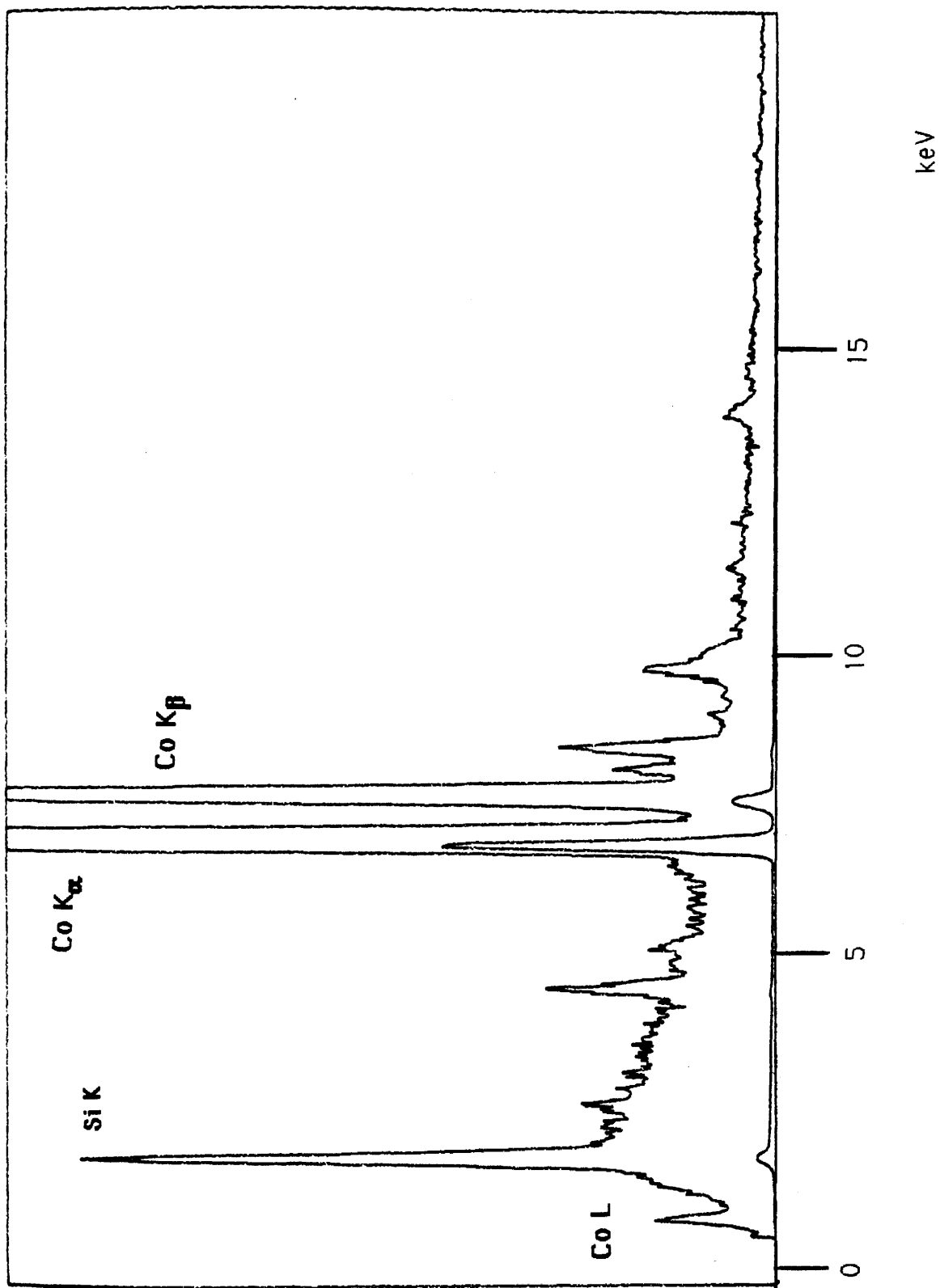
Figure 4.3 Spectrum recorded from Co at 200keV
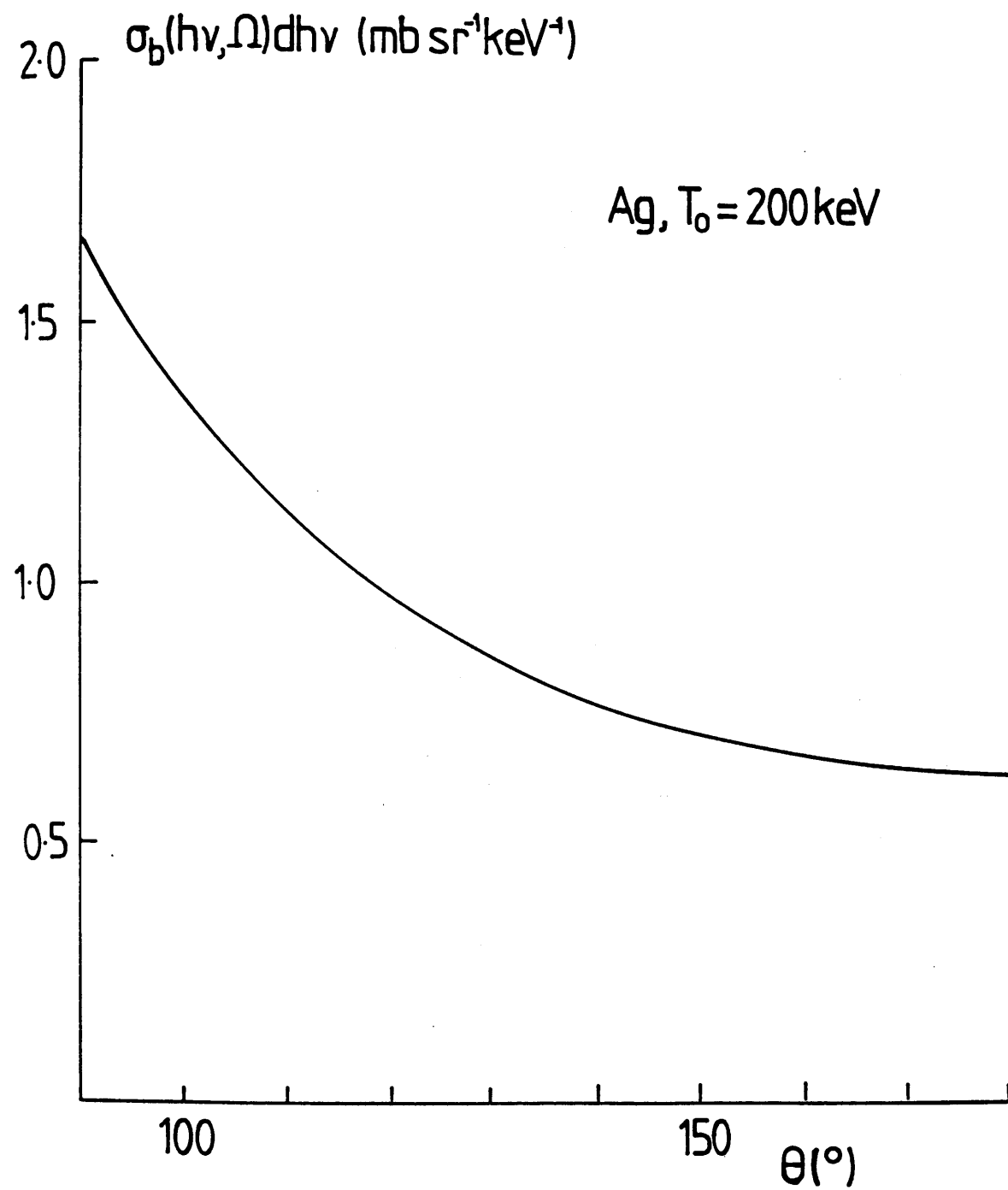
Figure 4.4 $\sigma_b(h\nu,\Omega)dh\nu$ (calculated using the MBH equation) vs. take -off angle θ for Ag, with T_0=200keV.
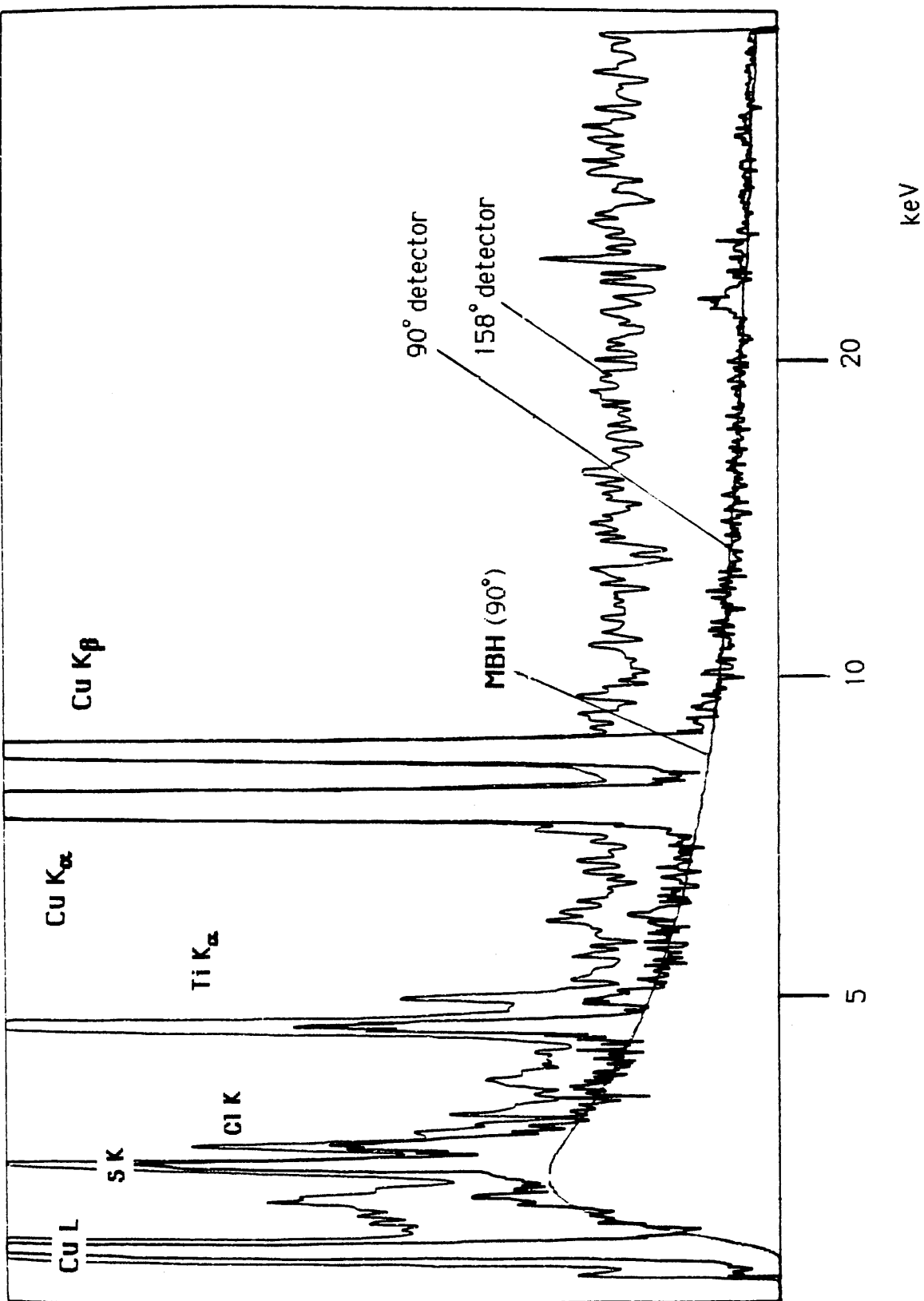
Figure 4.5   Spectra recorded from Cu using the 90° and 158° detectors on the JEOL TEM. The spectra are normalised so that the height of the Cu K_α peak is the same in each case. An MBH background fitted to the 90° detector spectrum is also shown.

ranges close to the K_α peaks, and extracting the characteristic counts and mean background counts as before. The 158 degree detector values are shown with the corresponding 90 degree detector values in figure 4.2(c),(e) and (f). The former are always similar to or lower than the latter. This observation is consistent with the observations made from the shape of the spectra. It was considered that the data from the 158 degree were unlikely to provide useful information on the applicability of MBH at high take-off angles, or to provide useful cross section data. All subsequent results from this data set are obtained using the 90 degree detector data only.

4.7 Fitting cross section data to the Bethe form

Equation 4.3 can be rewritten in the form .

$$\sigma_{iK} \, l_K^2 \, U_K = 1.32 \times 10^5 \, b_K \, (\ln U_K + \ln c_K) \qquad (4.10)$$

where $U_K = T_0 / l_K$ is the overvoltage. Energies are expressed in keV and σ_{iK} is expressed in barns. The experimental results are plotted in the form $\sigma_{iK} \, l_K^2 U_K$ against $\ln U_K$. This gives a Fano plot (Fano, 1954) from which values of b_K and c_K can be deduced. Table 4.2 lists the following values for each experimental point: T_0, l_K and U_K, $\ln(U_K)$; experimental P/B; $\sigma_b(h\nu,\Omega)$ d$h\nu$; σ_{iK} and σ_{iK} $l_K^2 \, U_K$. Figure 4.6(a) shows the Fano plot of this data. As expected the points lie approximately on a straight line. Linear fitting to the data followed the methods used by Gray et al. to allow direct comparison to be made of the results. The software for this was written in SuperBasic for a Sinclair QL microcomputer. Firstly a simple linear regression was carried out. The values of b_K and c_K produced were taken as a starting point for a routine which minimised the quantity F given by

$$F = \sum_j \frac{| \sigma_{iKj}^{experimental} - \sigma_{iKj}^{calculated} |}{\sigma_{iKj}^{experimental}} \qquad (4.11)$$

element	T_0 (keV)	U_K	$\ln(U_K)$	P/B	$\sigma_b(h\nu,\Omega)dh\nu$ (b sr^{-1}keV^{-1})
Cr	80	13.3	2.59	1523	5.23
	100	16.8	2.82	1672	4.27
	120	20.1	3.00	1729	3.62
	140	23.3	3.15	1846	3.16
	160	26.8	3.29	1855	2.80
	180	30.0	3.40	2350	2.52
	200	33.4	3.51	2398	2.29
Fe	80	11..2	2.42	1307	5.07
	100	14.0	2.64	1465	4.15
	120	16.9	2.83	1782	3.52
	160	22.4	3.11	1787	2.72
	180	25.3	3.23	2017	2.45
	200	28.2	3.34	2029	2.23
Co	80	10.4	2.34	1496	5.00
	120	15.7	2.75	1693	3.47
	140	18.2	2.90	1843	3.02
	160	20.7	3.03	1830	2.69
	180	23.3	3.15	2313	2.42
	200	26.0	3.26	1904	2.20
Cu	80	8.94	2.19	1553	4.85
	100	11.1	2.41	1717	3.97
	120	13.3	2.59	1824	3.37
	140	15.6	2.75	2037	2.94
	160	17.8	2.88	2101	2.61
	180	20.1	3.00	2365	2.35
	200	22.2	3.10	2267	2.14
Mo	80	4.01	1.39	844	3.98
	100	5.00	1.61	946	3.25
	120	5.99	1.79	1062	2.76
	140	7.03	1.95	1239	2.41
	160	8.00	2.08	1390	2.15
	180	9.03	2.20	1443	1.94
	200	9.97	2.30	1435	1.77
Ag	80	3.13	1.14	567	3.69
	100	3.94	1.37	688	3.00
	120	4.71	1.55	799	2.55
	140	5.48	1.70	880	2.23
	160	6.30	1.84	899	1.98
	180	7.02	1.95	920	1.79
	200	7.85	2.06	1073	1.64

Table 4.2. Data used to produce non-relativistic Fano plot. *(part 1)*

element	T_0 (keV)	σ_c (b sr^{-1})	σ_i (b)	$\sigma_i I_K^2 U_K$ (b keV^2)
Cr	80	7.96	407	0.746
	100	7.14	365	0.836
	120	6.27	320	0.880
	140	5.82	297	0.955
	160	5.19	265	0.973
	180	5.92	302	1.25
	200	5.49	281	1.29
Fe	80	6.63	280	0.611
	100	6.08	257	0.700
	120	6.28	265	0.867
	160	4.87	206	0.896
	180	4.94	209	1.02
	200	4.53	191	1.04
Co	80	7.48	289	0.683
	120	5.88	227	0.806
	140	5.57	216	0.892
	160	4.91	190	0.898
	180	5.59	216	1.15
	200	4.19	190	0.957
Cu	80	7.53	243	0.669
	100	6.81	220	0.756
	120	6.15	198	0.819
	140	5.99	193	0.930
	160	5.49	177	0.974
	180	5.56	180	1.11
	200	4.86	157	1.08
Mo	80	3.36	66.1	0.405
	100	3.07	60.5	0.463
	120	2.93	57.7	0.531
	140	2.99	58.8	0.631
	160	2.99	58.8	0.720
	180	2.80	55.1	0.760
	200	2.54	50.1	0.767
Ag	80	2.09	38.3	0.299
	100	2.07	37.8	0.369
	120	2.04	37.3	0.437
	140	1.96	35.8	0.490
	160	1.78	32.6	0.510
	180	1.65	30.2	0.531
	200	1.76	32.2	0.629

Table 4.2. Data used to produce non-relativistic Fano plot. *(part 2)*
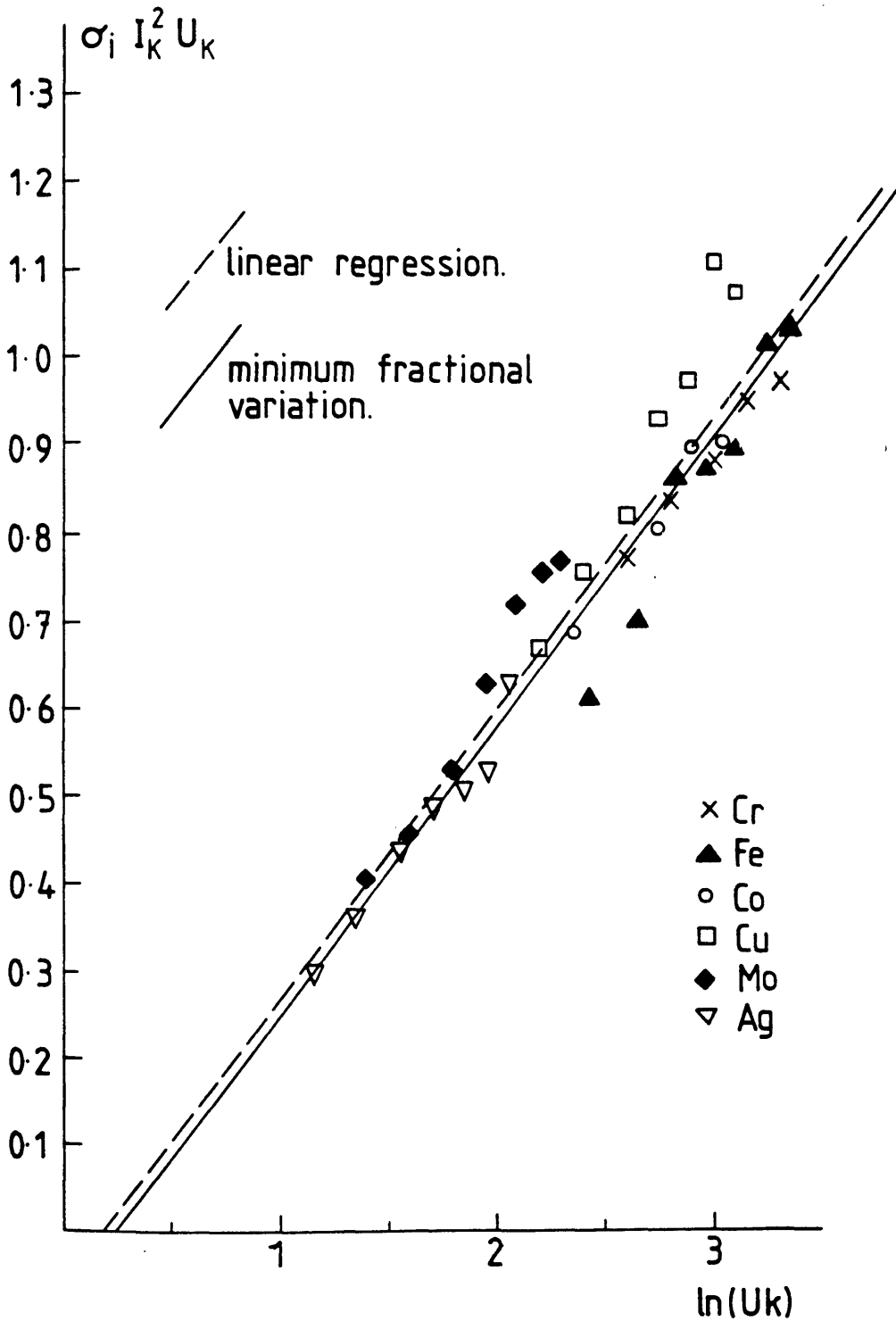
Figure 4.6 (a) Fano plot of $\sigma_{iK}I_K{}^2U_K$ vs. $\ln(U_K)$ for all the data from the JEOL TEM. ($U_K=T_0/I_K$)

where j sums over all the data points. This procedure minimises the total fractional variation of the data points from the fitted straight line. This criterion should allow cross sections to be predicted with reasonable accuracy over a wide range of elements, even at low overvoltages, where large fractional errors can occur using a linear regression. The program calculates F for a range of values of b_K and c_K, and selects those parameters which correspond to the minimum value.

Steele (1987) re-analysed the cross section data of Gray et al. using the relativistic form of the Bethe model, as given in chapter 2. The relativistic equivalent of equation 4.10 is

$$\sigma_{iK} I_K{}^2 U_K' = 1.32 \times 10^5 \, b_K \, (\ln U_K' - \ln(1-\beta^2) - \beta^2 + \ln c_K) \quad \textbf{(4.12)}$$

where $U_K' = m_0 v^2/2 I_K$, $\beta = v/c$ and v is the velocity of the incident electrons. The equivalent Fano plot is obtained by plotting $\sigma_{iK} I_K{}^2 U_K'$ against $\ln U_K' - \ln(1-\beta^2) - \beta^2$. No significant improvement was found in the fit for that data set, in which the largest value of accelerating voltage used was 100kV. It was expected that relativistic effects would be more significant here, a large proportion of the data being recorded with accelerating voltages $> 100kV$. Table 4.3 lists the values of $m_0 v^2$, U_K', $\ln U_K'$, β and $\sigma_{iK} I_K{}^2 U_K'$ for all the data points. Figure 4.6(b) shows the relativistic Fano plot.

It is apparent from the figures that the two linear fitting methods produce similar results for this data set. Table 4.4 shows the values of b_K and c_K obtained using all the combinations of cross section model and fitting method, together with the equivalent values obtained by Gray et al. and Steele. Table 4.5 lists the corresponding fractional variations for each data point, and the mean variation in each case. Regarding minimisation of fractional variation as the preferred method, the results obtained here agree well with the previous work. The relativistic model appears to give a slightly better description of the data.

Some workers (Schreiber & Wims ,1981; Zaluzec ,1984; Rez ,1984), have suggested that the Bethe parameters should not be constant for all elements. Examination of figure 4.6(a) suggests that the data from each element could be

element	T_0 (keV)	β	U_K'	$\ln(U_K')$	$\sigma_i I_K^2 U_K'$ (b keV^2)
Cr	80	0.502	10.8	2.37	0.601
	100	0.548	12.9	2.56	0.642
	120	0.587	14.7	2.69	0.645
	140	0.620	16.3	2.79	0.669
	160	0.648	18.0	2.89	0.653
	180	0.673	19.3	2.96	0.804
	200	0.695	20.7	3.03	0.797
Fe	80	0.502	9.07	2.20	0.493
	100	0.548	10.8	2.38	0.538
	120	0.587	12.4	2.52	0.635
	160	0.648	15.0	2.71	0.601
	180	0.673	16.3	2.79	0.656
	200	0.695	17.4	2.86	0.642
Co	80	0.502	8.37	2.12	0.551
	120	0.587	11.5	2.44	0.591
	140	0.620	12.7	2.54	0.625
	160	0.648	13.9	2.63	0.602
	180	0.673	15.0	2.71	0.740
	200	0.695	16.1	2.78	0.591
Cu	80	0.502	7.20	1.97	0.539
	100	0.548	8.55	2.15	0.580
	120	0.587	9.77	2.28	0.600
	140	0.620	11.0	2.39	0.652
	160	0.648	11.9	2.48	0.653
	180	0.673	12.9	2.56	0.714
	200	0.695	13.7	2.62	0.667
Mo	80	0.502	3.24	1.17	0.326
	100	0.548	3.84	1.35	0.356
	120	0.587	4.39	1.48	0.389
	140	0.620	4.92	1.59	0.442
	160	0.648	5.37	1.68	0.483
	180	0.673	5.80	1.76	0.489
	200	0.695	6.16	1.82	0.474
Ag	80	0.502	2.52	0.924	0.241
	100	0.548	3.02	1.11	0.283
	120	0.587	3.45	1.24	0.320
	140	0.620	3.83	1.34	0.343
	160	0.648	4.22	1.44	0.342
	180	0.673	4.52	1.51	0.342
	200	0.695	4.85	1.58	0.388

Table 4.3. Additional data for relativistic Fano plot
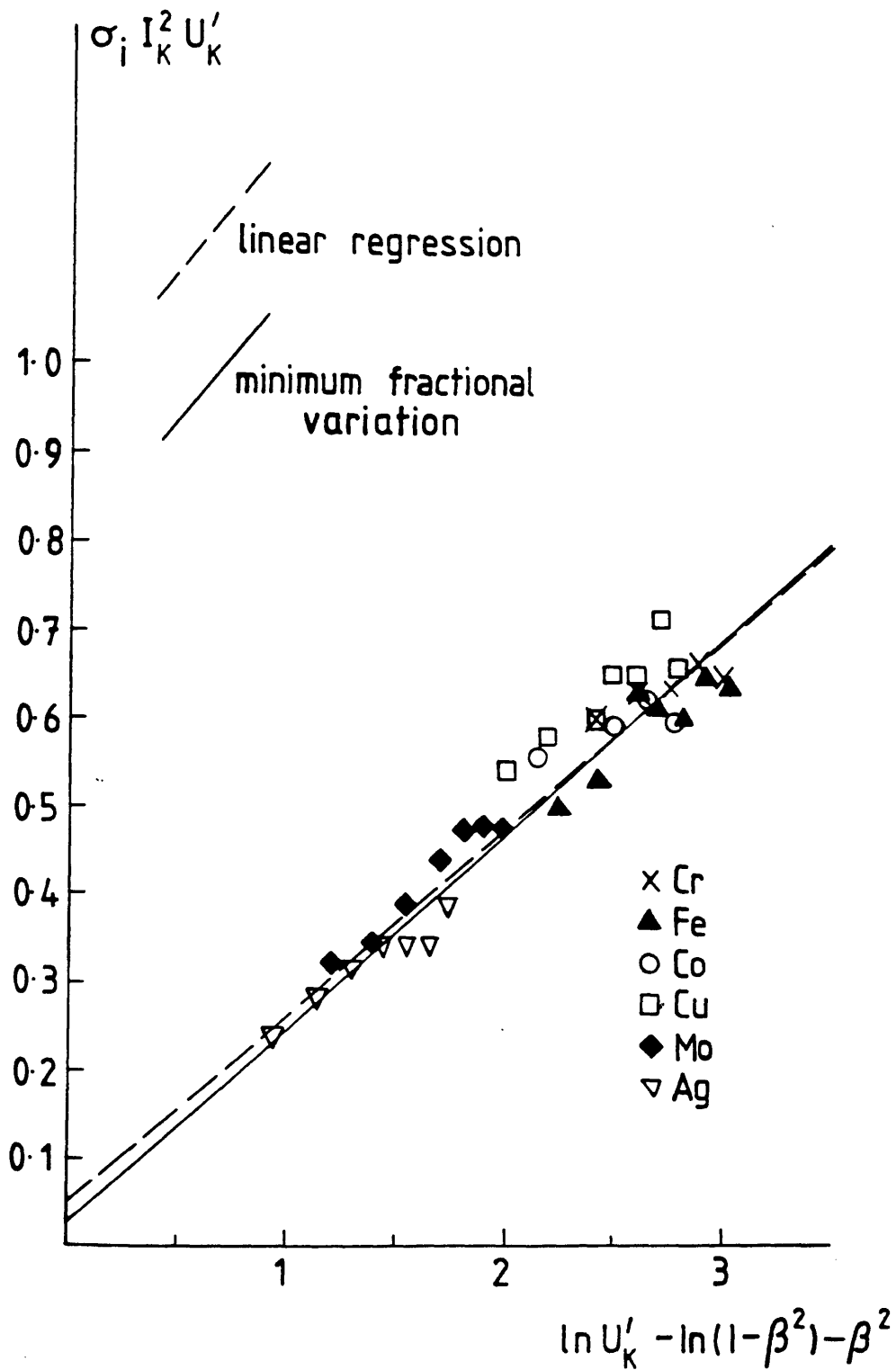
(b) Fano plot of $\sigma_{iK}I_K{}^2 U_K{}'$ vs. $\ln(U_K{}')-(1-\beta^2)-\beta^2$ for all the data from the JEOL TEM. ($U_K{}'=1/2m_0v^2/I_K$)

Fitting method	b_K	c_K
This work:		
non-relativistic linear regression	0.67	0.82
minimum fractional variation	0.67	0.79
relativistic linear regression	0.43	1.26
minimum fractional variation	0.45	1.11
Gray et al.:		
non-relativistic linear regression	0.60	1.16
minimum fractional variation	0.67	0.89
relativistic linear regression	0.48	1.40
minimum fractional variation	0.56	1.04

Table 4.4. Comparison of the values deduced for the Bethe parameters by linear fitting to the data points from this work and from that of Gray et al.

element	T_0(keV)	non-relativistic		relativistic	
		LR	MFV	LR	MFV
Cr	80	0.065	0.048	0.052	0.056
	100	0.042	0.027	0.045	0.045
	120	0.058	0.043	0.002	0.004
	140	0.027	0.014	0.007	0.011
	160	0.056	0.043	0.072	0.078
Fe	80	0.21	0.19	0.083	0.075
	100	0.16	0.14	0.068	0.065
	120	0.082	0.006	0.041	0.041
	160	0.079	0.066	0.10	0.10
	180	0.013	0.025	0.042	0.046
	200	0.003	0.008	0.096	0.10
Co	80	0.041	0.023	0.062	0.071
	120	0.052	0.036	0.003	0.001
	140	0.006	0.008	0.008	0.008
	160	0.047	0.034	0.069	0.071
Cu	80	0.011	0.030	0.10	0.11
	100	0.028	0.045	0.096	0.10
	120	0.030	0.045	0.070	0.075
	140	0.089	0.10	0.098	0.10
	160	0.085	0.098	0.064	0.064
	180	0.16	0.17	0.11	0.11
	200	0.11	0.12	0.022	0.020

LR - linear regression   MFV - minimum total fractional variation

Table 4.5   Fractional variations of data points (JEOL TEM
low take-off angle detector) from the values
calculated using the fitted Bethe parameters.

element	T_0(keV)	non-relativistic		relativistic	
		LR	MFV	LR	MFV
Mo	80	0.023	0.054	0.046	0.090
	100	0.12	0.14	0.009	0.044
	120	0.005	0.028	0.009	0.037
	140	0.078	0.098	0.061	0.082
	160	0.13	0.15	0.091	0.11
	180	0.13	0.14	0.056	0.071
	200	0.090	0.11	0.013	0.000
Ag	80	0.045	0.004	0.068	0.001
	100	0.54	0.020	0.060	0.009
	120	0.027	0.001	0.042	0.001
	140	0.018	0.007	0.052	0.018
	160	0.069	0.045	0.13	0.10
	180	0.095	0.072	0.19	0.16
	200	0.017	0.037	0.10	0.080

Table 4.5. (continued)

fitted better to a line with different gradient and intercept to that fitted to the whole data set. Non-relativistic Fano plots for the individual elements are shown in figure 4.7(a) to (f), and the resultant values of $b_K(Z)$ and $c_K(Z)$ obtained by fractional variation minimisation are listed in Table 4.6. There is a modest variation in $b_K(Z)$, the results being generally higher than the overall value. The variation in $c_K(Z)$ is wider, but the value of σ_{iK} predicted by equation 4.5 is relatively insensitive to the value of c_K for the overvoltages used here. No clear trend is discernable in the variation of these parameters with Z. Schreiber & Wims and Rez predict a weak dependence of the Bethe parameters on Z. There are not sufficient data here to determine the parameters for individual elements accurately enough to detect such small variations. Zaluzec describes $b_K(Z)$ and $c_K(Z)$ in terms of polynomials, suggesting wide variation in both parameters with Z. The two parameters vary in opposite directions, however, which smooths out the overall variation. There is a suggestion that the results of Zaluzec do not give sufficient basis for belief in such a wide variation of $b_K(Z)$ and $c_K(Z)$. There is therefore no clear contradiction of the results of any of these workers in the results deduced here, but the accuracy is not sufficient to give a strong confirmation of their predictions.

4.8 Comparison of cross section data from different microscopes

Characteristic x-ray production cross sections depend purely on the scattering processes involved. Experimental values determined using different microscopes should therefore not differ. P/B values, however, are affected by the variation of $\sigma_b(h\nu,\Omega)dh\nu$ with θ, and so depend on the geometry of the detector configuration used. The detectors on the two VG STEMs are mounted at 100.5 degrees to the beam direction, compared with 90 degrees for the lower angle detector on the JEOL TEM. MBH predicts therefore that P/B values recorded on the VG STEMs should be typically ~15% higher than the corresponding results from the JEOL TEM. To investigate this, data were recorded on the STEMs and analysed in the same way as the TEM data. Consistency within the data set would support the belief that the results obtained did represent true cross sections.

Spectra were recorded from thin evaporated foils of Fe, Co, Ni, Cu, Ge, Ag and Sn, supported on holey formvar; from ion-beam thinned foils of Si, Fe, Ni,
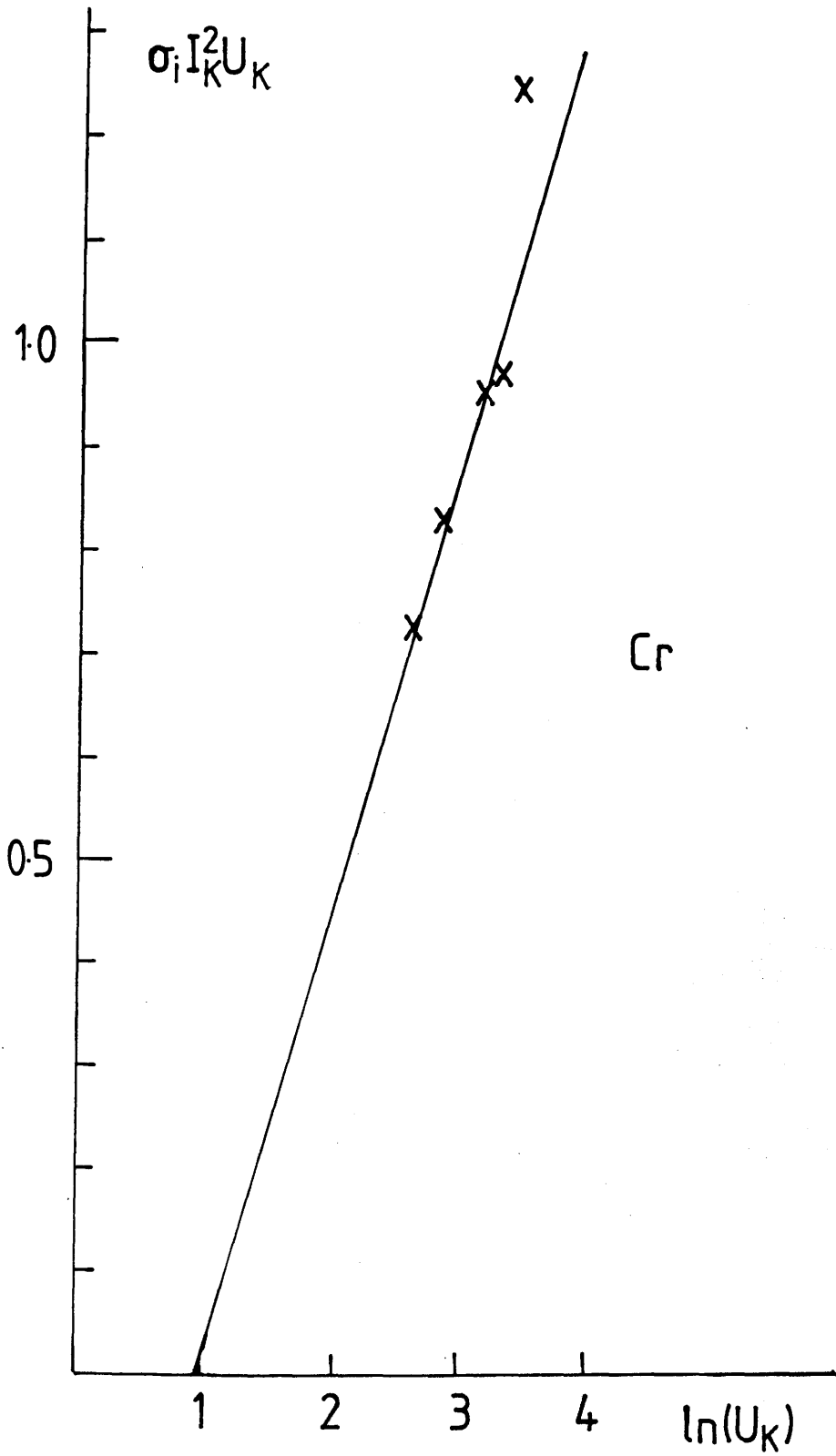
Figure 4.7 Fano plots of $\sigma_{iK}I_K{}^2U_K$ vs. $\ln(U_K)$ for individual elements (data from the JEOL TEM).

(a) Cr

(b) Fe

(c) Co

(d) Cu
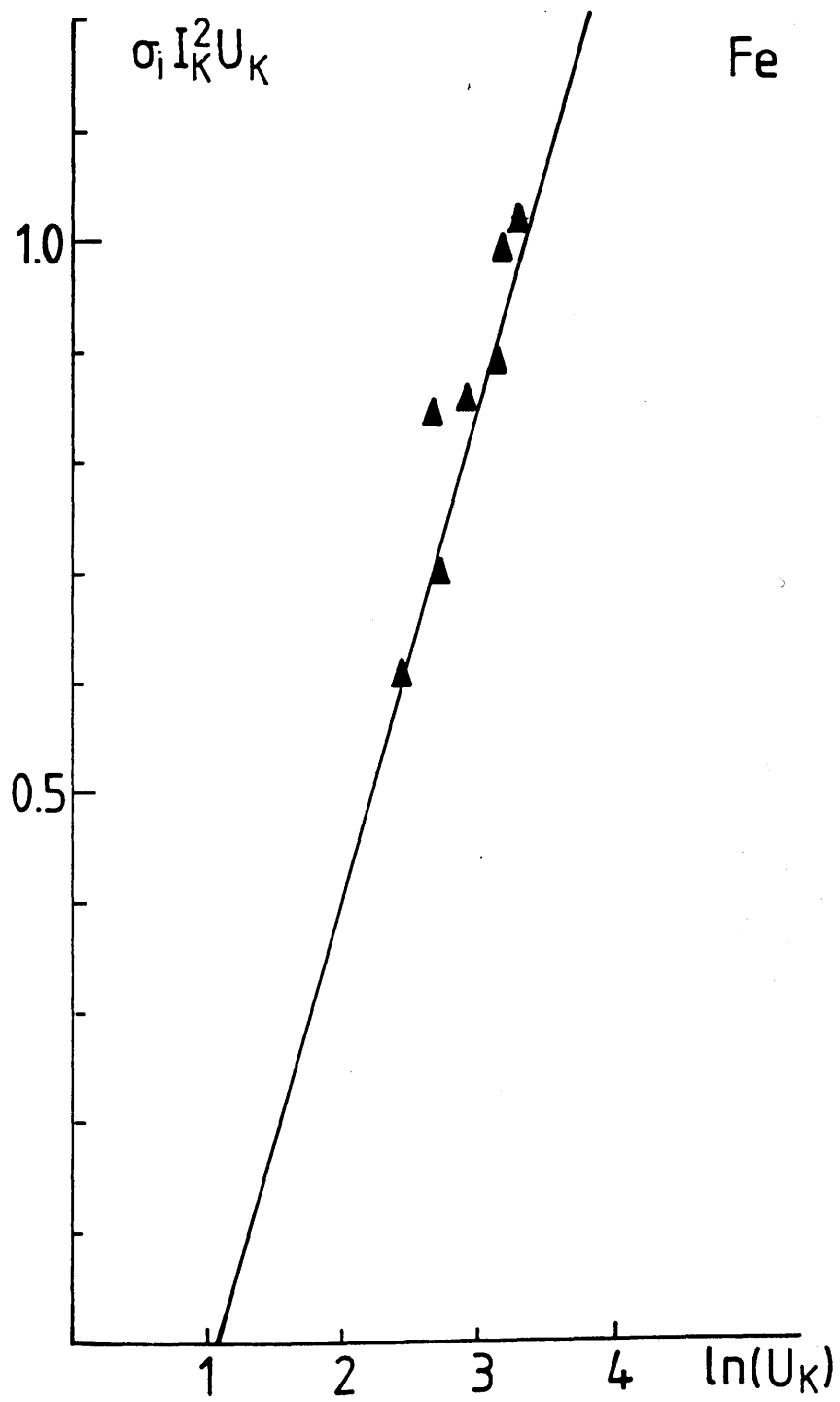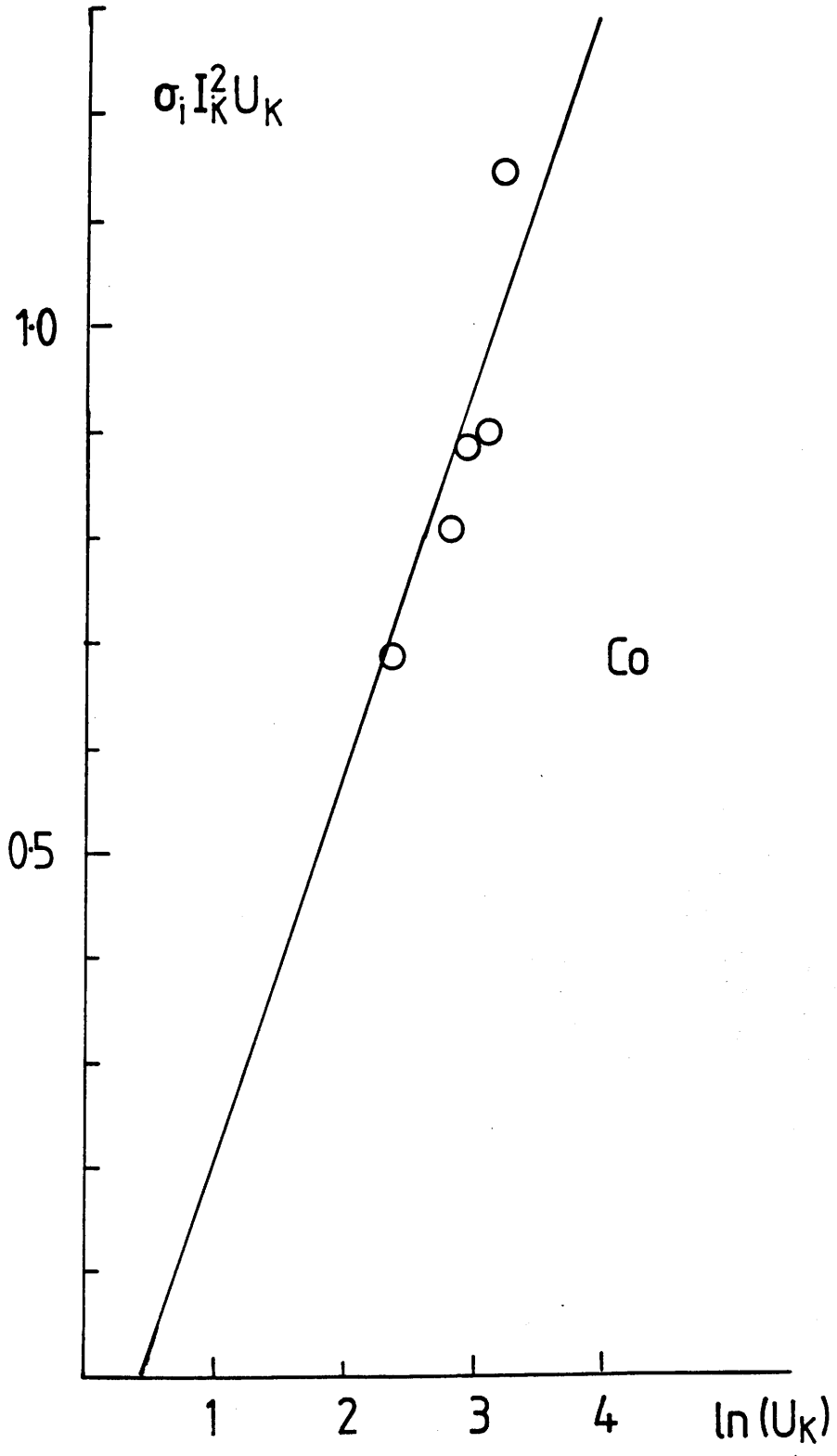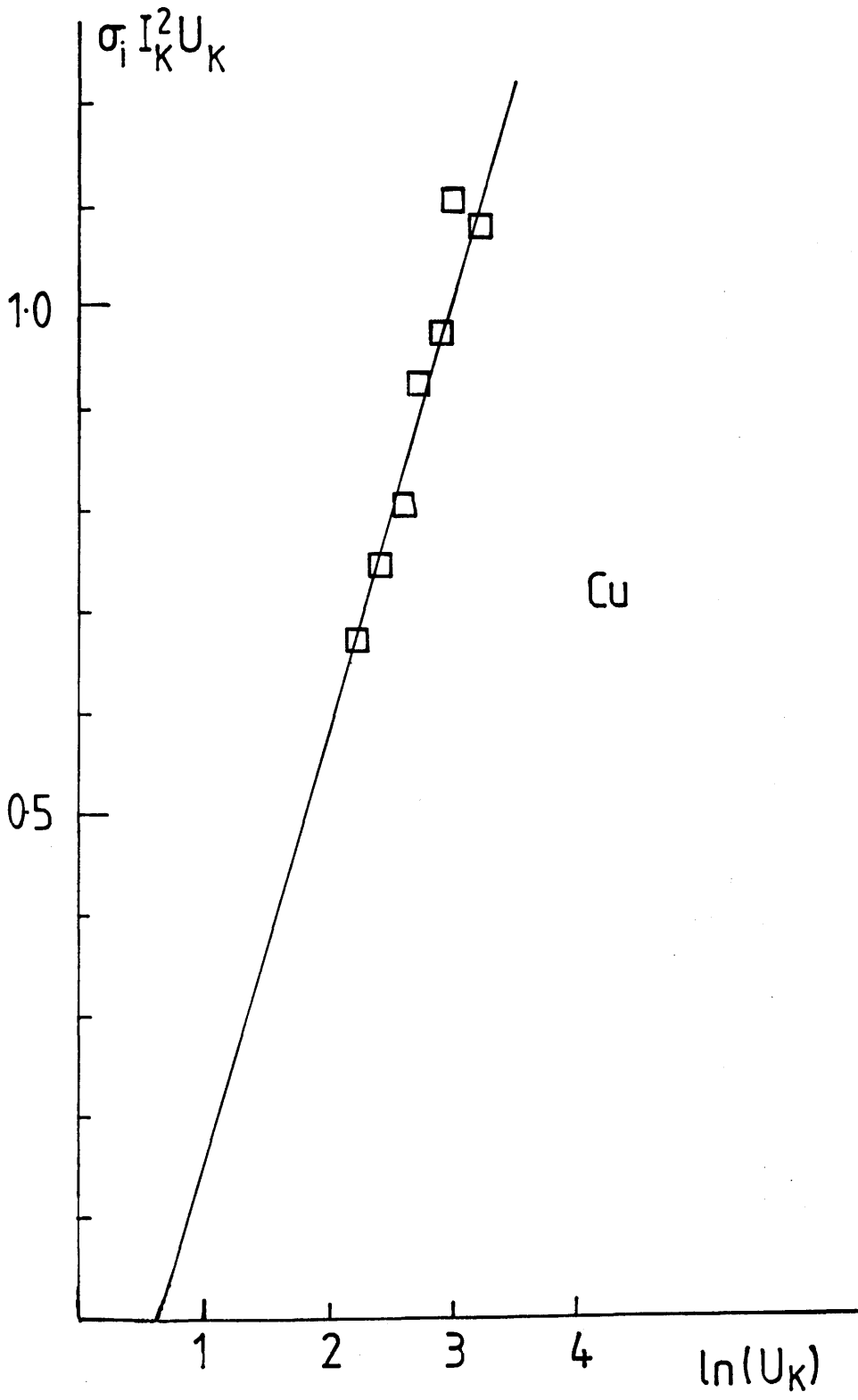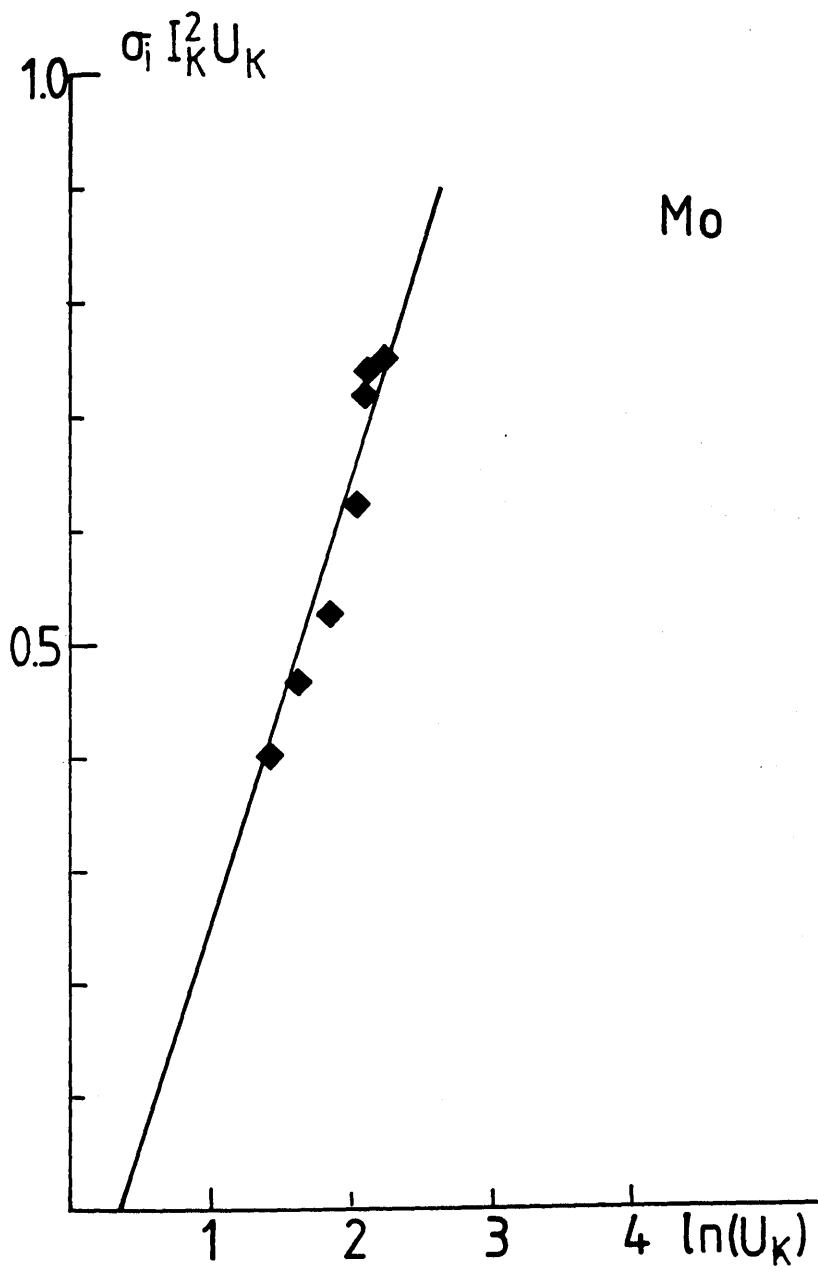
(e) Mo
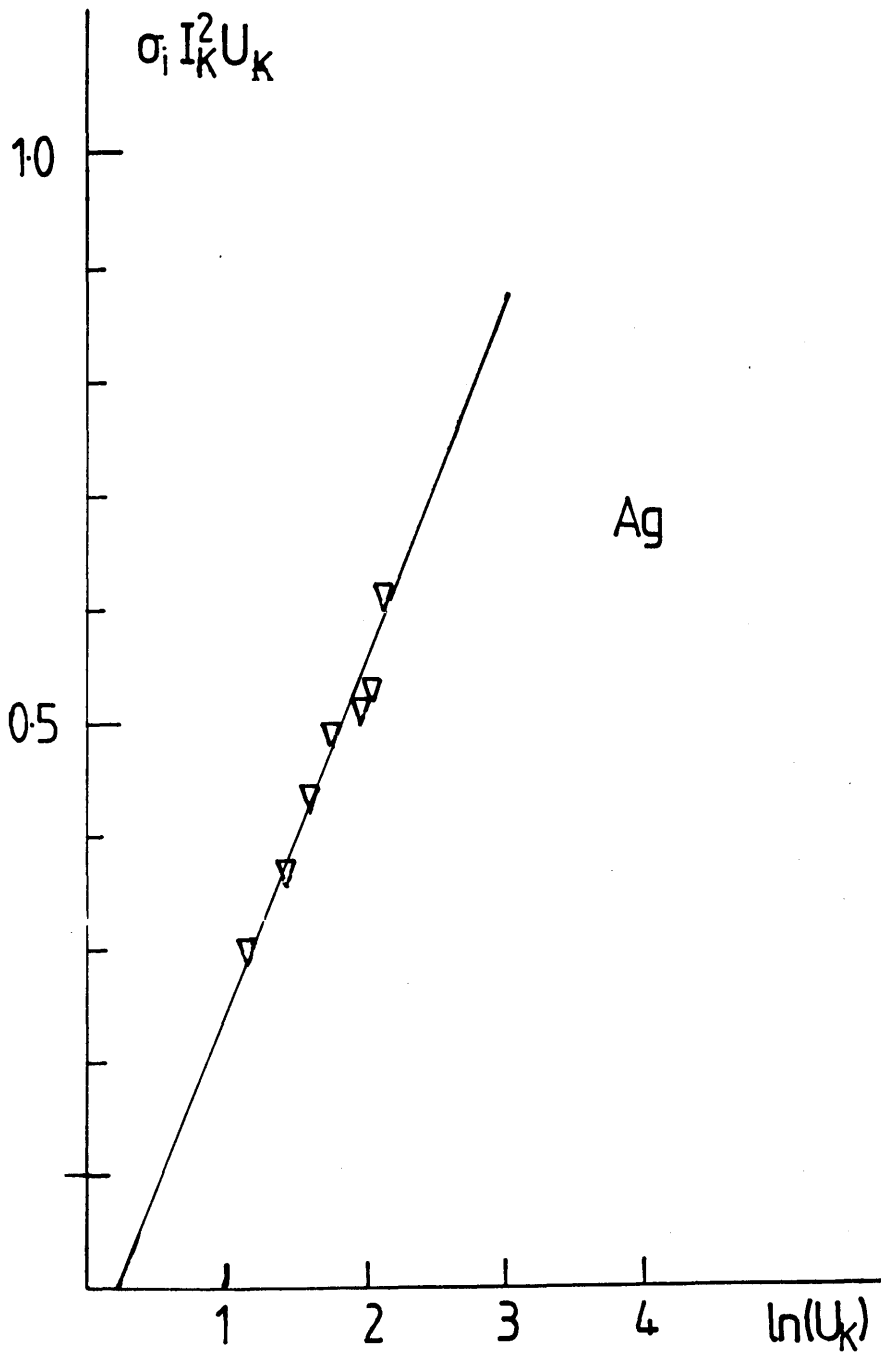
(f) Ag

element	$b_K(Z)$	$c_K(Z)$
Cr	0.74	0.57
Fe	0.95	0.32
Co	0.74	0.61
Cu	0.94	0.46
Mo	0.83	0.65
Ag	0.64	0.82

Table 4.6. Values of the Bethe parameters deduced by fitting separately to the data points from each element

and NiO; and from MoO_3 crystals supported on holey carbon. The method used to prepare the holey backing films is described in appendix C. All spectra were recorded at an accelerating voltage of 100kV. Where there was a holey backing film, spectra were recorded from areas of the specimen which were above holes so the the backing would not contribute to the bremsstrahlung. As before, the size of the instrumental peaks indicated that the associated background contribution was small. One of the STEMs was equipped with a windowless x-ray detector, which allows the presence of any significant amounts of C and O to be detected. The specimen holders used in many cases were Be cartridges (see chapter 3), however, from which no characteristic line could be detected, even with the windowless detector. Background contributions from these light elements would be most likely to affect the P/B values obtained from Si, the lightest element studied here, due to the approximate Z^2 dependence of bremsstrahlung intensity .

The high photon energy effi?ciencies for both detectors were determined by the method used for the detector on the JEOL TEM (see section 4.5). Experimental and theoretical backgrounds were compared in spectra from Ag and Sn, recorded over the range 0-40kev. The crystal thickness deduced for the detector on the HB5 was 0.21cm. Initial measurements yielded a value of 0.10cm for the detector on the HB501. The measurement was repeated after modifications were made by the manufacturer to the electronics of the detection system, yielding a value of 0.14cm. Both before and after modification, the background shapes obtained from this detector fitted well to MBH with exponential thickness corrections. It appears, therefore that electronic modifications can change the effective thickness of the active part of the detector crystal.

Table 4.7 shows the P/B values obtained together with the type of specimen holder used in each case. There are not sufficient data to allow any firm conclusions to be made concerning the relative performances found using the different types of holder. There is some evidence from the results for the transition metals and Ge that there is a greater background contribution from the Be double-tilt type than from the others. This observation agrees with the measurements of Adam (1986) on the Be and the fixed "low-background" holder. It is nevertheless somewhat disturbing that such variations are found between separate measurements of the same quantity, ie P/B for a given element at a given value of T_0, when the quality of the background fit gives no indication of artefacts in the spectra. Figure 4.8(a) and (b) show two different

element	specimen type	microscope	cartridge type	P/B
Si	th.	HB5	DT	1850
Fe	th.	HB501	ST	2000
Co	evap.	HB501	DT	1870
Ni	evap.	HB501	DT	1850
Ni	th.	HB501	ST	2150
Cu	evap.	HB501	DT	1700
Ge	evap.	HB501	DT	1580
Ge	evap.	HB5	LB	1700
Mo	cryst.	HB501	ST	1100/1240
Mo	cryst.	HB5	DT	1290
Ag	evap.	HB501	DT	900/1100
Ag	evap.	HB5	LB	1100
Sn	evap.	HB501	DT	810
Sn	evap.	HB5	DT	690/870

key: specimen type   th. – ion-beam thinned
evap. – evaporated film on holey substrate
cryst. – crystals on holey substrate

cartridge type   DT – Be double-tilt
ST – ferritic single-tilt
LB – fixed low-background (HB5 only)

Table 4.7 Experimental conditions for the P/B values recorded on the VG STEMs
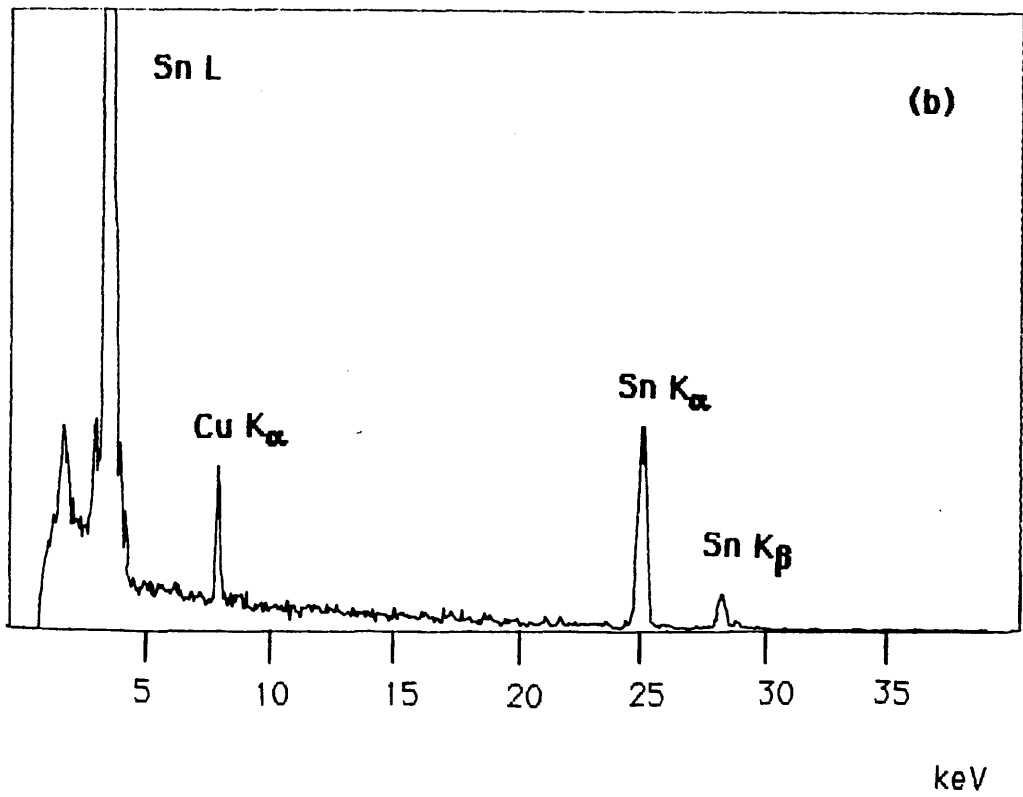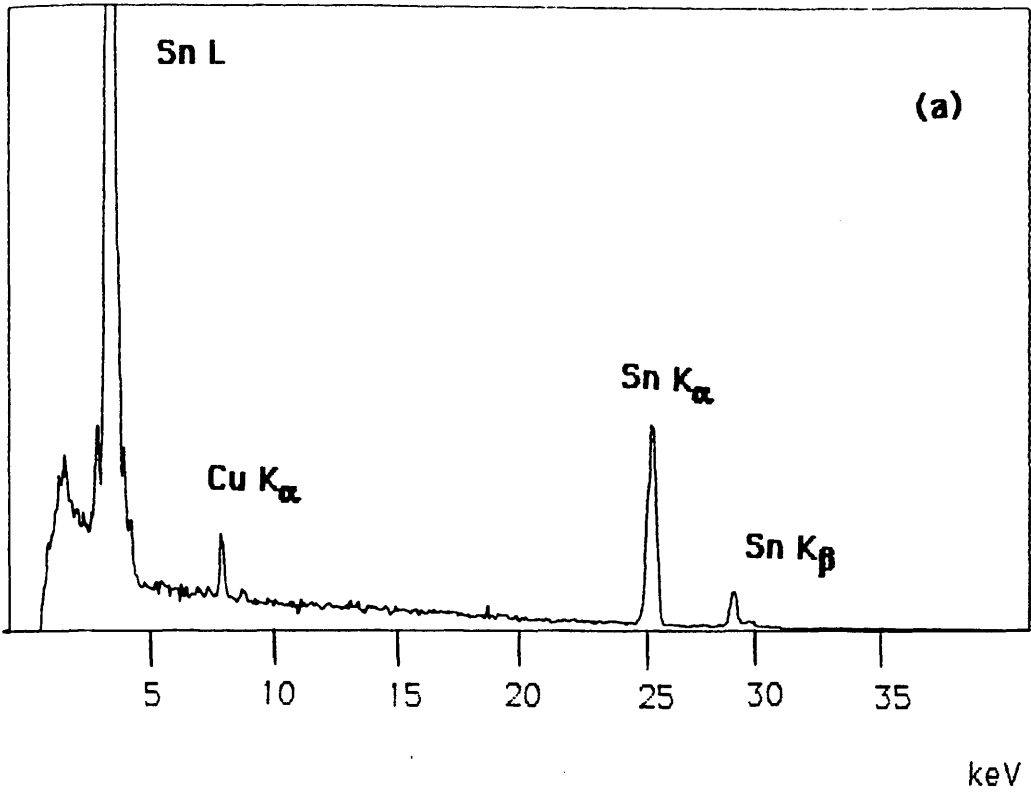
Figure 4.8 Two spectra recorded using the VG HB5 from the same Sn specimen

spectra from Sn, both recorded on the HB501 at 100keV. In both cases MBH fits well to the background, and there is no obvious reason why one should give a more valid result for P/B than the other. However, the spectrum in figure 4.8(a) yields a P/B value of 690, while that in figure 4.8(b) gives a P/B value of 890, the difference being appreciably outwith the limits of statistical error.

Analysis of this data followed the procedure described in section 4.7. Tables 4.8 and 4.9 list the equivalent values to those in tables 4.2 and 4.3 for the additional data points. Again the non-relativistic and relativistic forms of the Bethe model were investigated. Figures 4.9(a) and 4.9(b) show the respective Fano plots obtained from the complete data set from all three microscopes. In both cases there is a reasonable degree of consistency between the values obtained using the different microscopes. The magnitude of the overall variation is not appreciably greater than the variation in the data from each individual microscope. New values of b_K and c_K were deduced from a linear fit to all the points. Since the purpose was now to produce the 'best' values for the parameters rather than direct comparison with previous work, a slightly different approach was adopted. The method of minimising fractional variations was retained, but it was considered advantageous for the general accuracy of the predicted cross sections to minimise the largest fractional variation of any point within the data set. The values of the parameters thus obtained were $b_K = 0.62$ and $c_K = 0.90$ (non-relativistic case) and $b_K = 0.43$ and $c_K = 1.26$ (relativistic case). Table 4.10 shows the fractional variation for each point and the mean variation in each case. The inclusion of a substantial number of data points recorded at an accelerating voltage of 100kV has the effect that the relativistic model now appears to offer no significant advantage.

4.9 Conclusions

The accuracy with which ionisation cross sections for incident electron energies in the range 80keV to 200keV over a wide range of elements can be predicted by a simple approximate model has been investigated. Experimental values for σ_{iK} have been determined using a TEM and two STEMs. The consistency within the overall data set suggests that the method used, involving the measurement of P/B values, produces values which are, as expected, independent of the instrument used. Variations outwith statistical error were found in P/B measurements for some elements on the same microscope at the
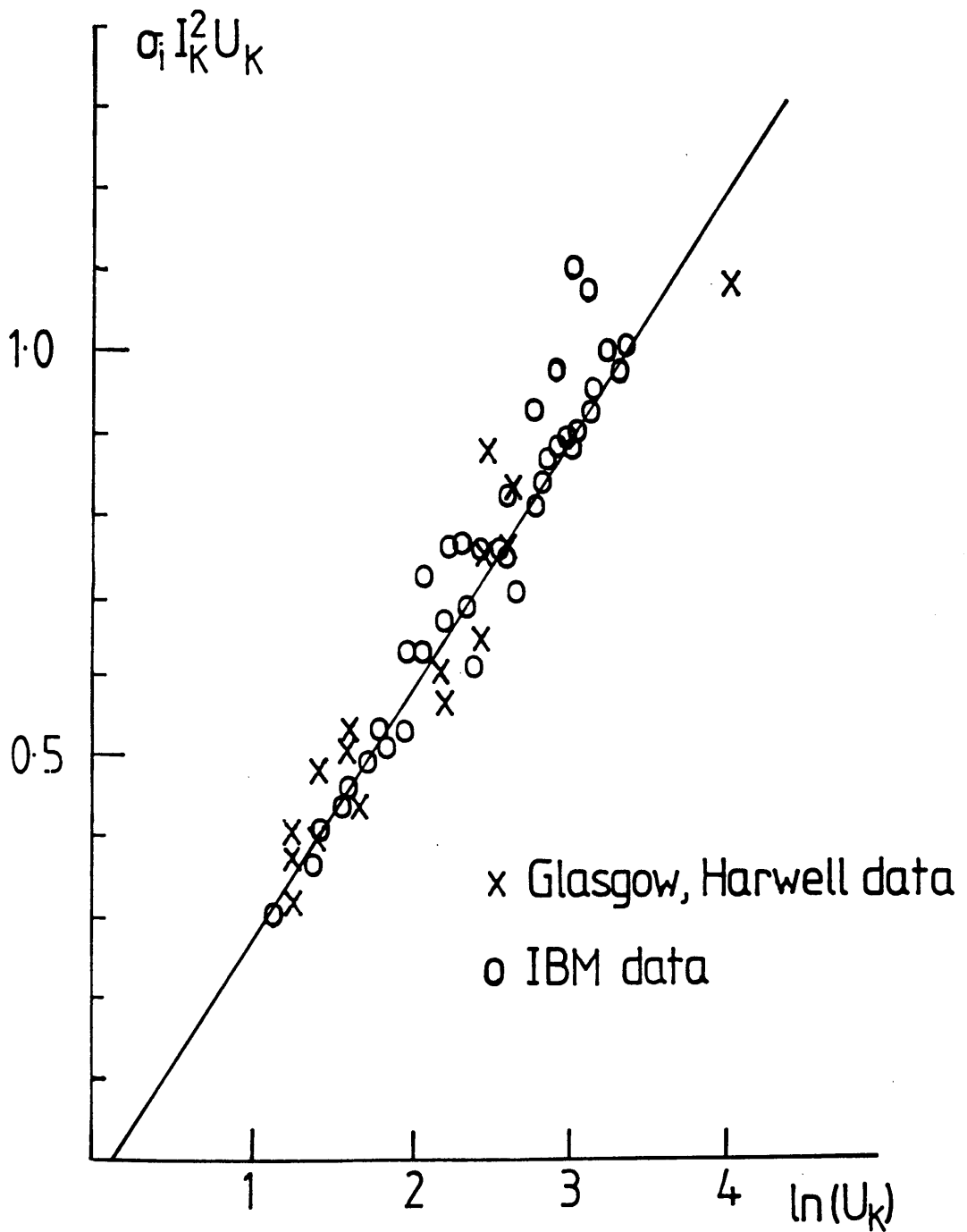
Figure 4.9 (a) Fano plot of $\sigma_{iK}I_K{}^2U_K$ vs. $\ln(U_K)$ for the data from all three microscopes. ($U_K = T_0/I_K$)
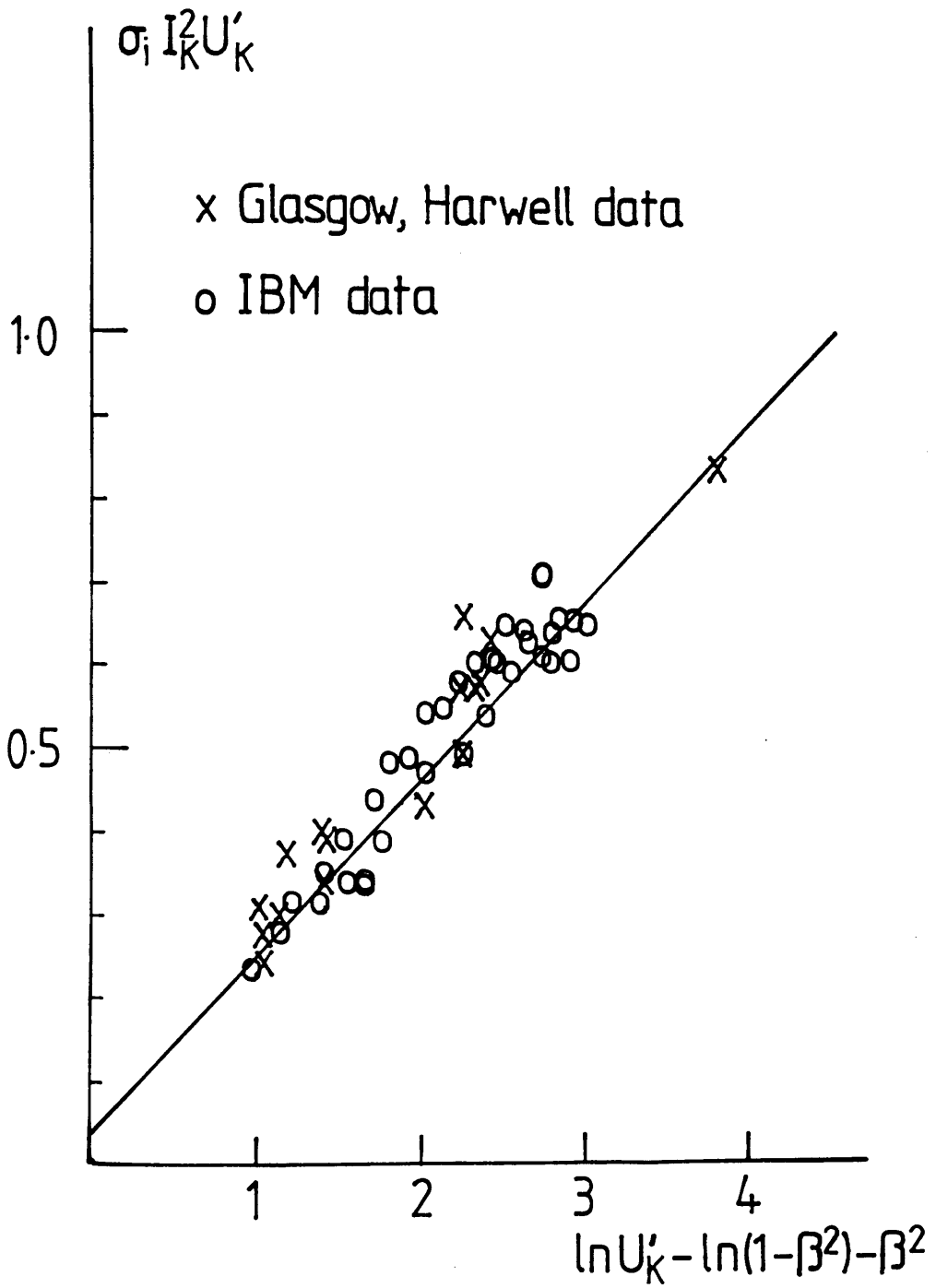
(b). Fano plot of $\sigma_{iK} I_K^2 U_K'$ vs. $\ln(U_K') - (1-\beta^2) - \beta^2$ for the data from all three microscopes. ($U_K = 1/2 m_0 v^2 / I_K$)

element	T_0 (keV)	U_K	$\ln(U_K)$	P/B	$\sigma_b(h\text{v},\Omega)dh\text{v}$ (b sr^{-1}keV^{-1})
Si	100	54.6	4.00	1370	4.35
Fe	100	14.0	2.64	2000	3.57
Co	100	12.9	2.56	1870	3.51
Ni	100	12.1	2.49	1850	3.45
	100	12.1	2.49	2150	3.45
Cu	100	11.1	2.41	1700	3.39
Ge	100	9.03	2.20	1580	3.22
	100	9.03	2.20	1700	3.22
Mo	100	5.00	1.61	1100	2.69
	100	5.00	1.61	1240	2.69
	100	5.00	1.61	1290	2.69
Ag	100	3.94	1.37	900	2.45
	100	3.94	1.37	1100	2.45
Sn	100	3.42	1.23	690	2.31
	100	3.42	1.23	810	2.31
	100	3.42	1.23	870	2.31

Table 4.8. VG STEMs data used to produce non-relativistic Fano plot from overall data set. *(part 1)*

element	T_0 (keV)	σ_c (b sr^{-1})	σ_i (b)	$\sigma_i I_K{}^2 U_K$ (b keV^2)
Si	100	5.95	1552	1.09
Fe	100	7.13	302	0.821
Co	100	6.56	254	0.749
Ni	100	6.38	234	0.747
	100	7.41	272	0.869
Cu	100	5.76	186	0.639
Ge	100	5.08	133	0.564
	100	5.47	143	0.607
Mo	100	2.95	58.1	0.445
	100	3.33	65.5	0.502
	100	3.46	68.2	0.522
Ag	100	2.20	40.3	0.394
	100	2.69	49.3	0.481
Sn	100	1.60	28.8	0.322
	100	2.01	36.3	0.405
	100	1.87	33.8	0.377

Table 4.8. VG STEMs data used to produce non-relativistic Fano plot from overall data set. *(part 2)*

element	T_0 (keV)	β	$U_K{}'$	$\ln(U_K{}')$	$\sigma_i I_K{}^2 U_K{}'$ (b keV^2)
Si	100	0.548	41.9	3.74	0.837
Fe	100	0.548	10.8	2.38	0.630
Co	100	0.548	9.93	2.30	0.575
Ni	100	0.548	9.26	2.23	0.574
	100	0.548	9.26	2.23	0.667
Cu	100	0.548	8.55	2.15	0.491
Ge	100	0.548	6.93	1.94	0.433
	100	0.548	6.93	1.94	0.466
Mo	100	0.548	3.84	1.35	0.342
	100	0.548	3.84	1.35	0.385
	100	0.548	3.84	1.35	0.401
Ag	100	0.548	3.02	1.11	0.303
	100	0.548	3.02	1.11	0.369
Sn	100	0.548	2.63	0.966	0.247
	100	0.548	2.63	0.966	0.311
	100	0.548	2.63	0.966	0.289

Table 4.9. Additional VG STEMs data used to produce relativistic Fano plot from overall data set.

element	T_0(keV)	non-relativistic		relativistic	
		LR	MFV	LR	MFV
Cr	80	0.054	0.041	0.044	0.057
	100	0.027	0.014	0.039	0.049
	120	0.039	0.027	0.006	0.002
	140	0.006	0.004	0.010	0.002
	160	0.032	0.022	0.074	0.067
Fe	80	0.20	0.18	0.095	0.078
	100	0.15	0.13	0.077	0.063
	120	0.007	0.018	0.035	0.045
	160	0.059	0.047	0.10	0.095
	180	0.033	0.043	0.044	0.037
	200	0.019	0.029	0.098	0.091
Co	80	0.037	0.022	0.051	0.067
	120	0.038	0.025	0.009	0.002
	140	0.010	0.021	0.003	0.013
	160	0.029	0.017	0.073	0.064
Cu	80	0.011	0.026	0.090	0.11
	100	0.034	0.047	0.086	0.10
	120	0.040	0.052	0.062	0.075
	140	0.10	0.11	0.092	0.10
	160	0.10	0.11	0.059	0.068
	180	0.18	0.19	0.11	0.12
	200	0.12	0.13	0.018	0.026

LR - linear regression   MFV - minimum largest fractional variation

Table 4.10. Fractional variations of data points from the
values calculated using Bethe parameters
fitted to the overall data set.

element	T_0(keV)	non-relativistic		relativistic	
		LR	MFV	LR	MFV
Si	100	0.12	0.12	0.032	0.032
Fe	100	0.023	0.035	0.082	0.093
Co	100	0.038	0.024	0.023	0.036
Ni	100	0.13	0.14	0.046	0.060
	100	0.011	0.003	0.18	0.19
Cu	100	0.14	0.13	0.082	0.064
Ge	100	0.18	0.16	0.12	0.10
	100	0.095	0.078	0.044	0.024
Mo	100	0.081	0.058	0.062	0.026
	100	0.042	0.062	0.058	0.091
	100	0.079	0.098	0.094	0.13
Ag	100	0.030	0.005	0.034	0.011
	100	0.16	0.18	0.15	0.19
Sn	100	0.13	0.094	0.15	0.088
	100	0.11	0.13	0.089	0.13
	100	0.039	0.066	0.021	0.071

LR – linear regression   MFV – minimum largest fractional variation

Table 4.10. (continued)

same value of T_0. It must be concluded that it is possible to have some contributions to the background which are not easily detected by a poor fit to the appropriate MBH shape. This limits the certainty with which a single value of P/B may be determined. The background shape can indicate the presence of serious artefacts, for example the unacceptably high extraneous background contribution recorded with the high take-off angle detector on the JEOL TEM.

The values obtained for the parameters b_K and c_K of the Bethe model agree well with previous work. There is some evidence that it is advantageous to use the relativistic form of the Bethe model in cases where the incident electron energy is towards the high end of the range studied here. There is some evidence from this and other work that b_K and c_K are not independent of Z, but there are not sufficient data here to draw any firm conclusions on such a variation. In any case, the assumption of constant Bethe parameters is useful in that it allows the prediction of ionisation cross sections over a wide range of elements, within the accuracy indicated previously. It is therefore not necessary to deduce parameters separately for every element which is to be studied.

Although the standardless approach in EDX is often convenient, the results presented here indicate the limitation on the accuracy which can be expected using the Bethe model to calculate σ_{iK}. Over the range of Z and T_0 investigated there were discrepancies between the experimental and calculated values of up to ~20%. It is not certain with what accuracy the model may be applied to elements lighter than Si. The implications of this for light element analysis in windowless EDX are discussed in chapter 6. More accurate analyses generally result from the use of reliable standards if they are available. The Bethe model does, however, provide a simple method of calculating σ_{iK} in a useful range of experimental situations.

Chapter 5

Analysis of EDX data from the L-shell

5.1 Introduction

The previous chapter described the general procedures for EDX analysis as applied to the particular case of K-shell signals. In this chapter, the applicability of these methods to the L-shell is considered. Unlike the K-shell, the L-shell is split into three sub-shells. In the EDX spectrum it is not generally possible to resolve the signals from the individual sub-shells well enough to analyse them separately, and so the total L-shell signal is usually measured. Section 5.2 discusses problems which can arise when using the usual method for estimating the low energy efficiency of a Be window detector, as applied to data from one of the Be window detectors on the JEOL TEM. The results illustrate the uncertainties which can affect attempts to quantify the L-shell signals from transition metals using such a detector. Section 5.3 describes how the low energy efficiency of the windowless detector was estimated.

Since the work described previously had provided reliable information on the K-shell, it seemed that the most convenient approach to obtaining similar information on the L-shell lay in comparing the signals from the two shells. Section 5.4 describes a series of measurements of K_α/L-line count ratios. As for the K_α production cross section measurements of chapter 4, values were measured where possible using different microscopes and detectors to check for consistency. For the lighter elements studied, however, the L-shell signal could only be measured accurately using the windowless detector on the VG STEM at AERE Harwell. These count ratios were converted to x-ray production ratios. The low energy detector efficiencies were based on the methods and results described in sections 5.2 and 5.3. The high energy efficiencies were estimated using the effective crystal thickness method described in chapter 4. The values of x-ray production cross section which result are listed and compared with corresponding values in the literature. The application of reliable K/L-shell cross section data to the estimation of absorption effects in EDX spectra is then

discussed.

Section 5.6 describes how these data were used to try to deduce information on the L-shell ionisation cross sections. The process of x-ray production for the L-shell is complicated by the probability of redistribution of ionisation between the three sub- shells. This takes place by means of radiationless Coster-Kronig transitions. The aim of this work was to assess how well the ionisation cross sections for the three sub-shells could be described by the simple Bethe model which had some success in describing the K-shell. The method used for this made use of the relative insensitivity of cross sections calculated by the Bethe model to the c parameter with the high overvoltages corresponding to ionisation of the L-shell by 100keV electrons. The final section examines the variation of K_α/L ratio with incident electron energy. The results are compared with the variation predicted by the Bethe model, and the effect of varying the c_L parameter is assessed.

5.2 Low energy detector efficiency for a Be window detector

As described in chapter 3 the efficiency of an x-ray detector falls below unity at low energies due to absorption of the incoming photons before they reach the active part of the detector crystal. Absorption of low energy photons before detection by a Be window detector occurs in the Be window; in the Au contact layer at the front surface of the detector crystal; and in the Si dead layer at the front surface. (It is convenient to assume for the purposes of efficiency calculation that the last of these is a layer of completely inactive Si. The work of Craven et al (1985, 1987) on ICC shows that this assumption is an over-simplification). Absorption in the window is the most significant of these effects. If all three parameters are known, the detector efficiency $\varepsilon(h\nu)$ for photons of energy $h\nu$ can be calculated using the expression

$$\varepsilon(h\nu) = \exp(-\mu/\rho_{Be}(h\nu)x_{Be}-\mu/\rho_{Au}(h\nu)x_{Au}-\mu/\rho_{Si}(h\nu)x_{Si}) \quad (5.2)$$

where $\mu/\rho_Z(h\nu)$ is the mass absorption coefficient for photons of energy $h\nu$ in element Z, ρ_Z is the density of element Z and x_Z is the thickness of the layer of element Z. As mentioned in chapter 4, effective values for the Be window

thickness can be deduced by comparison of spectra with appropriate MBH curves. The use of an effective Be thickness gives a good approximation to the absorption in the three layers. Calculation of low energy efficiency using values of the detector parameters quoted by the manufacturer or previously determined experimentally relies on the assumption that there is no change in these with time. Experimental determination by comparison with MBH allows measurements to be made periodically to check the constancy of the efficiency, and to revise the values adopted if necessary.

Spectra recorded on the JEOL TEM low angle Be window detector were examined in order to deduce an effective thickness value for its window. The specimens and experimental conditions are described in section 4.5. Figure 5.1 shows the low energy region of a spectrum from Cu. An MBH curve was fitted to the background over regions where the detector efficiency was assumed to be unity, as described in section 4.5. The theoretical background was corrected for absorption in a range of thicknesses of Be. In each case the theoretical and experimental backgrounds were compared over the regions l_i in figure 5.1 using a chi-squared test. The background shown is that which gave the lowest value for χ^2 of 1.56. This fit is sufficiently good that there are no obvious indications of any problems with this spectrum. The deduced Be thickness is 30µm, however. This is much greater than the nominal window thickness of ~10µm. This result is highly typical of all these spectra. It is unlikely the window is really 30µm thick, and the difference would not be accounted for by realistic values of Au contact and Si dead layer thicknesses. There must therefore have been some other source of absorption. The accumulation of a layer of ice on the window could give rise to such an effect. If this is the case then a problem is encountered in the deduction of the detector efficiency for lines with energies at the lower limit of detectability. It is not possible to tell from fitting to the spectrum as described in what proportions the absorption is due to O (in the ice) and the usual detector parameters, approximated by an effective thickness of Be. The effect of assuming different combinations of Be and ice thickness on efficiencies calculated by extrapolating to energies below region 1 was investigated. The spectrum used for this was from Co. The effective Be thickness deduced using the method described before was again 30µm, with $\chi^2=1.53$. In this case, however, a fixed value for the window thickness was chosen initially. The MBH background was then corrected for absorption in this fixed thickness of Be plus a range of thicknesses of O. As before a chi-squared test over region 1
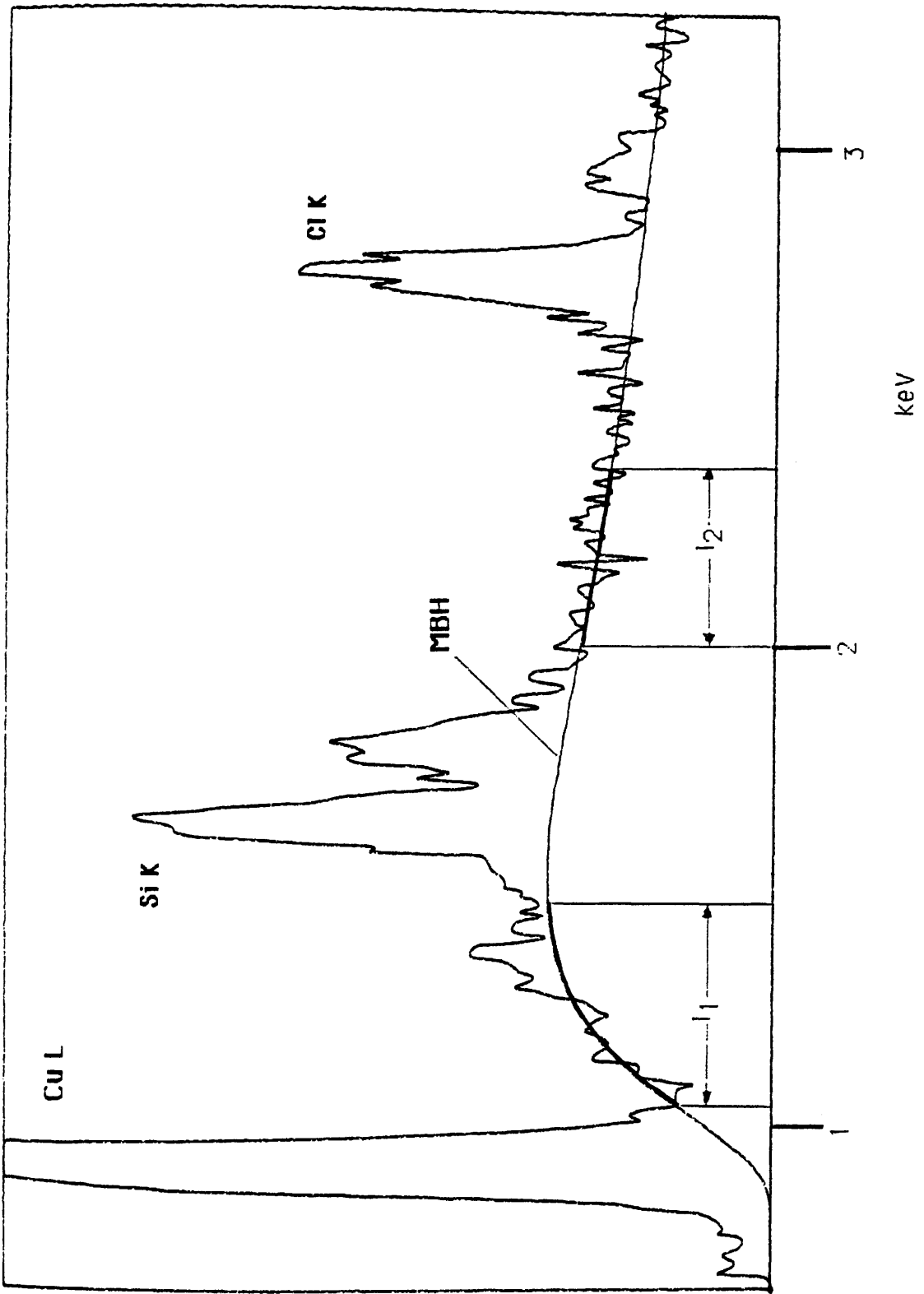
Figure 5.1 The low energy end of a spectrum recorded from Cu using the 90° detector on the JEOL TEM. The fitting regions used to determine the effective Be window thickness are indicated.

yielded the value of O thickness which best described the experimental background. This process was carried out for fixed Be thicknesses of 5μm and 10μm. The values for O thickness deduced were 6.3μm and 5.0μm in the respective cases. Table 5.1 lists the efficiencies calculated for transition metal L-lines assuming each of these combinations of Be and O absorption, and the variation of the ratio of the efficiency curves for each case with photon energy is shown in figure 5.2.

For the Cu L-line, the values of efficiency calculated vary by ~10% about their mean, and the discrepancy is greater for the lighter elements. This illustrates the errors which can occur in the measurement of L-shell x-ray production for these elements using Be window detectors, even if care is taken to model the the background in each spectrum. If the manufacturer's quoted figures for the detector parameters had been assumed in this case then serious errors would have resulted. Measurements in this energy region are likely to produce reliable results only if a windowless or UTW detector is used.

5.3 Estimating the low energy efficiency of the windowless detector

The absence of any Be window allows a windowless detector to detect low energy photons with a far greater efficiency than a conventional detector. Some absorption occurs in the Au contact layer and Si "dead" layer however, and so the efficiency still falls significantly below unity at low energies. In principle the efficiency can still be calculated if the values of these parameters are known, eg Thomas (1984). It should again be possible to deduce effective values of absorber thickness by comparison of spectra with MBH. Significant errors can be expected in any efficiency values for very low energies (<~0.5keV) due to uncertainties in the values of mass absorption coefficients in this region. There must also be some doubt concerning the applicability of MBH theory at such energies. The experimental measurements with which Chapman et al. compared the predictions of MBH were all made at photon energies >3keV. However, numerical calculations by Pratt et al. (1977) show good agreement with MBH theory for energies down to 0eV.

Three attempts were made to estimate the efficiency of the windowless detector

element	L-line energy (keV)	$\epsilon_{10\mu m:Be,5\mu m:ice}$	$\epsilon_{5\mu m:Be,6.3\mu m:ice}$
Cr	0.571	2.4×10^{-9}	9.0×10^{-10}
Fe	0.704	2.5×10^{-5}	1.6×10^{-5}
Co	0.775	3.6×10^{-4}	2.6×10^{-4}
Cu	0.928	1.03×10^{-2}	0.85×10^{-3}

Table 5.1. Detector efficiencies for the L-lines of selected
elements, calculated assuming Be window
thicknesses of 10μm and 5μm. The respective
ice layer thicknesses were deduced from
comparison of the low energy end of experimental
spectra with MBH.
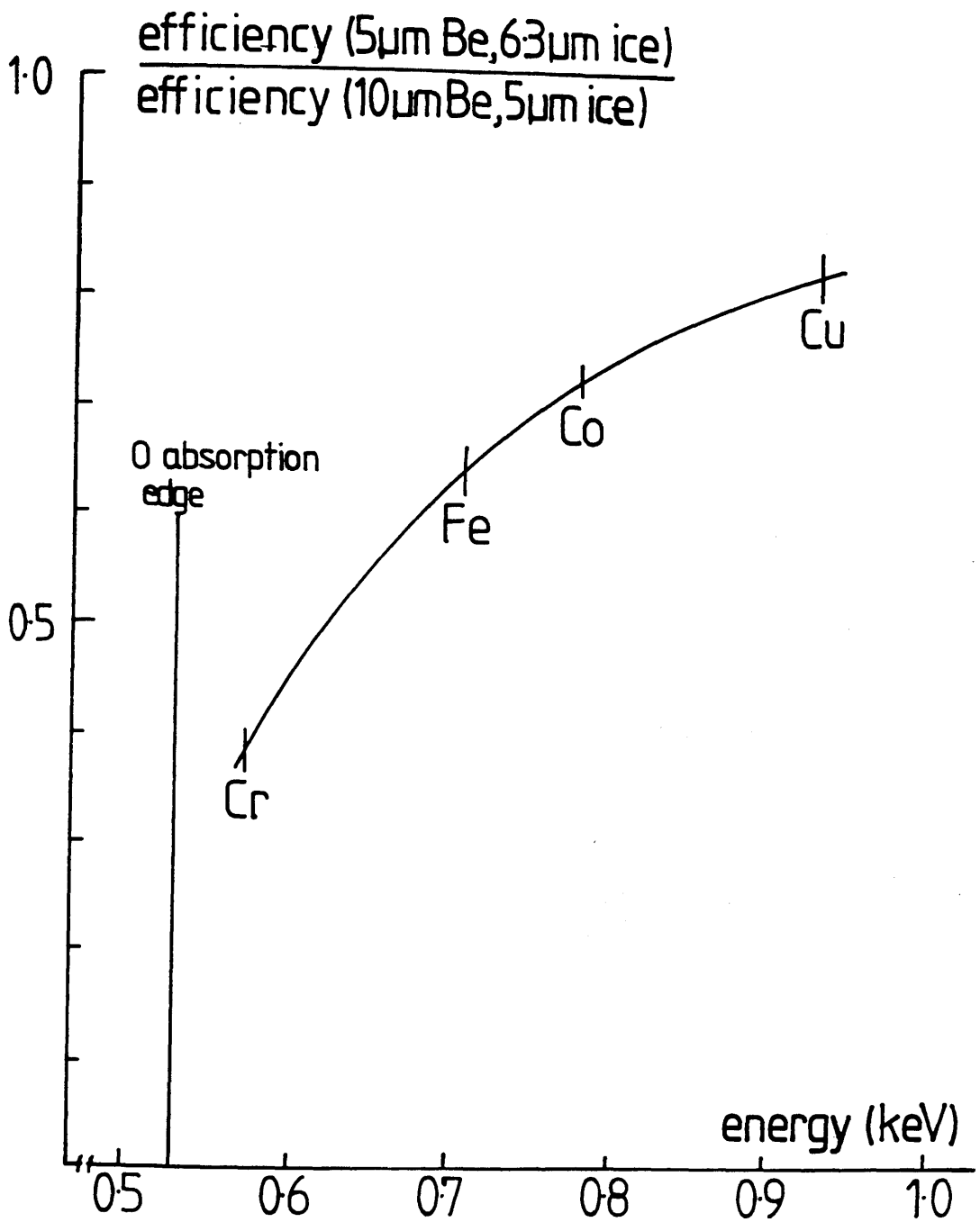
Figure 5.2   Illustration of the effect on the calculated detector efficiency of a Be window detector of assuming differing proportions of Be thickness and ice layer thickness. The graph shows how the ratio of the efficiencies calculated assuming two plausible configurations varies with photon energy hν.

for energies down to ~0.7keV, so that efficiency corrections could be made for the transition metal L-lines. Ideally, this would require a spectrum with no peaks in this region to allow a simple comparison to be made with MBH. The three estimates gave a wide variation in the predicted efficiencies. There were grounds for belief that two of the estimates were affected by artefacts in the spectra used.

The first estimate was based on the Sn spectrum shown in figure 5.3. This shows a suitable peak free region as far down in energy as the unresolved series of peaks due to the Sn M and O K lines. The MBH curve shown was fitted over suitable regions in the mid- energy part of the spectrum, and values of efficiency at the relevant line energies were deduced by comparison of the experimental and theoretical backgrounds. These values are listed in the first column of table 5.2. They are generally significantly lower than the values calculated by Thomas (1984), who described the efficiency in terms of absorption in 200Å of Au and 0.15μm of Si.

This estimate relies on the assumption that this spectrum is not subject to any absorption effects. The thickness of the film was estimated at the time of evaporation to be ~150Å. Such a thickness corresponds to specimen self-absorption of ~0.5% of the Sn L-line. This is consistent with the observation of no evidence in the spectra of any absorption in the region of the Sn L-line. This thickness of Sn would, however, absorb ~15% of photons at the energy of the Fe L-line. Absorption of low energy radiation could be more severe still if the film thickness was underestimated. Such an error would be difficult to detect. A film of twice the estimated thickness, ie ~300Å, would still absorb <1% of the Sn L-line signal, but would absorb ~25% of photons with the energy of the Fe L-line. It seemed desirable to make further estimates, if possible from spectra where absorption was known not to be significant at low energies. The spectra recorded from Si showed a useful region between the Si K peak and the C K peak. There was, however, a small Cu L peak in the middle of this region, rendering direct comparison of experimental and theoretical backgrounds impossible for most of the transition metal L-line energies. Figure 5.4 shows a typical spectrum. It was decided to try to estimate an effective absorber thickness as was done for the Be window detectors. It was not clear whether it would be best to work in terms of an effective thickness of Au, Si or some combination of the two. Two theoretical backgrounds were fitted separately
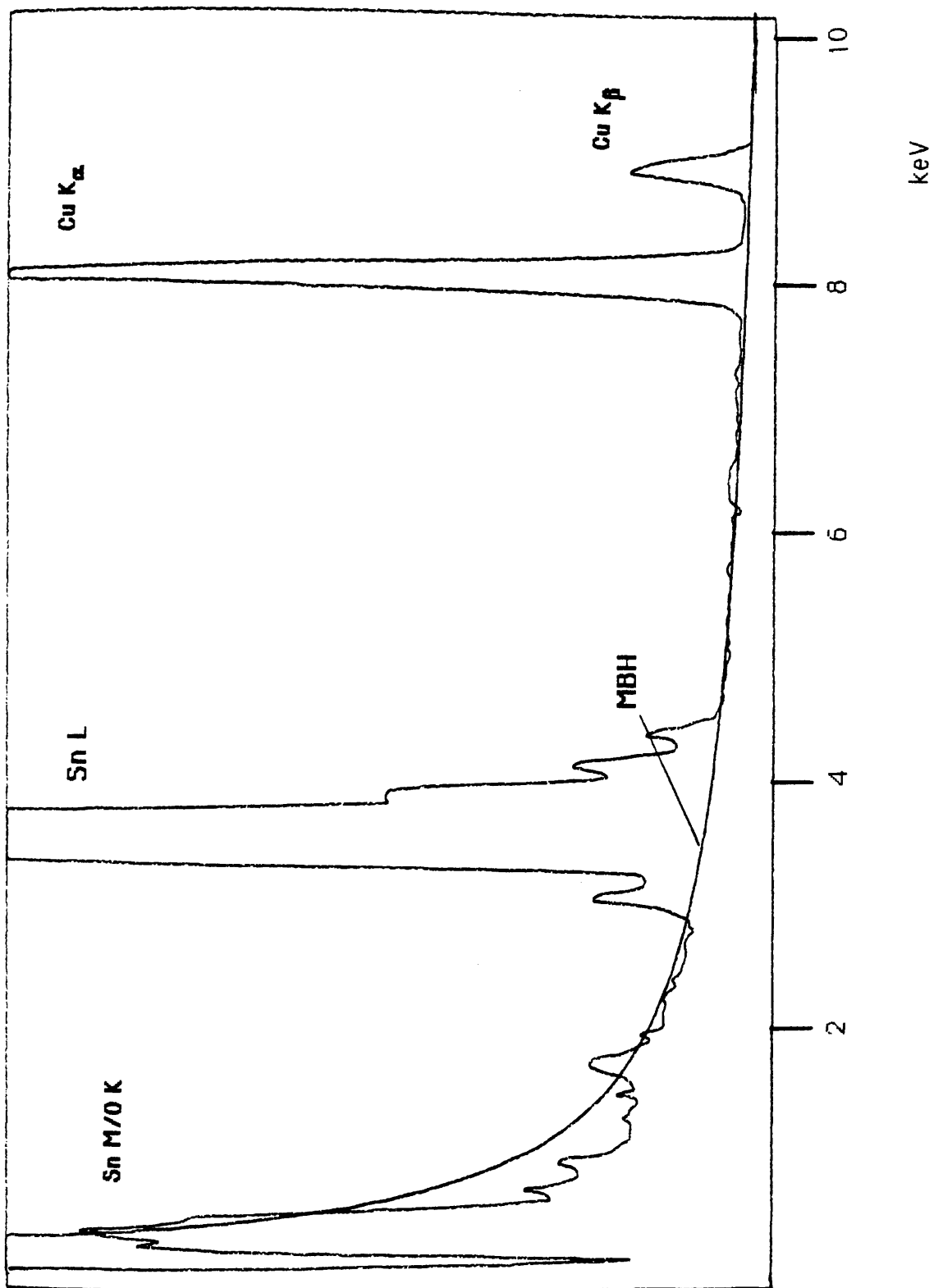
Figure 5.3   Low energy end of a spectrum recorded from Sn on the VG HB501, together with an MBH background with no correction for low energy efficiency.

line	1st. estimate (from Sn)	2nd. estimate (from Si)	3rd estimate (from Ni/NiO)	Thomas (1984)
Fe L	0.43±0.02	0.76±0.06	0.53±0.05	0.61
Co L		0.79±0.05	0.59±0.05	0.67
Ni L	0.52±0.03	0.83±0.04	0.66±0.04	0.71
Cu L	0.59±0.04	0.86±0.04	0.71±0.03	0.75

Table 5.2. Detector efficiencies for transition metal L lines estimated by the three methods described in the text, together with the values calculated by Thomas (1984).
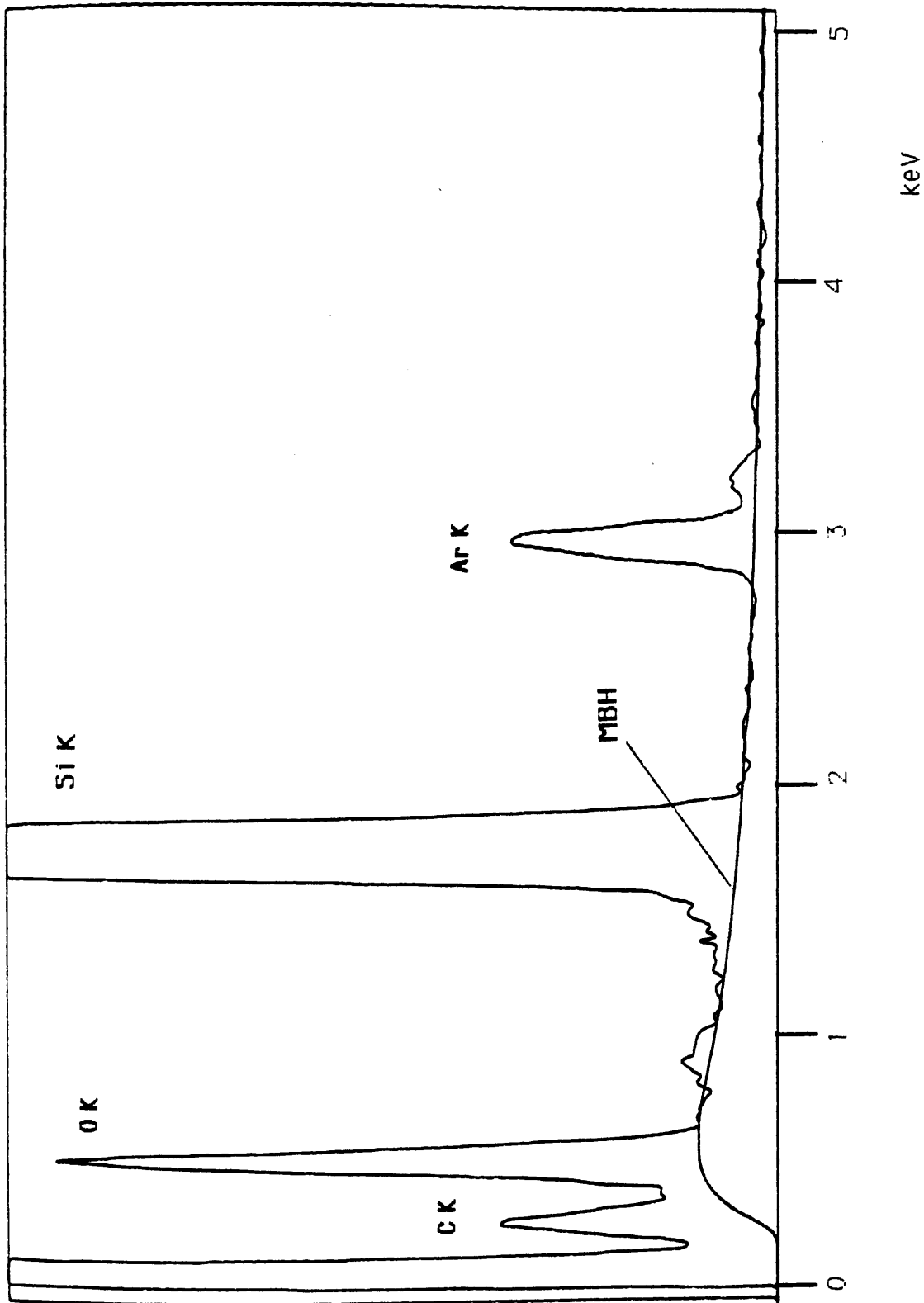
Figure 5.4 Spectrum recorded from Si on the VG HB 501, together with an MBH background corrected for absorption in 110Å of Au.

to each spectrum, corrected for absorption in Au only and in Si only. This process suggested that the experimental background shape could be explained in terms of absorption in either 110Å Au or in 1.30μm Si. Figure 5.5 shows the efficiencies calculated in each case for a range of energies up to ˜1keV. The figure suggests that the absorption mechanism assumed does not affect the efficiency calculated for the transition metal L-lines, though differences become significant at lower energies. It was decided arbitrarily to decribe the efficiency in terms of an effective Au thickness. The second column of table 5.2 lists the efficiency values deduced. Clearly there is a significant discrepancy between the results listed in the first two columns, suggesting that absorption may have been significant in the Sn spectrum. The values deduced from the Si spectra are appreciably higher than would be expected from the work of Thomas. The background region used for fitting in these spectra was close to the large Si K peak, on its low energy side. The Si peak should not be strongly affected by ICC, but there may be a sufficiently strong effect to raise the background level in this region to an extent that a spuriously high efficiency estimate results.

A new value of effective Au thickness was deduced from spectra from Ni and NiO. The spectra chosen were those which yielded the lowest values for the K_α/L count ratios, and so were considered to show the smallest absorption effects. The energy region used was close to the Ni L peak, on its high energy side. There were no other large peaks in the vicinity which could cause the background to be distorted by ICC. A spectrum from Ni is shown in figure 5.6. The limiting factor in the accuracy of the efficiency estimate based on these spectra lay in the need to extrapolate the background shape deduced from the spectrum below the Ni L peak in order to obtain values for the transition metal L-line energies. In the fitting region the efficiency is changing relatively slowly, and the fit is therefore relatively insensitive to the value of Au thickness. Clearly the size of the error can be expected to increase rapidly as the photon energy decreases. A range in the values of effective Au thickness from 210Å to 280Å was found. The resultant variation about the mean value of efficiency calculated for each line was used to estimate the corresponding uncertainty. These results are listed in the third column of table 5.2. They lie between the results of the first and second estimates, and are in better accord with those of Thomas. It was considered that, despite the uncertainties caused by the need to extrapolate, this last estimate was the most reliable of the three, since the artefacts which were
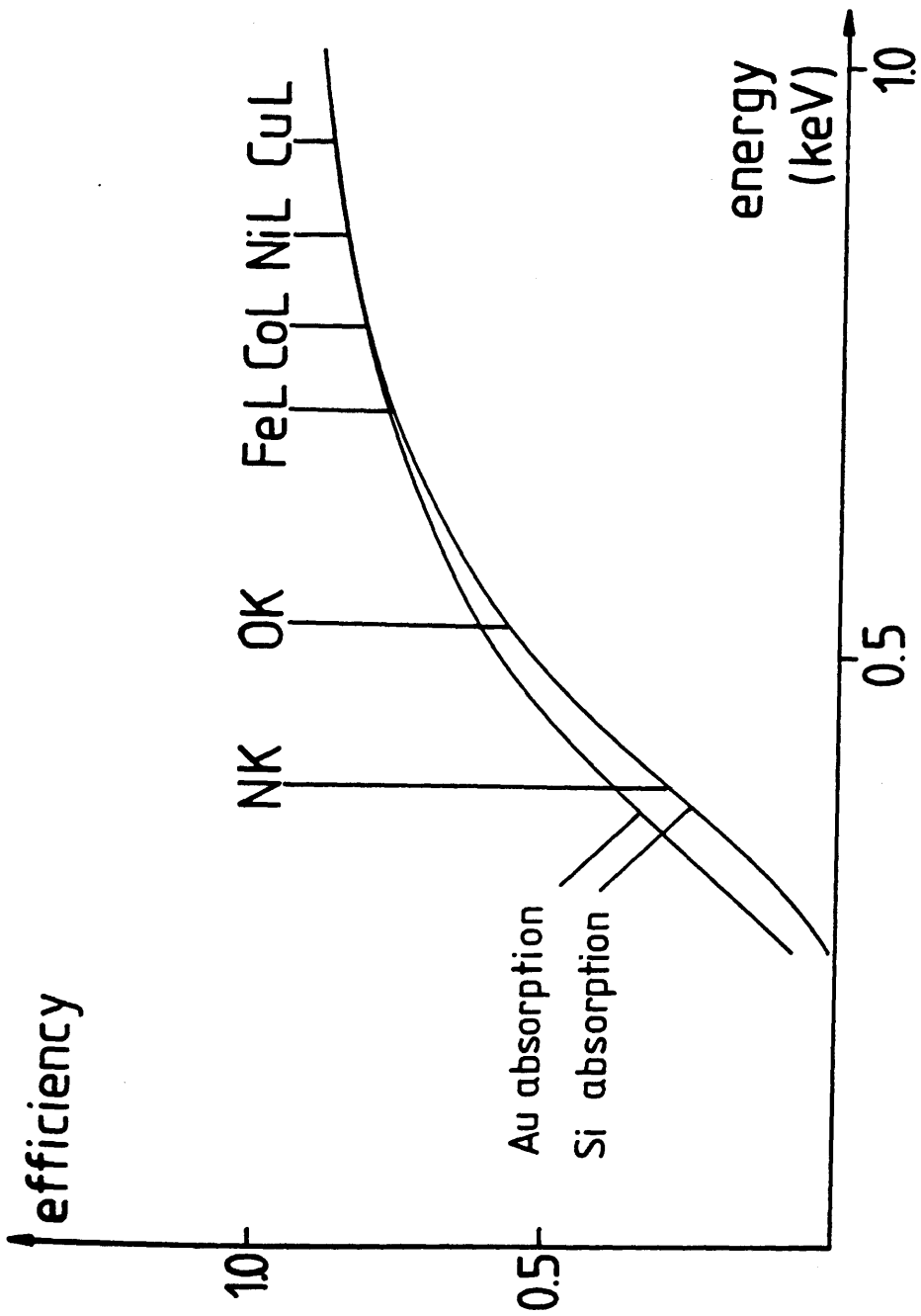
52

Figure 5.5   Illustration of the effect on the calculated efficiency of a windowless detector of assuming that all the absorption takes place in either the Au contact layer or a Si dead layer. The graph shows the calculated efficiency vs. photon energy for each case. The effective thickness in each case has been deduced by fitting to the same Si spectrum.
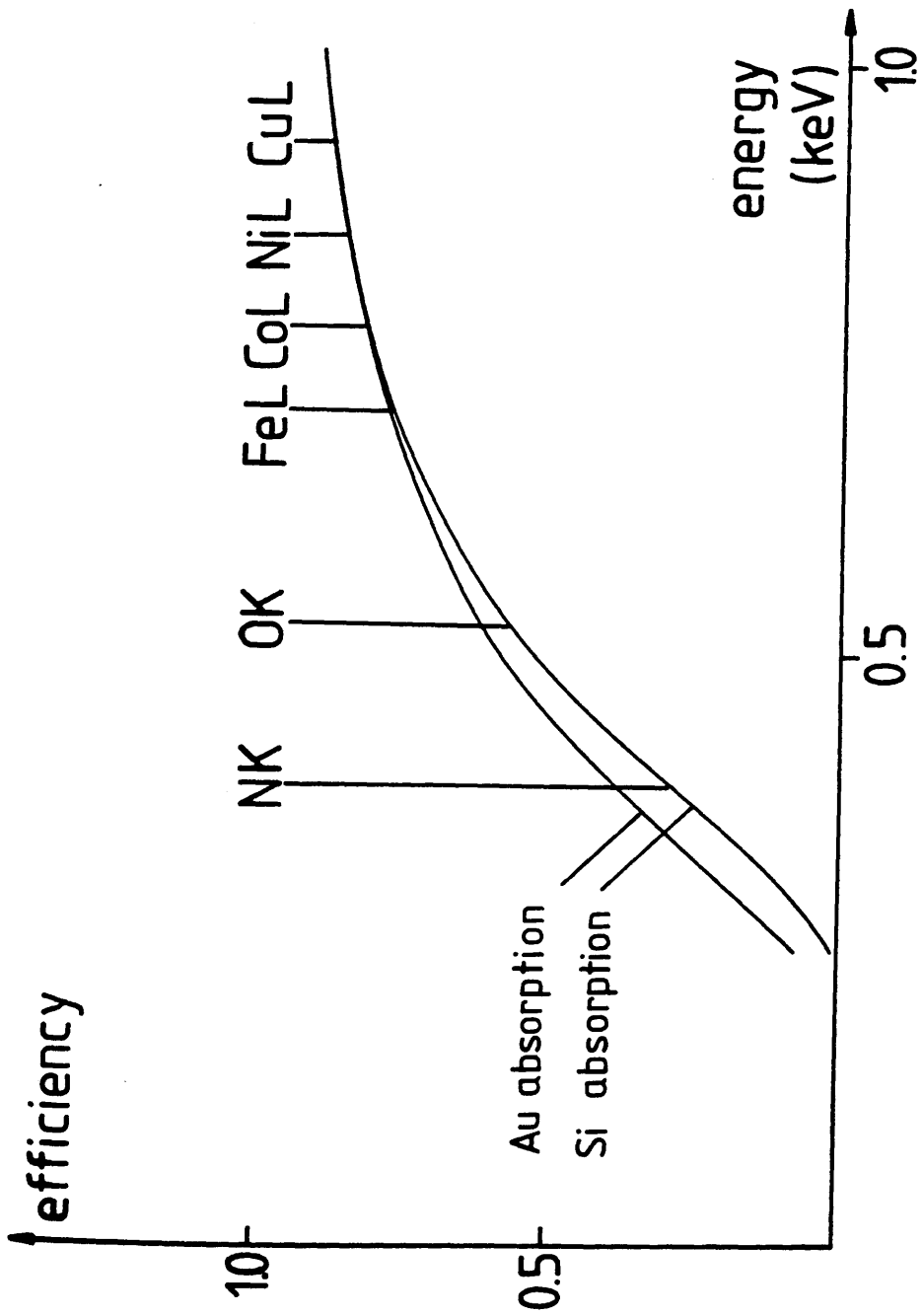
Figure 5.5   Illustration of the effect on the calculated efficiency of a windowless detector of assuming that all the absorption takes place in either the Au contact layer or a Si dead layer. The graph shows the calculated efficiency vs. photon energy for each case. The effective thickness in each case has been deduced by fitting to the same Si spectrum.
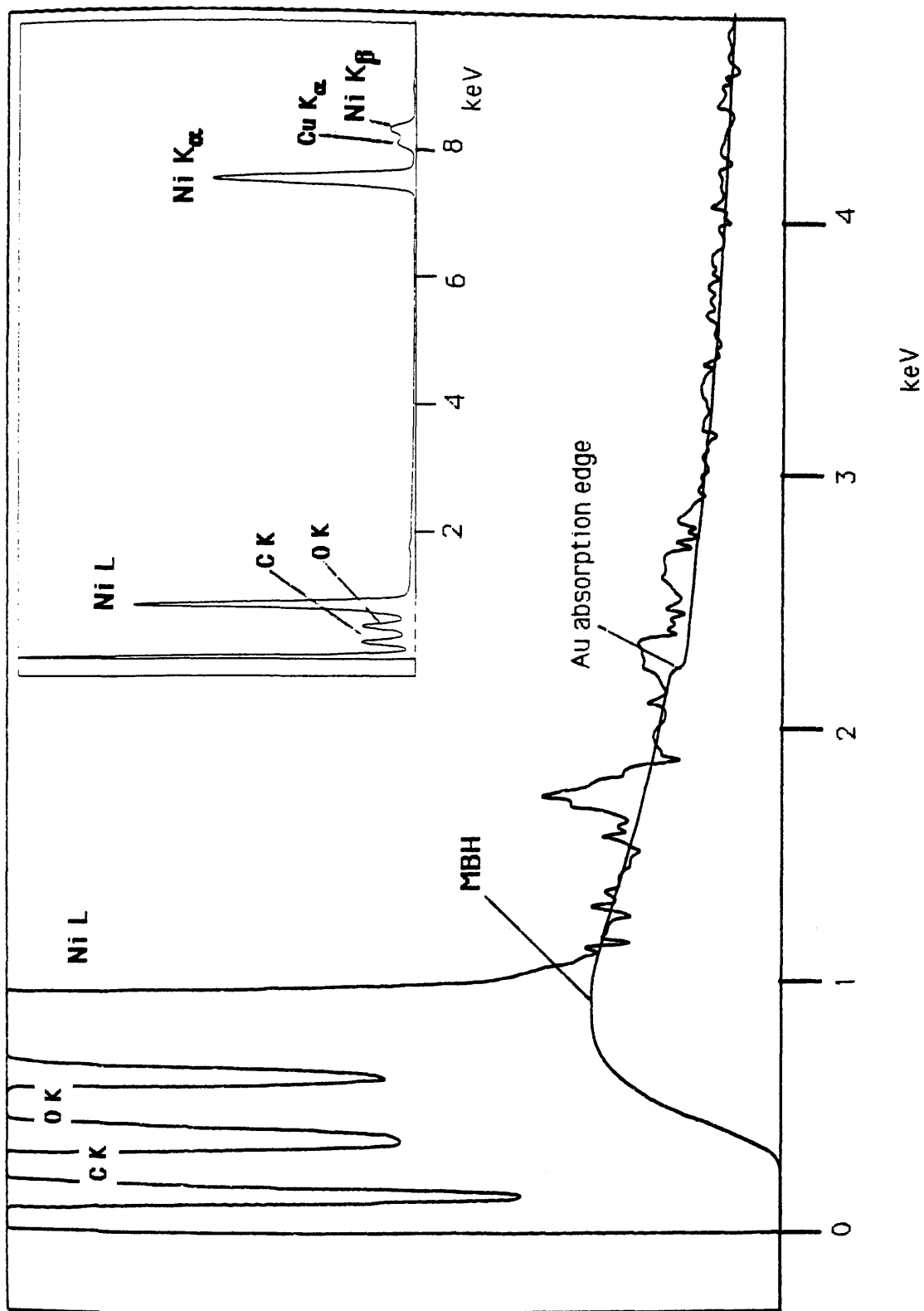
Figure 5.6 Spectrum recorded from Ni on the VG HB501, together with an MBH background corrected for absorption in 280Å of Au.

suspected to affect the other estimates were unlikely to be present here.

5.4 Measurements of K_α/L count ratios

The aim of the measurements described here was to produce reliable, artefact-free values for K_α/total L-line x-ray production cross section ratios for a wide range of elements. The first step was to measure the ratios of the counts in these lines for each element. These ratios could then be converted to production ratios by incorporating appropriate detector efficiency corrections. Since only one element at a time was to be studied, single-element specimens seemed likely to produce spectra which would contain the required information and be simple to analyse. The specimens used for the K-shell cross section measurements of chapter 4 were therefore also suitable for this work. The results detailed here were obtained using the VG STEMs only. Details of the specimens used are given in section 4.8. Clearly, to conform to the requirement stated above, the values must be as free as possible from the effects of specimen self-absorption, which is the artefact most likely to affect spectra from single-element samples. The methods used to ensure that this was the case varied depending on the type of specimen used. Absorption corrections generally depend on knowledge of specimen thickness. This can be difficult to measure accurately, particularly where the thickness is not uniform, as is the case with several of the specimens studied here.

Evaporated films can usually be expected to have reasonably uniform thickness. Measurements by interferometry suggested that the evaporated Fe, Co, Ni, Cu and Sn films were $<\sim 15nm$ thick; the Ag film thickness was $\sim 50nm$. The holey formvar backing films allowed spectra to be recorded from the specimen film only so that there would be no absorption in the backing. The holes were generally small, however, typically $\sim 0.1-1$ μm in diameter. The thickness of the specimen appeared from the image to be greater round the edges of many holes than anywhere else, suggesting that the formvar here may have been curling up or folding over. Without any better indication of the local geometry, it is not possible to estimate whether there was any additional absorption due to this effect. Figure 5.7 illustrates two situations which could give rise to spurious absorption. The specimens were generally loaded with the metal film facing the incident beam so that the situation of figure 5.7 (a) would
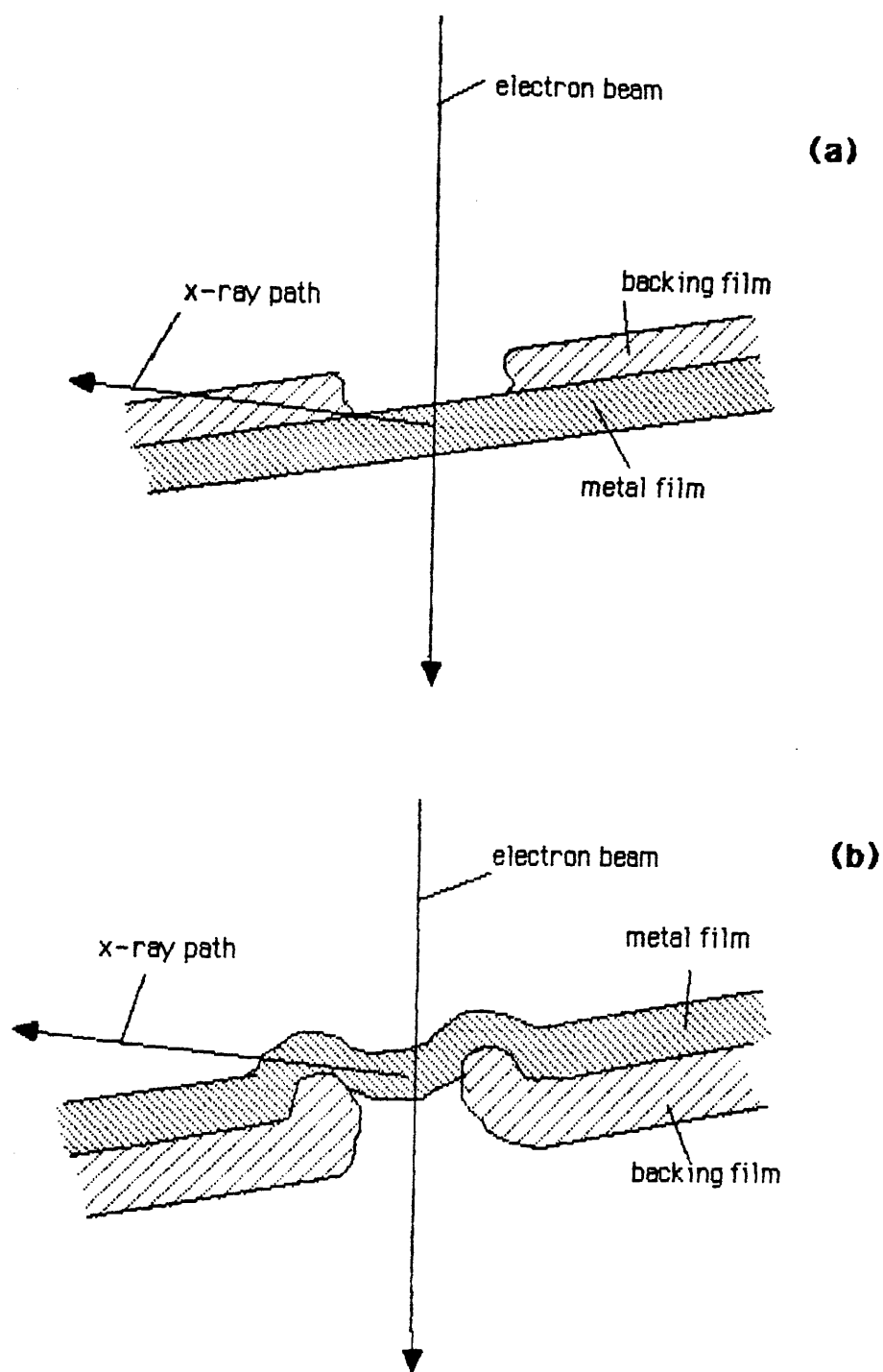
Figure 5.7 Two possible absorption mechanisms for the case of a specimen comprising an evaporated metal film supported on a holey backing film. In both cases, the absorption path of the x-rays within the specimen is greater than would be the case for a uniform metal film alone, and depends on the local geometry of the specimen.

not arise. Spectra were recorded at several different values of specimen tilt, between ~15 degrees and ~30 degrees to the horizontal. Figure 5.8 shows the variation of K_α/L count ratio with nominal tilt angle for Fe, Ni and Cu. These results were obtained using the windowless detector. The K_α counts were extracted using MBH background fitting as described in chapter 4. L-shell counts were extracted using simple linear or quadratic background subtraction. It was considered that modelling the background using MBH would not be practicable here since the amount of absorption present was not known a priori for each spectrum.

The Fe specimen suffered from oxidation, giving rise to large O K peaks in the spectra. The Fe L-line overlapped significantly with the O K-line, the latter always being the larger of the two. The L-peak was assumed to be symmetrical and the counts in the higher energy half of the peak were measured and doubled. There is a wide variation of K_α/L with tilt for Fe, suggesting that the L-line is being absorbed strongly at low angles. The variation has not flattened out completely by the time the tilt has increased to its largest value. It was roughly estimated from the shape of this graph that ~10% of the Fe L-line is being absorbed at this angle. The variations for the other two elements are smaller. The differences between sets of measurements from different areas of the specimens suggest that some local geometry effects are present. The K_α/L ratios tend towards constant values at high tilt angles. The K_α/L values corresponding to the highest tilts were assumed to be unaffected by absorption. No significant variation of K_α/L ratio with tilt was found for Co or Sn. Only the Fe value was therefore corrected for absorption. The crudity of signal extraction and absorption correction render this value subject to a much larger error than the other values. Spectra from the Ag film were not recorded at a large enough range of tilt angles to estimate absorption in this way. Comparison of the background in the vicinity of the L-peak with an MBH curve fitted to the bacgkground in the mid-energy region indicated the need for a small correction for absorption. Figure 5.9 shows part of an Ag spectrum, in the vicinity of the Ag L-peak. The MBH curve lies slightly above the background on both sides of the peak. The difference between theoretical and experimental backgrounds suggested that ~10% of the Ag L signal was being absorbed, and a correction was made accordingly.

In the cases of the ion-beam thinned specimens and the MoO_3 crystals spectra
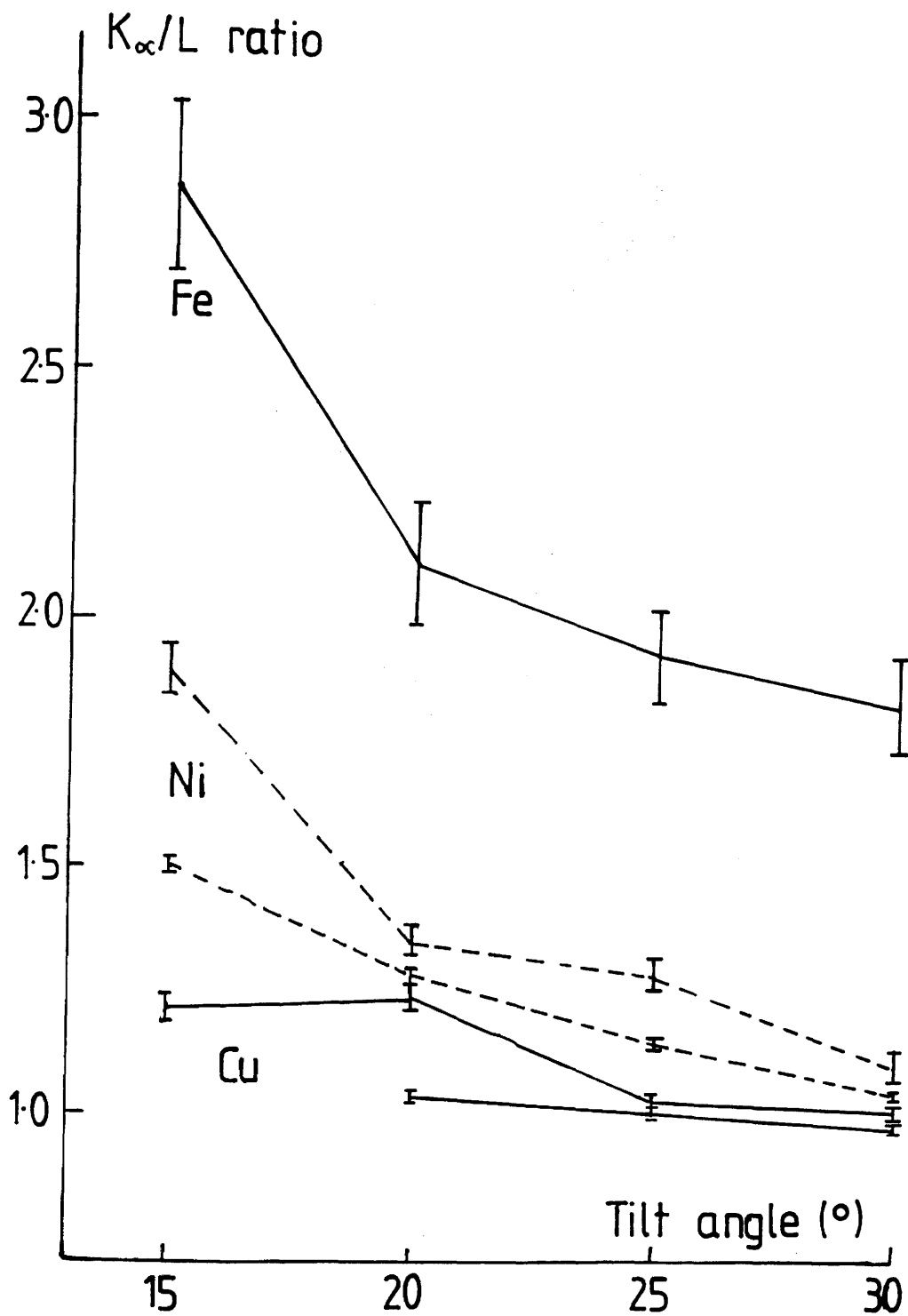
Figure 5.8 K_α/L count ratio vs. specimen tilt for spectra recorded from Fe, Ni and Cu using the VG HB501. For each of Ni and Cu, values are shown for sets of spectra recorded from two different areas of the specimen.
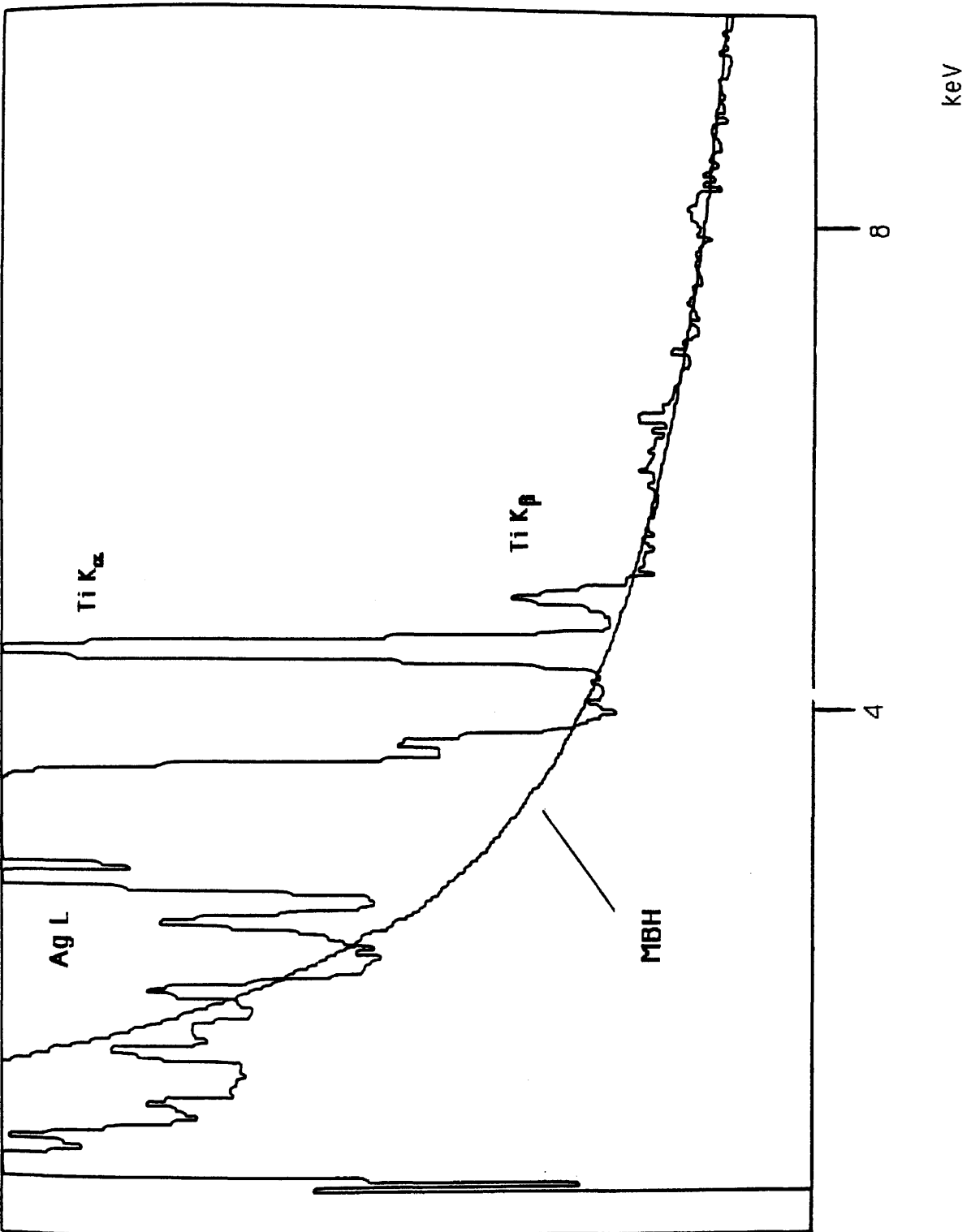
Figure 5.9   Low energy end of spectrum recorded from Ag on the VG HB501, together with a fitted MBH background

were recorded from several different areas of each specimen, over a range of the apparent thickness based on observation of the image. The smallest value of K_α/L was always adopted since it was assumed to correspond to the least absorption. The good agreement between the Ni K_α/L values deduced from evaporated Ni, thinned Ni and thinned NiO spectra suggests that the effects of absorption can be successfully eliminated by these methods.

Other artefacts are apparent in some of these spectra. Figure 5.10 shows a typical spectrum from Ag recorded using the windowless detector. The shape of the background just below the L-peak suggests that the windowless detector suffers relatively little from incomplete charge collection effects at the front face of the crystal. There seems to be a feature associated with the K_α peak, however. This takes the form of a "bump" in the background shape extending from ~15keV up in energy to the K_α peak. This feature was avoided when selecting background fitting regions. The MBH curve fits the spectrum well below the bump and above the peak, but lies appreciably below the spectrum in the bump region. It was assumed that counts from the K_α peak were being redistributed over a range of energies below the peak energy. This may have been due to some ICC effect at the back face of the crystal, a possibility which is discussed in appendix E. The effect was found in spectra from Sn, Ag and Mo only. In these cases the counts in the bump region above the level predicted by the scaled MBH curve were included with the peak counts to give K_α count values. The K_α/L values measured using the windowless detector, corrected where necessary for absorption and for "back face ICC" are shown in the first column of table 5.3.

The ICC effects inherent in the Be window detector on the Glasgow STEM had been carefully studied previously (Craven et al., 1985). The L-lines from Mo, Ag and Sn were affected significantly, and corrections were made following the above reference. Due to the low energy fall-off in efficiency for this detector, no K_α/L measurements were made for elements lighter than Mo. Comparison of the background shapes with appropriate MBH curves for these spectra showed the presence of some absorption which was considered unlikely to be due to the specimens alone. Figure 5.11 shows a spectrum from Ag together with an MBH background fitted to it over a region in the middle of the energy range. This spectrum was recorded from the same specimen as that shown in figure 5.9. This difference between these spectra was considered to be due to a problem
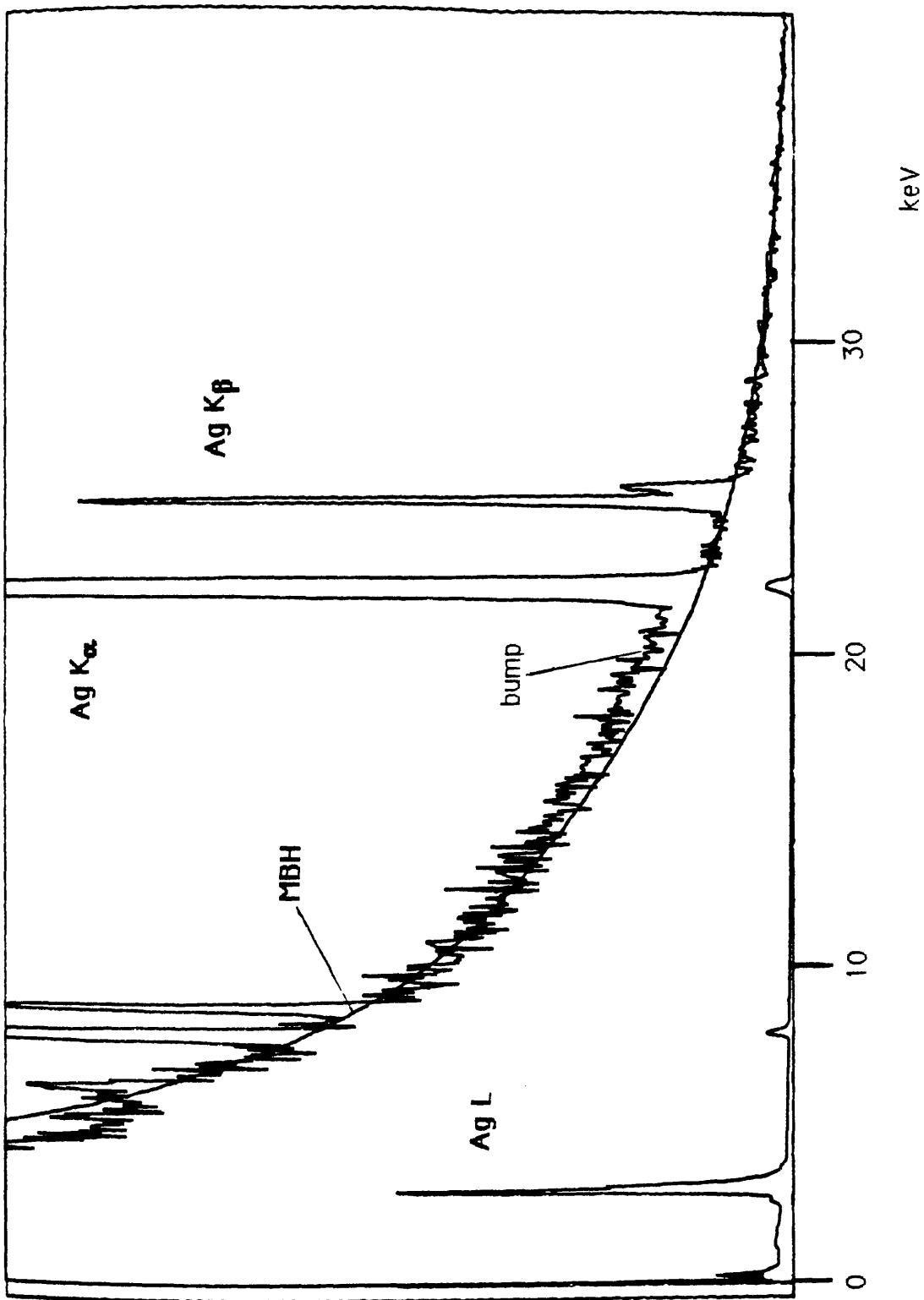
Figure 5.10 Spectrum recorded from Ag on the VG HB501, showing the "bump" in the background near the K_α peak.

element	windowless (HB501)	Be window (HB5) uncorrected > ICC corrected > absn. corrected		
Fe	1.6±0.2			
Co	1.30±0.02			
Ni	1.02±0.02			
Cu	0.95±0.01			
Ge	0.57±0.02			
Mo	0.20±0.01	0.39±0.01	0.29±0.02	0.20±0.03
Ag	0.105±0.005	0.190±0.002	0.16±0.01	0.14±0.02
Sn	0.072±0.001	0.110±0.005	0.10±0.02	0.09±0.02

Table 5.3. K_α/L count ratios measured using the detectors on the two VG STEMs. Values measured using the Be window detector on the HB5 are shown as measured, and after successive stages of correction.
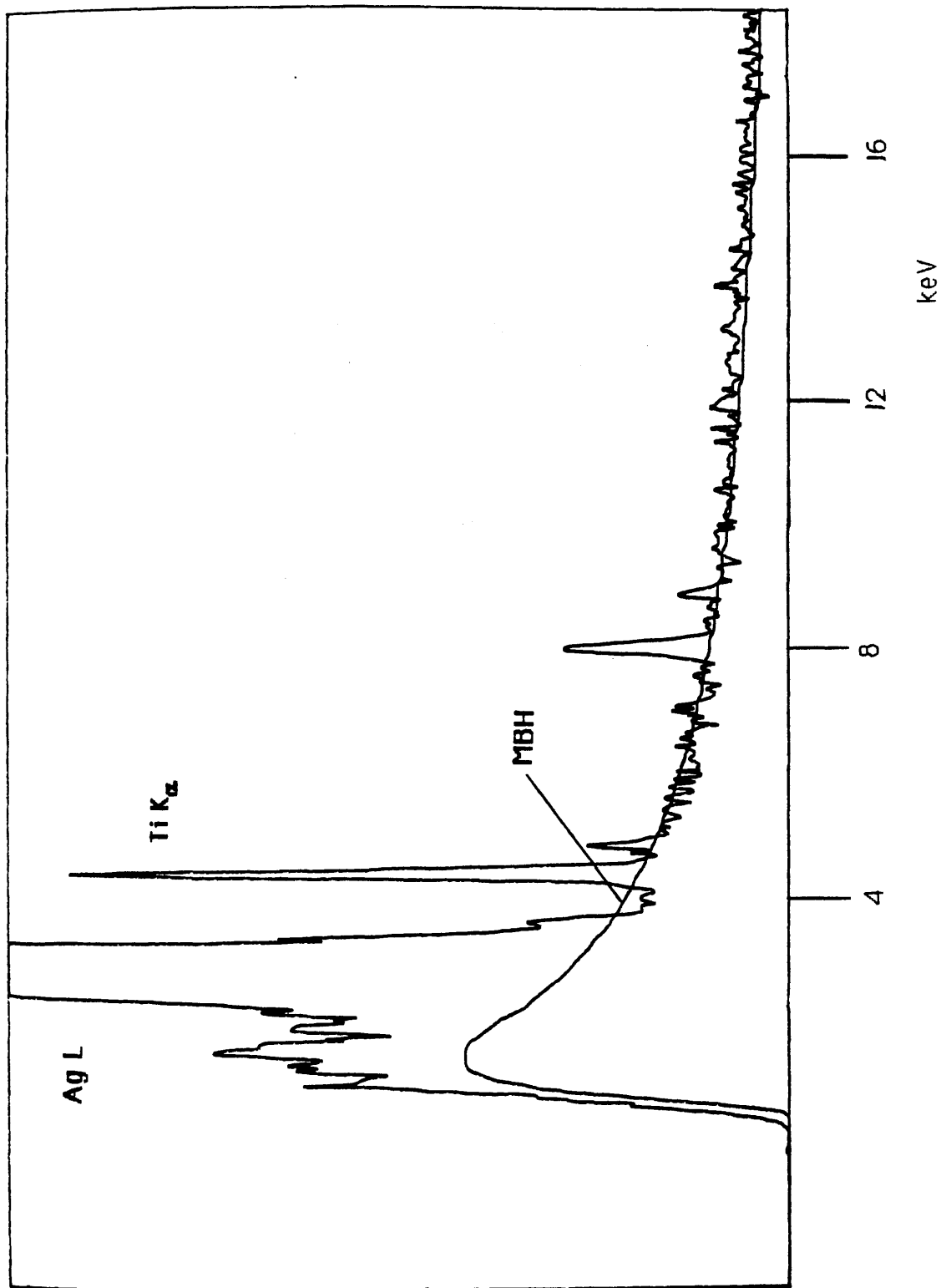
Figure 5.11 Low energy end of spectrum recorded from Ag on the VG HB5, together with a fitted MBH background

with the collimation of the detector. Approximate corrections were made from comparison of experimental and theoretical spectra. The process was the same as that described for the Ag spectra from the windowless detector. The magnitude of the correction required here was generally much greater, however, giving rise to larger errors. The necessity to make corrections for ICC and absorption introduced additional errors into the K_α/L ratios from the Be window detector. The uncorrected values and those after each stage of correction are shown in the remaining columns of Table 5.3.

5.5 K_α/L x-ray production cross section ratios

The first column of table 5.4 lists the values of K_α/L count ratios measured as described in section 5.4. As would be expected, different values were measured using the detectors on the two VG STEMs. If the detector efficiency is correctly taken into account, however, the resultant values should be independent of which detector was used to make the measurement. Where the efficiency fell below unity at low photon energies, values were estimated using the methods of sections 5.2 and 5.3. At high photon energies, the efficiencies were deduced from the effective crystal thickness measurements described in chapter 4. The second and third columns of table 5.4 list the estimated value for the efficiencies for the K_α and L lines respectively of each element. The final column shows the results of correcting the count ratios for detector efficiency and therefore represents values for K_α/L x-ray production cross section ratios. For Mo, Ag and Sn, where comparison is possible, the results from the two detectors agree within the estimated errors. This suggests that the high energy efficiency estimates correctly account for the observed differences in count ratio. For the lighter elements values were measured using only the windowless detector, and so no similar indication can be given by comparison for the success of the low energy efficiency estimate for this detector.

Table 5.5 lists values of K/L ratio measured by Wirmark & Nordén (1984). They based their efficiency estimate on an 8μm Be window, a 150Å Au layer and a 0.1μm Si dead layer, with a crystal thickness of 3mm. They list L/K-shell count ratios: the values listed in table 5.5 have been converted to K_α/L production ratios to allow direct comparison with the results of this work. Efficiency corrections have been made assuming the above parameters, using the mass absorption coefficients listed by Heinrich (1987). The discrepancies

element		K_α/L counts	ε_K	ε_L	K_α/L production ratio
Fe	W	1.6+0.2	1	0.53+0.05	0.85+0.13
Co	W	1.30+0.02	1	0.59+0.05	0.77+0.07
Ni	W	1.02+0.02	1	0.66+0.04	0.67+0.04
Cu	W	0.95+0.01	1	0.71+0.03	0.67+0.03
Ge	W	0.57+0.02	1	0.82+0.02	0.47+0.02
Mo	W	0.20+0.01	0.81+0.04	0.95	0.23+0.01
	Be	0.21+0.03	0.97	0.92	0.20+0.03
Ag	W	0.105+0.005	0.58+0.03	0.97	0.17+0.01
	Be	0.14+0.02	0.84	0.95	0.16+0.02
Sn	W	0.072+0.001	0.45+0.3	1	0.15+0.01
	Be	0.08+0.02	0.67	1	0.12+0.03

W – windowless detector (HB501)
Be – Be window detector (HB5)

Table 5.4. K_α/L count ratios and detector efficiencies to give K_α/L x-ray production cross section ratios.

element	K_α/L production ratio	
	Wirmark & Nordén (1984)	this work
Co	8.81	0.77
Ni	3.89	0.67
Cu	2.56	0.67
Mo	0.32	0.21

Table 5.5. K_α/L production cross section ratios as measured by Wirmark & Nordén (1984) and in this work.

between these results and the values measured here become large for the lighter elements. From their comparison of their results with theory, based on a different cross section model, they concluded that they were overestimating the detector efficiency significantly at energies <1.8keV. Comparison with this work supports this conclusion. This example illustrates the problems associated with detector efficiency estimation described in section 5.3.

A set of reliable values for K_α/L production cross section ratios can provide a useful means of detecting absorption effects in certain situations. A typical example might be a spectrum, recorded using a windowless detector, in which there are peaks present due to a light element, such as O or N, and to a transition metal. In this case the L peak from the heavier element will lie close to the K peak from the lighter. Any variation in the K_α/L ratio for the heavier element from the expected value may indicate suppression of the L line signal due to absorption. This absorption would also affect the K line of the light element, and might not otherwise have been detected, resulting in an erroneous value being deduced for the concentration ratio. The application of this is illustrated for NiO in chapter 6.

5.6 X-ray production from the L-shell

In principle it should be possible to use the knowledge of K-shell cross sections previously gained, together with the K_α/L production cross section ratios to deduce values for L-shell production and ionisation cross sections. The relationship between ionisation and x-ray production is, however, more complicated for the L-shell than for the K-shell. The equivalent expression to equation 4.7 gives the L-shell x-ray production cross section/sr σ_{cL} as

$$\sigma_{cL} = \frac{\omega_{L_1}\sigma_{iL_1} + \omega_{L_2}\sigma_{iL_2} + \omega_{L_3}\sigma_{iL_3}}{4\pi} \qquad (5.3)$$

Unlike the K-shell, the L-shell is split into three sub-shells. The σ_{iL_j}, where j=1,2,3, are the ionisation cross sections for the individual sub-shells. X-ray

production from the L-shell is further complicated by the existence of radiationless Coster-Kronig transitions within the shell (Dyson, 1973). After an atom has been ionised in the L-shell, these transitions can cause a redistribution of the electrons between the sub-shells. An electron in the L_3 sub-shell may undergo transitions to fill vacancies in L_2 or L_1; and an L_2 electron may udergo a transition to L_1. The effect of this is that the L_3 and L_2 ionisation cross sections are enhanced. The σ_{iLj} in equation 5.3 are the ionisation cross sections for each shell in isolation. In order that production from the sub-shells is described in the correct proportions, the w_{Lj} must therefore be the effective fluorescence yield values for the sub-shells. These are obtained by modifying the simple fluorescence yields to take into account the Coster-Kronig yields. The details of the relationship between the fluorescence yields and the effective fluorescence yields are given in appendix D.

Clearly, before any information can be deduced from the experimental K_α/L ratios about the ionisation cross sections, values had to be attributed to the w_{Li}. The review paper by Bambynek et al. (1972) lists two distinct sets of values, neither of which is complete. A set of values for the elements studied here was generated by taking the published data and filling in as many gaps as possible by interpolation. These values are listed in the first two columns of table 5.6. Other L-shell fluorescence yield data have been published by Listengarten (1960), who listed semi-empirical values for Z>45; Burhop & Asaad (1972), who published an analytical expression for ω_{L3}; and Fink & Rao (1974), based on least-squares fits to experimental ω_{L2} and ω_{L3} data. Krause (1979) published a complete L-shell fluorescence yield data set for 12<Z<110, based on original theoretical and experimental work, claimed to be consistent with the data available to that time. The values relevant here are listed in the final column of table 5.6.

The conclusions made here were based on the values of Bambynek et al. and Krause. Examination of table 5.6 shows appreciable discrepancies between the three data sets, which will clearly affect the values deduced for the ionisation cross sections.

	Bambynek "b"			Bambynek "c,d"			Krause		
	v_1	v_2	v_3	v_1	v_2	v_3	v_1	v_2	v_3
Fe	5.8	5.8	5.6	1.4	1.5	1.5	**6.5**	**6.3**	**6.3**
Co	*7.0*	*7.1*	*6.9*	*2.0*	*2.2*	*2.2*	**7.8**	**7.7**	**7.7**
Ni	8.2	8.5	8.0	2.6	3.0	2.8	**9.2**	**8.9**	**9.3**
Cu	*10*	*10*	*9.5*	3.5	4.0	3.8	**11**	**10**	**11**
Ge	*13*	*14*	*13*				**14**	**13**	**14**
Mo	**38**	**39**	**37**	**20**	**28**	**26**	**36**	**39**	**37**
Ag	**61**	**64**	**60**	**16**	**49**	**45**	**53**	**59**	**52**
Sn	**75**	**78**	**74**	62	65	64	**67**	**75**	**64**

<u>all values x10^{-3}</u>

key : **complete data set listed for this element**

incomplete data set listed for this element-missing
values deduced from surrounding trends

*no data listed for this element - values deduced
by interpolating between elements.*

Table 5.6. Effective fluorescence yields v_i listed by Bambynek
et al. (1972) and Krause (1979).

5.7 Applying the Bethe model to the L-shell

It was shown in chapter 4 that the simple Bethe form could successfully be used to predict K-shell ionisation cross sections. The theoretical calculations of Rez (1984) suggested that this model should also apply to the L-shell. The aim here was to discover whether the experimental results from the L-shell were in agreement with this prediction/he form of the Bethe model for the L_j sub=shell is

$$\sigma_{iL_j} = 2 N \pi e^4 b_L \ln \left(\frac{c_L T_0}{I_L} \right) / T_0 I_L \qquad (5.4)$$

where N is the electron occupancy of the L_j sub-shell. N=2 for L_1 and L_2, 4 for L_3. (nb. the dependence on electron occupancy was not stated explicitly for the K-shell in equation 4.5. N=2 for the K-shell.) The Bethe parameters are assumed here to be identical for the three sub-shells. The final column in table 5.5 represents experimentally determined values of K_α/L x-ray production cross section ratios Q_{KL}^e. The theoretical expectation Q_{KL}^t is given by the following expression, obtained by combining equations 4.7 and 5.3.

$$Q_{KL}^t = \frac{\omega_K S \sigma_{iK}}{\omega_{L_1} \sigma_{iL_1} + \omega_{L_2} \sigma_{iL_2} + \omega_{L_3} \sigma_{iL_3}} \qquad (5.5)$$

The values of Q_{KL}^e were substituted for Q_{KL}^t in equation 5.5 in order to obtain values for the ratio b_K/b_L which would result if the σ_{iL_j} were assumed to follow the Bethe form. Acording to Rez, this ratio should be close to unity, and should not vary markedly with Z. The data used here was all recorded at 100keV and so there was only one experimental value for each element. It would therefore not be possible to deduce simultaneously values for both the Bethe parameters b_L and c_L. The cross section values calculated from the Bethe model for the L=shell are not particularly sensitive to the value of c_L since the

overvoltage is generally large in the case of the L-shell. A value of 1 was selected. This choice was to some extent arbitrary, but was of an order of magnitude in accord with expectation from results from the K-shell and the predictions of Rez. The value of c_K was taken as 0.90, following the results of the previous work. These values, together with the $Q_{KL}{}^e$ values were used by the SuperBasic programs SIGRATIO_KRAUSE, SIGRATIO_BAMBYNEKB and SIGRATIO_BAMBYNEKCD to calculate the b_K/b_L ratios resulting from the use of each of the three sets of fluorescence yield data. Appendix B contains listings of these programs.

Figure 5.12 shows the three sets of values of b_K/b_L as a function of Z. As expected, the exact value calculated for this ratio depends strongly on the fluorescence yield values chosen. Nevertheless it appears that there is no clear trend in b_K/b_L with Z. The values are in most cases within 50% of unity. The order of magnitude of the results is therefore in agreement with the predictions of Rez. This has not been the case with results published previously in the literature, for example those of Wirmark & Nordén, discussed in section 5.5. Considerable care has been taken to eliminate artefacts which could affect the reliability of the K_α/L production cross section ratios used to deduce these results. Clearly, before any firmer conclusions may be drawn, the uncertainty in the fluorescence yield values must be resolved. However, this work generally supports the applicability of the Bethe model to the L-shell.

5.8 Variation of the K_α/L production ratio with T_0

The results described in the previous sections were based on data recorded on the VG STEMs at $T_0 = 100$keV. In the cases of Mo and Ag there was also data available from the JEOL TEM over a range of values of T_0. This data was used to investigate the variation of the K_α/L production ratio with T_0. Assuming the Bethe model to describe the individual sub-shell ionisation cross sections, then equation 5.3 can be rewritten as

$$\sigma_{cL} = \frac{\sigma_{iL}(\omega_{L_1} + \omega_{L_2} + \omega_{L_3})}{4\pi} \qquad \textbf{(5.6)}$$
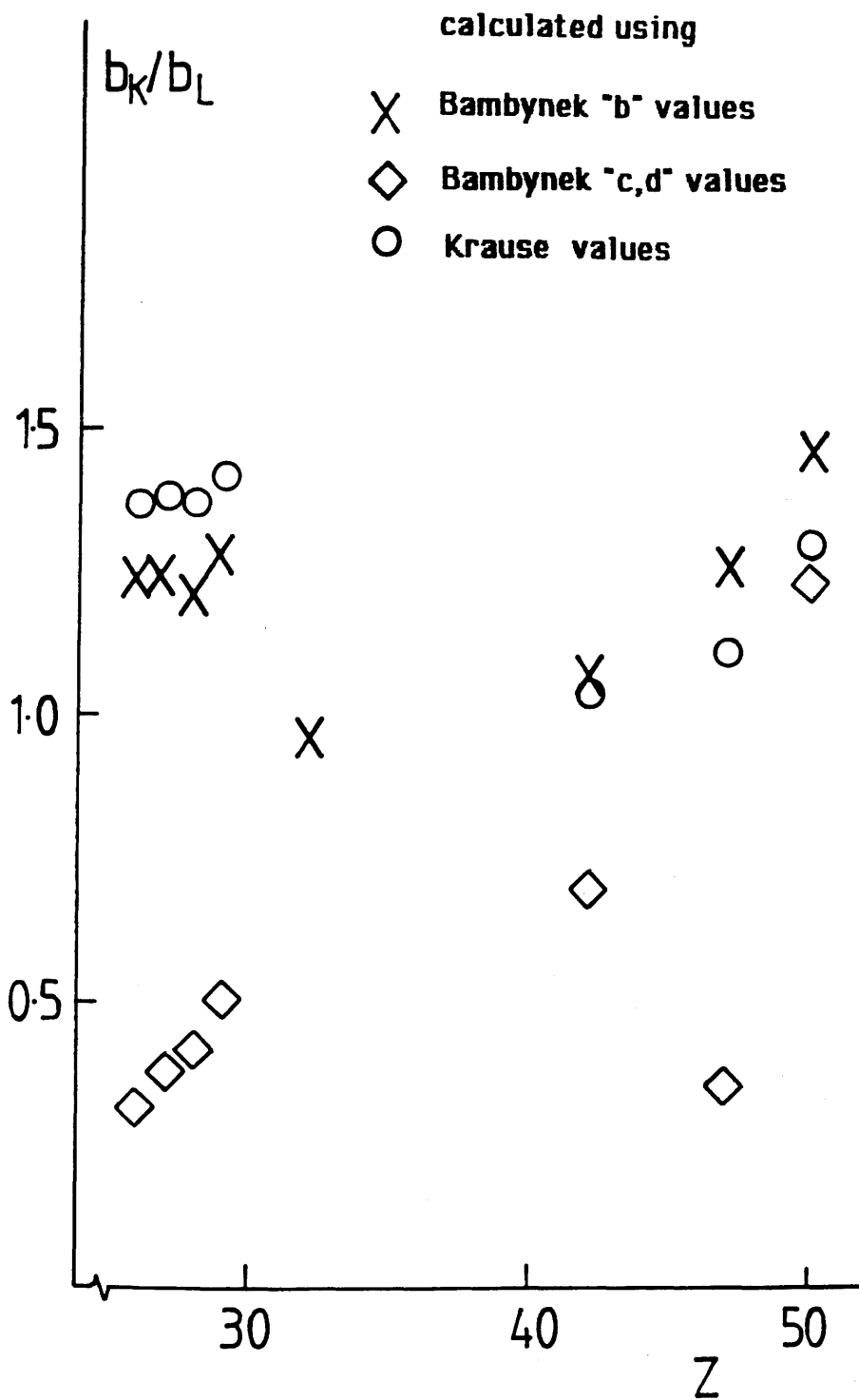
Figure 5.12 b_K/b_L vs. Z. The values of b_K/b_L have been calculated using each of the three sets of L-shell fluorescence yield data considered in this work.

where σ_{iL} is the ionisation cross section for a doubly occupied sub-shell. Equation 5.5 then becomes

$$Q_{KL}^t = \frac{\omega_K \, S \, \sigma_{iK}}{(\omega_{L_1} + \omega_{L_2} + \omega_{L_3}) \, \sigma_{iL}} \qquad (5.7)$$

Writing out the ionisation cross sections in full gives

$$Q_{KL}^t = C \, \frac{\ln\left(\dfrac{C_K \, T_0}{I_K}\right)}{\ln\left(\dfrac{C_L \, T_0}{I_L}\right)} \qquad (5.8)$$

where $C = s \, \omega_K \, b_K \, I_K \, / \, (\omega_{L1} + \omega_{L2} + 2\omega_{L3}) \, b_L \, I_L$ is constant for a given element. Thus the variation of Q_{KL}^t with T_0 depends on c_L, and not on b_L. The variation of Q_{KL}^e with T_0 should therefore allow information to be deduced about c_L.

Firstly, the K_α/L count ratios recorded at 100keV, corrected for detector efficiency to give production cross section ratios, were compared with the values from the other microscopes. The values measured using the low angle detector were 0.23 for Mo and 0.16 for Ag. These values agree well with the previous results. The values of count ratio measured for Ag at all values of T_0 using the high angle detector were greater than the low angle values by a factor of ~2. No estimate was made of the high energy efficiency for the high angle detector because of the spurious shape of the background in the spectra recorded using it. There is no reason to expect any anisotropy in the relative intensities of K-shell and L-shell radiation. As discussed in section 4.6, the spectra recorded from this detector did not follow the form which would be expected from x-ray production in thin films. Some doubt must surround any results obtained from them. The form of the spectra does not, however, give any clear

indication of any artefact which would give rise to the result observed here.

Figure 5.13 (a) and (b) show spectra from Ag recorded respectively on the low angle and high angle detectors. The background shape in figure 5.13(b) in the region of the Ag L-line does not suggest that this signal is suppressed with the high angle detector to a greater extent than is the case with the low angle detector. The discrepancy is too great to be explained purely in terms of a difference in efficiency at the Ag K_{α} line energy. No further conclusions were drawn from these data, but this anomaly must be noted with concern.

Figures 5.14(a) and (b) show the K_{α}/L count ratios measured using the low angle detector for Mo and Ag respectively as a function of T_0. The solid curves on these figures represent the values of Q_{KL}^{t} calculated from equation 5.8, adjusting the constant C so that the the Q_{KL}^{t} values are normalised to the value of Q_{KL}^{e} measured at $T_0=80keV$. Normalising at an extreme of the energy range should show up the maximum possibe effect of varying c_L. Curves are shown here for $c_L=0.3, 0.5$ and 1.0. It appears that taking $c_L=0.5$ gives the best fit to the data, but as expected the value of c_L can be varied widely without causing the calculated cross section ratio to change significantly. The ratios calculated for Ag at $T_0=200keV$ taking $c_L=0.5$ and 1.0 differ only by ~10%.

5.9 Conclusions

In this chapter measurements of K_{α}/L line count ratios have been described. It has been shown that in order to deduce reliable values for the corresponding x-ray production cross section ratios it is necessary to carefully take into account the high and low energy detector efficiencies. Calculations of effeciencies based on nominal values for the physical detector parameters can be rendered inaccurate by changes in the detector performance with time. Experimental determination of the efficiency offers the possibility of periodically reassessing the detector characteristics. Comparison of experimental spectra with MBH theory is generally successful in yielding values for detector efficiency, but even this method must be used with caution at the extremes of the range of applicability of the detector. In particular, the low energy efficiency estimate described for the windowless detector is not expected to give reliable results for very light elements.
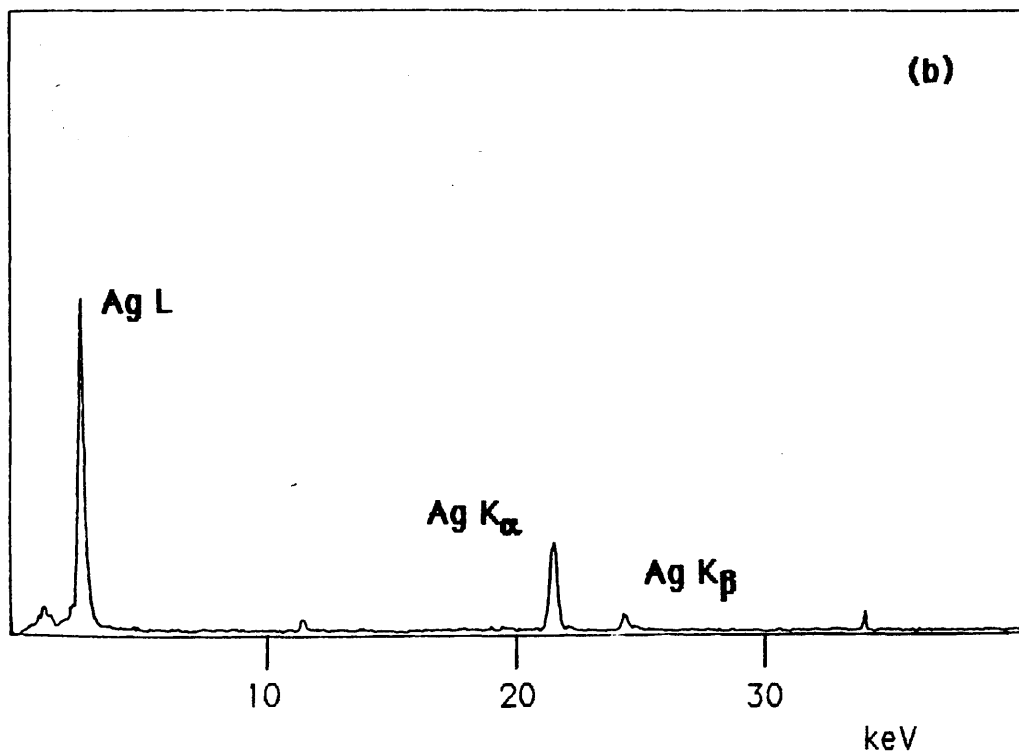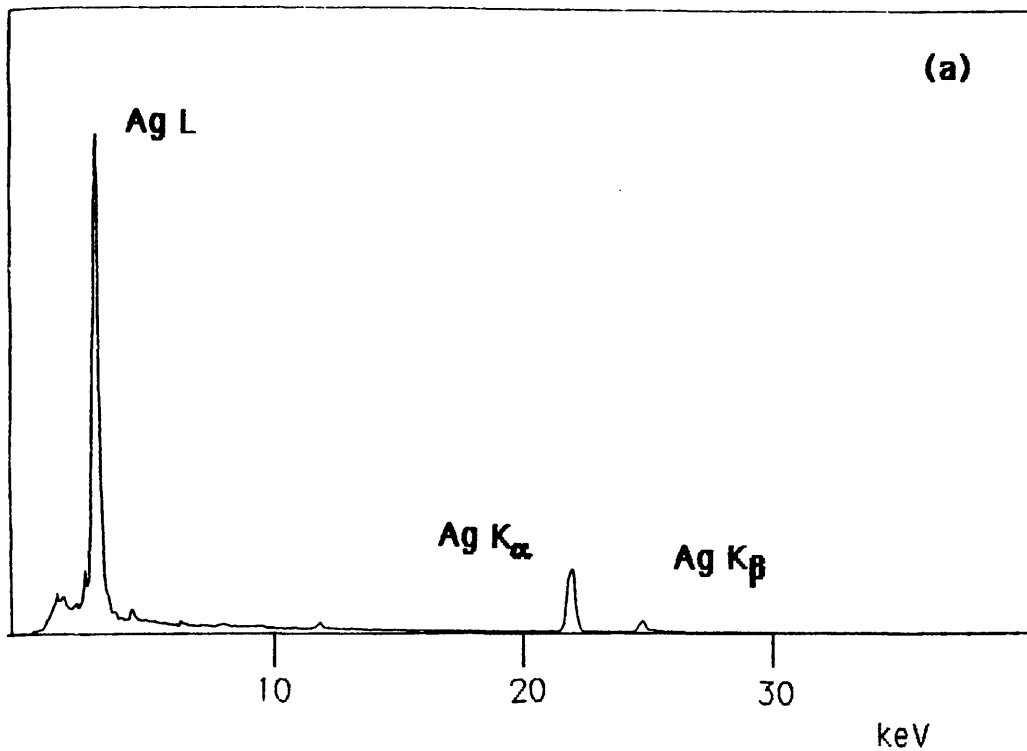
Figure 5.13 Spectra recorded from Ag using (a) the 90° detector and (b) the 158° detector on the JEOL TEM.
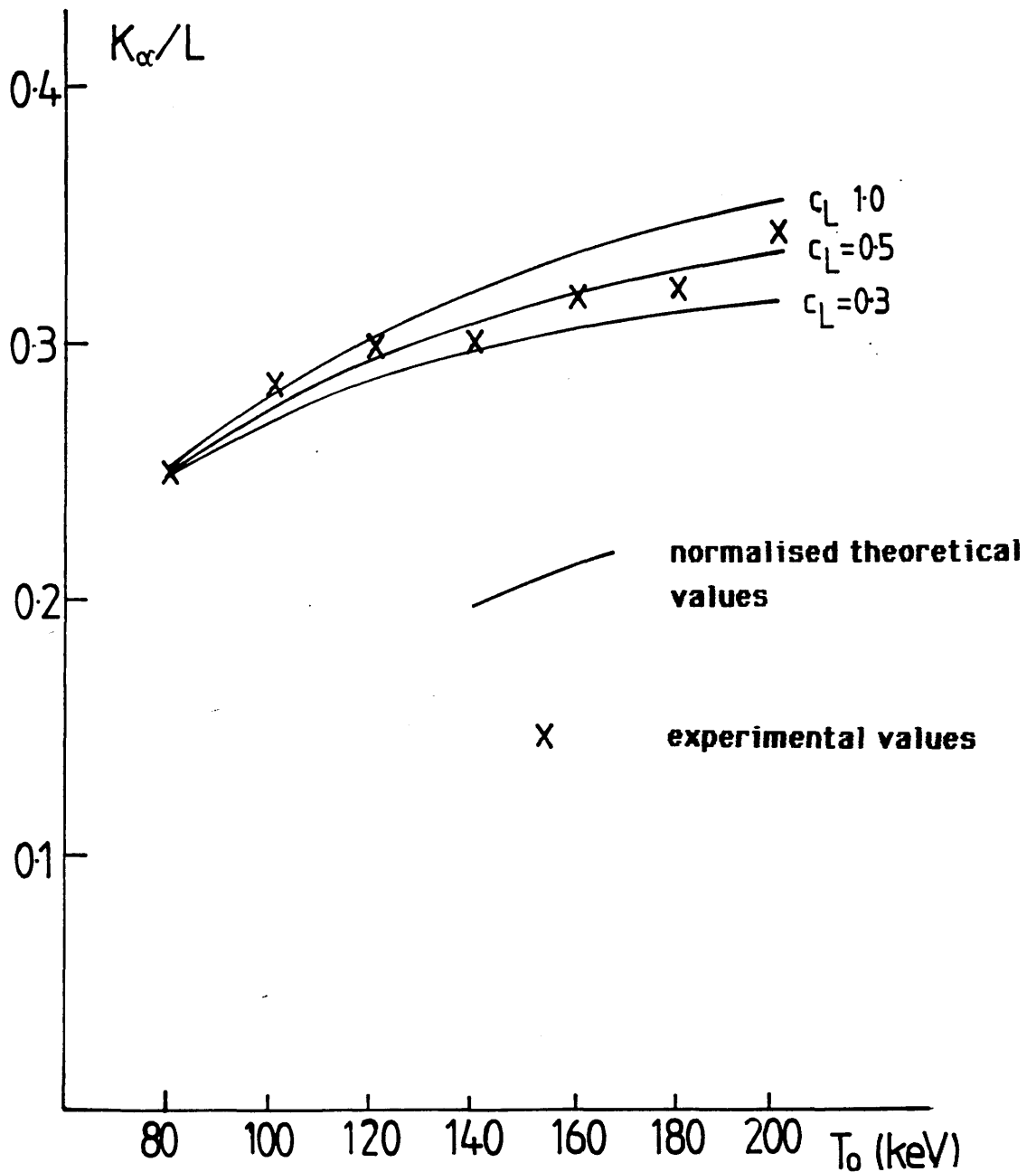
Figure 5.14 K_α/L count ratio vs. T_0 for data from the JEOL TEM. The solid lines represent the variation predicted by the Bethe form with the indicated values of c_L, the curves being normalised to the 80keV value.

(a) Mo

The values deduced here for K_α/L x-ray production cross section ratios are considered to be reliable within the stated accuracies. This data is useful in itself. It has been shown how these values may be used to detect the effects of absorption in certain cases. The data has been further used, however, to deduce information on L-shell ionisation cross sections. Theoretical work by Rez has suggested that, as for the K-shell, the Bethe model should provide a good description of L-shell cross sections. The K_α/L production ratios, together with the results previously obtained for the K-shell, have been used to investigate this. The results, while affected by the uncertainties in published fluorescence yield data for the L-shell, generally support these predictions.

Chapter 6

X-ray analyses involving light elements

6.1 Introduction

The main advantage of a windowless x-ray detector over the conventional Be window type lies in its ability to detect K-shell x-rays from elements with $5 < Z < 11$. Elements in this range cannot be detected at all using a conventional detector. The work in this thesis has been directed towards the quantitation of experimental data without recourse to standard specimens. It is therefore of interest to investigate the potential accuracy of such procedures as applied to these light elements which are now accessible for EDX analysis. This chapter describes the analysis using windowless EDX of three compounds whose chemical formulae were known. The materials studied were Si_3N_4, NiO and MgO. In each case the analysis involved two stages, following the general procedure outlined in chapter 4. Section 6.2 describes the extraction of the characteristic signals from the background in the spectra. This process is subject to relatively little error due to the generally high signal to background ratios found in EDX spectra. The second stage involved determining the appropriate k-factors for the conversion of count ratios to elemental concentration ratios. The accuracy with which the quantities which contribute to the k-factors are known is discussed in section 6.3. The following section describes an attempt to use the results of the analyses of the three materials to determine the detector efficiency for O and N. Finally, an assessment is given of the prospects for standardless light element analysis.

6.2 Experimental details and count ratios

6.2.1 Si_3N_4

All the data discussed in this chapter were recorded using the VG HB501 STEM at AERE Harwell, since it was the only instrument available which was equipped with the necessary windowless x-ray detector. The Si_3N_4 specimen consisted of a membrane, supported on a bulk Si mount, as illustrated in figure 6.1. The specimen was supplied by the Department of Electrical and Electronic Engineering at Glasgow University. The thickness of the membrane was nominally $\sim$500Å. It was mounted in the single tilt holder. Spectra were recorded at various values of specimen tilt, scanning an area $\sim$ 20μm square each time. Figure 6.2 shows a typical spectrum. This spectrum clearly does not follow the form which would be expected in the case of a thin film specimen. The background appears to increase at high photon energies, suggesting that there is a large extraneous contribution to the spectrum. The reason for this is not clear, but may be connected with the specimen mount. The area of the membrane was much smaller than was typical for the specimens generally used for EDX analysis, its size being comparable with the depth of the mount. The form of any scattering which might take place from the mount is difficult to predict. For the purposes of this analysis, the spectral region of interest is that in which the characteristic peaks from Si and N lie. The effects of the extraneous backgrond contribution only become apparent at photon energies beyond this region. It was decided to proceed with the analysis on the assumption that the poor shape of the high energy end of the spectra would not significantly affect the characteristic signal ratios.

An MBH background was fitted to each spectrum. The uncorrected Si_3N_4 bremsstrahlung shape was created by producing MBH cross sections for Si and N separately using program CROSS, and adding them in proportion to the stoichiometric concentration for each element. The background was modified in each case to correct for absorption in an effective Au contact thickness. The deduced Au thickness was typically $\sim$80-100Å (cf. the value of 110Å deduced from the Si spectra in chapter 5). As before, the effective Au thickness is probably affected by ICC at the low energy side of the Si peak. The fitted background curve is shown with the spectrum in figure 6.2. The fit appears to be good over an energy range up to $\sim$6keV. Beyond this energy, the background

bulk Si

Si_3N_4 **membrane**

2mm

120μm

500A

335μm

640μm

bulk Si
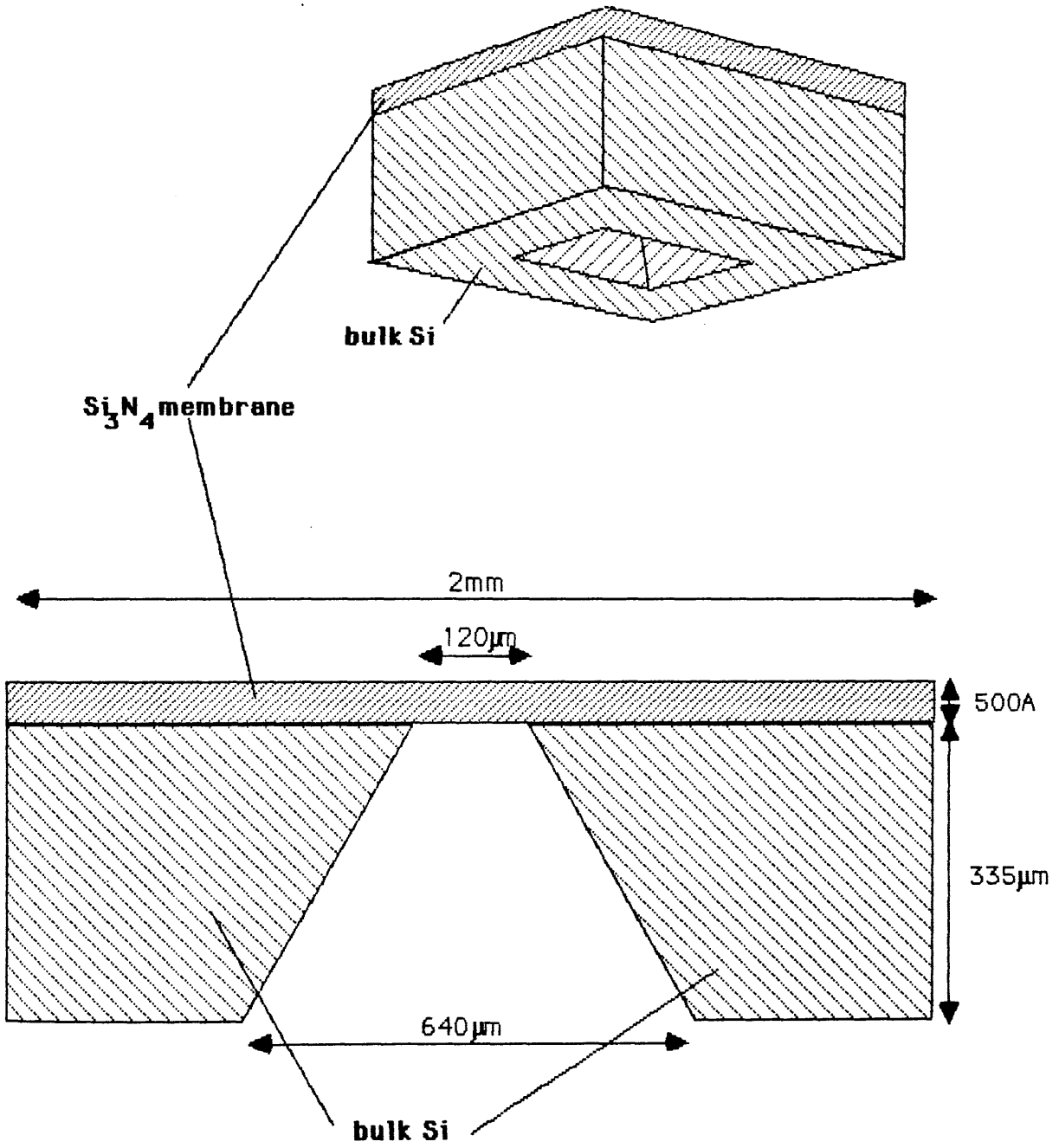
Figure 6.1 Schematic diagram of Si_3N_4 specimen
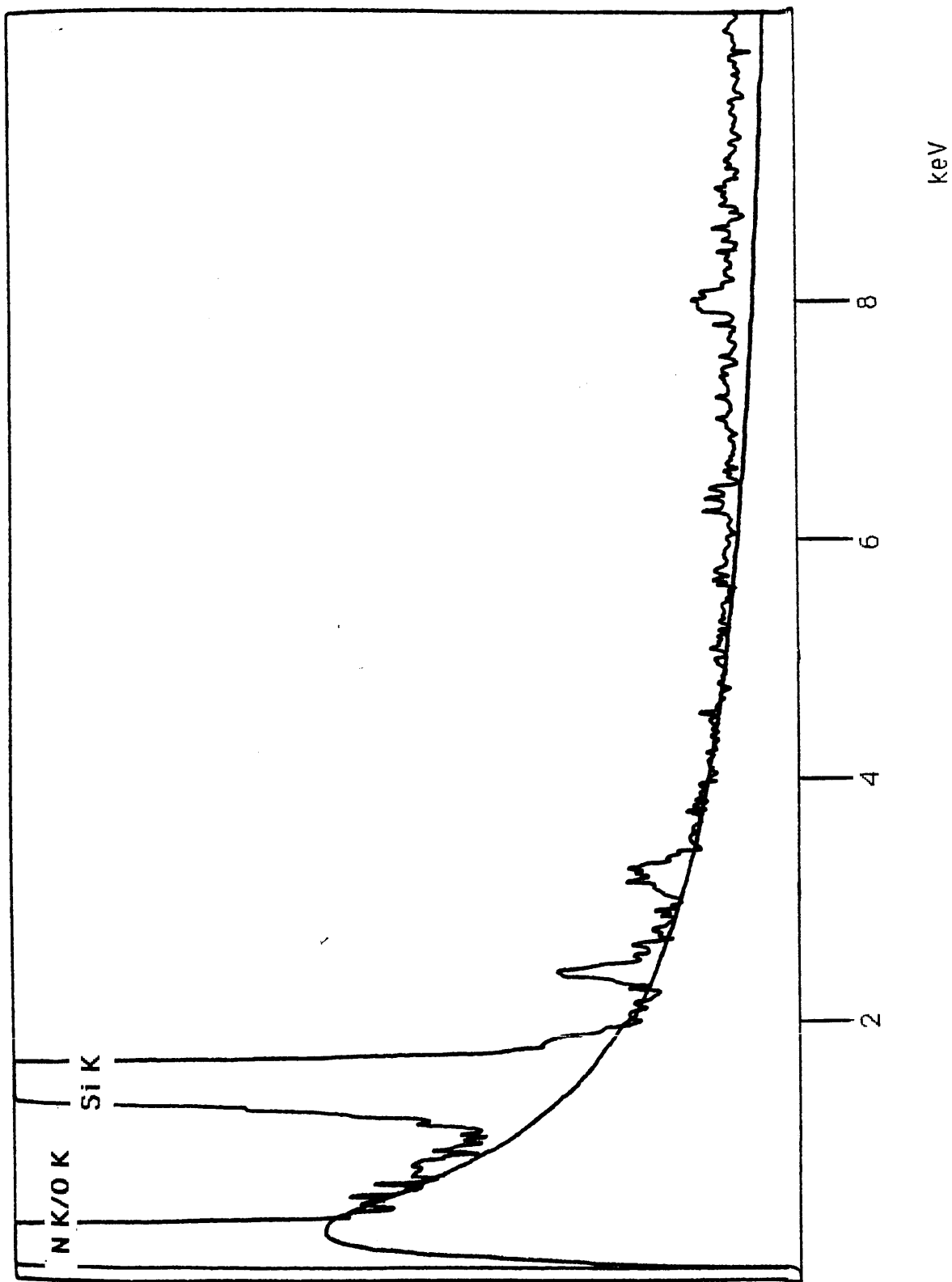
Figure 6.2 Typical spectrum recorded from Si_3N_4

lies appreciably above the level predicted by MBH.

Extraction of the characteristic Si counts involved simply subtracting the fitted background from the spectrum in the Si peak region for each spectrum. The statistical error in the extracted signal was typically <1%. If some ICC was present, as was suspected because of the background level on the low energy side of the peak, then a proportion of the characteristic counts would lie outside the peak region. This effect, although significant for the background shape, would constitute a very small correction to the characteristic signal, and was neglected.

Extraction of the characteristic N counts was more difficult due to the overlap of the N peak with the O K peak which was always present. A gaussian was fitted to each N peak. The number of counts in the fitted gaussian was taken as a measure of the characteristic N signal. Figure 6.3(a) shows the spectrum of figure 6.2 with the fitted gaussian removed. An alternative procedure would have been to remove the O signal in this way, leaving the isolated N peak. Figure 6.3(b) shows the same spectrum again, this time with the gaussian fitted to the O peak subtracted. This subtraction appears to be less successful than the subtraction of the N signal. The shape of the background suggests that too many counts have been subtracted in the O peak region. For this reason, the first approach was taken for all spectra. .

Table 6.1 lists the values of the Si/N count ratios for each spectrum, together with the specimen tilt angle at which the spectrum was recorded. There is no clear trend in the variation of the count ratio with tilt, which suggests that no absorption correction is necessary. The mean value of the Si/N count ratio from these results is 4.3 ± 0.3.

6.2.2 NiO

These spectra were recorded from an ion-beam thinned NiO foil, mounted in the single tilt holder. Reference has previously been made to this data set in chapter 5. A total of 50 spectra were recorded from several areas of various thickness. Two spectra from different areas are shown in figure 6.4(a) and (b). Visual inspection of these spectra suggests that the K_α/L-line ratios for Ni in these spectra differ appreciably, which implies that the L-line is being absorbed at
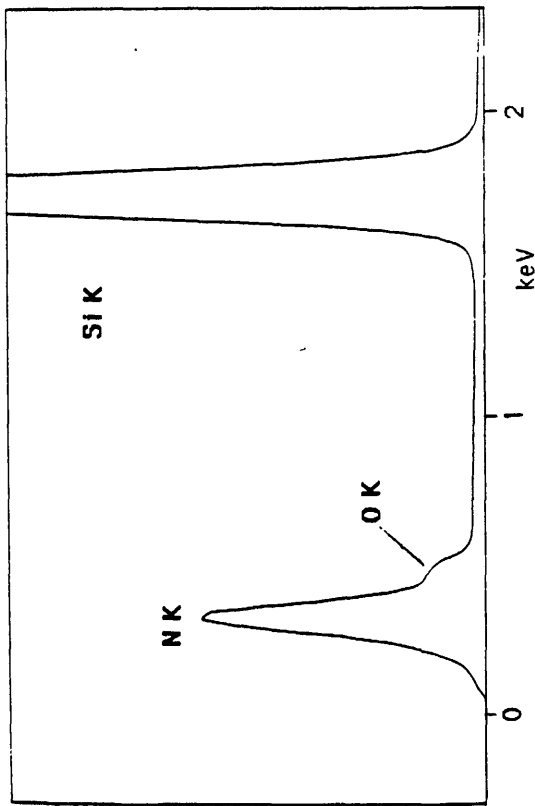
Figure 6.3

Extraction of N counts from Si_3N_4 spectrum.
The unprocessed spectrum is shown on the left.

(a) N counts removed by gaussian fitting and subtraction
(b) O counts removed by gaussian fitting and subtraction
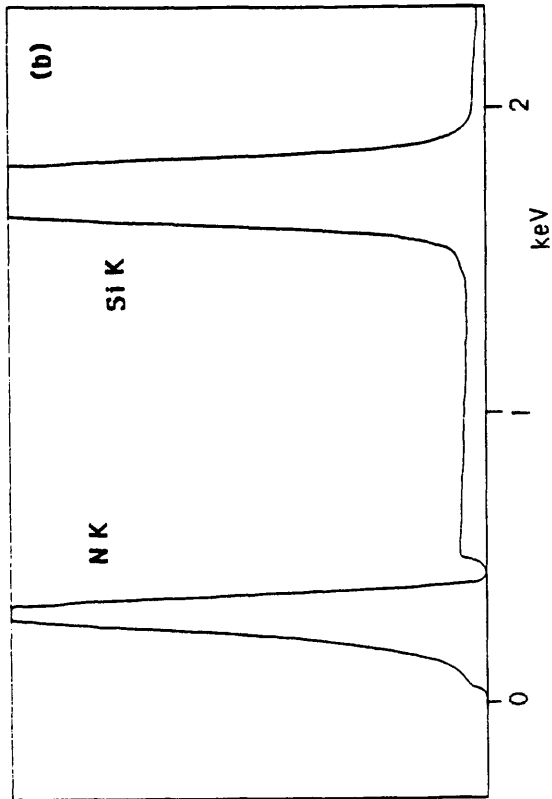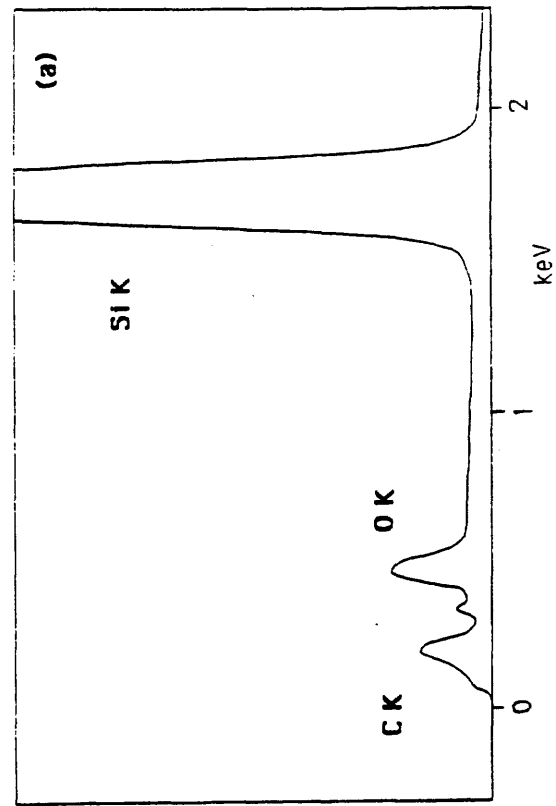
specimen tilt	Si/N count ratio
10°	3.98
30°	4.68
0°	4.09
60°	4.66

Table 6.1   Count ratios measured from each spectrum recorded from Si_3N_4, together with the approximate value of the specimen tilt for each case.
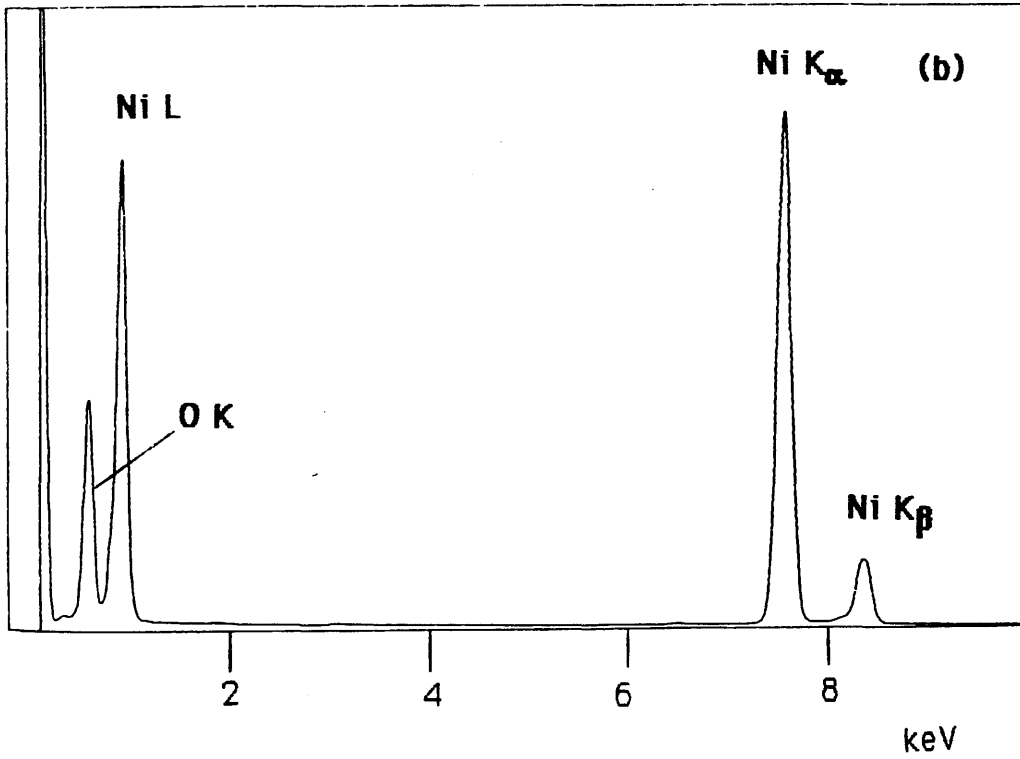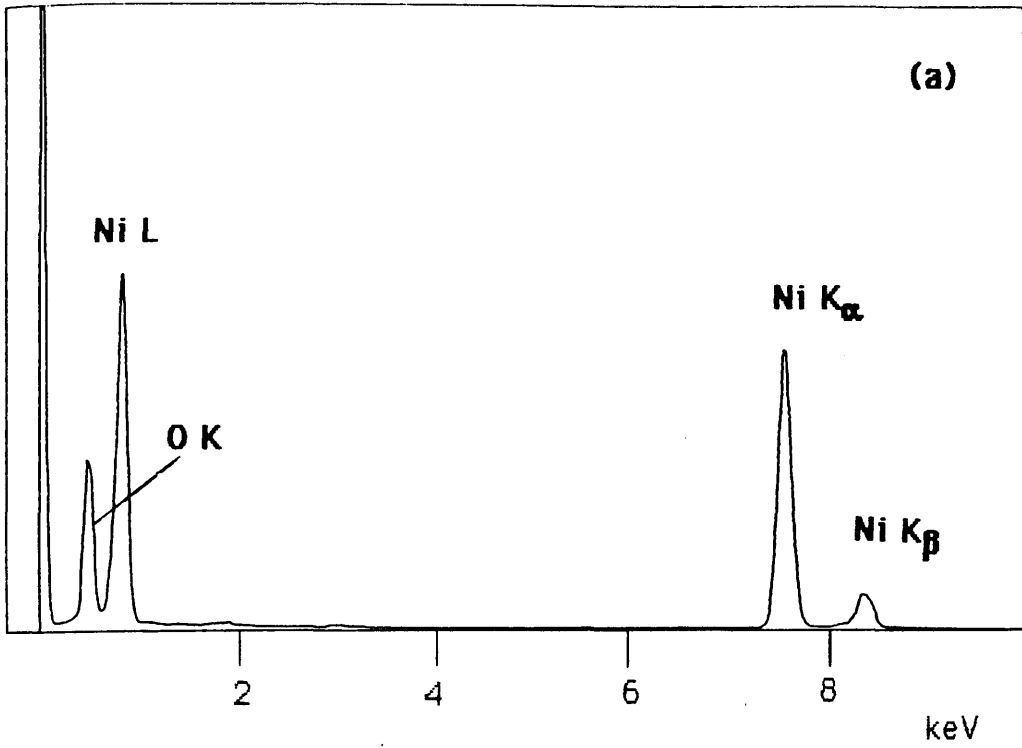
Figure 6.4 Two spectra recorded from different areas of the same NiO specimen, showing the variation within this data set of the Ni K/L ratio.

different rates in the two cases. This difference is representative of the variation of the Ni K_α/L ratio within the data set. The mass absorption coefficient for the Ni L-line in NiO is $19153 cm^2 g^{-1}$, while that for O K is $28561 cm^2 g^{-1}$ (Heinrich, 1987). This implies that any absorption which affects the Ni L signal will affect the O K signal to a somewhat greater degree. A value of the differential may be determined by deducing an effective absorption path length from the Ni K_α/L ratio, and using this to calculate the O K absorption. The differential determined in this way is as much as ~25% for a few spectra, but in most cases is <10%. This suggests, as discussed in chapter 5, that the Ni K_α/L ratio may be used to give some indication of the level of absorption present in any spectrum.

An MBH background was fitted to each spectrum. The background was corrected for absorption in a 110Å Au contact layer, and no other absorption corrections were included. It was shown in chapter 5 that the background fit depended strongly on the thickness assumed for the Au contact, and on the extent of the specimen self-absorption. Because of the high signal to background ratios here, however, the sizes of the extracted characteristic signals were not particularly sensitive to the precise nature of the correction made to the background.

The characteristic Ni K_α, Ni L and O K signals were extracted by subtracting the theoretical background from the spectra in the appropriate peak regions.

The first column of table 6.2 lists the value of the Ni K_α/L count ratio for each spectrum. The values vary between 1.06 and 1.89. The sets of values grouped together correspond to spectra recorded from the same region. The figures in brackets represent the gross number of counts per second in each spectrum. This latter quantity gives a very approximate indication of the specimen thickness, although it is also dependent on the beam current, which varies slowly with time. Examination of the two sets of figures shows some correspondence between K_α/L ratio and thickness, which is to be expected. There are, however, substantial deviations from this simple relation, which may arise due to the particular local geometry of the specimen in each area. The thickness as indicated by the Ni K_α/L ratio varies much more widely than that indicated by the number of counts in the spectrum, which suggests that the absorption path between the point of creation of the x-rays and the detector can differ

spectrum	Ni K_α/L	(gross counts/sec)	Ni K_α/O K	Ni L/O K
1	1.61	(585)	3.78	2.35
2	1.61	(567)	3.73	2.32
3	1.62	(569)	3.76	2.32
4	1.63	(551)	3.80	2.33
5	1.64	(546)	3.82	2.33
6	1.65	(536)	3.83	2.32
7	1.58	(761)	3.66	2.32
8	1.60	(690)	3.75	2.34
9	1.63	(621)	3.81	2.34
10	1.89	(592)	4.12	2.18
11	1.87	(574)	4.08	2.18
12	1.87	(584)	4.13	2.21
13	1.84	(593)	4.14	2.25
14	1.83	(577)	4.16	2.27
15	1.42	(1557)	3.29	2.32
16	1.42	(1630)	3.25	2.29
17	1.42	(1701)	3.27	2.30
18	1.21	(551)	2.93	2.42
19	1.25	(558)	2.99	2.39
20	1.28	(531)	3.18	2.48
21	1.16	(314)	3.38	2.91
22	1.18	(359)	3.26	2.76
23	1.19	(222)	3.61	3.03
24	1.18	(266)	3.40	2.88
25	1.18	(317)	3.24	2.77
26	1.17	(307)	3.22	2.75
27	1.17	(320)	3.27	2.79

Table 6.2 Count ratios from NiO data. Spectra grouped together were recorded from the same area.

spectrum	Ni K$_\alpha$/L	(gross counts/sec)	Ni K$_\alpha$/O K	Ni L/O K
28	1.16	(202)	3.39	2.92
29	1.16	(291)	3.26	2.81
30	1.13	(413)	3.36	2.97
31	1.21	(309)	3.39	2.80
32	1.17	(352)	3.31	2.83
33	1.15	(380)	3.14	2.73
34	1.18	(307)	2.98	2.53
35	1.13	(855)	2.67	2.36
36	1.11	(797)	2.96	2.64
37	1.14	(797)	2.97	2.61
38	1.13	(833)	3.08	2.73
39	1.13	(747)	3.15	2.79
40	1.14	(759)	3.21	2.82
41	1.17	(438)	2.79	2.38
42	1.13	(413)	2.50	2.21
43	1.12	(374)	2.60	2.33
44	1.06	(438)	2.57	2.42
45	1.12	(521)	2.56	2.29
46	1.14	(792)	2.57	2.25
47	1.11	(807)	2.61	2.35
48	1.12	(831)	2.66	2.38
49	1.13	(854)	2.57	2.27
50	1.11	(851)	2.67	2.41
51	1.12	(749)	2.56	2.29
52	1.15	(1046)	2.68	2.33

Table 6.2   *(continued)*

substantially from the thickness as indicated by the count rate. An example of the type of geometry which could produce such an effect is illustrated in figure 6.5.

The second column of table 6.2 lists the values of the Ni K/ O K signal ratio for each spectrum. As for the Ni K_α/L ratios, there is a wide variation in these values, from 2.50 to 4.16. Figure 6.6 shows a plot of the number of Ni K_α counts per second against the number of O K counts per second for each spectrum. A straight line on this plot would represent a line of constant measured composition. The clusters of experimental points appear to be scattered on both sides of the best straight line, fitted by linear regression, which is shown. The presence of significant amounts of absorption of low energy x-rays has already been noted. This effect would suppress the O K signal in the affected spectra, and so would cause some of the points to lie appreciably above a line which represents the stoichiometric composition. It was noted in the previous sub-section that the Si_3N_4 spectra contained significant O K signals, even though there was ostensibly no O in the specimen. Many of the other spectra shown in this thesis contain extraneous O (and C) signals, presumably from backing films or contaminants. Similar additional O signals, could have contributed to some of the NiO spectra. Such a signal cannot have been uniformly present, since the effect would then lead to a systematic error in the Ni K_α/ O K ratio. this error would be reflected in a positive intercept of the best line with the O K axis, which is not found. The gradient and intercept of the best line were 2.9 ± 0.1 and 16 ± 9 respectively. The former figure was taken as an initial estimate of the Ni K_α/O K count ratio.

The final column of table 6.2 lists the values of the Ni L/O K count ratio for each spectrum. This quantity should be less sensitive to the level of absorption than the NiK_α/O K ratio. The variation in these values, from 2.18 to 3.03, suggests that there were differences in composition between different areas of the specimen. It is assumed here that the Ni L and O K signals are absorbed at the same rate. It is recognised that this is an approximation. However, uncertainties in mass absorption coefficients at these photon energies would render any calculations of absorption differentials subject to considerable error. Figure 6.7 is equivalent to figure 6.6, except that in this case the number of Ni L counts per second rather than Ni K_α is plotted. As would be expected from the preceding discussion, the spread in these points is less than
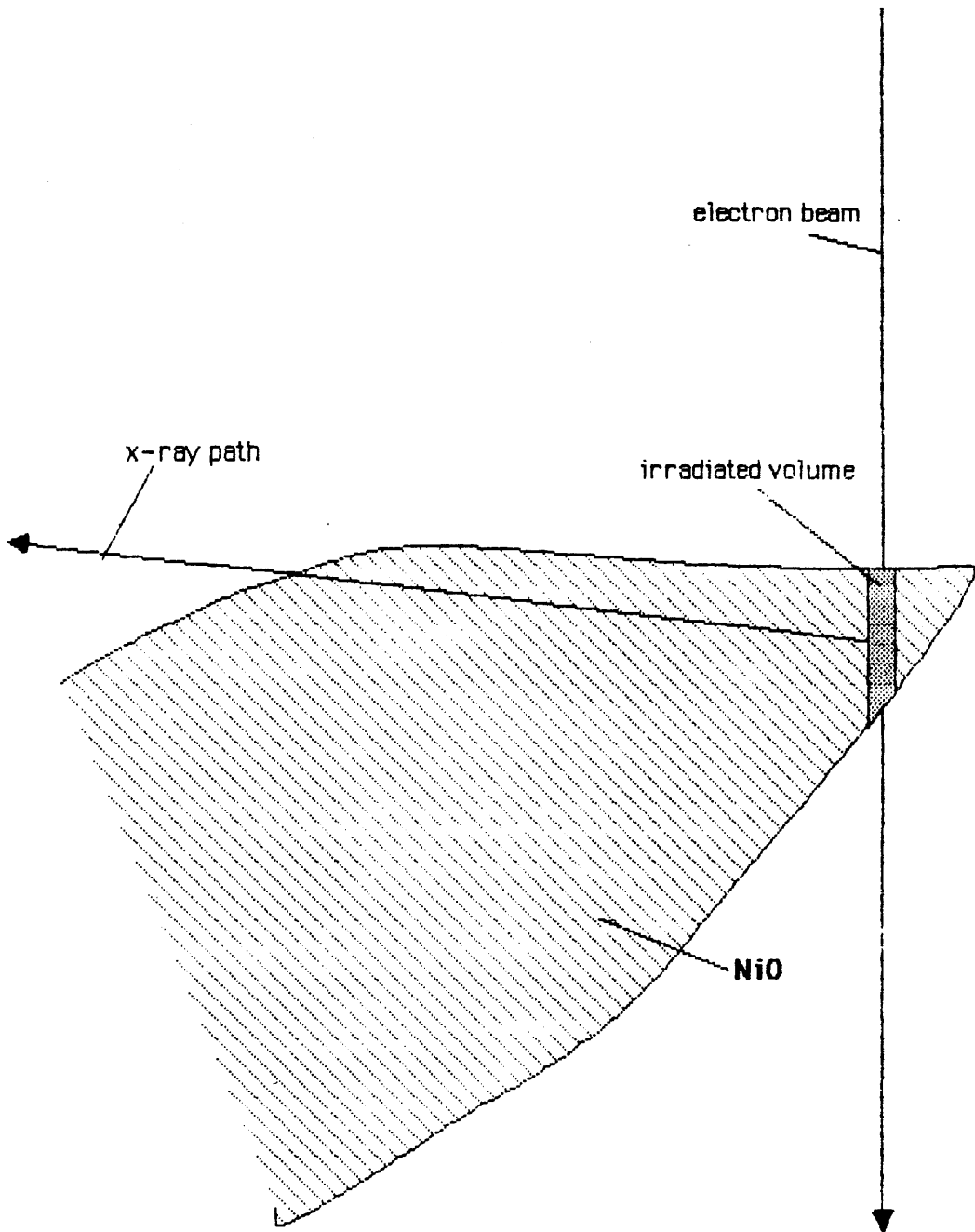
Figure 6.5 A possible mechanism for x-ray absorption in an ion-beam thinned NiO specimen. The proximity of thick material to the thin area from which a spectrum is recorded can cause x-rays to be absorbed much more strongly than would be the case for a uniform film. The effective thickness indicated by the K_α/L ratio will therefore be much greater than that indicated by the count rate, which is governed by the number of atoms in the irradiated volume.
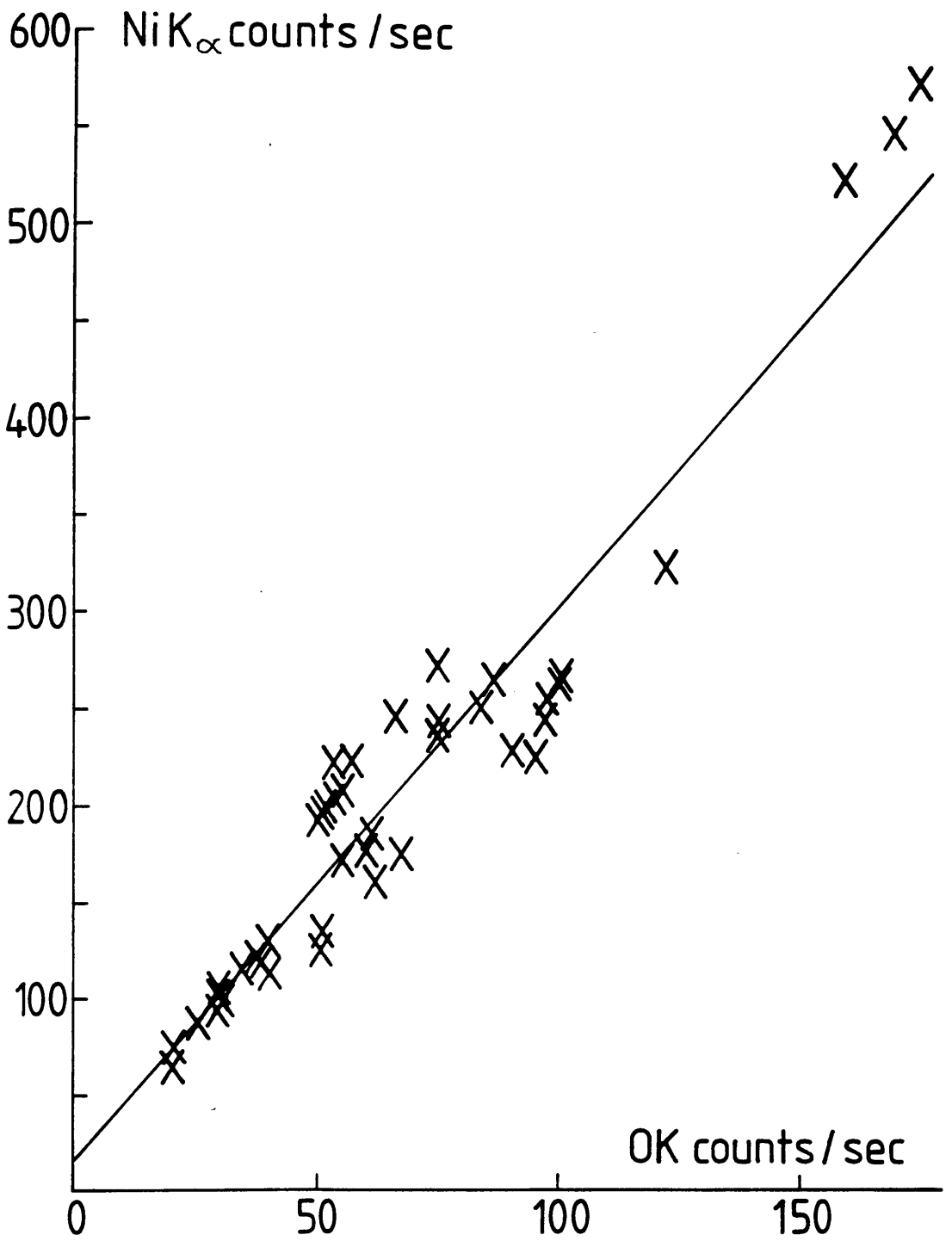
Figure 6.6   Ni K$_\alpha$ counts/sec vs. O K counts/sec for the NiO data from the VG HB501
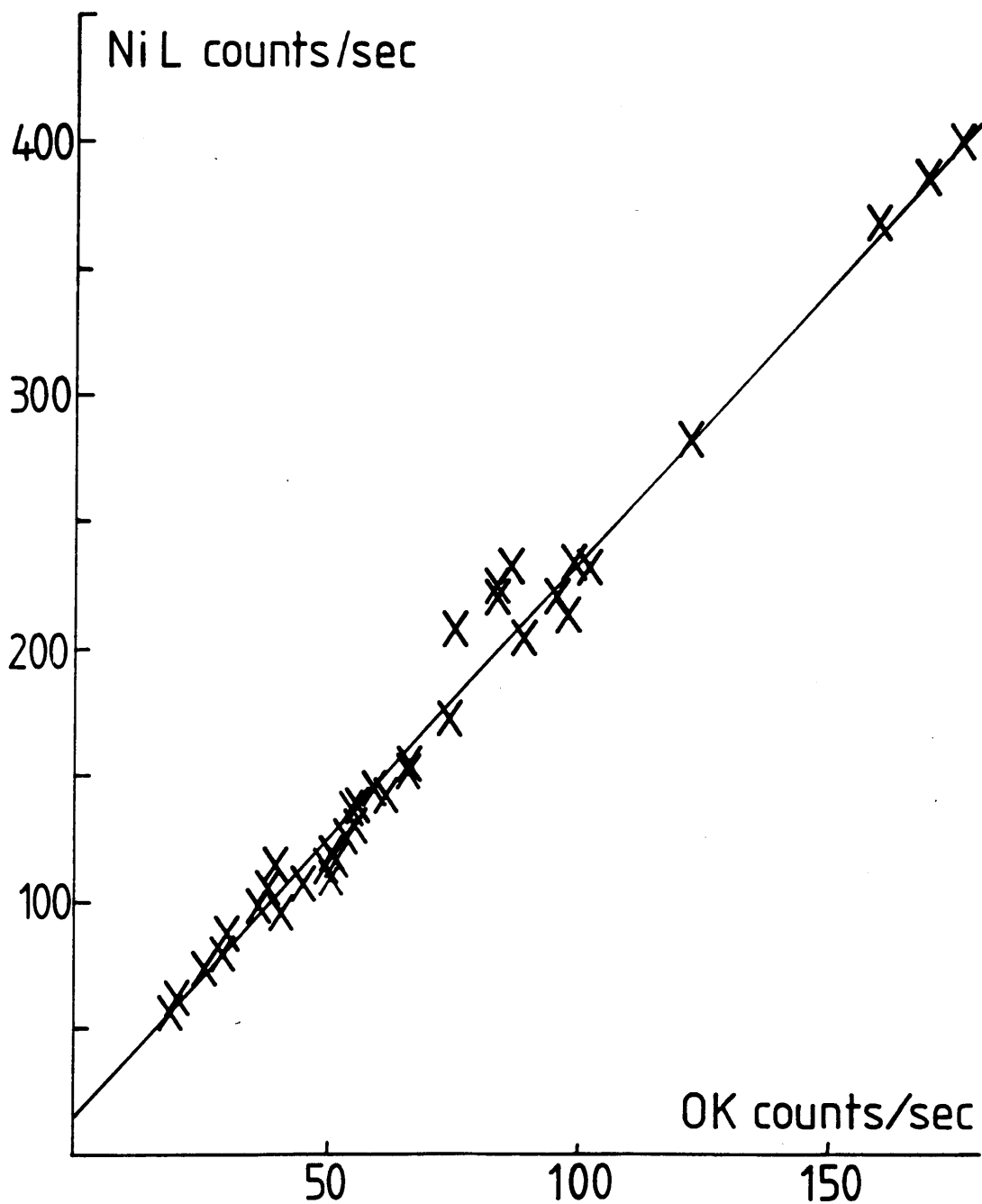
Figure 6.7   Ni L counts/sec vs. O K counts/sec for the NiO data
from the VG HB501

in the previous figure. The remaining spread is presumably due to the variations in the amount of O present, as discussed before, which would be reflected equally in both plots. Some of the spread will be due additionally to the errors introduced by the assumption of no absorption differential between the Ni L and O K signals. A straight line was again fitted to the data by linear regression, the gradient and intercept being 2.24 ± 0.05 and 11.6 ± 3.3 respectively. The former figure gives an estimate for the Ni L/O K count ratio. For the purposes of converting count ratios to concentration ratios it is desirable to consider signals from the K-shell only. The measurements described in chapter 5 of K_{α}/L-shell ratios yielded a value of 1.02 for the Ni K_{α}/L count ratio for this detector, in the absence of absorption. The required Ni K_{α}/O K ratio is therefore given by

$$\frac{Ni\ K_{\alpha}}{O\ K} = \frac{Ni\ K_{\alpha}}{Ni\ L} \cdot \frac{Ni\ L}{O\ K} = 1.02\ \frac{Ni\ L}{O\ K} \qquad \textbf{(6.1)}$$

The Ni K_{α}/O K count ratio, based on figure 6.7, is therefore given by $2.24\pm0.05 \times 1.02 = 2.28\pm0.05$.

Two estimates of the Ni K_{α}/O K count ratio have thus been obtained. The result derived from figure 6.7 is appreciably different to that derived from figure 6.6. This difference reflects the fact that when the Ni K_{α}/O K signal ratio is considered, the points for which absorption has a significant effect must force the gradient of the fitted straight line to be lower than the true value. Considering instead the Ni L/O K signal ratio substantially reduces the extent to which absorption affects the results, and so it was considered that the Ni K_{α}/O K count ratio deduced following this approach was likely to be a better estimate of the true value.

6.2.3 MgO

The specimen comprised MgO cubes on a holey carbon/formvar backing film, supported on a Cu single-hole mount. The backing film was prepared according to the method described in appendix C. The nature of the single-hole mount would minimise any bulk signal arising from it. The MgO cubes were introduced

by holding the backing film in the 'smoke' which resulted when metallic Mg turnings were ignited by heating in a crucible with a bunsen burner. Some cubes lay partially suspended over holes in the backing, allowing the contribution of the backing film to the spectra to be minimised. The specimen was mounted in the Be double-tilt holder. It was expected that self-absorption would not be a function of the specimen tilt-angle due to the random orientation of the individual cubes. Cubes which lay as much as possible over holes in the backing film were selected. Spectra were generally recorded with the beam scanning the entire area of each cube under investigation.

Two spectra from different sizes of cubes are shown in figure 6.8 (a) and (b). As was the case previously for NiO, there is clearly a variation in the Mg/O ratio within the data set. Characteristic signal extraction for both elements involved subtracting simple linear backgrounds defined by the background levels on either side of the peak. It was considered that this process would not introduce appreciable errors in the extracted counts. Table 6.3 lists the Mg K/O K count ratio for each spectrum, together with the approximate size of the cube studied in each case. Any dimension of one of these cubes should give an indication of its thickness as 'seen' by the emergent x-rays. Also shown in table 6.3 are the Mg K P/B ratio for each spectrum. There are wide variations in both the Mg K/O K count ratio and the Mg P/B ratio. Both, however, appear to follow a similar trend with the cube size. The lowest P/B corresponds to the lowest Mg K/O K. A low value of P/B suggests the presence of a contribution to the background other than that which would be expected from the material of interest. It should be noted that the highest value of P/B is considerably lower than would be expected from the discussion of this quantity in chapter 4, even when the expected O concentration from MgO is taken into account (see table 6.4). The concomitant variation of Mg K/O K suggests that the additional background contribution is associated with an extra O signal. It is not clear why the size of such a signal should depend on the specimen thickness. Figure 6.9 shows a plot of the number of Mg K counts per second against the number of O K counts per second. The result of the trends discussed above is that the points appear to lie on a curve rather than on a straight line. There is no clear indication of which, if any, of the points correspond to the stoichiometric Mg/O ratio. This example illustrates some of the difficulties which can occur in the analysis of compounds of O, and shows how the P/B ratio can be used to indicate problems with particular data sets. No further analysis of the MgO data was
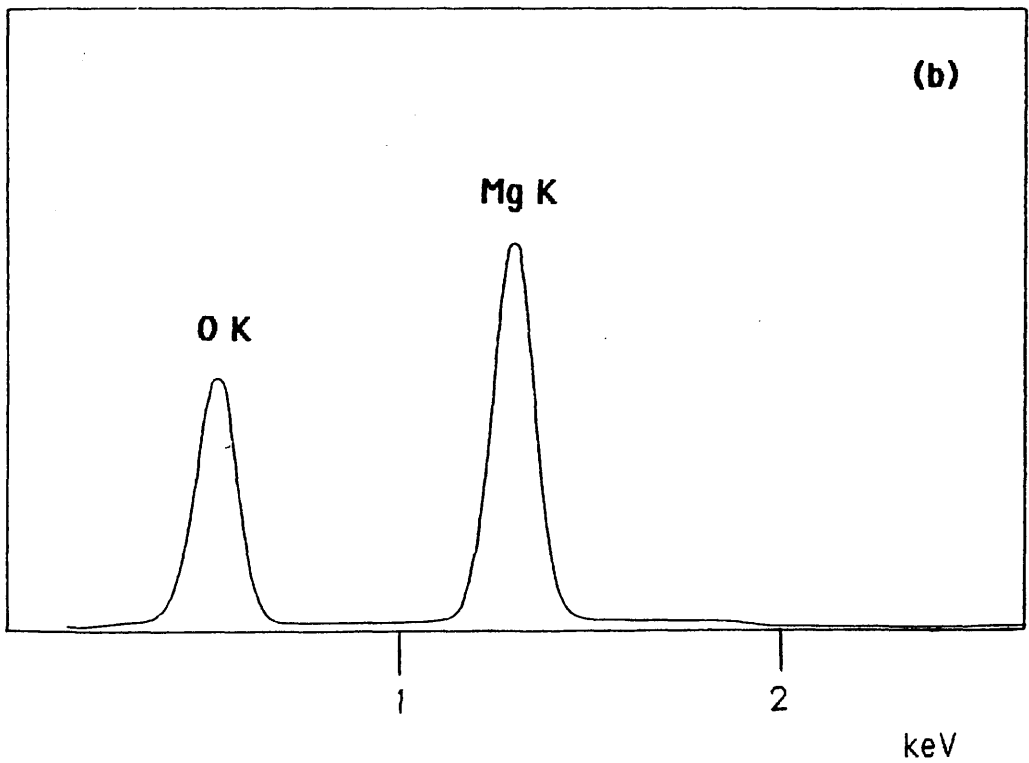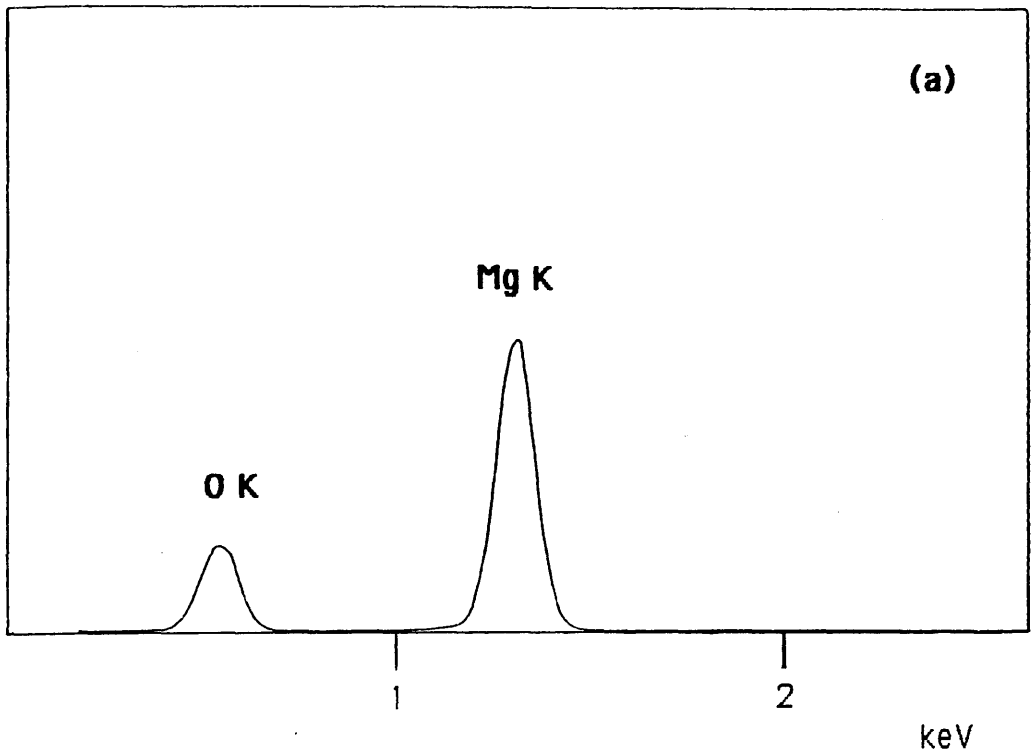
Figure 6.8 Two spectra recorded from different areas of the same MgO specimen, showing the variation within this data set of the Mg K/O K ratio.
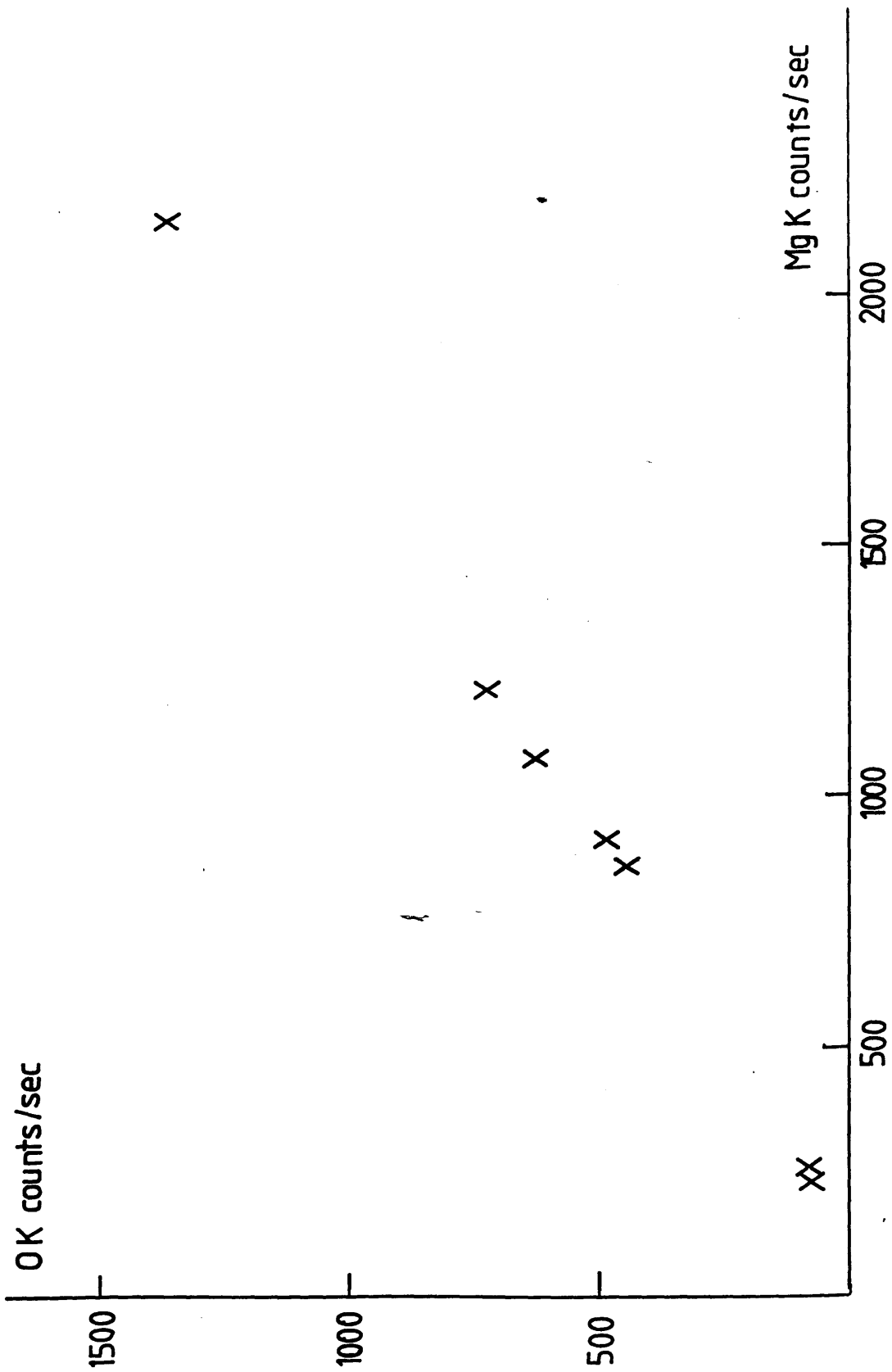
Figure 6.9   O K counts/sec vs.Mg Kcounts/sec for the MgO
data from the VG HB501.

spectrum	Mg K/O K	Mg K P/B
1	3.56	450
2	3.44	480
3	3.44	485
4	1.89	355
5	1.92	375
6	1.70	360
7	1.71	350
8	1.72	360
9	1.58	230

Table 6.3 Count ratios and Mg P/B values from MgO data. Spectra grouped together were recorded from the same area.

undertaken.

6.3 k factors for light element analysis

The conversion of count ratios in the EDX spectrum to elemental concentration ratios has been discussed in chapter 4. The two quantities are related by a k factor, which may be determined by reference to standard specimens, or may be calculated ab initio using equation 4.4. This equation is repeated here for convenient reference. For the K-shell signals from two elements a and b, the k factor is given by

$$k_{ab} = \frac{\varepsilon_b(h\nu_b)\,\omega_{Kb}\,s_b\,\sigma_{iKb}}{\varepsilon_a(h\nu_a)\,\omega_{Ka}\,s_a\,\sigma_{iKa}} \qquad (6.2)$$

where $\varepsilon_x(h\nu_x)$ is the detector efficiency, ω_{Kx} is the fluorescence yield, s_x is the K-shell partition function and σ_{iKx} is the ionisation cross section. For photon energies between ~3keV and ~20keV, the detector efficiency is essentially unity, the fluorescence yield and partition function are known with a reasonable degree of accuracy, and the ionisation cross section can be described by a parameterisation of the Bethe model as discussed in chapter 4. These factors are generally not so well known for the very low photon energies which are of interest here.

Determination of the low energy efficiency of the windowless detector used in this work has been discussed in chapter 5. It was considered that a reasonable estimate of the efficiency could be made for the L-lines of transition metals, i.e. for photon energies as low as ~700eV. The method of estimation involved fitting an Au absorption correction over a background region starting at ~900eV, and extrapolating the corrected background shape downwards in photon energy. Clearly the error associated with this procedure becomes greater as the range of the extrapolation increases. Further errors may arise due to the uncertainty in mass absorption coefficients at low photon energies (Heinrich, 1987). Estimates of the efficiencies made using this method for O and N will therefore

71

be subject to very large errors. There is no reason to believe that estimation of the efficiency using the manufacturer's quoted detector parameters, as adopted by, for example Thomas (1984) and Vandersande et al. (1987), should result in any greater accuracy.

It was noted in chapter 5 that a limitation was placed on the accuracy with which information could be deduced on the L-shell by uncertainties in the values of the fluorescence yield. A similar limitation is found in the case of the K-shell for light elements. The lighter the element is, the more severe the problem becomes. Two sources have been used here for K-shell fluorescence yield data. Both works, by Langenberg and Van Ecke (1974) and by Krause (1979), are based on large bodies of data from other workers. Table 6.5 lists the values of ω_K from both sources for the elements of interest here. As would be expected, the values for Ni are very similar. The K_α line of Ni, at 7.477keV, lies in the region in which ω_K is considered to be well known. As the K-line energy decreases, the discrepancies increase considerably. Krause e imates that the uncertainty in ω_K for $20<Z<30$ ranges from 5% to 3%; that for $10<Z<20$ from 10% to 5%; and that for $5<Z<10$ from 40% to 10%.

The partition function s is well known, and is essentially unity for elements with $Z<16$. No problems arise for light element analysis due to this factor.

The parameterisation of the K-shell ionisation cross section discussed in chapter 4 is strictly valid only within the range $14<Z<50$ over which it was carried out. The Bethe form is a convenient fitting function rather than a rigorous theoretical model, and the quality of the fit to experimental data gives no guarantee that the same functional form can describe the cross sections outwith the range of the data. The parameterisation of Powell(1976), however, was carried out over a range of lighter elements. Although the parameters produced by Powell differed appreciably from those deduced here, there is no suggestion here that the Bethe form loses validity for low Z. The derivation of the Bethe form, as described in chapter 2, does not introduce any approximations which break down for low Z. It was therefore considered likely that ionisation cross sections for any elements, including light elements, calculated according to the Bethe form with the Bethe parameters deduced in this work would not be seriously in error. The analysis described in the next section gives some indication of the correctness of this assumption.

72

element	ω_K	
	LVE	K
N	0.004	0.0052
O	0.006	0.0083
Si	0.0482	0.050
Ni	0.396	0.406

Table 6.5 Values published for K-shell fluorescence yield for elements of interest in this work by Langenberg and Van Eck (1974) (LVE) and Krause (1979) (K).

It is clear from this discussion that k_{xO} and k_{xN} factors calculated using equation 6.2 will be subject to large errors because of the uncertainties in the individual quantities which contribute to the k factor, particularly the detector efficiency and ωK. It is worth reiterating at this point that the expression in equation 6.2 for the k factor can be split into two parts: the ratio $\varepsilon_b(h\nu_b)/\varepsilon_a(h\nu_a)$, which depends only on the detector on a particular microscope; and the remaining terms, which are properties of the atoms of the specimen.

6.4 Determination of light element detector efficiency using experimental count ratios

The results given in section 6.2 were assumed to represent experimental count ratios which are directly related to the stoichiometric elemental concentration ratios by the appropriate k factors as defined by equation 6.2. In principle, it is possible to calculate the k factors accordingly, combine these with the count ratios, and return the value of the concentration ratio. Clearly the results will depend strongly on the values input for the detector efficiency. Alternatively, the k factors deduced assuming the count ratios to be correct may be used to determine detector efficiencies for O and N. The latter approach is followed here.

The stoichiometric Si/N concentration ratio for Si_3N_4 is 0.75. The SiK/N K count ratio was measured as 4.3 ± 0.3, giving $k_{SiN} = 0.17\pm0.01$. Substituting this value into equation 8.2 yields values of $\varepsilon_N(h\nu_N)/\varepsilon_{Si}(h\nu_{Si}) = 0.32\pm0.02$, if the ω_K values of Langenberg and Van Eck are used, and 0.26 ± 0.01 if those of Krause are used. The method of chapter 7 gives an estimate of 0.92 ± 0.02 for $\varepsilon_{Si}(h\nu_{Si})$. The respective values of $\varepsilon_N(h\nu_N)$ are therefore 0.29 ± 0.02 (Langenberg and Van Eck) and 0.24 ± 0.01 (Krause). Thomas(1984) estimated that $\varepsilon_N(h\nu_N)$ for a windowless detector should be ~0.35. It is not stated in that work what set of mass absorption coefficients have been used to produce this estimate. Extrapolation of the background shape fit described in chapter 5 gives a value of $\varepsilon_N(h\nu_N) = 0.18\pm0.05$. This figure is derived using the mass absorption coefficients of Springer and Nolan (1976), since these were the coefficients written into the fitting software. Using other coefficients, such as those of Heinrich (1987), for the background modelling would have resulted in a different estimate for the Au contact thickness. Assuming the transition metal

L-line efficiencies deduced previously to be accurate, the Au thickness was re-estimated to be 340 ± 30Å using the Heinrich coefficients. The resultant estimated efficiency for N is then 0.38 ± 0.03 The values of the detector efficiency for N derived here, although subject to considerable errors, show no major inconsistency with that which would be expected based on the above discussion.

The stoichiometric Ni/O concentration ratio for NiO is 1. The best value for the Ni K_α/O K count ratio was determined to be 2.28 ± 0.05, which implies that $k_{NiO} = 0.44 \pm 0.01$. Substituting into equation 8.2 gives $\varepsilon_O(h\nu_O)/\varepsilon_{Ni}(h\nu_{Ni}) = 0.76 \pm 0.02$ (Langenberg and Van Eck), or 0.57 ± 0.01 (Krause). Since the efficiency for the Ni K_α line is unity, these figures also represent $\varepsilon_O(h\nu_O)$. The estimate of Thomas in this case is that $\varepsilon_O(h\nu_O) \sim 0.5$. Extrapolation of the background fit of chapter 5 gives a value of 0.30 ± 0.05, or 0.46 ± 0.03 if the Heinrich coefficients are used. Taking into consideration these figures, and the efficiency estimated in chapter 5 for the Fe L-line, ~200eV higher in energy than the O K line, of 0.53 ± 0.05, it appears that the value of $\varepsilon_O(h\nu_O)$ suggested by this analysis is somewhat high.

Consideration of the efficiencies deduced here for N and O indicates that the values are not subject to any serious systematic errors. This in turn suggests that the values used for the fluorescence yields and the ionisation cross sections, though subject to considerable uncertainties, are not seriously in error. It does appear, however, either that the oxygen signal may have been overestimated, or that the efficiency for O is higher than the Au contact layer absorption model predicts.

The former situation could have arisen if some of the points plotted in figure 6.7 reflected the presence of a substantial extra O signal, causing the gradient of the fitted line to be greater than the true value. This effect was recognised in section 6.2 to have been a possible contributory factor to the spread of the plotted points, but is difficult to quantify the effect on the gradient of the best line. The P/B ratio could not be used as in the case of MgO to indicate the presence of extra O (see section 6.2), since the difference in Z between Ni and O results in the background for NiO being mainly due to Ni. The situation may have been further complicated by the possibility that the composition of the NiO may have varied from the stoichiometric value. The EELS results of Crozier (1985)

and the work of Ostyn and Carter (1982) suggest that an O deficient surface layer can exist in ion-beam thinned NiO specimens. Clearly, the scope with these specimens for variations in composition, and absorption results in considerable uncertainty in the interpretation of these data in terms of simple count ratios.

The latter case may have arisen if a substantial amount of the absorption which limits the low energy detector efficiency was taking place in a layer of ice rather than purely in the Au contact layer. The O K-line, lying just below the O K absorption edge, would then be absorbed relatively less strongly than the transition metal L-lines which lie above the absorption edge Additionally, incoming photons could produce an additional O signal by fluorescence of the O in the ice layer.

6.5 Conclusions on the potential of light element analysis by EDX

The results obtained here illustrate some of the problems which arise in the quantitation of signals in the EDX spectrum from light elements. It should be noted that the spectra studied here suffer relatively little from peak overlap at low energies, which will cause further difficulties in the analysis of more complex spectra. The problems associated with the calculation of k factors according to the expression in equation 6.2 have been discussed in detail. The accuracy of standardless light element analysis is inherently limited by the accuracy with which the quantities which contribute to the k factor are known. It seems inevitable that the overall error arising from these will be greatest for low photon energies, even when K-shell x-rays only are considered. Possibly the most serious limitation will prove to be the uncertainty in the values of ω_K. The wide range of values quoted in the literature and the uncertainties estimated by Krause suggest that this is a very difficult quantity to measure for light elements.

The efficiency of a windowless x-ray detector for low photon energies is at present difficult to measure accurately. It is possible to make estimates, based on nominal detector parameters or on background modelling over limited regions as described in chapter 5. These methods will give reasonable figures for the efficiency, but the associated errors must become increasingly

significant as the photon energy decreases. It is also possible, as has been attempted here, to estimate the efficiencies for particular elements by examination of spectra from specimens of known composition. The results described in this chapter illustrate that such a procedure is not always simple. The results from NiO and MgO show that, particularly in the case of oxides, it is difficult to prepare specimens whose composition is known with a high degree of certainty. Even if the composition of the specimen has been determined independently, for example by EELS analysis, the effects of specimen self-absorption and, to a lesser extent, fluorescence, can complicate the interpretation of the spectra. The problems which arise in this region are therefore not restricted to standardless analysis only.

There are positive indications from this work. It is significant that the estimates of the detector efficiencies here showed no evidence of serious systematic errors. As stated earlier, there is an indication that the cross-section model investigated in chapter 4 does not seriously break down for light elements. It appears that it is possible to extract meaningful quantitative information from the low energy region of the windowless EDX spectrum, although there are significant errors associated with any results. Chapter 9 will compare this potential with the capability of EELS for similar analyses.

Chapter 7

EELS analysis procedures

7.1 Introduction

This chapter decribes the procedures used for the extraction of quantitative information from EELS spectra. Firstly, the general form of the spectrum is described. Figure 7.1 shows the features found in a typical EELS spectrum. The spectrum consists of two distinct regions. The low loss region is due to electrons which have lost no energy, or small amounts of energy due to valence electron excitation as described in chapter 2. The region which is mainly of interest for microanalysis occurs at higher energy losses. The electrons which contribute here have been inelastically scattered by collisions with inner shell electrons. For each element in the specimen, there are threshold energy losses corresponding to the ionisation energies of each shell or sub-shell. For every shell whose threshold energy loss is within the range detectable by the EELS acquisition system, there is a step in the spectrum at the threshold. Inner shell scattering therefore leads to the occurrence of characteristic edges in the spectrum. The signal in each edge extends far beyond the threshold energy loss. These edges sit on top of a background which is generally due to the edges of lower threshold energy loss This general form is discussed in detail in section 7.2. For quantitation, it is necessary to extract these characteristic signals from the background. This is usually done by fitting a curve to the background region before the edge and extrapolating below the edge. This procedure is discussed in section 7.3. Considerable errors can result from the extrapolation of the fitted background, particularly when the extent of the pre-edge region is limited. A new approach was proposed by Steele et al. (1985). This method involved simultaneously fitting over pre-edge and post-edge regions. In the latter case a scaled theoretical edge shape was included in the function to be fitted. It is mainly this approach which is used in this work, and it is discussed in section 7.5.

The fitted background can then be subtracted, leaving the stripped

zero-loss peak

inner-shell edges

low loss
peak

energy loss

energy loss

low loss region

higher energy loss region, shown on an
expanded vertical scale in the inset
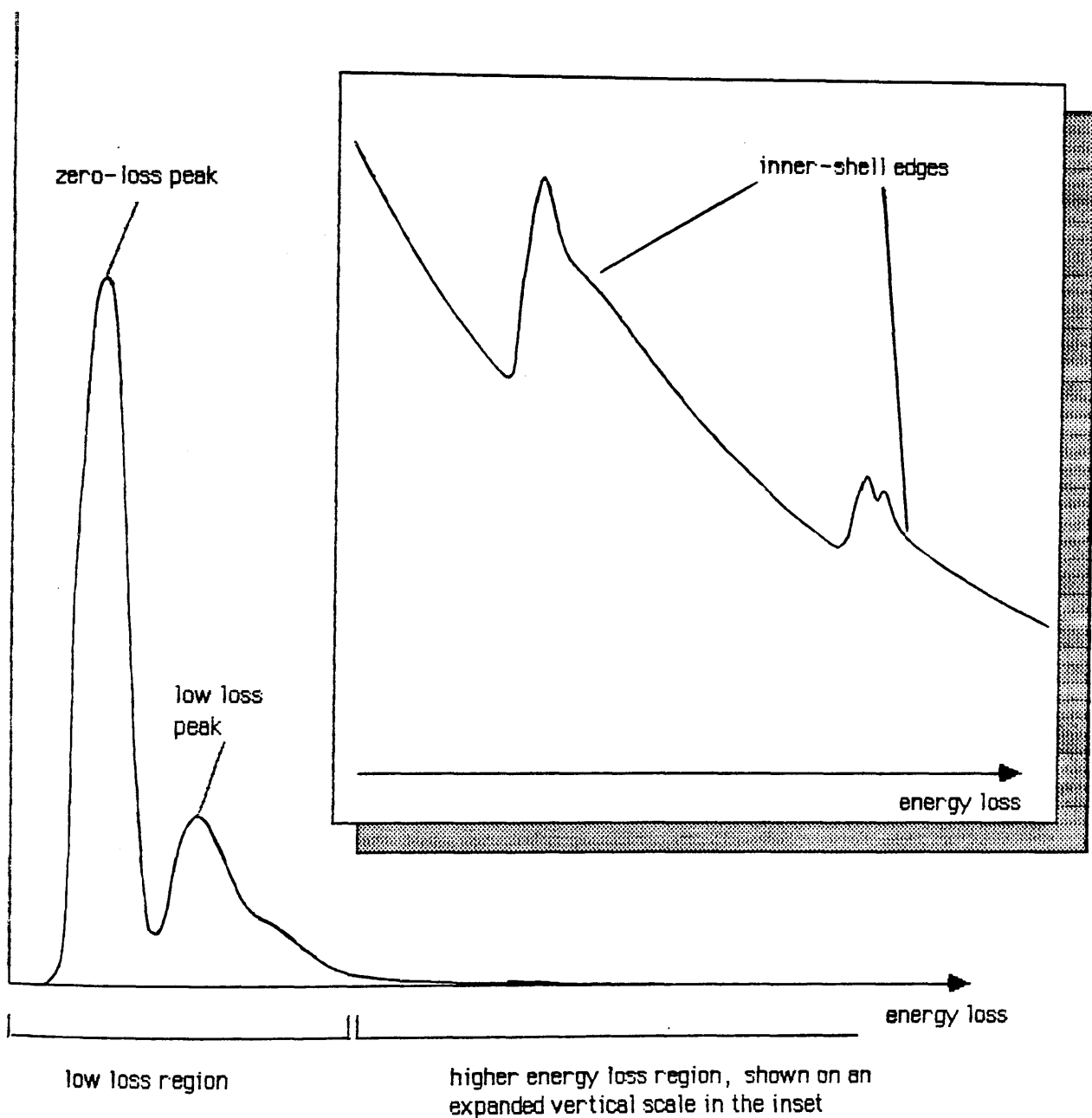
Figure 7.1   The general form of the EELS spectrum

characteristic edge. Information on elemental composition may be deduced by comparison of the stripped edges with theoretical cross sections. As discussed in chapter 2, the available theoretical cross sections are based on atomic models, and do not predict all the features of real edges. The difficulties in using these are described in section 7.6. Corrections to theoretical edge shapes to make them correspond more closely to experimental edge shapes are also described.

Finally, a summary is given of the steps required in the use of the analysis routine described in section 7.7.

7.2 The form of the EELS spectrum

7.2.1 The low loss region

The shape of the low loss region depends strongly on the specimen thickness. For thin specimens the main feature is the zero-loss peak, centred at 0eV. This peak is mainly due to electrons which have passed through the specimen unscattered. Electrons which have only undergone elastic scattering will also contribute. Additionally, electrons which have lost small amounts of energy, ie less than the resolution of the spectrometer, will be included.

Electrons which have interacted with valence electrons in the specimen also contribute to the low loss region. They typically produce a broad peak in the spectrum at ~30eV. The shape of this low loss peak can depend on the chemical environment of the scatterers, but it is not generally possible to extract much useful information from it. As discussed in chapter 2, the probability of valence electron scattering increases with specimen thickness. This is reflected in the relative proportions of the zero loss and low loss peaks. Unless the specimen is very thin, the height of the low loss peak can be similar to or greater than that of the zero loss peak. The tail of the low loss peak extends into the range where the characteristic signals of interest lie. If the specimen is thick, this can result in very low signal to background ratios and distortion of the background shape, which can lead to great difficulties in characteristic signal extraction. It is possible to use the low loss region shape to measure specimen thickness (Egerton, 1984b; Colliex and Mory, 1984). In this work it was not of interest to have accurate knowledge of the thickness. The shape of the low loss region

was, however, useful when searching for suitable areas of the specimen from which to acquire spectra. It was possible by looking at this region soon after starting the acquisition to judge whether or not the area was thin enough to provide useful data, and so to decide if it was worthwhile to continue acquisition from it.

7.2.2 Inner shell edges

As described in the introduction to this chapter, the region beyond the low loss peak consists of a background on top of which characteristic edges due to the elements in the specimen sit. The background has some contribution from the tail of the low loss peak. For all edges except that with the lowest threshold energy loss, the background is also due to the tails of the preceding edge or edges. The size of the background beneath a particular edge therefore depends strongly on the thickness of the specimen, and on what other elements are present. For these reasons the signal to background ratio for a characteristic edge can vary widely, even if the concentration of the element which gives rise to it remains constant. The signal to background ratio can be defined in a number of ways . A simple definition is the jump ratio for the characteristic edge. This ratio is unlikely to exceed 10 for any edge, even in the thinnest specimen. The EELS signal to background ratios are much smaller than those generally found in EDX spectra (cf. the peak to background ratios measured in chapter 4). EELS spectra are normally recorded over an energy range between 0keV and 2keV. This places a restriction on the range of signals which are detectable. K-shell signals can only be detected for elements with atomic number $Z < 14$. For elements of medium Z, only the L-shell signal is available, and heavier elements can only be detected by their M or higher order shell signals. It was noted in chapter 2 that the available theoretical cross sections were likely to be most accurate for K-shell ionisations. The restrictions described here suggest that EELS should be most useful for analyses involving only light elements. Analyses involving elements of widely differing Z will require comparison of signals from different shells, which may introduce considerable inaccuracies.

The inner shell signal is very much smaller than the low loss signal, since most of the incident electrons pass through the specimen unscattered, or scattered only by valence electrons. The number of counts in a channel in a characteristic edge will typically be smaller than the number of counts in the

OeV channel by a factor of ~10^6. In order to detect both regions correctly, the EELS acquisition system must have a very wide dynamic range. In most systems, the gain is changed at pre-selected energy loss during acquisition. The system used in this work, as described in chapter 3, applied two different counting techniques to the signal from the detector. Two spectra were always recorded simultaneously, in one of which the low loss region was correctly represented, the other showing the inner shell scattering correctly. The two spectra had to be merged to produce a single spectrum. The software for this process has been described in detail by Craven and Buggy (1984).

7.3 Background subtraction by extrapolation

The estimate of the background used to extract the characteristic signals has a particularly critical effect on the accuracy of quantitation in EELS because of the rapid variation in the background throughout the spectrum, and because the signal to background ratio is low. The background can only be seen on the low energy side of the edge. This necessitates some form of extrapolation in order to deduce a background shape below the edge. A functional form must be fitted to the background region before the edge. The most commonly used form is suggested by the approximate adherence of the cross section to an inverse power law, as noted in chapter 2. Accordingly, the background is usually fitted to a function of the form

$$B(E) = AE^{-r} \qquad \textbf{(7.1)}$$

where A and r are taken to be constants. r can, however, only be expected to be constant over a limited range of energy loss. This can give rise to inaccuracies if the background is extrapolated over a large range of energy loss. Other functional forms are sometimes used which take some account of the energy variation of r (eg. Bentley et al.,1982). Whatever functional form is used, problems can arise when the energy region before the edge is restricted or distorted by the close proximity of a preceding edge. These are particularly serious when the preceding edge is much larger than the edge of interest.

Software to enable the Toltec computer described in chapter 3 to perform such background fitting has been written by Dr. P.A. Crozier. The routines have been incorporated into the Toltec analysis programs, and are available as options from the standard EELS menu. The development of these routines has been described in detail by Crozier (1985). A brief summary of the procedure for using this software to fit a background for a single edge follows here. Reference should be made to figure 7.2. Most programs on the Toltec deal with energies relative to the energy loss marked by the position of a cursor, known as the "bug". The extent of the fitting region is expressed as a difference between the bug energy and the start energy of the region. E in equation 7.1 is,however, always the absolute value of the energy loss for each channel. Before entering the fitting routine, the bug is positioned by the user at an energy loss T just before the edge onset. The fitting program then asks for the extent of the energy window W_f over which the fitting is to be done. W_f extends downwards in energy loss from T, and should be chosen so that it does not include anything other than a clear background region. A weighted least squares fit is carried out on this region to determine values for the parameters A and r in equation 7.1. The curve described by these parameters is then extrapolated below the edge over a preselected energy range corresponding to the window W_e in figure 7.2, and subtracted from the experimental spectrum to leave the stripped edge. The goodness of fit over W_f is indicated by a chi-squared test. The chi-squared test will be returned to in section 7.5.

7.4 The ratio technique for EELS

In principle, the relative concentrations of any two elements in a specimen can be deduced from the counts in the corresponding characteristic edges in the EELS spectrum. In the case of two elements a and b, the ratio of the atomic concentrations N_a/N_b is given by

$$\frac{N_a}{N_b} = \frac{\sigma(\delta,\beta)_b}{\sigma(\delta,\beta)_a} \cdot \frac{I(\delta)_a}{I(\delta)_b} \qquad (7.2)$$

$I(\delta)_i$ is the number of counts in the characteristic edge within an energy loss
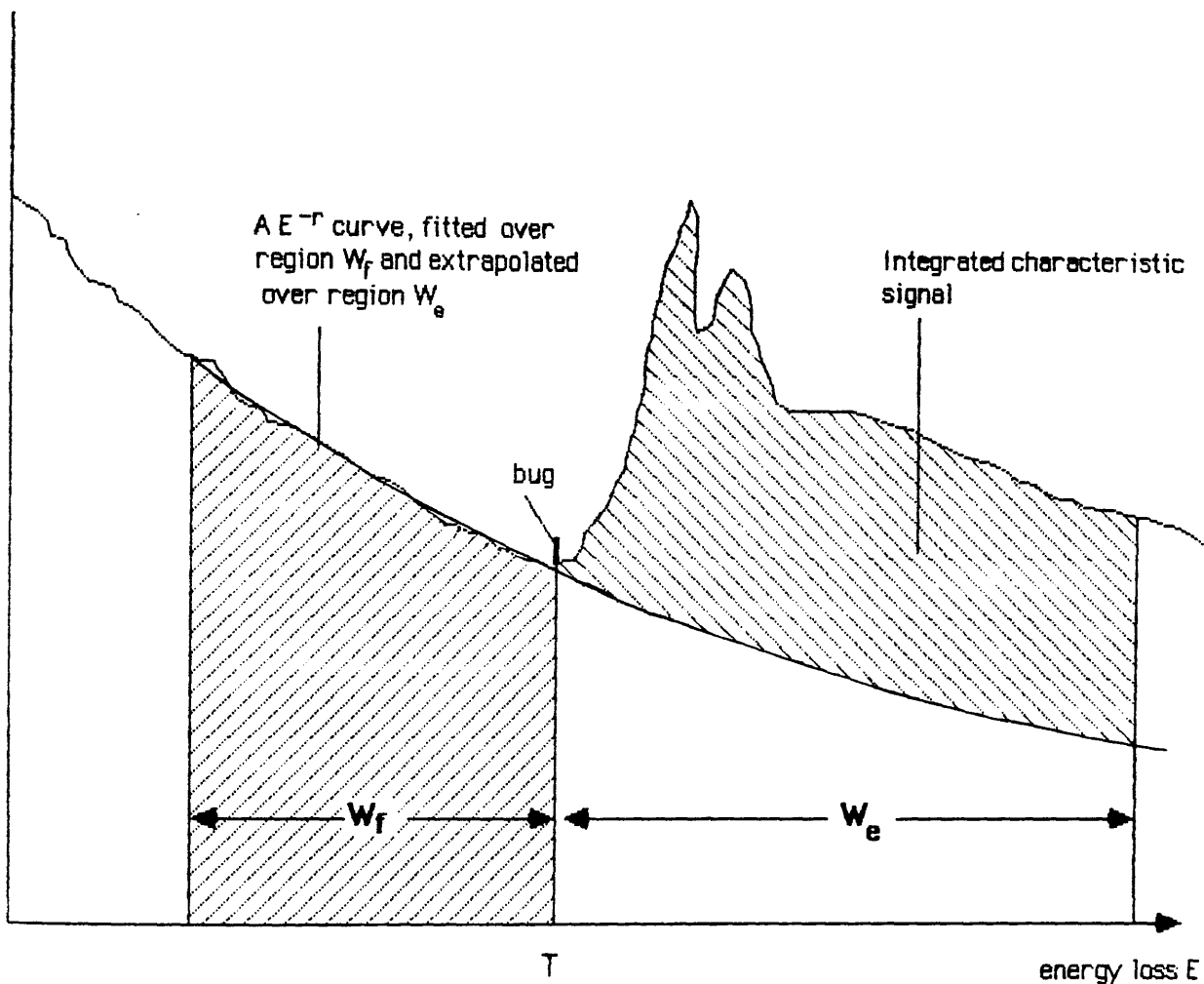
Figure 7.2 Illustration of spectral regions used for characteristic EELS signal extraction by the standard extrapolation technique.

range δ of a starting point E_i. $\sigma(\delta,\beta)_i$ is the partial cross section described in chapter 2 for scattering within an energy loss range δ, and up to a cut-off angle β corresponding to the spectrometer collection angle. In chapter 2 it was implicit that the starting point E_i for integrating the cross section would generally be the same as the ionisation energy, approximately equivalent to the edge threshold energy. This is not necessarily true here, and it will be shown that it is often desirable to introduce an offset between the edge threshold and E_i.

This procedure assumes that the variations of $I(\delta)_i$ and $\sigma(\delta,\beta)_i$ within the specified energy window are identical. For this to be true, the background subtraction must be carried out correctly. The previous section has outlined some of the inaccuracies which may arise in this process. Additionally, it was noted in chapter 2 that the available theoretical cross sections assume single scattering by isolated atoms, and so do not include the multiple scattering and solid state effects found in experimental spectra. In the next section an alternative approach to background fitting, involving the use of scaled theoretical cross sections, is described. Section 7.6 goes on to discuss theoretical edge shapes in detail.

7.5 Background fitting incorporating the use of scaled cross sections

The problems which may arise in using the usual method for background fitting have been described in section 7.2. It is apparent that a prime source of error lies in the need to extrapolate an oversimplified functional background shape over an energy range often greater than the fitting region. A way of reducing such uncertainty might be to fit a function to regions both before and after the edge onset. For the latter region, the function used should include a description of the shape of the characteristic signal. Such a technique was proposed by Steele et al.(1985). It involved fitting over pre-edge and post-edge regions using a functional form

$$f(E) = A\, E^{-r} + k\, \sigma(E) \qquad (7.3)$$

where $\sigma(E)$ is the energy differential cross section, which is zero in the pre-edge region. k is a scaling factor for the cross section, and acts as a third fitting parameter. Using this technique, the background shape is constrained to be sensible both before and after the edge onset. Note that k is proportional to the number of atoms which contribute to the characteristic edge. This fact enables equation 7.2 to be rewritten as

$$\frac{N_a}{N_b} = \frac{k_a}{k_b} \qquad (7.4)$$

where k_a and k_b are the cross section scaling factors for the edges associated with elements a and b. Because of this, the fitting program can also yield the required elemental concentrations. This led Steele to term the process a "single-stage" technique. There is some implication in this terminology that the new process is more convenient than the extrapolation technique. In practice, the removal of the need to make a separate comparison of the extracted signal with the theoretical cross section is more than offset by the extra complication and running time involved. The anticipated advantage lies in an improvement in the accuracy of the background fit, and for this reason the process is referred to in this thesis as the "constrained fitting" technique.

Software to allow this technique to be used on the Toltec computer was written by Dr. J.D. Steele, and is described in detail in his PhD thesis (Steele, 1987). A brief outline of the algorithm is given here. The energy regions and offsets which are referred to are illustrated in figure 7.3. As for the extrapolation program, the energy E is the absolute energy loss, while all fitting ranges and offsets are defined relative to the bug position. The range over which r is varied is specified by the user. For the result to be sensible, the fitted background must pass through the pre-edge region. The program steps through 11 equally spaced values of r from r_{min} to r_{max}. For each value of r, the program first of all fits the function of equation 7.3 to the selected pre-edge region, region W_1 in figure 7.3. The fitting involves the minimisation of a reduced chi-squared function of the form

The figure shows a plot with energy loss E on the horizontal axis. Labels on the curve include AE^{-r} and $AE^{-r}+k\sigma(E)$, where $\sigma(E)$ is a theoretical edge shape convolved with low-loss region. Regions marked W_1, O_c, W_2 along the horizontal axis, O_a marked vertically, "bug" pointing to a feature, and T marked below the axis.
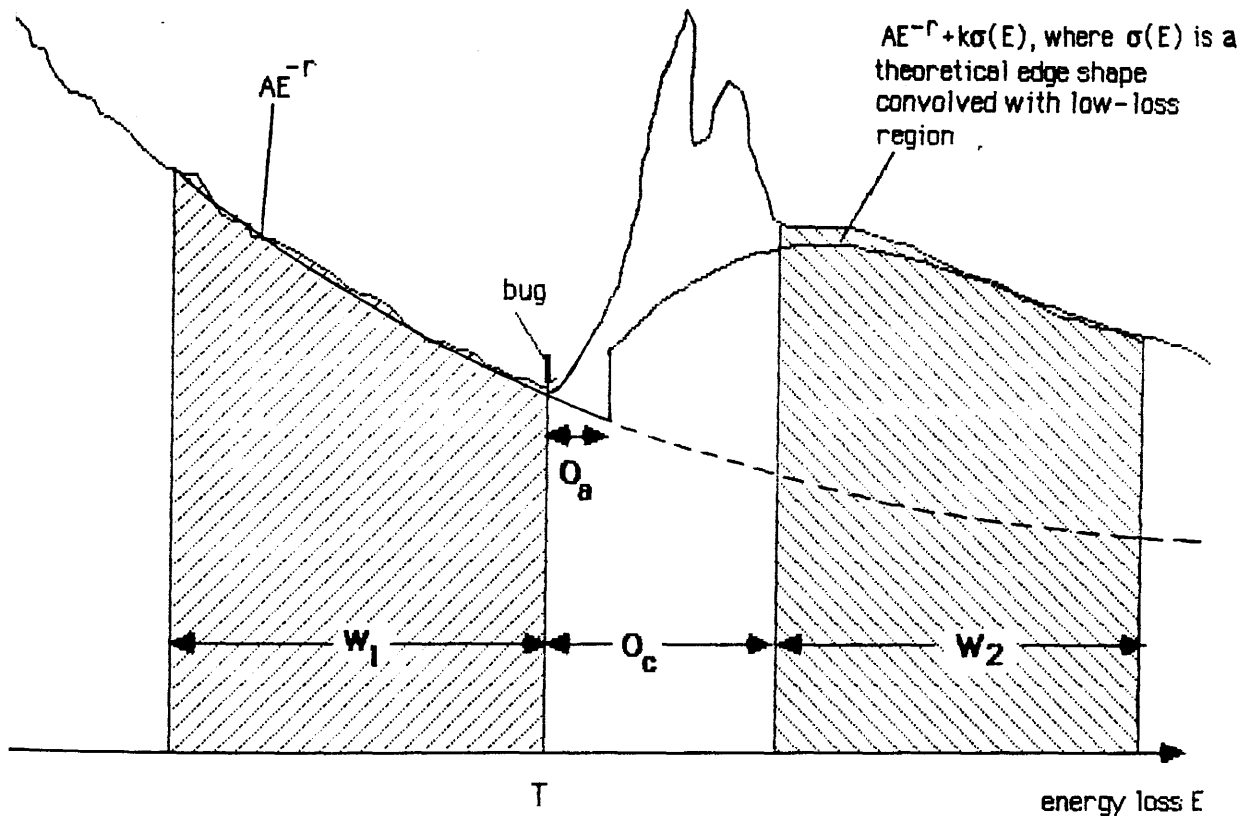
Figure 7.3 Illustration of spectral regions and offsets used for characteristic EELS signal extraction by the constrained fitting technique.

$$\chi_1^2 = \frac{1}{N_1 - 1} \sum_i \frac{(c_i(E) - A E^{-r})^2}{c_i(E)} \qquad (7.5)$$

where $c_i(E)$ is the number of counts in the ith channel of W_1. The only variable here is A. N_1 is the number of channels in the fitting region, and so $N_1 - 1$ is the number of degrees of freedom. The variance of $c_i(E)$ is assumed here to be equal to $c_i(E)$, which is the case if the noise in the spectrum follows Poisson statistics. A reduced chi-squared test should, if the shape under investigation is correctly described by the chosen functional form, yield a value for χ^2 which is close to unity. In real spectra, the background will rarely follow an AE^{-r} form exactly, so higher values of χ^2 may be expected.

Having produced an optimum A value for a given r, the program then fits over the post edge region W_2 by minimising another chi-squared function of the form

$$\chi_2^2 = \frac{1}{N_2 - 1} \sum_j \frac{(c_j(E) - (A E^{-r} + k\sigma(E))^2}{c_j(E)} \qquad (7.6)$$

$c_j(E)$ is the number of counts in the jth channel of W_2. N_2 is the number of channels in the post edge region. The data for $\sigma(E)$ must be read in from a buffered data file in which the theoretical edge shape is stored.

In this way 11 sets of values of the three fitting parameters are produced, with optimum values of A and k for each r. The program selects one of these on the basis of minimising a combined chi-squared value, given by

$$\chi^2 = \chi_1^2 + \chi_2^2 \qquad (7.7)$$

When applied to real experimental spectra, it is often the case that the values of r at which each of χ_1^2 and χ_2^2 is minimum are different. The selected fit then has a value of r in between the two. If the range of r selected is too small, then in general no minimum will be found in the variation of χ^2 with r, and a value at one or other extreme will be selected. To avoid this possibility, a wide range of r should be chosen initially. Successively smaller ranges are then chosen about the preferred values, until the increments in r are sufficiently small that the variation in χ^2 between two r values at the minimum is small, typically $\sim 10^{-3}$. Obtaining a background for a single edge can therefore often require the fitting routine to be run three or four times.

The program requires two energy offsets to be specified. The first of these is the alignment offset O_a, as shown in figure 7.3. This offset is required because of the smearing of the experimental edge offset due to the finite resolution of the spectrometer. Some of the counts in the edge are redistributed below the real edge threshold energy. The bug must be positioned before the edge onset, and so cannot be at the true threshold energy. When the theoretical edge is read in from the data file, it is positioned in the memory starting at the bug energy. In order that it is correctly aligned with the experimental edge, it must then be shifted upwards in energy loss. The extent of this shift is specified by O_a. O_a may also have to include a correction for a difference between the edge threshold and the vacuum level, which is the energy of the start of the continuum. The theoretical cross sections used account only for transitions to the continuum. This point is discussed in the next section.

Previous discussion, in chapter 2, suggested that the experimental edge shape will not be predicted accurately close to the edge onset. This point will be illustrated in the next section. For this reason it is generally undesirable to fit over a post-edge region which starts at the edge onset. The convergence offset O_c specifies the difference in energy between the bug position and the start of the fitting region W_2.

The extrapolation technique has only two values which can be varied by the user, namely the end point and extent of the pre-edge fitting region. Constrained

fitting introduces three additional variables in the form of the starting point and extent of the post-edge fitting region, and the alignment offset. The value of the last of these can only vary sensibly over a range of a few eV. It will be shown in chapter 5 that such variations generally have negligible effect on the resulting values of k. The optimum fitting regions will clearly vary according to the background regions available in the spectrum. Steele suggested varying the pre and post-edge fitting regions and using the standard deviation in the mean of the k values as an estimate of the uncertainty in the background fitting. Trebbia (1987) suggests that if different estimates of the extracted signal in an EELS edge are to be combined in this way, then they should be weighted according to their variances. He details a method by which the variance of an individual estimate can be calculated for the extrapolation technique by the variation of the χ^2 value with A and r. In principle such a method could be extended to the three parameter case of the constrained fitting technique. For this work, however, the simpler approach of Steele was considered to be adequate. The use of the constrained fitting technique will be discussed further in chapter 8.

7.6 Theoretical cross sections for constrained fitting

In order to compare theoretical and experimental edge shapes it was necessary to be able to read the former on the Toltec computer memory and display. Cross sections calculated according to the hydrogenic model were produced using versions of Egerton's SIGMAKR and SIGMALR programs. These programs have been modified by Dr. P.A. Crozier to run on the Toltec, and produce output in the form of buffered data files which can be read either into other Fortran programs, such as the constrained fitting program, or into the spectrum display. The versions of SIGMAKR and SIGMALR are called SGK4 and SGL4 respectively. Hartree-Slater cross sections produced by program INTG, as described in chapter 2, are in the form of sets of values for the energy-differential cross section evaluated at intervals of 5eV or 10eV. Fortran interpolation routines INT5 and INT10 were written for the IBM mainframe. These were used in the respective cases to produce sets of values corresponding to intervals of 1eV, which could be typed into buffered data files on the Toltec. These files could be used in the same way as those produced by the hydrogenic programs.

Figures 7.4 (a), (b) and (c) show theoretical L-edge shapes for Cr, Mn and Fe respectively. In each case edges calculated according to the hydrogenic model (denoted H) and the Hartree-Slater model (denoted HS) are shown. The edges have been further processed to take account of spectrometer resolution, multiple scattering and spin-orbit splitting. These corrections will be discussed in detail later in this section. These elements all feature in the material under investigation in the first part of chapter 5. The hydrogenic cross sections follow a similar shape for all three elements, the edge onset having a rounded shape in each case. The Hartree-Slater model predicts a similar shape for Mn and Fe, but predicts a sharp edge onset for Cr. The hydrogenic model uses the same analytic form for each element, and so it is not surprising that no differences in shape between them are predicted. The variation of the edge shapes between these elements will be compared with corresponding experimental data in chapter 8. Figure 7.4 also illustrates the difference in the magnitude of the cross sections predicted by the two models. These differences can be expected to be reflected in the k values yielded by the constrained fitting program when using theoretical edge shapes calculated using the two models.

Figures 7.5 and 7.6 illustrate the differences between theoretical and experimental edge shapes. Figure 7.5 shows a stripped B K-edge, while figure 7.5(a),(b) and (c) show stripped L-edges from Cr, Mn and Fe. The subtraction and theoretical edge scaling required to produce these figures was carried out using the constrained fitting procedure. H cross sections were used in both cases, and the appropriate scaled theoretical edges are also shown in figure 7.5. The post-edge fitting ranges are indicated. Experimental details for these spectra are given in chapter 8. As anticipated in the previous section, in both cases the greatest discrepancy between experiment and theory occurs close to the edge onset. The overall discrepancy is due to several sources. The fine structure close to the onset of the B K-edge is due to ELNES, as described in chapter 2, which is not predicted by the theory. The Fe L-edge features two "white lines" which occur due to transitions to bound states above the Fermi level. The theoretical cross sections only account for transitions to the continuum, and so again do not predict the structure in the experimental edge.

If it is assumed that all states above the Fermi level are unoccupied, then the edge threshold energy should be the same as the Fermi energy. In a solid, the Fermi level is not identical to the vacuum level. Since continuum cross sections
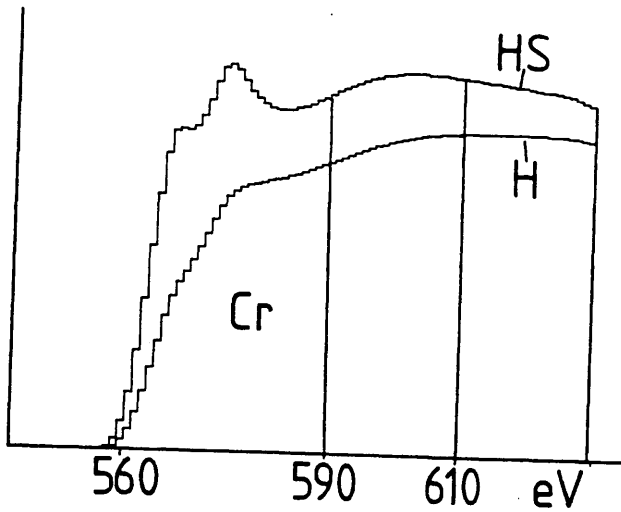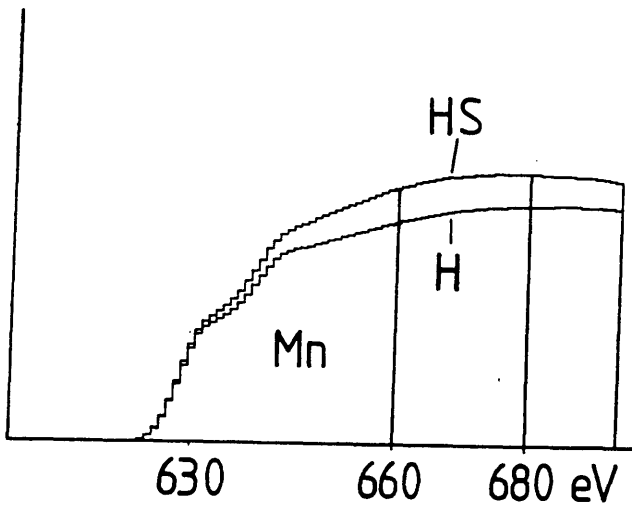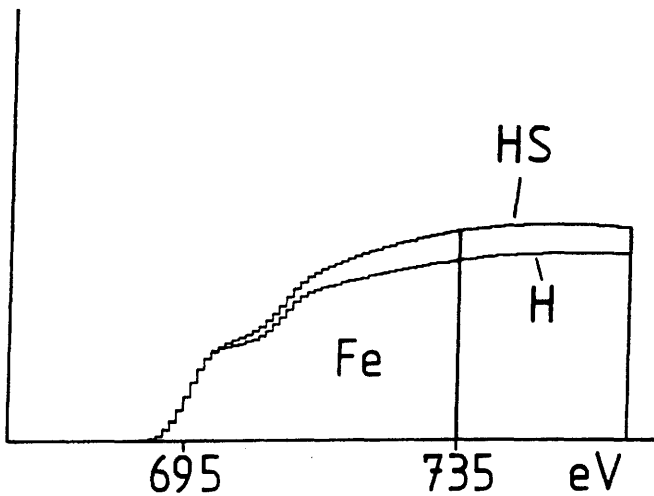
Figure 7.4 Theoretical L-edge shapes for Cr, Mn and Fe, calculated according to the hydrogenic (H) and Hartree-Slater (HS) models. The part of each edge typically fitted to an experimental spectrum is indicated. These were the same for either model except in the case of Fe, where the region indicated is that used for fitting using the HS shape.
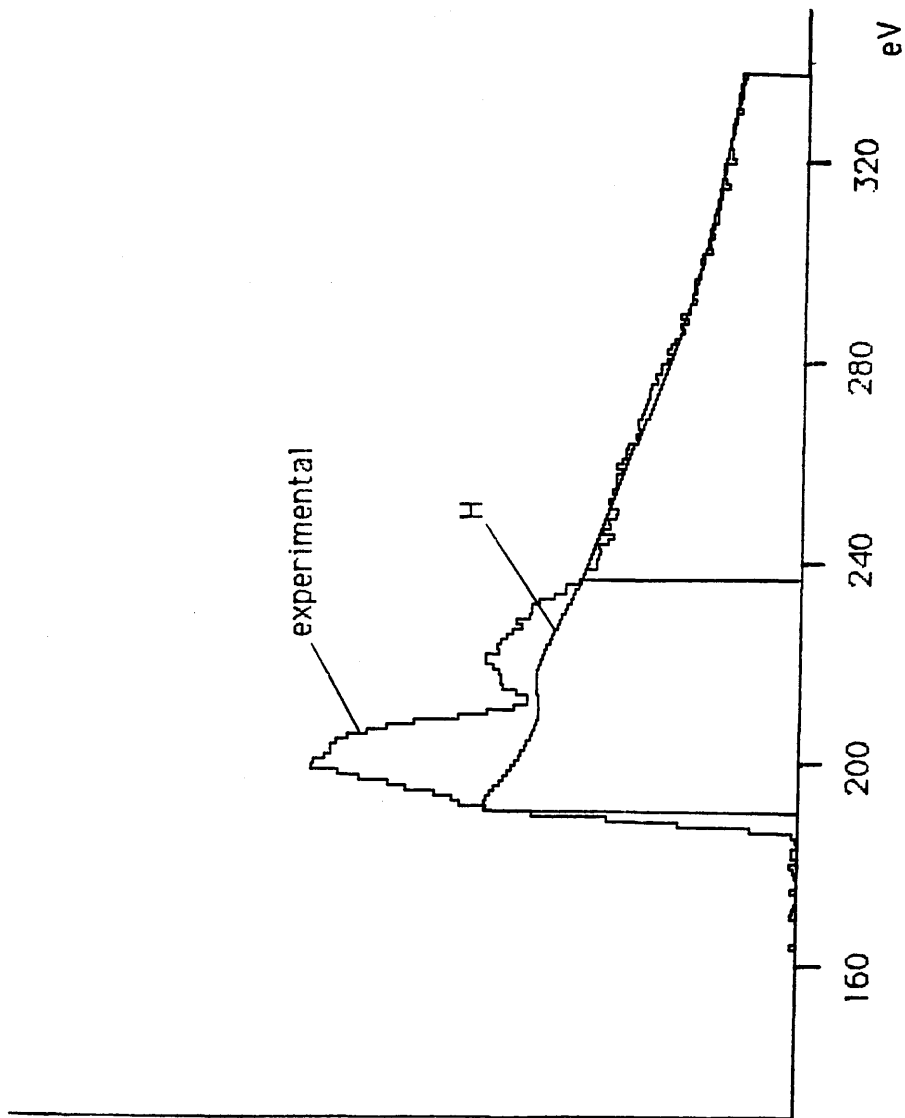
Figure 7.5 Experimental B K edge from a CrB$_2$ spectrum, extracted using constrained fitting, together with the appropriate scaled B K cross section.
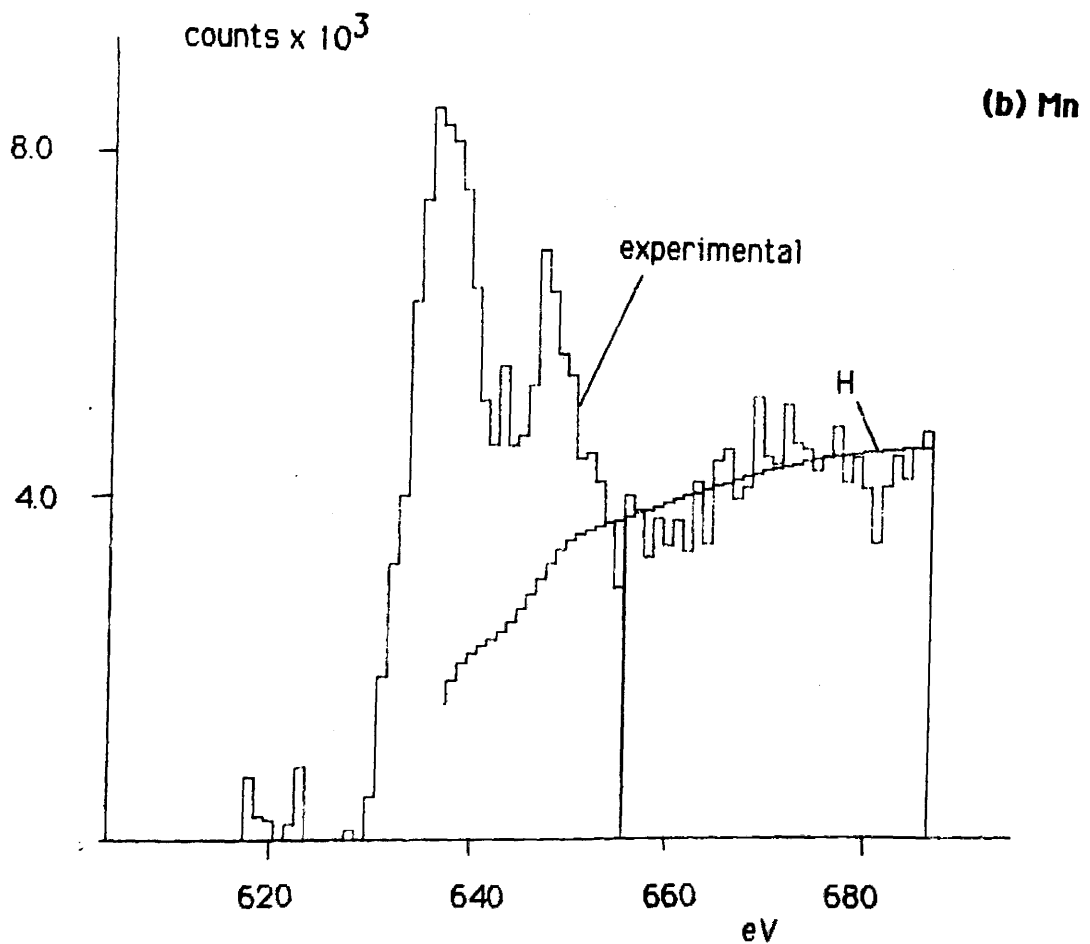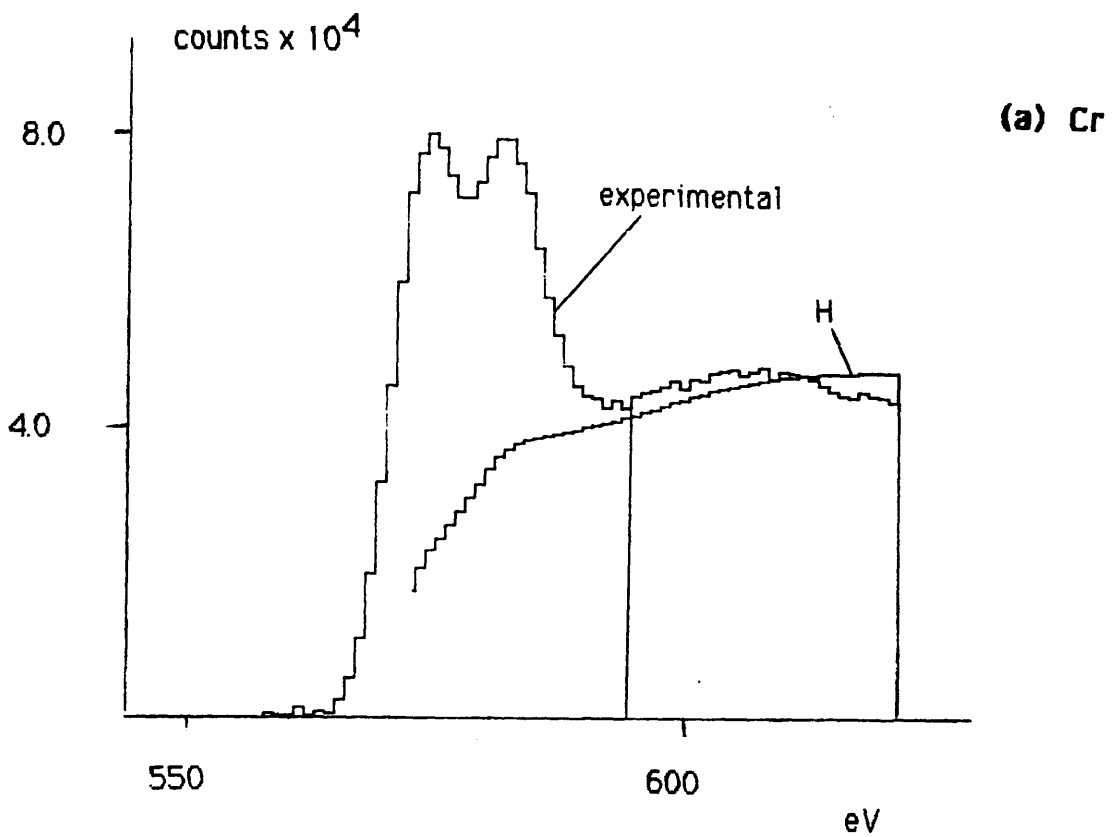
Figure 7.6   Experimental edge shapes from carbide spectra, extracted using constrained fitting with H cross sections. The scaled theoretical H edge shapes are also shown.

counts x 10^4

(c) Fe

experimental

H

650   700   750   800   850

eV
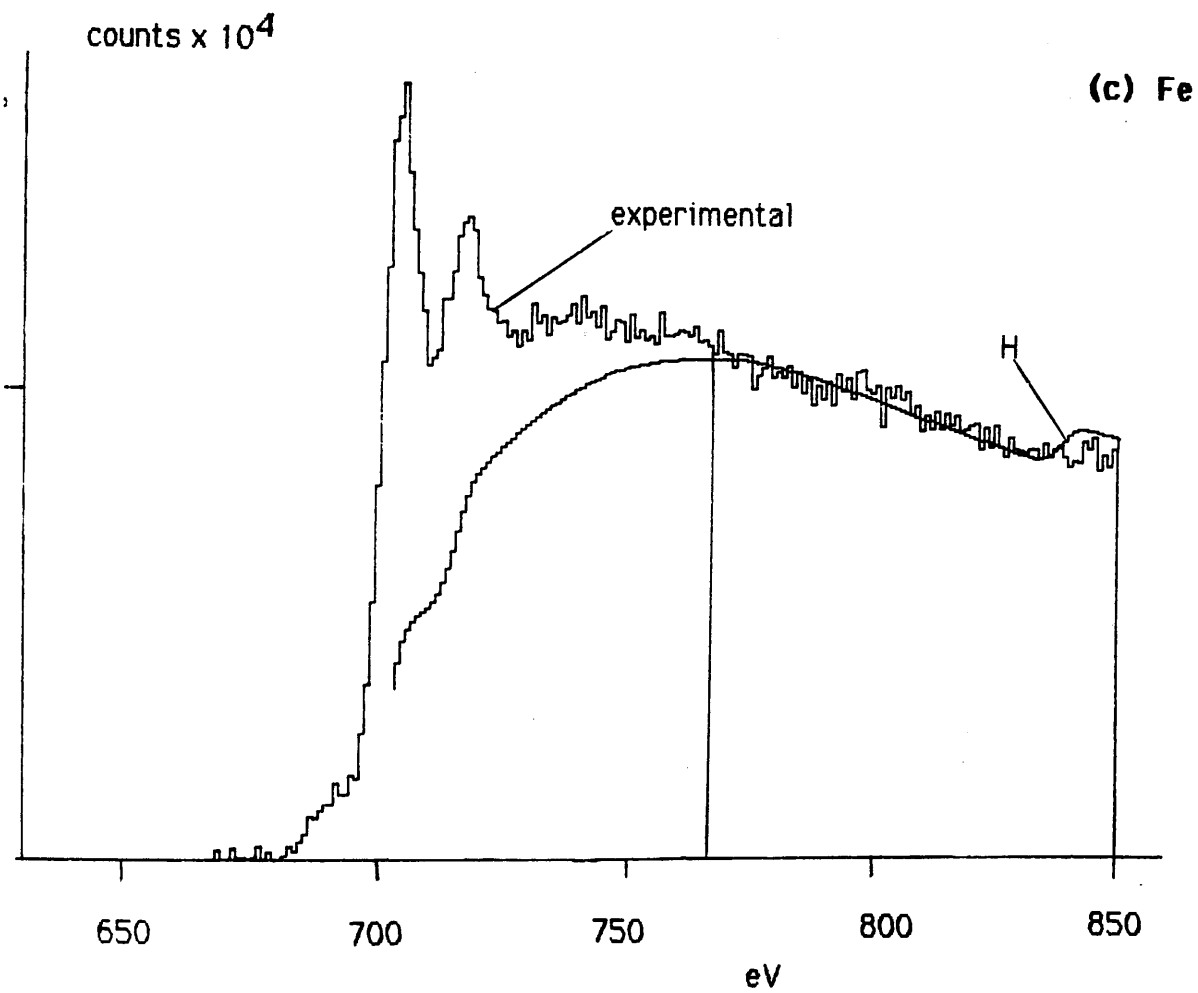
Figure 7.6 *(continued)*

are used here, the above consideration implies that the point in the spectrum with which the start of the theoretical edge is aligned should differ from the experimental edge threshold by the same amount that the vacuum level differs from the Fermi level. Estimates based on white line width (Leapman et al., 1982) and on the work function suggest that this energy difference should be ~5eV for transition metals.

The L-shell is split into three sub-shells. The 2s level is known as sub-shell L_1, and contains two electrons. The 2p state has two levels with values of the total angular momentum quantum number j=1/2 and 3/2. These are known as sub-shells L_2 and L_3 respectively. L2 contains two electrons, while L_3 contains four. The two 2p levels are non-degenerate because of spin-orbit coupling. This is due to the interaction of the electron spin magnetic dipole moment with the magnetic field of the nucleus (Eisberg and Resnick, 1974). As a result, an L-edge may appear in the EELS spectrum as three separate edges if the resolution is better than the spin-orbit splitting, so that the L_2 and L_3 edges are separated. The L_1 edge is well separated in energy from these, and appears at an energy loss typically ~100eV greater for transition metals. In the Fe edge in figure 7.6(c), the effect of spin orbit splitting can be clearly seen by the separation of the white lines due to transitions from the two 2p levels. The magnitude of the splitting appears to be ~13eV. These effects are characteristic of the materials studied.

The experimental spectrum is further affected by factors which depend on the specimen thickness and the experimental conditions. Electrons which are scattered by inner shell electrons can also be scattered by valence electrons. This multiple scattering causes a redistribution of the counts in the edge. The experimental edge is also "smeared" out due to the finite energy resolution of the spectrometer. The spectra from which the edges shown were taken were recorded using rather large values of the spectrometer collection angle, and so the resolution is particularly poor. If chromatic aberrations are ignored, the effects of multiple scattering and finite resolution may be described approximately as a convolution of the edge with the low loss region of the spectrum.

Many workers remove the effects of multiple scattering and finite resolution from experimental spectra by deconvolution procedures (eg. Egerton, 1984b).

It was decided here to take the simpler inverse approach of convolving the theoretical edge shape in each case with the low loss region of the spectrum with which it was to be compared. By such a convolution, combined with a correction for spin-orbit splitting, "theoretical" edge shapes could be produced which would as far as was possible be directly comparable with each individual spectrum. A Fortran program, called CC, was written by the author to run on the Toltec to read in theoretical edge data from buffered files, carry out the required processing, and write the corrected data back to a buffered file. A listing of the code is given in appendix B. The program first of all gives the user the option of applying a spin orbit correction, and asks for the magnitude of the splitting to be input. As noted earlier, the L_3 subshell has twice as many electrons as L_2. Following Ahn and Rez (1985), it was assumed that the L_3 and L_2 cross sections per electron were identical, and that the L_2 signal could be added to the L_3 signal after being shifted by the appropriate amount. The program calculates the L_2 and L_3 cross sections as 1/3 and 2/3 respectively of the 2p level cross section originally predicted. The resultant edge is formed from this L_3 cross section, starting from the threshold energy, and the L_2 cross section added on with the specified energy shift. If applied directly to the cross sections predicted by the hydrogenic programs, this process would also cause an unwanted split in the L_1 edge. To prevent this, a version of SGL4 has to be run which calculated the cross section for the 2p level only. The output from the two versions of SGL4 is subtracted to leave the 2s level cross section. The splitting described above is carried out on the 2p level cross section, and the 2s added on afterwards at the appropriate energy to give the complete cross section. The cross sections predicted by the Hartree-Slater model were calculated for the 2p level only, and so a slightly different version of CC, called CCHS, was created which did not carry out this last procedure. The energy range available in the Hartree-Slater data was not generally large enough to reach the L_1 edge energy.

Once the complete edge, corrected for spin orbit splitting, has been created, it is then convolved with the appropriate low loss region. For this procedure to be valid, the energy resolution for the edge of interest should be the same as that for the low loss region. With the spectrometer used in this work, this was not generally the case. The procedure adopted was to record spectra in pairs, one with the spectrometer focussed on the zero loss peak, the other with the focussing done in the inner shell scattering region. This procedure is discussed in more detail in the descriptions of experimental considerations in the next

chapter. The cross sections which were to be compared with focussed edges were convolved with the corresponding focussed low loss regions. This convolution redistributes some of the counts in the edge below the the threshold energy, and so these are lost when the corrected cross section is written to a data file. This was not generally important since the theoretical and experimental edges were not compared numerically close to the edge onset. For the purposes of displaying the edges on the monitors or plots, an option was included in the program to allow the corrected edge to be written to the file with a 25eV shift upwards in energy. When read into the Toltec display, the edge could then be aligned with the experimental edge using spectrum manipulation routines. Figures 7.7(a), (b) and (c) show a theoretical Fe L-edge, calculated using the hydrogenic model, before correction and successively after spin-orbit splitting correction and convolution with the appropriate low loss region. The scale on the horizontal axis shows the energy loss relative to the threshold energy loss. The magnitude of the spin-orbit splitting was deduced from the separation of the white lines in experimental Fe edges .

7.7 Summary of the procedure for constrained fitting

Proper use of the constrained fitting technique assumes that for each experimental edge there has been an equivalent low loss region recorded with the same energy resolution. The following steps should then be followed:-

1. The low loss region is read into a buffered data file. The file should then be edited so that any zero entries at the start of the file are removed. The number of entries before the maximum value in the zero loss peak should be noted, as the convolution program requires this information.

2. An uncorrected theoretical edge shape is generated, of either H or HS form. The number of channels of information calculated should exceed the number of channels from the experimental edge onset to the end of the largest post-edge fitting region to be used.

3. The appropriate convolution program is run, CC for H edge shapes, CCHS for HS edge shapes. For the case of K-edges, the 'convolution only' option should be selected; for L-edges, 'convolution and spin-orbit splitting' should be
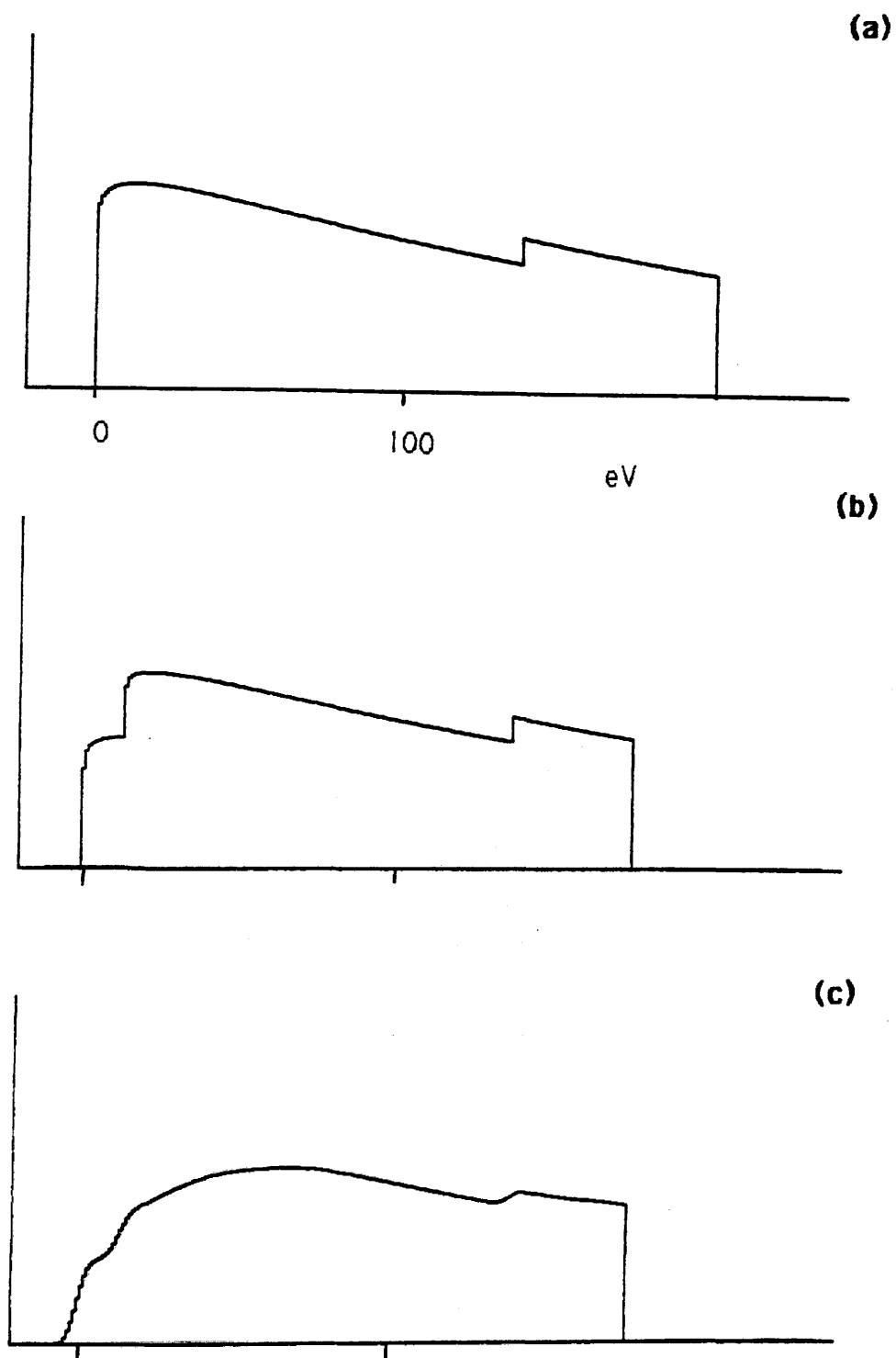
Figure 7.7 A theoretical hydrogenic Fe L-edge (a) as calculated by SGL4, (b) after correction for spin-orbit splitting, and (c) after correction for spin-orbit splitting and convolution with the low-loss region of a carbide spectrum.

selected. The magnitude of the spin-orbit splitting should be input on request, as should the position of the zero loss peak in the low loss region file. For writing to disk, the 'unshifted' option should be chosen.

4. The standard Toltec analysis program INIT is run, and the spectrum read into the memory. The bug should be positioned just before the start of the edge to be analysed, and the constrained fitting program chosen from the user routine menu. Energy ranges, minimum and maximum values of r and offsets should be input on request. The ranges over which A and k are varied should also be input. Criteria for choosing these are detailed by Steele (1987). The program should be re-run for finer ranges of r until the variation observed in χ^2 is sufficiently small. The selected values of A, r, χ^2 and k are noted. The spectrum display can then be instructed to show either the fitted background or the stripped experimental edge. In the latter case, the theoretical edge can also be read into the display for visual comparison.

The entire process is repeated for each edge of interest in the spectrum, and the k values substituted in equation 7.4 to give results for elemental concentrations.

Chapter 8

EELS analyses using constrained background fitting

8.1 Introduction

This chapter describes the application of the EELS constrained background fitting technique, detailed in the previous chapter, to spectra from two types of specimen. In order to assess the reliability of the technique, a data set which had previously been analysed using the conventional extrapolation technique was re-analysed. These data, recorded from second phase carbides in ferritic steel, were provided by P.A. Crozier, and had been analysed by him using the extrapolation method (Crozier, 1985). This analysis presents a particularly severe test of a fitting procedure because of the close proximity of the edges which occur. The edges of interest were L-edges from Cr, Mn and Fe. The relative proportions of these elements varied widely between spectra. Crozier investigated the correlation between concentration ratios obtained using simultaneously recorded EDX and EELS data. In order for the new technique to be considered useful, the correlation between the EDX results and those from the re-analysed EELS data should be as good as or better than before. The first part of the chapter describes this analysis. Experimental details have been described by Crozier et al.(1983, 1984): these are summarised briefly here. The choice of fitting ranges possible in these spectra is then discussed, and the stability of the fits when these regions are varied is investigated. The values of the concentration ratios deduced using H and HS cross sections, as described in chapters 2 and 7, are then compared with the EELS and EDX results of Crozier.

It was of interest in this work to assess the accuracies of both EELS and EDX for specimens containing elements of both low and medium atomic number. EELS analyses were carried out on specimens of TiB_2 and CrB_2. It was hoped that the analyses would yield the stoichiometric values for the elemental concentrations in these cases. The section starts by describing the preparation of the specimens and the spectrum acquisition conditions. These spectra allow a much wider choice of fitting regions than those analysed before. The selection of optimum regions is discussed, and the deduced concentrations detailed. The results

indicate that these specimens were not in fact stoichometric.

8.2 The analysis of second phase carbides.

8.2.1 Experimental details

Crozier et al.(1983, 1984) recorded simultaneous EELS and EDX spectra from second phase carbide particles prepared as an extraction replica from a ferritic steel. The data were used to investigate the correlation between the elemental concentrations deduced using each technique. The EELS spectra show K-edges from C and O, and L-edges from Cr, Mn and Fe. A Be window x-ray detector was used, and so no signals from C or O appeared in the EDX spectra. These spectra contained K-signals from the three transition metals detected in the EELS spectra. The comparison of the two techniques was based on deduced Cr/Fe and Mn/Fe concentration ratios. The K signals from Cr, Mn and Fe all lie away from the extremes of the energy range detected in EDX. The discussion in chapter 1 suggests that these signals present no particular problems for EDX analysis, and so a high degree of accuracy can be expected in the results. Crozier et al. estimated the accuracy of the measured Cr/Fe and Mn/Fe concentration ratios to be better than ~4%. The accuracy of the EELS analysis was expected to be much poorer. Discrepancies between the two sets of results were therefore assumed to be due to errors in the EELS analysis. The correlation between the EELS and EDX results was used to assess the accuracy of the EELS analysis. The EELS data have been re-analysed here using the constrained background fitting technique described in chapter 4. For full details of the acquisition of the EELS and EDX spectra, the reader's attention is directed to the reference. The factors which are relevant to the analysis of the EELS spectra are reiterated here.

The EELS spectra were recorded using the VG HB5 STEM at Glasgow University, and its associated EELS acquisition system, as described in chapter 3. A 100μm VOA was used, defining a probe convergence angle of 25mrad. PSL1 was used in conjunction with a 250μm CA to define a collection angle β of 27mrad. Crozier (1985) calculated that the error which would arise due to the assumption of parallel illumination would be ~1%, and concluded that β need not be corrected to take account of the convergent probe. Acquisition of each spectrum was started immediately after flashing the tip, and continued to 300sec. It was considered desirable to optimise the resolution in the spectrum in the vicinity

of the L-edges, while also having a focussed low loss region in order to permit thickness measurements to be made. For these reasons, pairs of spectra were recorded from each particle of interest, with the excitation of PSL1 set to focus respectively on the zero loss peak and on the Cr edge energy. This procedure is the same as that suggested in section 7.6 to allow convolution of theoretical cross sections with the low loss region, although the motivation in this case was not the same. The adoption of this procedure by Crozier et al. makes this data set particularly suitable for re-analysis using the constrained fitting technique. Crozier et al. estimated that none of the particles was more than 400A thick, and so the effects of multiple scattering were not expected to be serious.

Figure 8.1 shows the region containing the edges of interest in one of the spectra. The three L-edges can be seen, as can the O K-edge. This spectrum is typical in that the Cr and Fe edges are much larger than the Mn edge and the O edge. There was a wide variation between the particles in the proportions of Cr and Mn relative to Fe. There was also a considerable variation in the thickness of the particles, giving a resulting variation in the signal to background ratios. The Mn edge is a small signal on top of, and rather close to, the much larger Cr edge, and so represents an example of the case where the most serious inaccuracies can be found when using an extrapolated background. Crozier found that accurate quantitation of the Mn signal presented particular difficulties.

8.2.2 Selection of offsets and fitting ranges

The approach taken to the analysis of the set of spectra , nine in number, was to decide upon one set of values for the various offsets and fitting ranges required for the constrained fitting technique, and to use these values as far as possible for each spectrum. One spectrum was chosen for preliminary investigation. The EDX results indicated that the spectrum chosen should yield Cr/Fe and Mn/Fe concentration ratios away from the extreme values within the data set. The signal to background ratio was neither untypically high nor untypically low. The range of interest in this spectrum is shown in figure 8.2. Energy windows corresponding to the fitting regions are marked in the figure. Regions corresponding to different edges are indicated by different kinds of hatching. The high energy end of the pre-edge region in each case is the bug position used for each edge. The difference between the low energy end of the post-edge region and the bug position is the convergence offset O_c in each case.
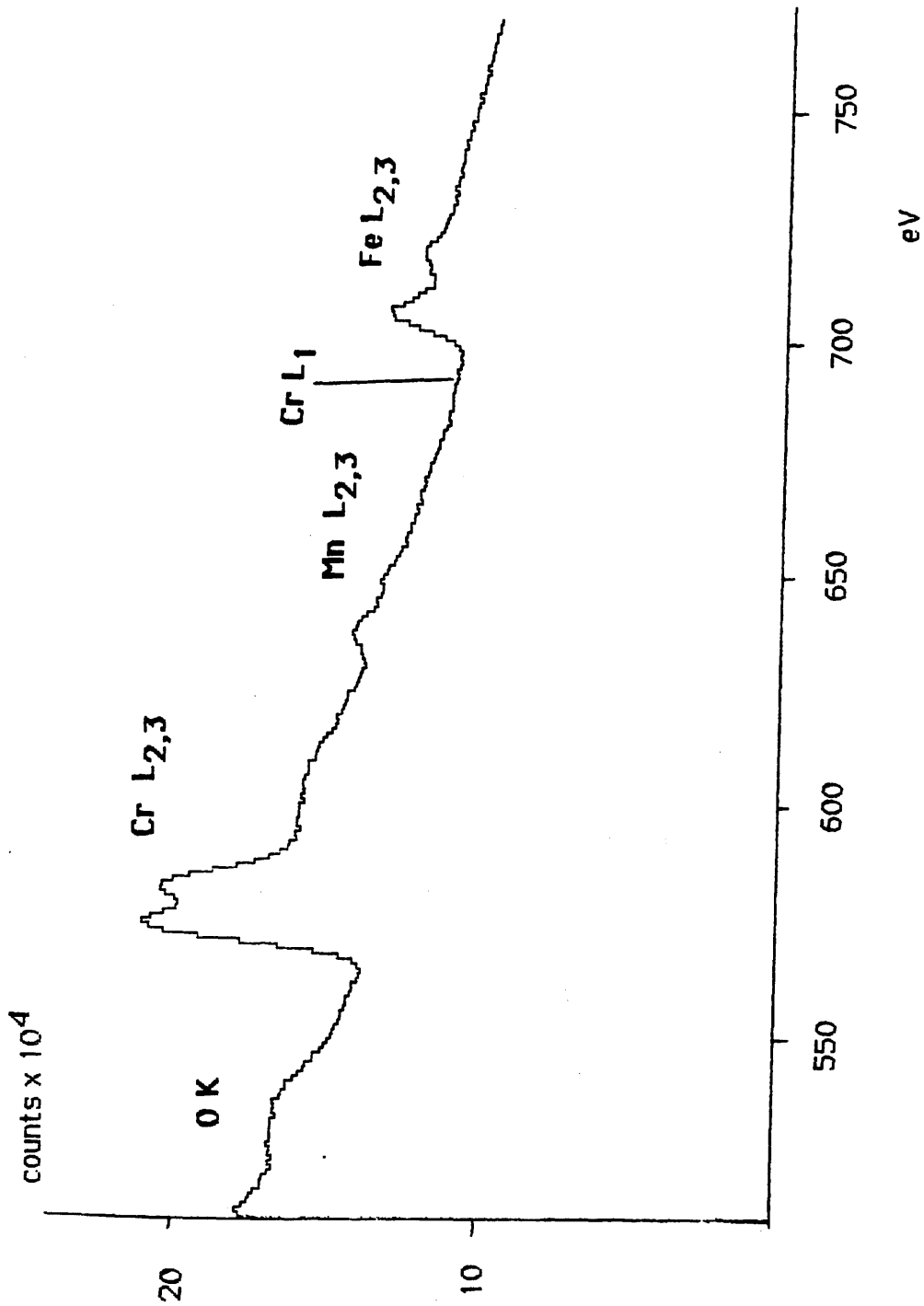
Figure 8.1 Part of a typical carbide spectrum, showing the region containing the transition metal L-edges.
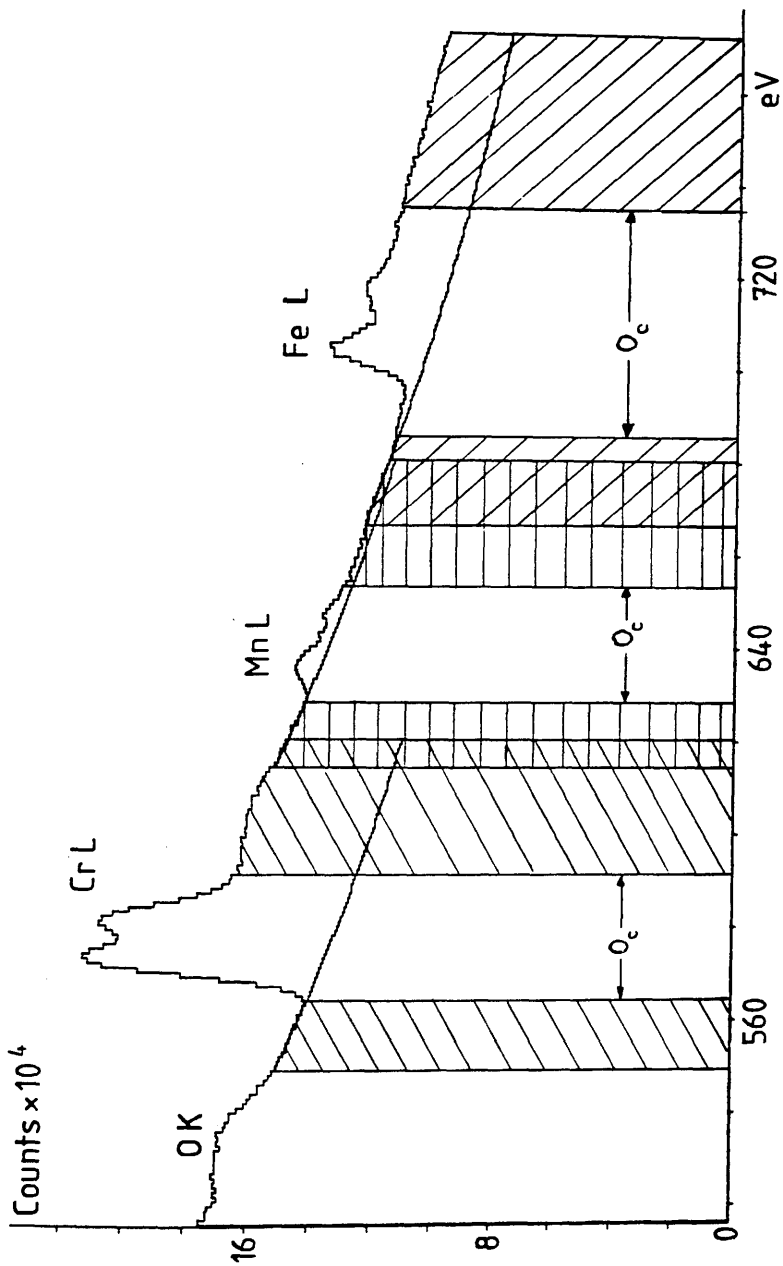
Figure 8.2   The same spectrum region as shown in figure 8.1, with the fitting regions indicated for each edge.

Figure 8.2 illustrates the limitations placed on the fitting regions by the close proximity of the edges in these spectra. The pre-edge region for the Cr edge is restricted by the structure in the O K edge, while the corresponding post-edge region must fall in the range between the Cr edge white lines and the Mn edge onset. The Mn pre-edge region is similarly restricted by the structure in the Cr edge, while the upper limit of the post-edge region is set by the small Cr L_1 edge. This Cr L_1 edge presents a problem when selecting a pre-edge region for the Fe edge. If the bug is positioned at the Fe edge onset, and the region is chosen to extend downwards no further than the Cr L_1 edge onset, then the usable energy range is only ~10-15eV. Extending the range further down would result in a step being present in the fitting region, with unpredictable results. The solution adopted was to place the bug at the Cr L_1 edge onset and extend the pre-edge fitting region as far down as was allowed by the presence of the Mn edge. The difference between this bug position and the Fe edge onset was included in the alignment offset and the convergence offset. It was considered desirable to avoid as much as possible the use of very small post-edge regions, since it was recognised that the algorithm might become less well conditioned in such cases (Steele, 1985, private communication). The regions chosen for each spectra were those which maximised the energy ranges used, while avoiding obvious structure in the edges which could have a detrimental effect on the fitting. The resultant regions varied slightly from spectrum to spectrum. Typical values are shown in table 8.1. It can be seen from the table that in the case of the Fe edge different post-edge regions were chosen depending on whether H or HS theoretical edges were used. The size of this region is not restricted by any structure in the spectra, and so can be large if H cross sections are used. It is restricted if HS cross sections are used by the limited energy range available in the theoretical edges, as was mentioned in chapter 7. There is a putative advantage for the purposes of comparison in using the same region in both cases. Such an approach would in effect be placing an artificial restriction in the case of fitting with H cross sections, and it was considered preferable to use the most advantageous conditions allowed in both cases.

The effect of varying the alignment offset for each edge was investigated. The discussion in chapter 7 suggests that the value of this offset should be given by the half width of the zero loss peak plus some additonal value to account for any difference between the apparent edge onset and the threshold energy of the theoretical continuum cross section. For this spectrum the offsets should

	Cr	Mn	Fe
pre-edge region (eV)	15	15	15
post-edge range (eV)	55	50	165(H), 80(HS)
O_c(eV)	30	25	85(H), 55(HS)

Table 8.1 Fitting regions for each edge in the carbide spectra. All energies are relative to the bug energy.

therefore be >4eV. Table 8.2 shows the selected values of r, A, k and χ^2 for each of the three edges when the alignment offset is varied over a wide range, from 4eV upwards. Note that the post-edge region of the experimental spectrum over which the fitting takes place remains the same. Varying O_a merely changes the alignment of the theoretical edge with the spectrum. In the case of the Fe edge, the bug was positioned 15eV before the edge onset because of the presence of the Cr L$_1$ edge, and so 15eV had to be added to the alignment offset, so that the values varied from 19eV upwards. These results show little change in the fitting parameters while the offset is varied over the first 5eV. The solution changes more rapidly as the offset is further increased. It appears that the fits are stable   while the offsets are small, and become less stable for larger offsets. The trend in the variation of χ^2 shows a decrease in value with increasing offset up to ~20eV. The discussion in chapter 7 gives no reason to expect the difference between the fermi level and the vacuum   level for the start of the continuum to be any more than ~5eV. This contradicts the conclusions which might be drawn by considering the χ^2 values alone. It is possible that the χ^2 test is not as well behaved as would be desired for this type of spectrum, particularly with the rather small fitting regions used here. A χ^2 test may not be very sensitive when fitting a theoretical shape, which does not vary much over a short range, to an experimental edge whose variation within such a range is similarly small, but not necessarily identical. It was considered that, while minimisation of χ^2 for a fixed set of regions and offsets should give the best fit for that situation, it may be unwise to place much reliance on the precise values of χ^2 when comparing fits achieved using different conditions. Taking these results into consideration, it was decided that there would be little disadvantage in considering the theoretical cross sections to start at the edge threshold. The alignment offset was hereafter always assigned the value of 4eV.

The extracted experimental edges and associated scaled theoretical edges for the case of H cross sections for this spectrum were shown in figure 7.6 The equivalent edges for the case of HS cross sections are shown in figure 8.3 (a), (b) and (c). The corresponding fitted backgrounds were shown with the spectrum in figure 8.2. In all cases the backgrounds and extracted edge shapes look sensible. The correspondence between experimental and theoretical edge shapes is good over energy ranges equivalent to the post-edge fitting regions. As expected, there are considerable discrepancies close to the edge onsets whichever theoretical model is used.

	O_a(eV)	r	A	k	χ^2
Cr					
	4	2.1	0.755×10^{11}	52.10	4.454
	9	2.2	0.143×10^{12}	52.97	4.150
	14	2.4	0.506×10^{12}	55.54	3.731
	19	2.6	0.179×10^{13}	58.50	3.139
	24	2.9	0.119×10^{14}	64.79	23.29
Mn					
	4	2.5	0.126×10^{13}	3.336	1.237
	9	2.5	0.126×10^{13}	3.318	1.233
	14	2.6	0.239×10^{13}	5.030	1.121
	19	2.7	0.456×10^{13}	7.048	1.020
	24	2.5	0.126×10^{13}	3.910	1.374
Fe					
	19(=0)	2.9	0.173×10^{14}	54.37	2.076
	24(=5)	3.0	0.332×10^{14}	56.77	2.016
	29(=10)	3.05	0.459×10^{14}	57.83	2.332

Table 8.2 Variation of fitted parameters with alignment offset O_a. All energies are relative to the bug energy. For the Fe edge, the equivalent offset relative to the edge threshold is also shown.
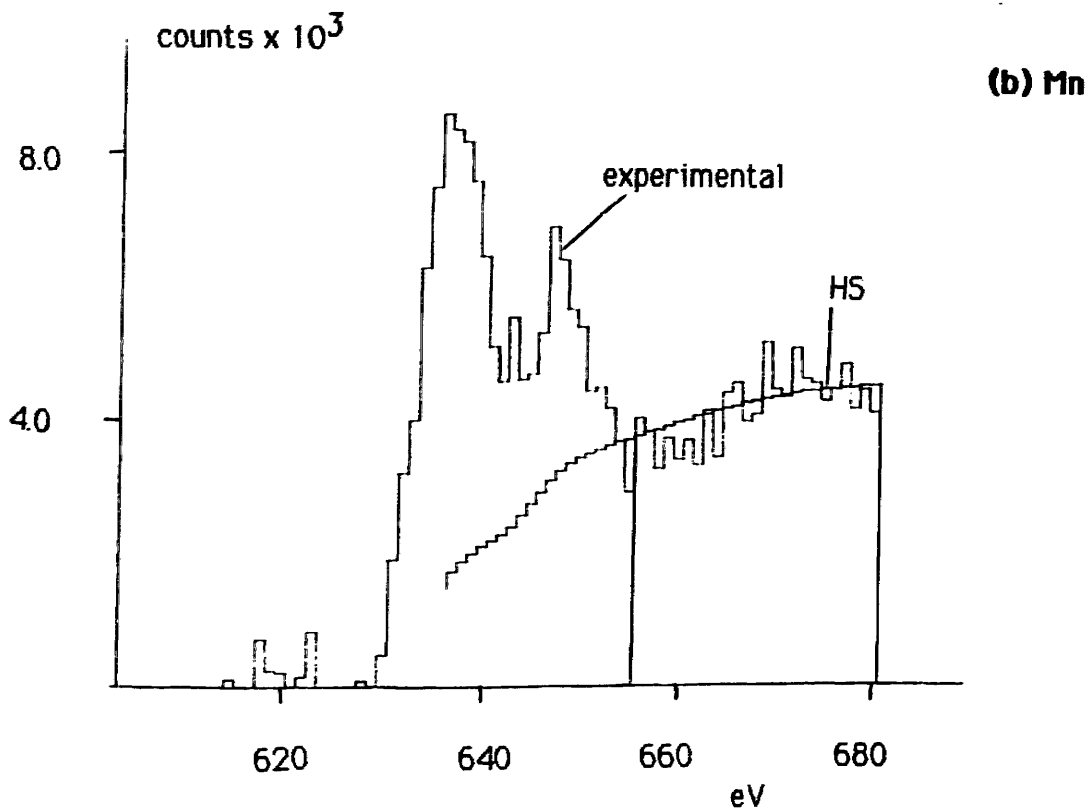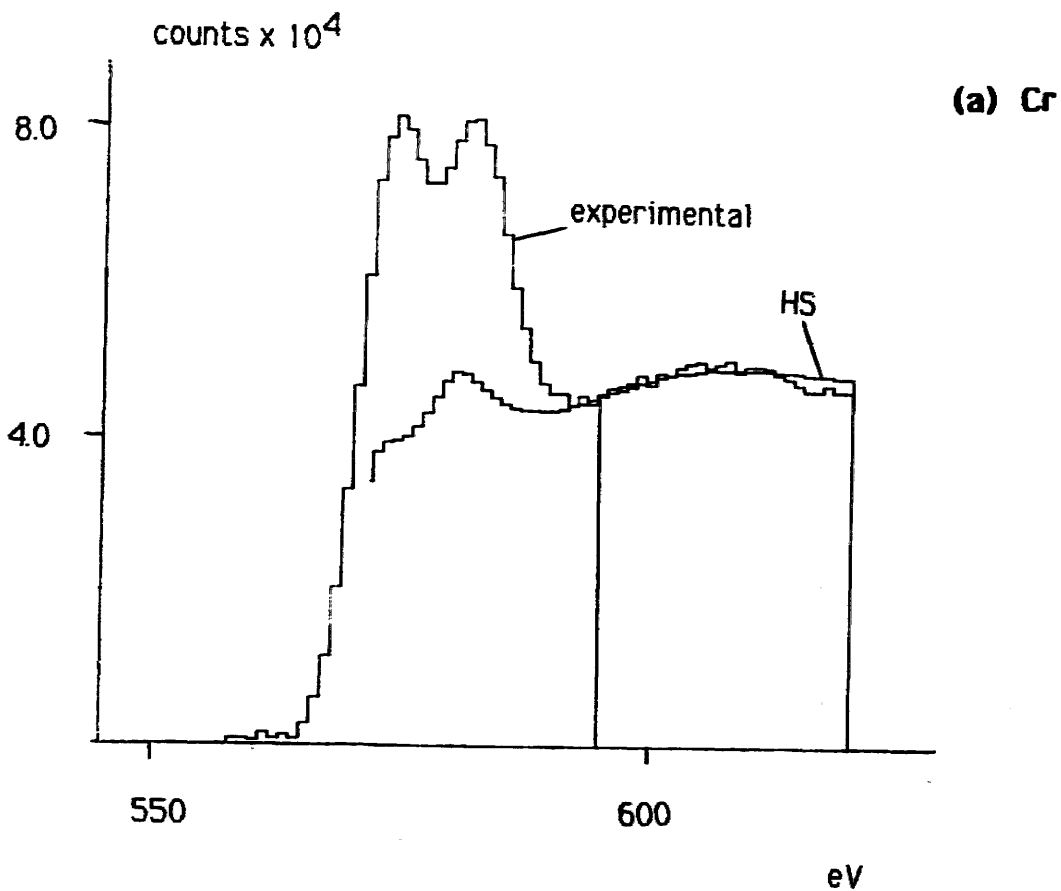
Figure 8.3   Experimental edge shapes from carbide spectra, extracted using HS cross sections. The scaled theoretical HS edge shapes are also shown.
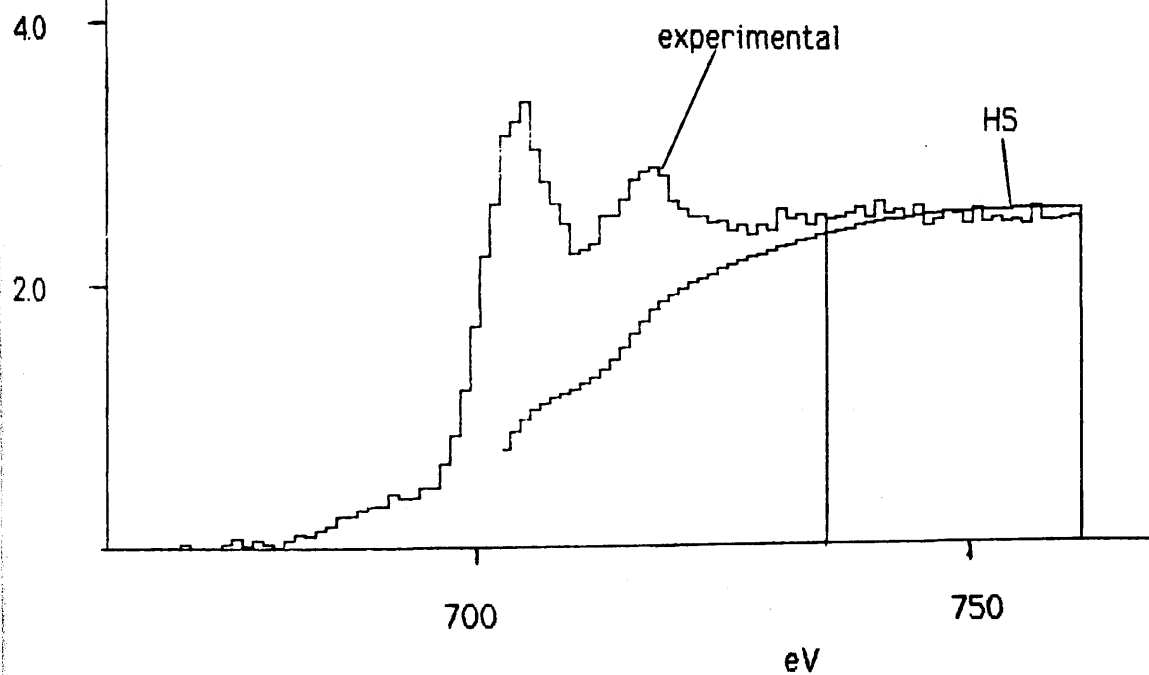
Figure 8.3 *(continued)*

The size of the characteristic signal extracted using the extrapolation technique can vary widely for different pre-edge fitting regions. It was of interest to investigate whether constrained fitting offered any improvement in stability in this respect. Such an investigation was possible to a limited extent with this data. Two spectra were analysed using extrapolation and constrained fitting techniques. The pre-edge fitting region for each edge was extended from 15eV to 30eV in 5eV steps. For constrained fitting, H cross sections were used, and the post-edge regions were held constant. The counts in the extracted edges in windows equivalent to the constrained fitting post-edge regions were noted. Table 8.3 shows the mean number of such counts for each edge as the pre-edge region was varied, together with the associated standard deviations. The variations obtained using either technique were <10% for the Cr and Fe signals, but were considerably greater for the smaller Mn signal. In the latter case the spread obtained using constrained fitting was considerably smaller than that for extrapolation. For the Fe edges in both spectra, it appears that extrapolation yields the more stable solution. The only feature of the Fe edge which might introduce greater instability than is found in the case of the Cr edge is the inclusion in the post-edge fit of the Cr L_1 signal, which may distort the Fe edge shape. The Cr L_1 signal would not have affected the fitting for the extrapolation technique, since the bug was positioned before its onset. The Cr L_1 counts would, of course, be included in the characteristic Fe signal extracted using either technique.

This evidence suggests that, for small signals, constrained fitting may offer an improvement in the stability of the fit over extrapolation when the pre-edge region is varied. These data were not considered suitable for the investigation of the stability of the fit when the post-edge region is varied. Discussion of this factor is included in the analysis which forms the latter part of this chapter.

It is clear from table 8.3 that the two fitting techniques yield significantly different values for the characteristic counts in these edges. It is expected, therefore, that the concentration ratios deduced accordingly will also differ. Such discrepancies will be reflected in differences in the correlation with the EDX results of the EELS results of Crozier et al, and those obtained in this work.

8.2.3 Correlation between EELS and EDX results

All nine spectra were analysed using constrained background fitting. Each

spectrum was analysed using H and HS cross sections. The correlation between the results of each of these analyses and the corresponding EDX results can be illustrated by means of a correlation plot, in which the EELS result for, say, the Cr/Fe concentration ratio in from each spectrum is plotted against the corresponding EDX result. Correlation plots of the Cr/Fe ratio for these data obtained using H and HS cross sections are shown in figure 8.4 (a) and (b) respectively. The line of ideal correlation, which has a gradient of 1 and passes through the origin, is marked in each case. Crozier et al. showed such plots for the Cr/Fe and Mn/Fe ratios. Linear regression on the points in each plot yielded values for the gradient and intercept in each case. These are listed in table 8.4. The Mn/Fe plots for this analysis are shown in figure 8.5 (a) and (b). The gradients and intercepts for figures 8.4 and 8.5 are also shown in the first two lines of table 8.4

The form of the correlation plot is subject to systematic errors, which can be due to an error in the cross section ratio or to errors in the signal extraction. In practice there will be a combination of both of these situations. The effects of systematic errors have been discussed by Crozier (1985). Variation in the latter type of error between spectra leads to a spread in the results. It appears from these figures that the correlation achieved here for Cr/Fe is rather worse than that obtained by Crozier et al. For Mn/Fe, there is a large spread in the results, and so it is difficult to assess the overall correlation. It is important when making these comparisons to note the different approaches taken to the extraction of the Fe signal by Crozier et al. and in this work. As described in the previous section, the approach taken here leads to the inclusion of part of the Cr L_1 signal in the Fe counts. This will cause the Fe signal to be overestimated by an amount which depends on the size of the Cr signal. This effect will cause the Cr/Fe ratio to be underestimated to an extent which increases as ratio itself increases. Such a systematic error would be expected to cause the correlation plot to curve downwards from the ideal line. This would result in a low value for the gradient, but would not significantly affect the intercept. The results found generally agree with these expectations. The Mn concentration is not directly related to the Cr concentration, and so the inclusion of the Cr L_1 counts in the Fe signal will cause the Mn/Fe ratio to be overestimated by an amount which does not depend on that ratio. The result should be to increase the spread in these values about the line of correlation, while reducing the gradient. Again there is no contradiction between the anticipated effect and the results found.
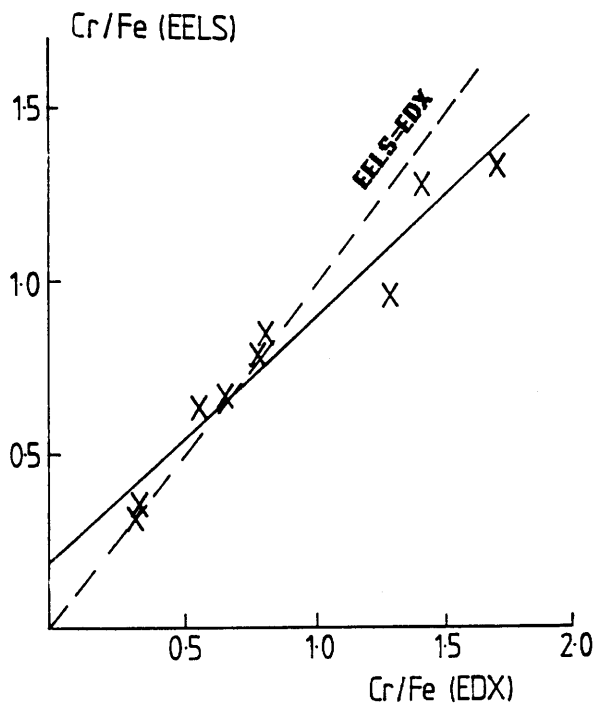
Figure 8.4 Correlation plots of Cr/Fe (EELS) vs. Cr/Fe (EDX)
(a) using H cross sections
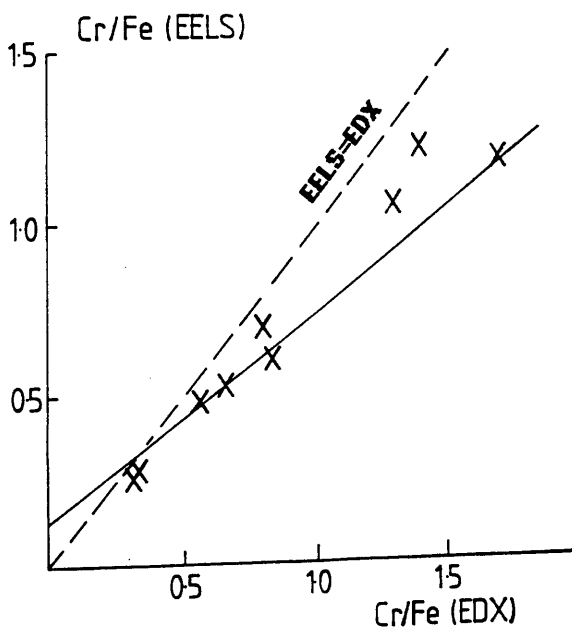
(b) using HS cross sections
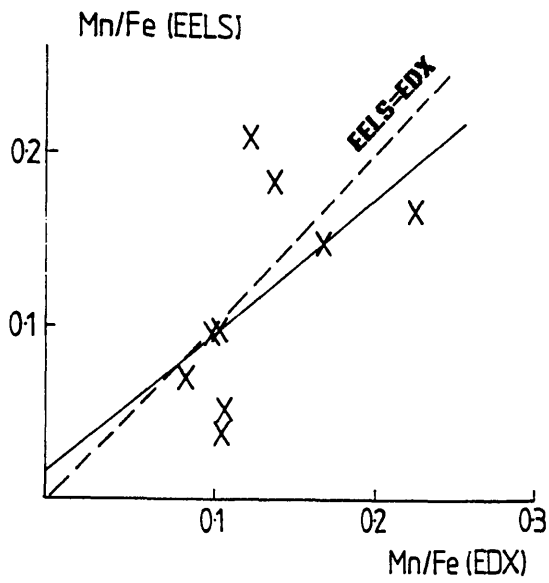
Figure 8.5 Correlation plots of Mn/Fe (EELS) vs. Mn/Fe (EDX)
(a) using H cross sections
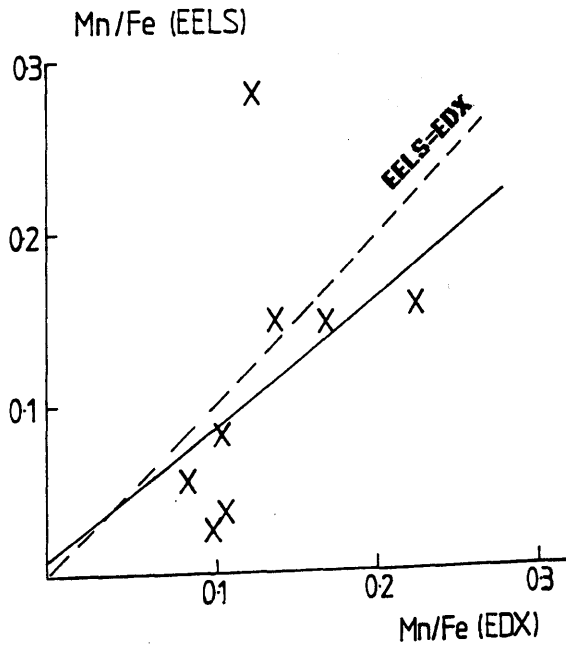
(b) using HS cross sections

	Cr/Fe	Mn/Fe	Mn/Cr
H			
gradient	0.71±0.07	0.81±0.42	1.29±0.25
intercept	0.19±0.07	0.015±0.06	-0.06±0.05
H5			
gradient	0.62±0.07	0.76±0.65	1.27±0.30
intercept	0.12±0.07	0.01±0.09	-0.05±0.05
H with $Cr L_1 corr^n$.			
gradient	1.00±0.09	1.34±0.50	-
intercept	0.11±0.09	-0.02±0.07	-
H5 with $Cr L_1 corr^n$.			
gradient	1.00±0.07	1.23±0.79	-
intercept	-0.03±0.07	-0.08±0.11	-
Crozier et al. (H5)			
gradient	0.97±0.025	0.52±0.09	-
intercept	0.007±0.02	0.051±0.015	-

Table 8.4 Gradients and intercepts of EELS vs. EDX correlation plots.

Crozier et al. used a 40eV pre-edge region in front of the Fe edge. This region included that part of the Cr L_1 signal which appears before the Fe edge. This approach would prevent the inclusion of the Cr L_1 signal in the extracted Fe counts, but it is not clear what the effect might be on the fitted background.

In order to improve the correlation for the results of this work, a correction to the Fe k value to remove the unwanted Cr contribution was necessary. The correct number of Fe counts nFe is given by

$$n\,Fe = n'Fe - n\,Cr\,p/q \qquad \textbf{(8.1)}$$

where n'Fe is the uncorrected number of Fe counts. p/q is the ratio of the Cr L_1 partial cross section integrated over the Fe post-edge fitting region to the Cr L_2+L_3 partial cross section integrated over the Cr post-edge region. Noting that

$$n_X = k_X\,\sigma_X \qquad \textbf{(8.2)}$$

where k_X and σ_X are the k value and partial cross section appropriate for each edge, gives

$$k_{Fe} = k'_{Fe} - k_{Cr}\,f \qquad \textbf{(8.3)}$$

where the dash has the same meaning as before, and f is given by

$$f = \frac{\sigma_{Cr}}{\sigma_{Fe}} \cdot \frac{p}{q} \qquad \textbf{(8.4)}$$

In order to apply this correction, a value for p/q is required. In the case of H cross sections, this ratio can be easily found using SIGMALR. For the regions typically used in this case, the value of f was calculated to be 0.179. As stated

in chapter 7, the HS cross sections used here do not include the contribution from the 2s level, and so p/q cannot be obtained. In this case the value of p/q was calculated using SIGMALR, but substituting the regions which were used in the extraction of the signals using HS cross sections. The value of f which resulted was 0.188. The Cr/Fe and Mn/Fe concentration ratios were re-calculated using the corrected values of kFe. The resultant correlation plots are shown in figure 8.6 (a) and (b) (Cr/Fe) and figure 8.7 (a) and (b) (Mn/Fe). The gradients and intercepts calculated for these plots are shown in the last two lines of table 8.4. The results show a marked improvement in correlation for Cr/Fe, whichever cross section model is used. The gradients in both cases are very close to 1, and the intercepts are small, particularly in the case of HS cross sections. The correlation is therefore nearly ideal. The error on the gradient suggests, however, that the spread of the results is greater than that found by Crozier et al. This may be accounted for by the inclusion in those works of the large white line signal in the integration window for the characteristic signal. This could have had the effect of making the number of counts less sensitive to errors in the background fitting than if similar regions had been used to those adopted here.

The correction to the Fe signal has the effect of considerably increasing the gradient of both Mn/Fe plots. The spread is reduced slightly , but it is still large in both cases. In view of the uncertainty in the Fe signal caused by the need to subtract the Cr L_1 signal, it was considered that there might be some advantage in considering the Mn signal in terms of the Mn/Cr ratio rather than the Mn/Fe ratio. The correlation plots for the Mn/Cr ratio are shown in figure 8.8 (a) and (b). The corresponding gradients and intercepts are listed in the final column of table 8.4. The correlation in these cases is similar to that for Mn/Fe, but the spread in the results is considerably smaller. Taking the errors into account, the Mn results show reasonably good correlation between EELS and EDX.

The range of systematic errors to which all these plots may be susceptible prevents the interpretation of these results as firm vindication of the constrained fitting technique. It should be recognised that such errors may remain, but occur in such a way that they cancel each other out. The excellent correlation obtained between EELS and EDX results for Cr/Fe in particular may be spurious. Nevertheless, comparison of the results of extrapolation and constrained fitting for these spectra suggests that the new technique has yielded a useful improvement in the accuracy of these EELS results.
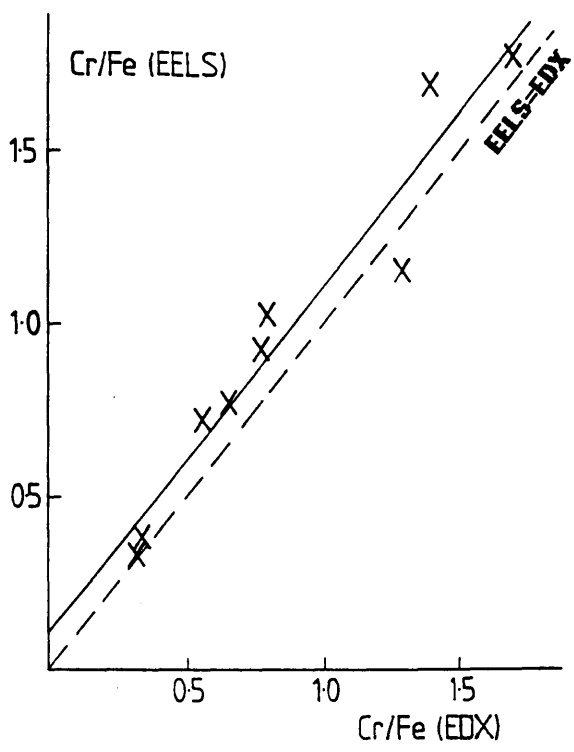
Figure 8.6 Correlation plots of Cr/Fe (EELS) vs. Cr/Fe (EDX). The EELS results incorporate a correction for the Cr L_1 counts in the Fe post-edge region.

(a) using H cross sections
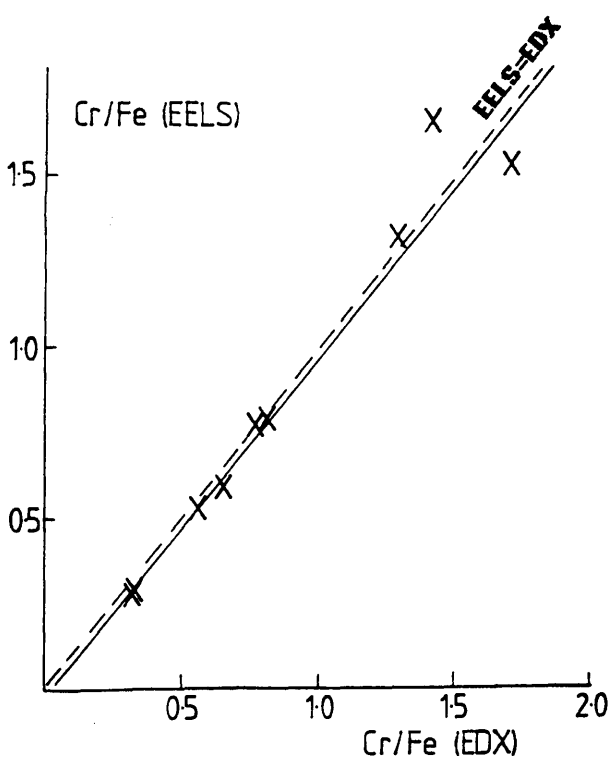
(b) using HS cross sections
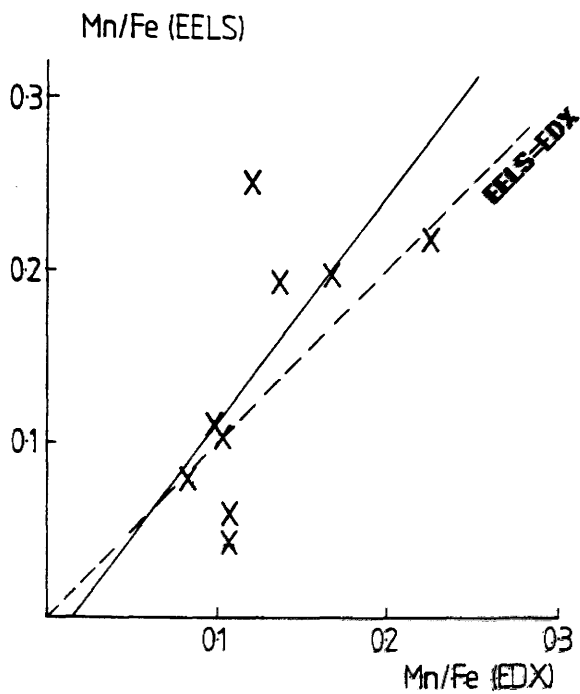
Figure 8.7 Correlation plots of Mn/Fe (EELS) vs. Mn/Fe (EDX). The EELS
results incorporate a correction for the Cr L_1 counts in
the Fe post-edge region.
(a) using H cross sections
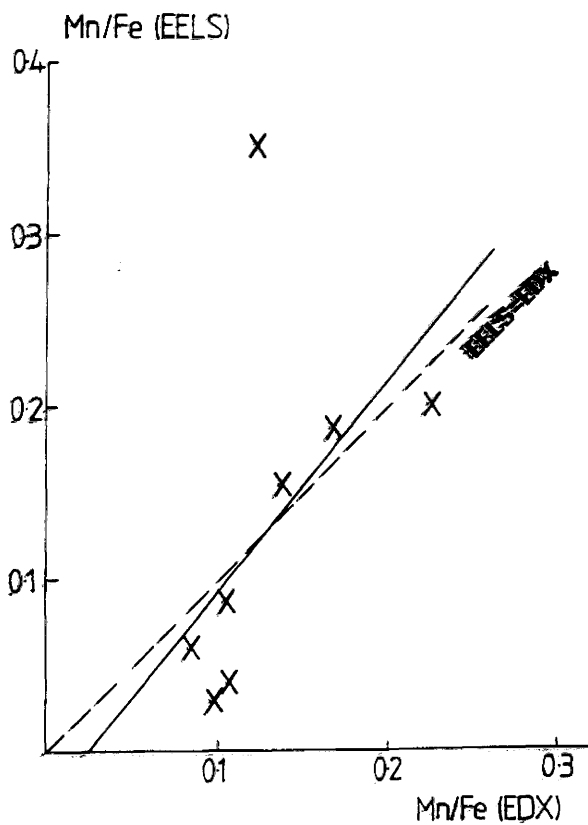
(b) using HS cross sections
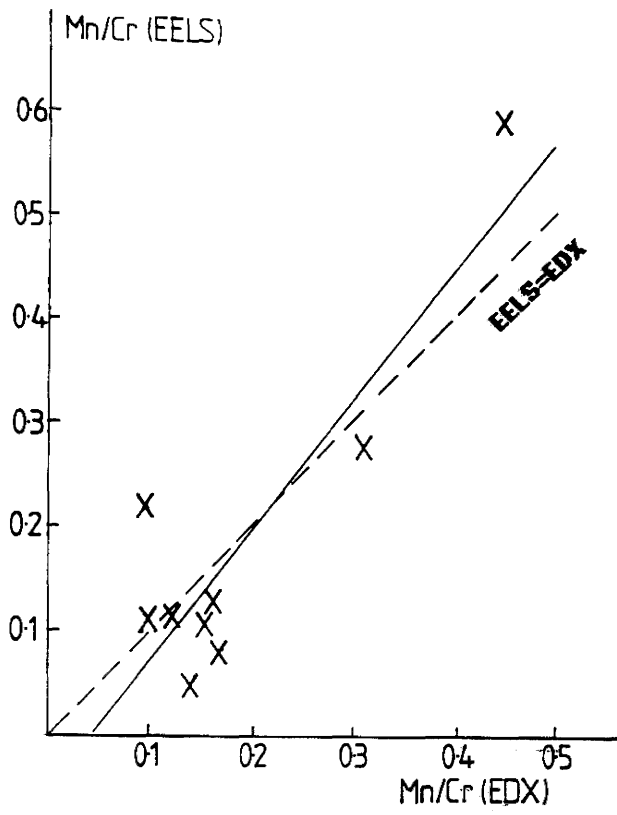
Figure 8.8 Correlation plots of Mn/Cr (EELS) vs.Mn/Cr (EDX).
(a) using H cross sections
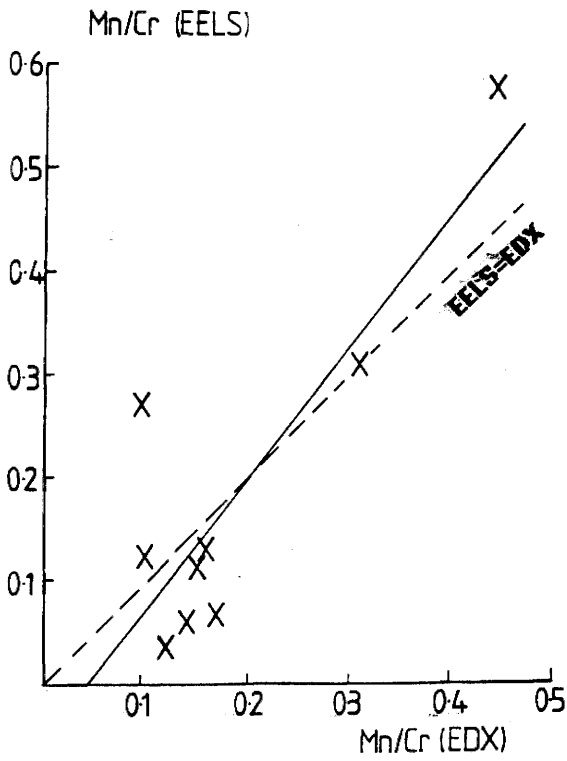
(b) using HS cross sections

8.3 The analysis of TiB_2 and CrB_2

The analysis of TiB_2 and CrB_2 presents problems of a different nature from those discussed in the previous section. The edges here are not close to each other, and so the available fitting regions are not restricted in the same way as before. Considerable uncertainty is caused, however, by the need to consider signals from different shells. Within the energy range available in EELS, only the K-shell signal from B is detected, while for Ti and Cr, only the L-shell signals are detected. Theoretical partial cross sections for the K-shell are considered to be reasonably accurate(Egerton,1979). It is not certain, however, to what degree of accuracy the L-shell cross sections are predicted. The previous section considered L-shell cross sections only, and it is possible that any errors may, to some extent, have cancelled each other out. Considerable errors may arise, however, in the ratios of K-shell/ L-shell cross sections. These would result in systematic errors in the deduced B/Ti and B/Cr concentration ratios. Hydrogenic cross sections only were used, since no Hartree-Slater cross sections were available for B.

8.3.1 Specimen preparation

It was necessary to produce specimens which contained very thin areas of the materials of interest. These specimens were prepared from TiB_2 and CrB_2 powders. The powder was hand ground using a mortar and pestle, to give small, irregularly shaped particles. This method was considered unlikely to produce particles which would be sufficiently thin throughout to allow EELS analysis. It was hoped that there would be suitable thin areas at the edges of some of the particles. A suspension was formed of each powder in pure ethanol. The specimen supports were holey carbon films mounted on Cu grids. Commercially available films on fine mesh grids were used. Holey films were used so that some particles would be positioned partly over holes. The carbon would therefore not contribute to the specimen thickness for EELS analysis. A pipette was used to place a drop of the appropriate powder/alcohol suspension on each backing film. It was important to ensure that the grid was placed on a non-absorbent surface for this process, otherwise the carbon film would collapse when the liquid was introduced. The alcohol was then allowed to evaporate, leaving the boride particles on the backing film. Examination of the

specimen in a TEM showed whether the density of particles on the film was acceptable. The required density was such that there was a high probability of finding some isolated particles overhanging holes in the carbon film. The density was adjusted when necessary by varying the proportions of powder and alcohol in the suspension.

8.3.2 Spectrum acquisition

The spectra were acquired using the VG HB5 STEM at Glasgow University. The characteristic edges from B and from either of Ti or Cr are separated in energy loss by ~300eV. The cross section ratios can therefore be expected to be subject to errors due to the effects of a convergent probe. The operating conditions were chosen to minimise such errors, and hence to eliminate the need for convergence corrections to the cross sections. In practice, this requires that the probe convergence angle α should be much smaller than the collection angle β. The 50μm OA was used to form the probe, giving α=9.2mrad. PSL1 was used in conjunction with the 500μm CA to give β=27mrad. Each spectrum was acquired for 300 seconds.

Spectra were generally recorded from areas very close to the edges of particles overhanging holes in the backing film. As described in chapter 7, an indication of the thickness of any region was obtained by examination of the low loss region Very thin regions were generally sought. The thickness of the particles tended to change rapidly close to the edges. For this reason it was necessary to interrupt acquisition, typically every 30seconds, in order to check for specimen drift, and to shift the specimen if required to ensure that the chosen area was always irradiated. Within the limits imposed by the requirements for EELS analysis, the thicknesses studied were allowed to vary widely between spectra. The ratio of the zero-loss peak to the low loss peak varied from ~1.5 to ~15. .

To suit the requirements of constrained background fitting , as discussed in chapter 7, pairs of spectra were recorded from each region. One spectrum was recorded with the excitation of PSL1 such that the zero-loss peak was in focus. PSL1 was then defocussed by -40 fine units, and another spectrum recorded. This figure was determined by autocycling on a Cr edge, and observing the effect on the resolution of varying the excitation of PSL1. (The autocycling routine in the Toltec analysis software allows a small region of the spectrum to be scanned repeatedly across the detector, and immediately displayed each time on the

monitor. In this way the effect of varying the PSL excitation can be seen directly, allowing focussing on that part of the spectrum.) This procedure was followed in all cases except those where series of consecutive spectra were recorded from the same region of the specimen. The materials investigated here are suspected to be susceptible to radiation damage. Such series of spectra, extending over periods of ~30 minutes, were recorded in order to look for any evidence of preferential loss of one element. These spectra were all recorded with the zero-loss peak in focus. Although such spectra are not ideal for the purposes of constrained fitting, it was considered that any large variations in concentration ratios would be detected.

8.3.3 Analysis of TiB_2

Three spectra from different particles in the same TiB_2 specimen are shown in figures 8.9 (a) to (c). These illustrate some of the variations which occur within these data. The spectrum in figure 8.9 (a) has clear edges from B and Ti, at ~180eV and ~450eV respectively. No other edges are apparent, and so extraction of the characteristic signals should present no particular problems. In the spectrum in figure 8.9(b) there is a small O edge at ~520eV, sitting on top of the Ti edge. There is also a change in the curvature of the background at ~280eV, which is probably due to the presence of a small C signal. The C and O signals could have come from the backing film, indicating that the region from which this spectrum was recorded was not completely over a hole. Figure 8.9 (c) shows a spectrum from the thickest region studied. The only edges visible are those from B and Ti, and the signal to background ratios are very much smaller than those in the other spectra.

In order to determine whether significant radiation damage was taking place, three spectra were recorded over a period of 25 minutes from the same area. Single spectra were recorded, focussed at the zero loss peak. The area chosen appeared from examination of the low loss region to have a thickness near the middle of the range specified before. There were no signals visible other than those from B and Ti. Backgrounds were fitted to each edge by constrained fitting, the same fitting regions being used for each spectrum. Pre-edge regions of 30eV were chosen for both the B and the Ti edges. The post-edge region in each case was chosen to extend to 190eV beyond the edge onset, with a convergence offset O_c of 100eV. This choice eliminated all near edge structure and most of the multiple scattering effects from the fitting region. The alignment offset O_a was
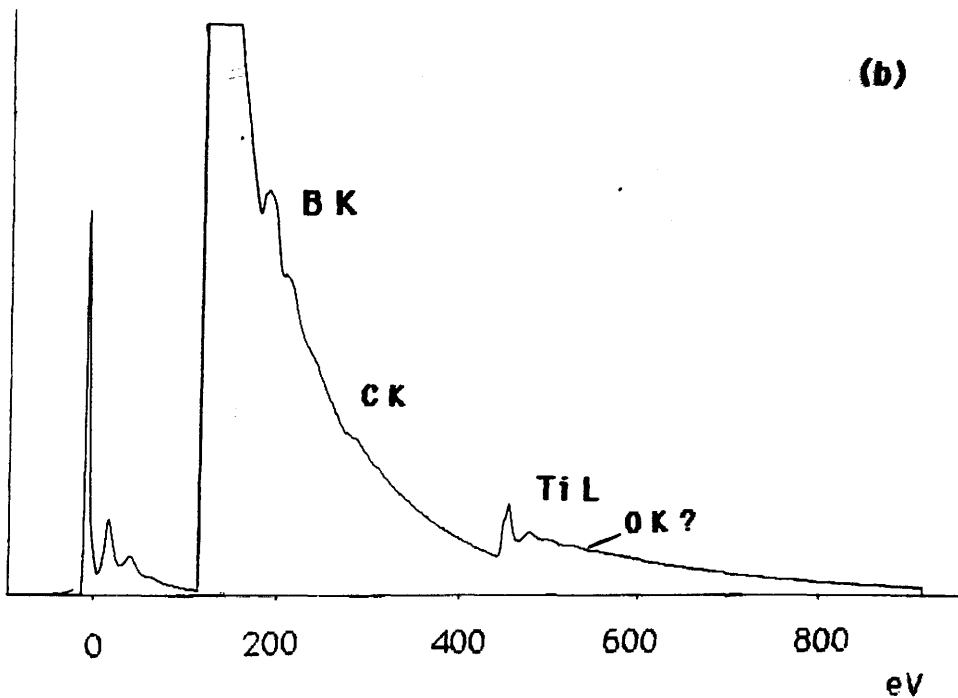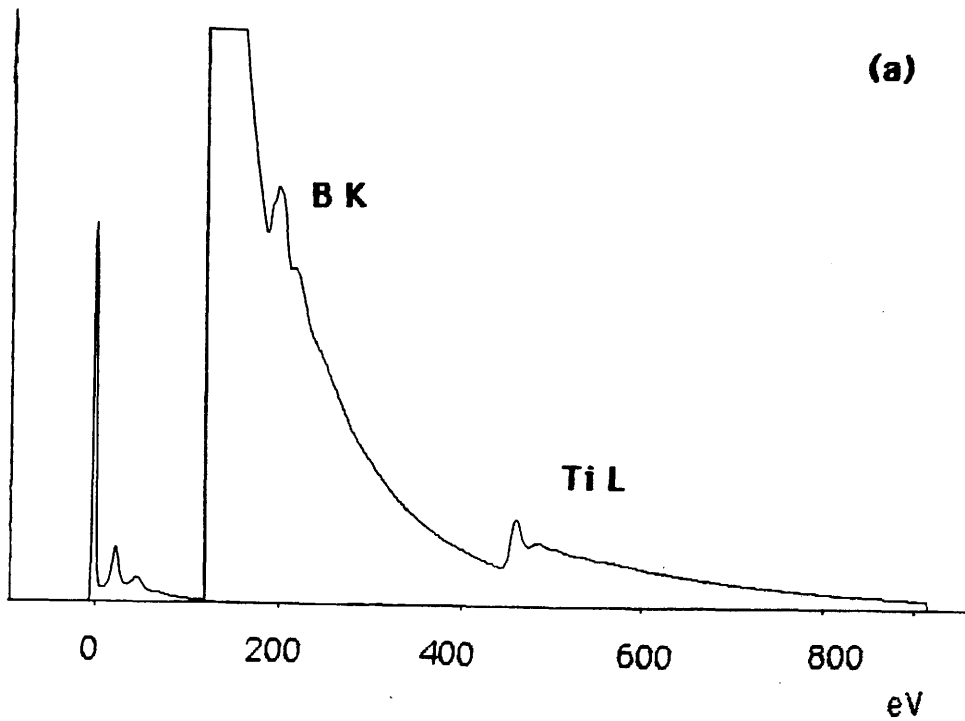
Figure 8.9   Spectra recorded from different regions of the same TiB$_2$ specimen. The spectrum in (a) shows signals from Ti and B only, while that in (b) shows an additional signal from C, and possibly a signal from O.
The spectrum in (c) was recorded from a rather thick region, and illustrates the reduced visibility of the characteristic edges which results.
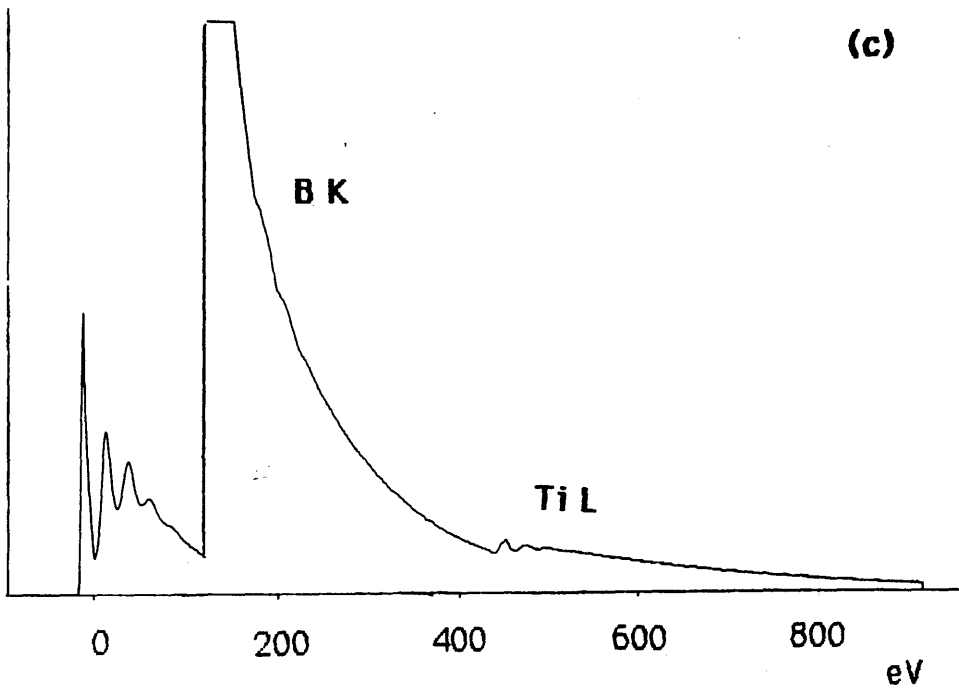
taken as 2eV for the B edge, and 3eV for the Ti edge, which was further from the point at which the spectrum was focussed. The values of r, A, k and χ^2 which resulted are shown in table 8.5, together with the deduced B/Ti concentration ratios. The values of χ^2 vary somewhat, but none are excessively large, and so no major problems are indicated with the background fitting. There is no clear trend in the variation of the B/Ti ratio with time, and so there is no evidence that either element was lost preferentially during this experiment.

Four more spectra, recorded from different areas, were analysed similarly. The pre-edge region was again chosen to be 30eV for each edge. Where possible, the same post-edge region as before was used for the B edges. In most cases, however, the presence of a C signal restricted the extent of the post edge region to <100eV beyond the edge onset. In the case of the spectrum in figure 8.9 (b), the post-edge range was varied, keeping 0_c constant at 50eV. A range of 90eV beyond the edge onset yielded a value of χ^2 of 4.67. Increasing the range to 100eV, so that the beginning of the C signal is included, gives $\chi^2 = 13.5$. A range of 150eV gives $\chi^2 = 60$. For spectra where a C signal was visible, a 90eV range with $0_c = 50eV$ was used for the B edge. For the Ti edges, the post-edge region was chosen to be the same as used for the previous spectra. This region started beyond the onset of any O signal which was present. It was considered that the presence of such a signal would not greatly affect the fitting. The values of χ^2 yielded were always <~5. The extra signal would, however, have the effect of slightly increasing the value of k.

The deduced B/Ti concentration ratios are listed in table 8.6. The result from the first of the previous series of spectra is included. There is a spread of ~15% in these values about their mean, which is outwith the limits of statistical error. The statistical error on each of these results is in the range 1-3%. This figure represents the smallest possible error, being based purely on the number of counts in the edge and in the background beneath the edge. Clearly there will be additional uncertainty introduced in the background fitting, as was discussed in chapter 7. There is no clear trend in the variation of the B/Ti ratio with thickness. The values of B/Ti are all appreciably smaller than the stoichometric value of 2.

8.3.4 Analysis of CrB_2

A series of thirteen spectra was recorded initially from CrB_2. Spectra 1-5

Spectrum		r	A	k	χ^2	B/Ti
1	B	2.756	0.236×10^{12}	15.92	3.759	
	Ti	2.99	0.122×10^{13}	9.859	1.701	**1.615**
2	B	2.72	0.172×10^{12}	14.38	2.950	
	Ti	2.84	0.439×10^{12}	8.240	2.930	**1.745**
3	B	2.86	0.200×10^{12}	9.831	2.083	
	Ti	3.10	0.1158×10^{13}	6.270	2.526	**1.568**

Table 8.5 Fitted parameters and B/Ti ratios for first set of spectra (all from same area).

Spectrum		pre-edge region	post-edge range, O_c	r	A	k	x^2
4	B	30	90,50	2.92	0.526×10^{12}	13.23	4.672
	Ti	30	190,100	3.24	0.563×10^{13}	9.153	5.062
5	B	30	190,100	2.48	0.131×10^{12}	17.87	11.47
	Ti	30	190,100	2.40	0.826×10^{11}	12.19	5.511
6	B	30	90,50	2.75	0.958×10^{11}	10.54	3.666
	Ti	30	190,120	3.4	0.666×10^{13}	7.898	1.762
7	B	30	90,65	2.74	0.243×10^{12}	13.73	5.436
	Ti	30	190,120	2.92	0.820×10^{12}	11.31	2.427

spectrum	Zero loss/ low loss	B/Ti
1	6.8	1.62
4	3.2	1.45
5	1.6	1.47
6	14.2	1.33
7	7.3	1.21

Table 8.6 Fitted parameters and B/Ti ratios for overall TiB_2 data set.

were recorded consecutively from the same area for 300 seconds each. Single spectra were recorded, focussed on the zero loss peak. The remaining spectra were recorded from different areas, with a range of thickness similar to that for TiB_2. Pairs of spectra were recorded from each area, focussed on the Cr edge and the zero-loss peak respectively. Two typical spectra are shown in figure 8.10 (a) and (b). As for TiB_2, some spectra showed edges only from the elements of interest. Such a spectrum is shown in figure 8.10 (a). Other spectra, such as that in figure 8.10 (b), had small additional signals from C and O. A small number of spectra contained signals from N, probably due to small amounts of boron nitride present in the mortar and pestle. Any additional B signal from the same source would slightly increase the apparent B concentration.

C signals placed similar restrictions on the post-edge region for B as before. The O signal, which when present lay in front of the Cr edge, placed a restriction on the available pre-edge region for the Cr edge. The pre-edge region was chosen to be 30eV for all edges except those Cr edges with appreciable O signals before them, for which cases 20eV regions were chosen. Two alternative post-edge regions were investigated for each edge. O_c in both cases was 50eV, and the two regions extended 100eV and 150eV beyond the edge onset respectively. Any significant artefact, such as a C edge, would be expected to be reflected in a much higher x^2 for the range in which it was most prominent. In such cases the fit with the higher value of x^2 was rejected. The B/Cr ratio for each spectrum was calculated by taking the mean value of the four possible combinations of the two k values for each edge. The deviation of the individual ratios about this mean would give an indication of the stability of the fit. The values of r,A, k and x^2 for each fit are shown in table 8.7. There is a wide variation in x^2 between spectra, particularly for the B edge. Only in the case of the B edge in spectrum 10 was the difference in x^2 between the two fitting ranges considered to be so large that the result from the larger range was discarded. The x^2 value for the B edge in spectra 7,9 and 11 were particularly high, irrespective of which post-edge range was chosen. The B edges extracted from these spectra using both post-edge ranges are shown in figure 8.11(a) to (d), together with that from spectrum 6, which gave a much lower value of x^2. Spectra 7 and 11 show the presence of a small C signal which might affect the quality of the fits over the longer range. There is, however, no obvious reason for the differences in the quality of the fits over the shorter range. It was found in the case of spectrum 7 that a post-edge range of 150eV, O_c=80eV, gave a
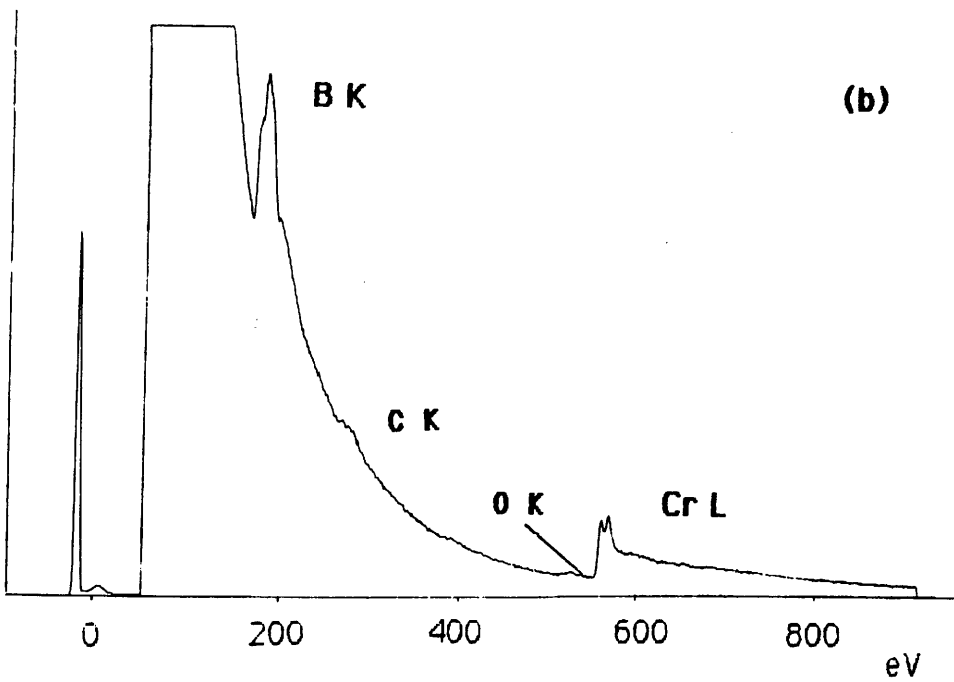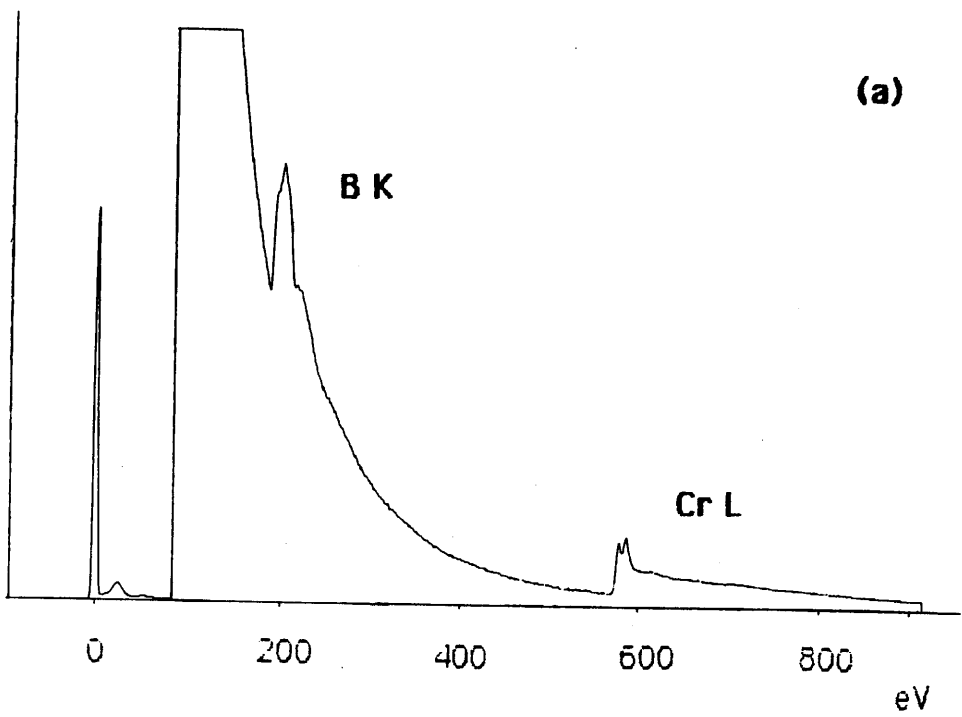
Figure 8.10   Spectra recorded from different regions of the same CrB_2 specimen. The spectrum in (a) shows signals from Cr and B only, while that in (b) shows additional signals from C and O.

Spectrum		pre-edge region	post-edge range, $^{O}_{C}$	r	A	k	χ^2
1	B	30.eV	100,50.eV	2.51	0.400×10^{11}	11.62	3.959
	B	30	150,50	2.50	0.380×10^{11}	11.54	4.042
	Cr	30	100,50	4.0	0.439×10^{15}	7.520	3.149
	Cr	30	150,50	3.9	0.234×10^{15}	7.458	2.990
2	B	30	100,50	2.48	0.287×10^{11}	9.299	4.405
	B	30	150,50	2.48	0.287×10^{11}	9.357	4.318
	Cr	30	100,50	3.8	0.102×10^{15}	6.795	3.075
	Cr	30	150,50	3.8	0.102×10^{15}	6.800	2.746
3	B	30	100,50	2.39	0.161×10^{11}	7.119	5.302
	B	30	150,50	2.38	0.153×10^{11}	7.148	7.918
	Cr	30	100,50	4.1	0.595×10^{15}	7.061	2.127
	Cr	30	150,50	3.8	0.903×10^{15}	6.924	2.701
4	B	30	100,50	2.42	0.149×10^{11}	5.262	3.601
	B	30	150,50	2.42	0.149×10^{11}	5.330	5.488
	Cr	30	100,50	3.9	0.125×10^{15}	6.102	2.124
	Cr	30	150,50	3.7	0.356×10^{14}	6.042	2.178
5	B	30	100,50	2.46	0.207×10^{11}	6.463	2.855
	B	30	150,50	2.47	0.218×10^{11}	6.582	3.942
	Cr	30	100,50	3.80	0.740×10^{14}	6.803	1.466
	Cr	30	150,50	3.72	0.448×10^{14}	6.773	2.667
6	B	30	100,50	2.68	0.625×10^{11}	6.082	2.992
	B	30	150,50	2.79	0.110×10^{12}	6.620	3.492
	Cr	20	100,50	4.50	0.549×10^{16}	5.581	3.759
	Cr	20	150,50	3.60	0.185×10^{14}	5.347	3.542
7	B	50	100,50	2.55	0.768×10^{11}	15.01	19.60
	B	50	150,50	2.50	0.597×10^{11}	14.43	18.63
	Cr	30	100,50	4.0	0.652×10^{15}	10.99	4.087
	Cr	30	150,50	3.48	0.245×10^{14}	10.58	3.646

Table 8.7 Fitted parameters for first CrB_2 data set.
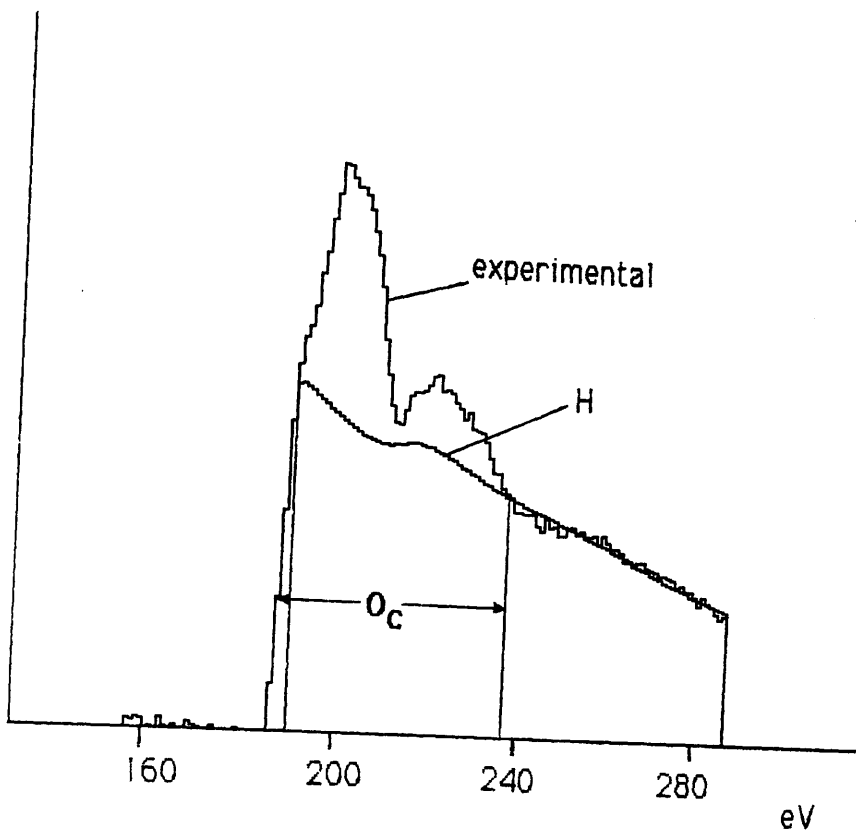
(a)   spectrum 6
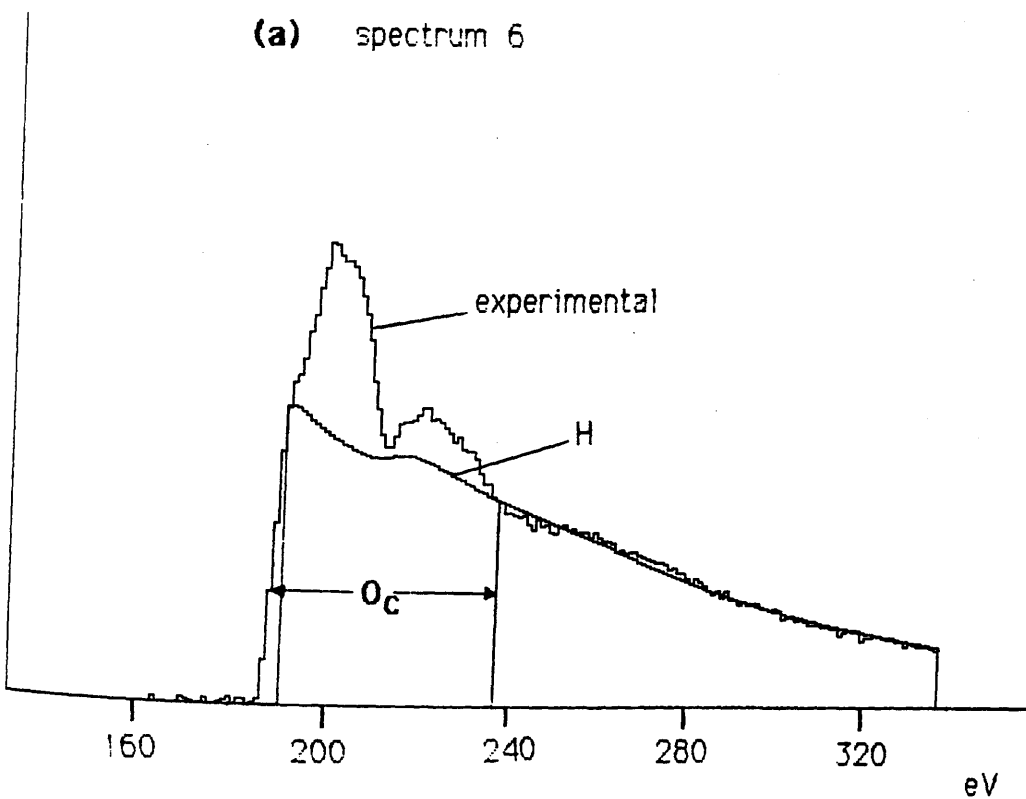
Figure 8.11   Stripped B edges from four spectra from the first CrB$_2$ data set, together with the appropriate scaled theoretical B K edges. The edges extracted using each of the two post-edge fitting ranges considered are shown for each spectrum (*cf.* table 8.7).

(b) spectrum 7

experimental

H

O_c

160   200   240   280

eV

(c)   spectrum 9

experimental

H

O_c

160   200   240   280   320

eV
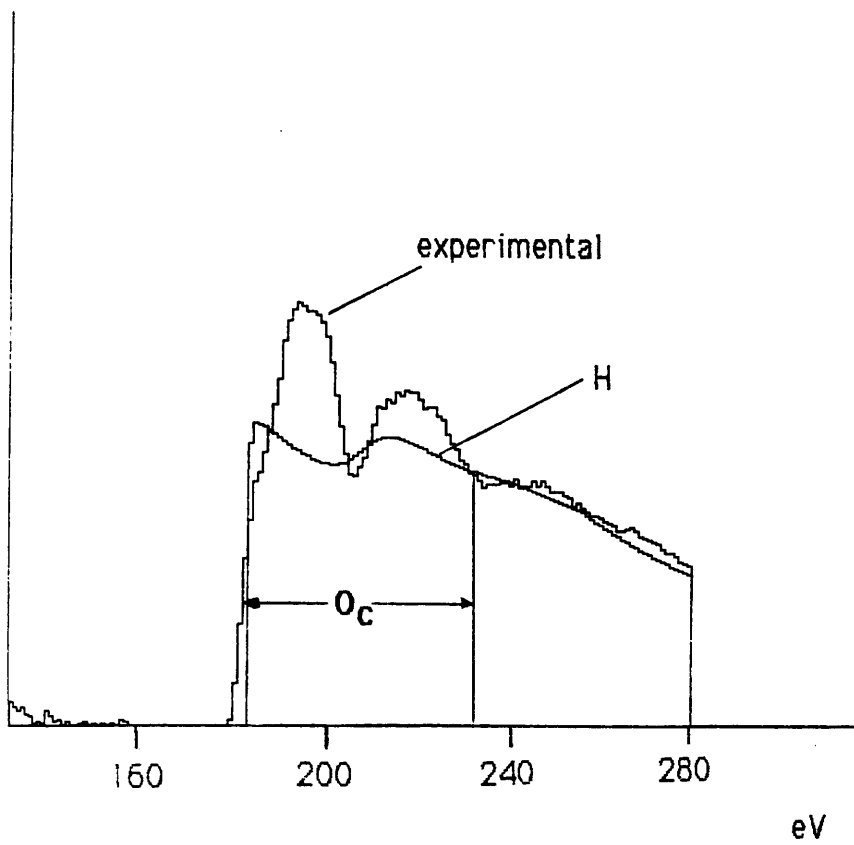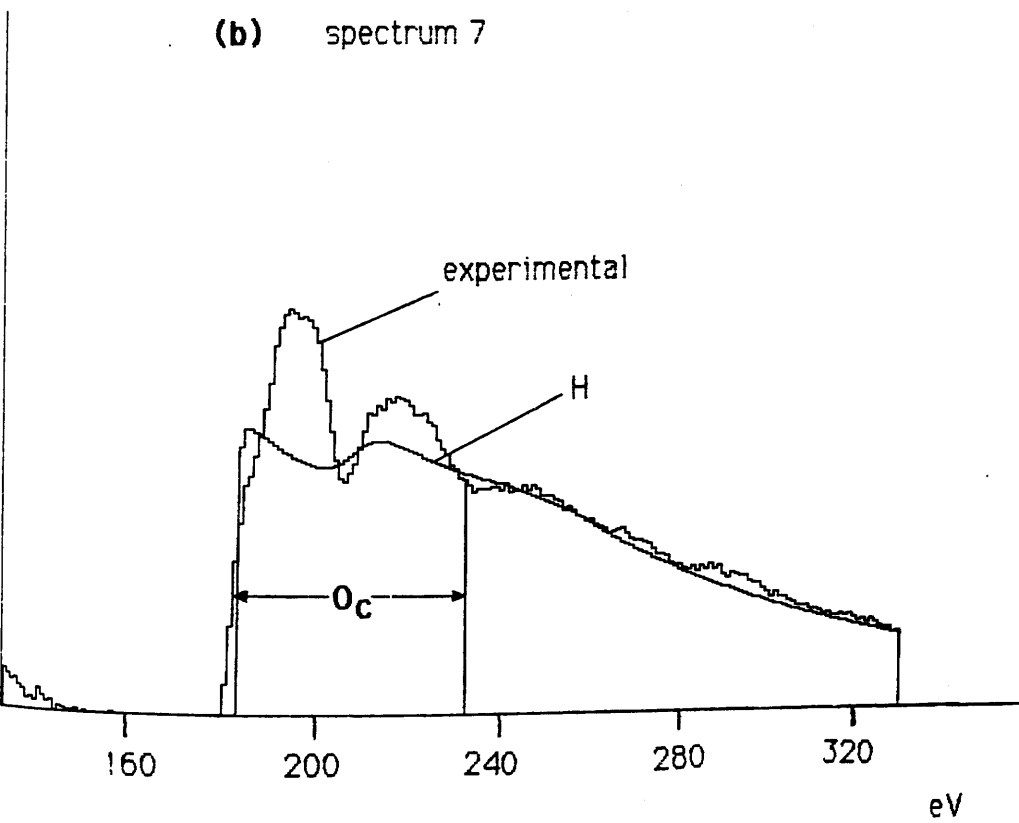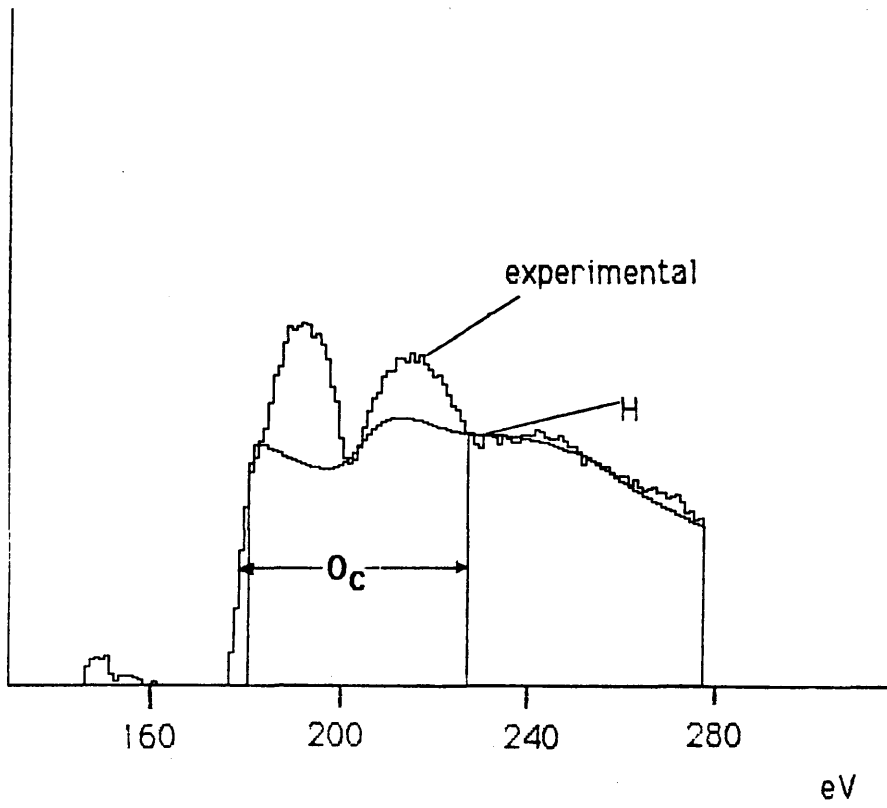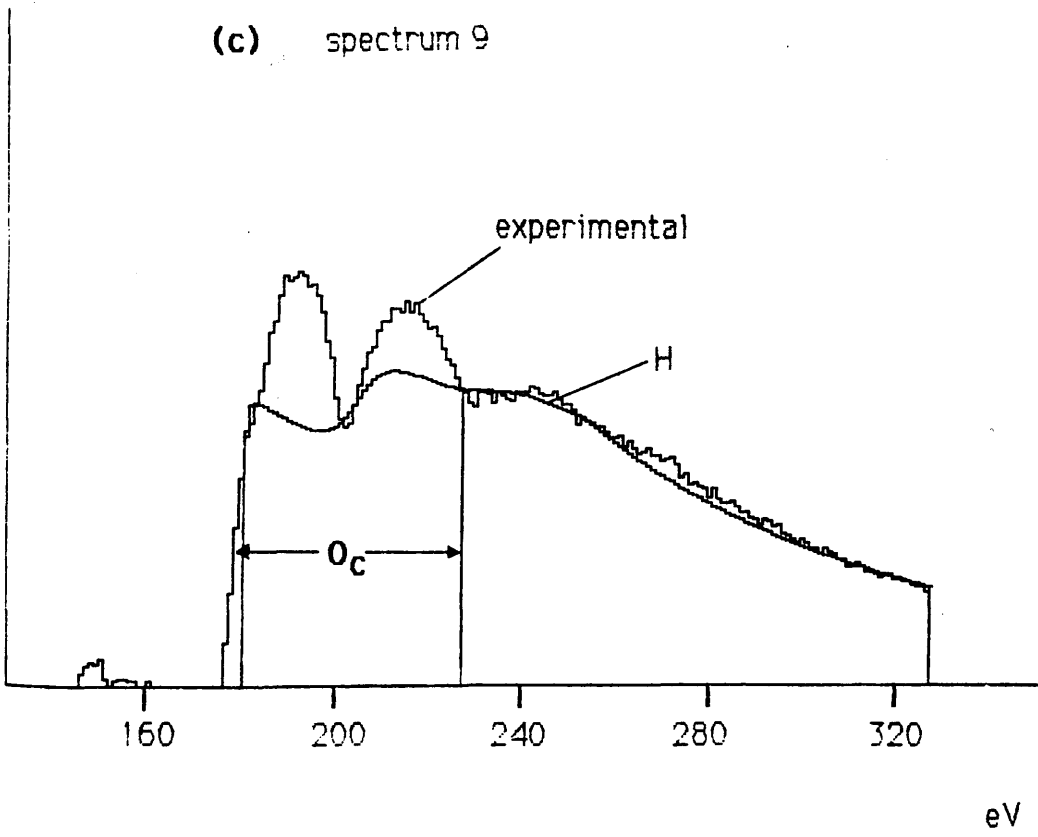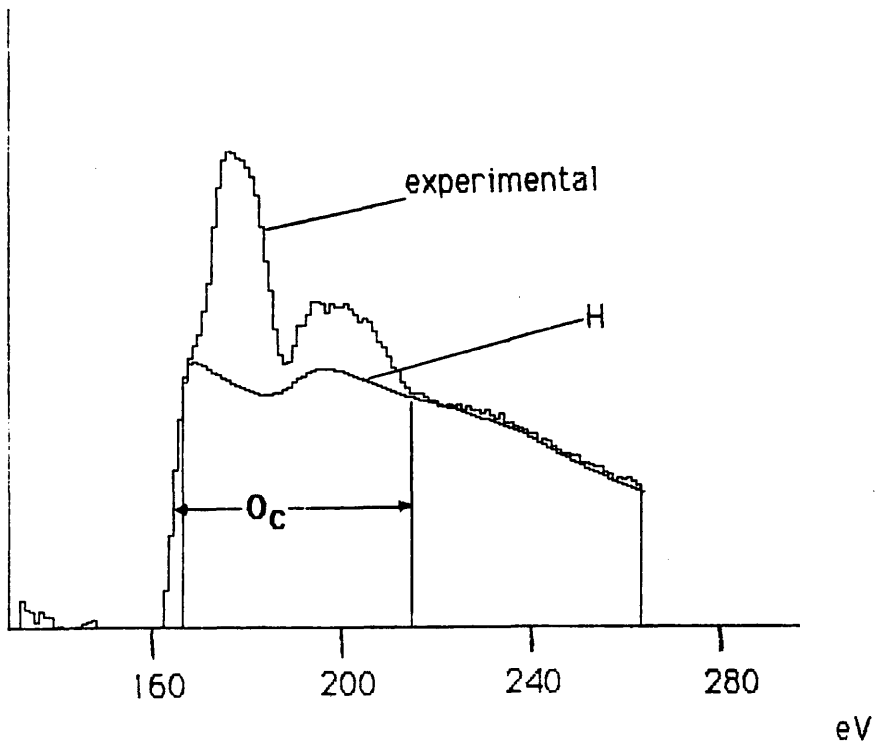
(d) spectrum 11
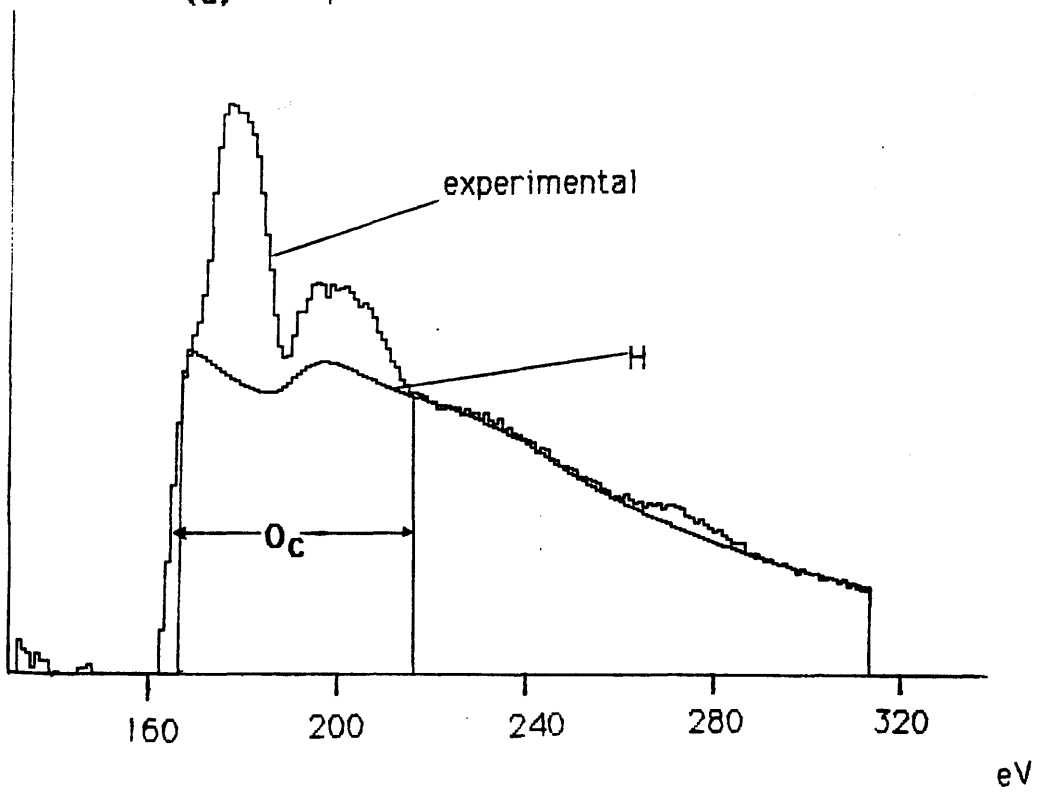
slightly better fit, but the value of χ^2 was still high, at 17.98. The corresponding value of k was 15.93. The deduced B/Cr ratios are shown in table 8.8. The statistical error on each result is again in the range 1-3%. These results show a similar spread to those from TiB_2. The B/Cr ratios from the spectra which gave high values for The B edge χ^2 are lie within the range of the rest of the results, so there is no evidence here that the poor fits had a appreciable effect on the magnitude of the extracted signals. Again the values of the B/Cr ratio are appreciably smaller than the stoichiometric value of 2. In this case, however, there is evidence from spectra 1-5 that a preferential loss of B takes place during acquisition.

A further series of spectra were recorded under the same conditions from the same spectrum. The acquistion time for each spectrum was reduced to 20s in order to limit the effects of radiation damage. These spectra were analysed in the same way as before. The values of r,A,k and χ^2 for each fit are shown in table 8.9. In these spectra, C edges were always visible, resulting in the values of χ^2 for the larger post-edge region being appreciably higher than those for the smaller region. The backgrounds fitted over the larger region were therefore disregarded. Note that the values of χ^2 are generally lower than before. Crozier (1985) observed that low values of χ^2 in the case of pre-edge fitting were found when noisy spectra were used. The deduced values of B/Cr are shown in table 8.10. The spread in these results is rather greater than before. There is a greater statistical error on each result, in the range 5-10%. The spread is still well outwith this limit.

8.3.5 Conclusions from these analyses

The results obtained from these identically prepared TiB_2 and CrB_2 specimens were very similar. In both cases, the concentration ratios deduced were smaller than the stoichiometric value. Such a finding is in agreement with, for example, Sklad et al. (1984), who measured a B/Ti ratio of 0.9 for an ion- milled specimen of TiB_2. They considered that this discrepancy could have been caused by inaccuracy in the theoretical cross section ratio. Such an error is made more likely by the fact that signals arising from different shells are being considered here. It seems unlikely, however, that the theoretical cross section ratio is in error by as much as a factor of two. The values deduced here are generally rather closer to the stoichiometric value. The spread in the results obtained here gives greater cause for concern. If the specimens were stoichiometric,

spectrum	B/Cr ratio
1	1.54 ± 0.02
2	1.37 ± 0.01
3	1.02 ± 0.01
4	0.87 ± 0.01
5	0.96 ± 0.01
6	1.19 ± 0.05
7	1.36 ± 0.06
8	1.30 ± 0.08
9	1.19 ± 0.08
10	1.00 ± 0.01
11	1.29 ± 0.03
12	1.06 ± 0.20
13	1.26 ± 0.11

Table 8.8   B/Cr ratios for first CrB_2 data set.

Spectrum		pre-edge region	post-edge range, O_C	r	A	k	χ^2
14	B	30	100,50	2.48	0.218×10^{10}	0.6547	1.639
	B	30	150,50	2.42	0.162×10^{10}	0.6216	2.337
	Cr	15	100,50	3.6	0.255×10^{13}	0.5451	1.174
	Cr	15	150,50	3.4	0.724×10^{12}	0.5360	1.396
15	B	30	100,50	2.7	0.112×10^{11}	1.035	1.844
	B	30	150,50	2.49	0.385×10^{10}	0.8424	3.387
	Cr	15	100,50	4.5	0.121×10^{16}	0.6741	1.376
	Cr	15	150,50	4.0	0.517×10^{14}	0.6445	1.221
16	B	30	100,50	2.69	0.592×10^{10}	0.8419	1.370
	B	30	150,50	2.48	0.322×10^{10}	0.7393	2.228
	Cr	15	100,50	3.08	0.115×10^{12}	0.6644	1.269
	Cr	15	150,50	3.7	0.575×10^{13}	0.6972	1.274
17	B	30	100,50	2.88	0.174×10^{11}	0.5441	1.257
	B	30	150,50	2.72	0.769×10^{10}	0.4653	1.781
	Cr	15	100,50	3.5	0.105×10^{13}	0.4986	1.214
	Cr	15	150,50	2.6	0.357×10^{10}	0.4719	1.343
18	B	30	100,50	2.82	0.203×10^{11}	1.123	1.804
	B	30	150,50	2.72	0.663×10^{10}	0.9471	2.589
	Cr	15	100,50	4.3	0.316×10^{15}	0.6917	1.783
	Cr	15	150,50	3.6	0.379×10^{13}	0.6545	1.592
19	B	30	100,50	2.66	0.103×10^{11}	0.5935	1.804
	B	30	150,50	2.46	0.372×10^{10}	0.4025	2.402
	Cr	15	100,50	6.1	0.246×10^{20}	0.8442	1.678
	Cr	15	150,50	3.3	0.528×10^{12}	0.7051	1.539

Table 8.9   Fitted parameters for second CrB_2 data set.

spectrum	B/Cr ratio
14	1.18 ± 0.04
15	1.42 ± 0.19
16	1.17 ± 0.10
17	1.04 ± 0.11
18	1.55 ± 0.19
19	0.65 ± 0.18

Table 8.10   B/Cr ratios for second CrB_2 data set.

then it would appear that the constrained background fitting method for extracting characteristic signals was subject to considerable errors. An ideal signal extraction procedure should yield a constant value for the concentration ratio, although a systematic error in the cross section ratio could cause this value to differ from the expected value. It is also possible that the differences in the measured concentration ratio between areas of the specimens reflected real variations in composition.

These results suggest that the accuracy of EELS analysis using constrained background fitting, or indeed any other procedure for characteristic signal extraction, can only properly be assessed if the specimen composition is known a priori. This would require that the specimen was known to be stoichiometric, or that an independent method of measuring the composition, such as the simultaneous acquisition of EDX data, was used. The latter approach was not feasible in this case due to the difficulty of obtaining quantitative information on B by EDX, even if a windowless detector had been available on the HB5.

Chapter 9

Conclusions and future work

In this work, careful consideration has been made of the accuracy with which elemental concentrations may be determined by two widely used microanalysis techniques, EDX and EELS. The interest throughout was restricted to standardless analysis. Such an approach, which relies on theoretical knowledge of the processes involved, is taken by most workers to EELS analysis. Removing reliance on standard specimens facilitates widening the range of applicability of EDX, although the use of standards may offer superior accuracy in certain cases. Of particular interest has been analysis of light elements, which have recently become detectable by EDX with the introduction of windowless x-ray detectors. Each technique has particular problems associated with it, and much of the work here has been aimed at reducing the effects of these. In the case of EDX, the bulk of the results has been concerned with measurement and parameterisation of ionisation cross sections, while the attention in EELS has been concentrated on the extraction of characteristic signals from the background in the spectra.

Standardless EDX analysis requires knowledge of, among other factors, the cross section for the ionisation of the particular inner shell or sub-shell by an incident electron. In the absence of a suitable accurate theoretical expression, it is convenient to describe this quantity by a simple functional form, containing empirical parameters which may be determined by fitting to experimental data. The form considered here, following, for example, Powell (1976) and Gray et al. (1984), was the Bethe form (Bethe, 1930), the basis of which was described in chapter 2. This form had previously been parameterised over a range of elements and accelerating voltages of interest in electron microscopy by Gray et al. Accelerating voltages up to 100keV were considered in that work. Chapter 4 described a similar parameterisation, for the K-shell, the range of T_0 in this instance being extended upwards to 200keV. The superior analytical performance attainable in a more modern microscope was reflected in the much smaller non specimen-related contribution to the spectra as compared with the data of Gray et al. This in turn allowed the required results to be obtained

without introducing errors by the subtraction of the extraneous background contribution. Determination of the ionisation cross section relied on measurements of the ratio of characteristic signals to the level of the bremsstrahlung background beneath the characteristic peaks. Chapman et al. (1983) showed that a reliable theoretical expression, the modified Bethe-Heitler (MBH) equation, describes the bremsstrahlung.

The Bethe form was fitted to data recorded on the JEOL TEM described in chapter 3 over a range of Z between 26 and 50, and T_0 from 80keV to 200keV. None of the experimentally measured values of σ_{iK} differed from the value calculated using the Bethe model with the parameters determined in this way by more than 21%. Additionally, examination of the variation of the cross section for a particular element showed good agreement with the prediction of the Bethe form. Using a relativistically corrected form of the Bethe model (see chapter 2), gave an alternative pair of parameters, and reduced the maximum deviation of any experimental value from the corresponding calculated value slightly, to 19%. These fits were repeated, with data included which were recorded on the two VG STEMS, also described in chapter 3, over a range of Z from 14 to 50, with T_0 always 100keV. Considering the non-relativistic Bethe form firstly, a pair of parameters was determined, the maximum deviation within the total data set being 19%. The degree of consistency between measurements from the different microscopes indicated that instrumental artefacts had generally been eliminated successfully from the data. The relativistic Bethe form offered no apparent advantage for the total data set.

The results quoted above from the JEOL TEM were obtained using a detector which was mounted at 90 degrees to the incident beam direction. This microscope was equipped additionally with a detector mounted at a higher take-off angle of 158 degrees. Such a detector offers in principle the advantages of reduced absorption effects, and higher P/B ratios. The results from the high angle detector , however, also given in chapter 4, showed no evidence of the latter, the P/B ratio being in many cases appreciably lower than the equivalent values from the low angle detector. The spectra showed evidence of large extraneous contributions to the background. It was considered that this particular detector configuration was highly unsuitable for microanalysis. Clearly, much development work is required on the way in which high angle detectors are installed before they can be considered to offer a genuine

improvement on standard configurations.

Chapter 5 extended the discussion to the L-shell. The L-shell is split into three sub-shells, and it has been predicted by the numerical calculations of Rez (1984) that the the Bethe form should be a suitable fitting function for the ionisation cross section for each sub-shell, with parameters which do not differ greatly from those for the K-shell. In order to obtain data concerning the L-shell over a reasonably wide range of elements, it was necessary to consider some elements whose L-lines lie within the low energy region which is accessible only with a windowless detector, namely the transition metals. For this reason most of the data were recorded using the VG STEM at AERE Harwell which was thus equipped. Additional data from heavier elements were recorded using the other two instruments.

The work was based on measurements of K-shell/L-shell cross section ratios. Unlike the P/B, the measurement of this quantity requires correction to be made for the detector efficiency, which falls below unity at both low and high energies. The general method for estimating the efficiency involved fitting corrected MBH background shapes to the experimental background to deduce an effective value for the relevant detector parameter. In the case of high photon energies, the relevant parameter is the thickness of the detector crystal, while the Au contact layer thickness affects the low energy efficiency of the windowless detector. The former case presented no particular problems, since extensive background regions were available for fitting at high energies. The low energy region proved to be more difficult. It was found that comparison of the background with MBH in spectra from four different specimens yielded widely differing estimates of the efficiency. It was considered that spectra from Ni and NiO specimens suffered least of these from artefacts which would cause the efficiency to be estimated incorrectly. The limiting factor in the accuracy of the results was the need to extrapolate the fitted background shape beneath peaks from Ni and O in order to obtain the required values at photon energies <1keV. The method was considered to give reasonable results for the L-lines of the transition metals.

Extracting characteristic K-shell and L-shell signals from the spectra, and correcting the measured count ratios for detector efficiencies yielded experimental values for K-shell/L-shell cross section ratios. These were then

compared with theoretical ratios calculated according to the Bethe form. The accuracy of the information which could be deduced from such a comparison turned out to be limited by uncertainties in the values in the literature for L-shell fluorescence yields. Nevertheless, the results obtained generally supported the applicability of the Bethe model to the L-shell.

Chapter 6 described the analysis of three compunds of light elements of known chemical composition in order to asses the applicability of EDX in this region. Two of the specimens were compunds of O, namely NiO and MgO, while the other, Si_3N_4, contained N. It was considered that the method of estimating the low energy detector efficiency, being dependent on extrapolation of a background shape, was unlikely to yield accurate values for energies as low as those of the O and N K-lines. It was instead decided to use the experimental count ratios to deduce values for the relevant efficiencies. This required knowledge of the other quantities which contribute to the k factor for the conversion of count ratios to elemental concentration ratios. Problems were encountered with the oxide specimens with specimen self-absorption, and with variations from the stoichiometric composition because of an additional O signal. Such an O signal is detectable only with the windowless detector, and is found in many spectra from it. Both of these effects would cause the observed count ratios to deviate from the true values. The former effect could be detected in the case of NiO by comparison of the Ni K_α/L ratio in each spectrum with the equivalent value given in chapter 5. The latter effect was shown up for MgO by observation of the MgP/B ratio, but could not be successfully eliminated. The MgO data was not considered further.

It was assumed in the absence of any alternative model that the Bethe form with the parameters determined in chapter 4 would provide a reasonable description of the ionisation cross sections for O and N. For light elements it turns out that uncertainty in the K-shell fluorescence yields limits the accuracy with which the required information may be determined. It was found that the values which were deduced for the relevant detector efficiencies, although subject to large errors, were in reasonable agreement with the values which might be expected from typical detector parameters.

This work illustrates two areas in which problems arise in light element analysis by EDX. Clearly, uncertainties in the cross sections, fluorescence

yields and detector efficiencies must introduce considerable errors into the results of any analysis. These could be lessened by the use of standards. The problems encountered with NiO and MgO, however, indicate that production of suitable standard specimens, particularly in the case of compunds containing O, is not easy. Clearly, whatever approach is taken, it can be useful to examine aspects of the spectra other than the count ratio for the K-shell signals. Factors such as transition metal K_{α}/L ratios, and P/B ratios in general can sometimes indicate artefacts which would lead to the concentration ratios being determined incorrectly.

Chapter 7 detailed the results obtained using a new approach to background fitting and characteristic signal extraction in EELS. The new procedure, proposed by Steele et al. (1985), incorporates scaled theoretical edge shapes in to the fitting function. Fitting can thus be carried out over regions both before and after the edge onset, eliminating the need for the background to be extrapolated beneath the edge. This approach was expected to be of particular advantage for complex spectra, where the pre-edge regions in some cases may be seriously restricted by the presence of preceding edges. The fitting procedure involves scaling a theoretical edge shape to each experimental edge, The scaling factor is proportional to the number of atoms which contribute to that characteristic signal, and so the ratio of scaling factors for two edges gives a measure of the corresponding concentration ratio. The procedure was tested on a data set which had previously been analysed using the conventional extrapolation techique by Crozier et al. (1983,1984). Simultaneous EELS and EDX data had been recorded, and the success of the EELS analysis was assessed in terms of correlation with the results of the EDX analysis. This analysis, of particles containing a variety of concentrations of Cr, Mn and Fe, presented no particular problems for EDX, and those results were considered to be highly accurate. The signals available in the EELS spectrum from these elements are all from the L-shell.

Preliminary investigation indicated that with the new technique, referred to as "constrained fitting", the size of the extracted signal was less sensitive to variation of the extent of the pre-edge region than was the case with extrapolation. This suggests that the use of constrained fitting is particularly advantageous for the case of a small edge on top of, and close to the onset of, a larger edge. For larger edges, it is less clear whether there is a significant

advantage with constrained fitting. The variation in the characteristic signal with the extent of the pre-edge region was smaller for Cr than using extrapolation, but was greater for the Fe edge.

The Cr/Fe, Mn/Fe and Mn/Cr concentration ratios were determined for nine spectra using constrained fitting. The overall correlation between these values and the EDX results was compared with that found by Crozier et al. As in the earlier work, results were obtained using cross sections calculated according to both the semi-analytic hydrogenic model of Egerton (1979,1984d) and the numerical Hartree-Slater model of Leapman (1980). In both cases, constrained fitting was found to give appreciably better correlation with the EDX results than extrapolation. The spread in the individual results about the mean value for each ratio was larger than that found by Crozier et al. This was attributed to the fact that Crozier et al. included in the extracted characteristic signal the large white line signal at the onset of each edge. These arise due to transitions to bound states above the Fermi level, and are not predicted by the theoretical continuum cross sections used here. The theoretical edges would clearly not fit to the white line regions, and so these regions were not included in the cross section scaling. The white line signal is generally large compared to the signal due to continuum transitions, and occurs at the onset of the characteristic edge. The magnitude of the extracted white line signal must therefore be less sensitive to errors in the background fitting than the signal in the post-edge fitting regions used here. It is to be expected therefore that inclusion of the white lines in the signal integration window for comparison with theory will lead to smaller random variations in the correlation plot than is the case if a continuum signal alone is used. The smaller spread in the results of Crozier et al. as compared to that found here is not therefore indicative that extrapolation yields smaller errors in the background fitting than constrained fitting.

The results of the analysis of these data were encouraging in that constrained fitting generally provided a degree of accuracy comparable to that of the conventional technique. In certain cases, particularly in the case of small signals with restricted pre-edge regions, the new procedure appeared to offer a significant advantage.

The results obtained from a further data set are also given in chapter 8. These data were recorded from specimens of crushed TiB_2 and CrB_2. Such an analysis

was of interest because of the need to consider the ratio of a signal from the K-shell to one from the L-shell in each case. As mentioned in chapter 2, calculated L-shell cross sections are expected to be less accurate than those for the K-shell. Taking a K-shell/L-shell ratio might show up any inaccuracy which had been masked in the previous analysis, where all the signals were from the L-shell. In fact, in both cases the interpretation of the results in these terms was rendered impossible by a rather large spread in the deduced concentration ratios. In the case of CrB_2, some systematic change in the Cr/B ratio with time was noted. This was attributed to some form of radiation damage whereby the lighter element was driven off. Further data were recorded such that the electron dose on each area of interest was much smaller. No radiation damage was observed with these data, but the spread in the results was even greater than before. It was not certain whether the spread was due purely to errors in the fitting, or whether there was a real variation in the composition between different areas of each specimen, and so no firm conclusions could be drawn concerning the success of the constrained fitting procedure.

The results described here allow some conclusions to be drawn about the performance of each of the two techniques relative to the other. Essentially, the problems traditionally associated with each technique remain. Alternative signal extraction techniques, of which the constrained fitting technique studied here is one example, can give some improvement in the accuracy of EELS analyses. The nature of the EELS spectrum dictates, however, that any signal extraction procedure is subject to error. The severity of such errors is dependent on the particular signals which are present in the spectrum. The availability of extensive fitting regions is always likely to facilitate accurate signal extraction. The incorporation of fitting to the post-edge region should allow a similar degree of accuracy even if the the pre-edge region for a particular edge is limited. An example of such a situation is described by Steele (1987), who applied constrained fitting to the extraction of the Ca signal in mineralised bone. The pre-edge region in that case was restricted by the presence of a C signal.

The constrained fitting technique is still at an early stage of development. The work described here should be considered as a preliminary investigation, which, together with the work on the technique by Steele, indicates that the new procedure may prove useful in many situations. Much more detailed work on the

precise nature of the variation of the various fitting parameters with different fitting regions and offsets is required. Direct comparison with extrapolation over a wider range of situations would establish more firmly whether the advantages evidenced here are found in general. It should be noted that the processing of the theoretical cross sections to take account of spectrometer resolution and multiple scattering is equally relevant when determining concentration ratios from signal ratios extracted by extrapolation. It is possible that a better approach to accounting for these factors lies in removing their effects from the experimental data by deconvolution (eg. Egerton, 1984b), rather than the somewhat crude inverse approach taken here. Additionally, it would be useful to consider how the way the χ^2 values vary could be used to give estimates of the error in the extracted signal introduced in the fitting. Such a procedure might be similar in principle to that proposed for extrapolation by Trebbia (1987).

There is little evidence here to indicate whether either of the two theoretical models used to calculate the cross sections is superior to the other. The discrepancy between the predictions of the two models is often appreciable, more so for the L-shell than for the K-shell. Experiments such as that attempted here with the TiB_2 and CrB_2 specimens, in which ratios of signals from different shells are considered, may be useful in determining which model calculates the cross sections more accurately. For such an experiment to be successful, the composition of the specimen must be well known, so that the accuracy of the measured concentration ratios may be assessed. The composition must not vary significantly between different areas, so that the interpretation of the results is not complicated by the combination of errors in signal extraction and uncertainty in composition.

Other problems in EELS should be minimised by the use of parallel detection. Acquisition of an EELS spectrum serially requires a considerable amount of time if a high degree of statistical significance in the data is to be obtained. Apart from the obvious practical limitation imposed by this requirement on the number of spectra which may be recorded in a day's work, problems can arise with specimen drift, and with the dose to which the specimen must be subjected. The latter consideration is very important for beam sensitive materials. Parallel acquisition allows equivalent statistical significance to be achieved with the beam impinging on the specimen for a much shorter time.

For analyses involving elements with K-lines of energy >1keV, EDX has been shown many times to be capable of providing a high degree of accuracy. Analysis by reference to standard specimens is generally considered to lead to the most accurate results. Cross sections calculated according to parameterisations of experimental data such as those of Powell (1976) and Gray et al. (1983), and that carried out here, allow standardless analysis also to yield accurate results. The range of specimens which may be analysed easily is much wider using the latter approach.

The work on K-shell cross sections here can be considered as an extension to higher values of T_0 of an approach to EDX analysis which had previously been shown to be useful over a wide range of elements. The results on the L-shell show that the uncertainies in the fluorescence yields limit the usefulness of L-shell signals in standardless analysis. In general, the investigations carried out in the low photon energy region show that windowless EDX is far from being established as an technique for accurate light element analysis. Before that becomes the case, it will be necessary for better methods to be found for estimating the detector efficiency for very low energy photons, such as those from O, N, etc. Such procedures could involve background modelling, as attempted here, or consideration of the characteristic signals from standard specimens. In the former case, chapter 5 indicates the difficulties which arise in finding spectra with suitable peak-free regions and artefact-free background shapes. In the latter case, chapter 6 shows how data from standard specimens may often be open to misinterpretation. For standardless light element analysis, better knowledge is required of the ionisation cross sections and of the fluorescence yields. It may be possible to extend the range of parameterisation of the Bethe form to include the light elements, and hence whether that model is applicable to the cross sections in that region, as was indicated by the results in chapter 6.

In conclusion, the results of this work emphasise that EDX and EELS remain complementary microanalysis techniques. It may be expected, however, that windowless EDX will develop considerably as a technique for light element analysis, and may yet challenge the superiority of EELS for this purpose. On the other hand, the EELS spectrum will continue to contain much information which is simply not available with EDX.

Appendix A

The modified Bethe–Heitler (MBH) equation

The reduced cross section σ'' is given by

$$\sigma'' = 2.31 \times 10^{-2} \frac{\beta_0[\ 1-\exp\,(-2\pi Z\ /\ 137\,\beta_0)]}{\beta[\ 1-\exp\,(-2\pi Z\ /137\,\beta)]} \cdot \frac{pT_0}{p_0}$$

$$\times \left\{ \frac{8\sin^2\theta_0\,(2E_0^2+1)}{p_0^2\,\Delta_0^4} - \frac{2(5E_0^2+2EE_0+3)}{p_0^2\,\Delta_0^2} - \frac{2(p_0-k)}{Q^2\,\Delta_0^2} + \frac{4E}{p_0^2\,\Delta_0^2} + \frac{L}{pp_0} \right.$$

$$\times \left[\frac{4E_0\sin^2\theta_0\,(3k-p_0^2E)}{p_0^2\,\Delta_0^4} + \frac{4E_0^2\,(E_0^2+E^2)}{p_0^2\,\Delta_0^2} \right.$$

$$+ \frac{2-2(7E_0^2-3EE_0+E^2)}{p_0^2\,\Delta_0^2} + \frac{2k(\,E_0^2+EE_0-1)}{p_0^2\,\Delta_0} \left. \right]$$

$$\left. -\frac{4\varepsilon}{p\,\Delta_0} + \frac{\varepsilon^Q}{pQ}\left[\frac{4}{\Delta_0^2} - \frac{6k}{\Delta_0} - \frac{2k(p_0^2-k^2)}{Q^2\Delta_0} \right] \right\}$$

where

$$L = \ln\left[\frac{(EE_0-1+pp_0)^2}{k^2+p_0^2\alpha^{-2}\Delta_0^{-2}} \right] \qquad \Delta_0 = E_0 - p_0\cos\theta_0$$

$$\varepsilon = \ln \left[\frac{E+p}{E-p} \right] \qquad \varepsilon^Q = \frac{1}{2} \ln \left[\frac{(Q+p)^4}{4(k^2 \Delta_0^2 + p_0^2 \alpha^{-2})} \right]$$

$$Q^2 = p_0^2 + k^2 - 2p_0 k \cos \theta_0 \qquad\qquad \alpha = \frac{108}{Z^{1/3}}$$

Table of symbols which are specific to appendix A

E_0, E Initial and final total electron energy ($m_0 c^2$ units)

p_0, p Initial and final electron momentum ($m_0 c$ units)

T_0, T Initial and final electron kinetic energy ($m_0 c^2$ units)

k, k Energy and momentum of emitted photon ($m_0 c^2$, $m_0 c$ units)

v_0, v Initial and final electron velocity

β_0, β v_0/c, v/c

θ_0 Angle between p_0 and k

Refer to main symbol table for other symbols.

A2

Appendix B

Notes on software

B1. Conversion between Link Systems formats-program LINKCON

As stated in chapter 3, all the spectral analysis required in this work was carried out using a Data General Nova 3 mini-computer, with additional hardware and software to allow it to emulate a Link Systems 290 analyser. The spectra recorded at Glasgow University were acquired using a Link Systems 860 analyser. This system can store spectra as disk files in a format known as 860/LDOS format. The spectra recorded at the IBM Almaden Research Center, originally acqired on a Kevex system, had been converted to 860/LDOS format also. Spectra recorded at AERE Harwell were acquired using a Link Systems AN10000 analyser, which stores spectra on disk files in a different format, referred to here as AN10 format. Clearly, before any analysis could be carried out it was necessary to convert each spectrum to 290 format, the format required by the Nova 3/Link 290 system. This section describes the software developed for this purpose by Dr. W.A.P. Nicholson and myself.

The differences between the three formats are illustrated in figure B1. A spectrum of any of these consists of a header block and a number of spectrum data blocks. The information is stored in each block in integer form. The header block contains information about the spectrum, such as acquisition time, spectrum label, etc. Full details of the information stored for each format can be found in the listing which follows of the conversion program LINKCON. The number of spectrum data blocks depends on whether the data are stored as 16-bit or 32-bit integers. In the former case, there are always 4 blocks of 256 words each. In the latter case, which can occur for 860/LDOS and AN10 formats, there are 8 blocks of 256 words each. 32-bit data are each stored as two words, the first of which is the most significant. Each type of spectrum can therefore contain an array of up to 1024 channels of data. In 290 format, the data corresponding to 0eV is stored in the channel 1 of the first spectrum data

290 format

header
block
(8 words)

16-bit spectrum data
(1024 words)

860/LDOS format
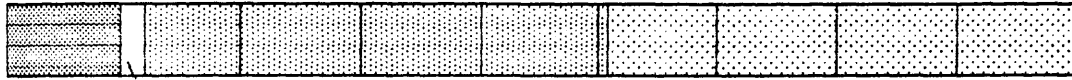
header
block
(256 words)

16-bit spectrum data
(1024-10 words)

10 channel shift

32-bit spectrum data
(2048-10 words)

AN10 format
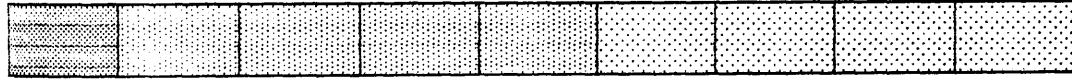
header
block
(256 words)

16-bit spectrum data
(1024 words)

32-bit spectrum data
(2048words)

Figure B1. Schematic illustration of Link Systems formats

block. In 860/LDOS format there is a 10 channel offset, so that the OeV data is stored in channel 11. Conversion between these formats therefore requires the spectrum data to be shifted accordingly within the array. In AN10 format, there is a floating point offset which determines what value of photon energy channel 1 corresponds to. This was generally 0, so that the OeV data was stored in channel 1. T

Program LINKCON is a main program which allows the user to specify the source and target formats for a particular conversion, and the filename of the source spectrum. Data are stored in four arrays: a header array for each format of the appropriate size (IHED29, IHED86 & IHEDAN), and a spectrum data array (ISPEC) with 1024 elements. The header arrays are assigned default contents initially, and ISPEC is set to zero. The program calls the appropriate spectrum read routine, which reads the header block into the appropriate header array and the spectrum data into ISPEC. The 860/LDOS read routine, SRED86, also shifts the spectrum data in the array by 10 channels, so that the OeV data is in channel 1. The AN10 read routine, SREDAN, copes with 32-bit data by reading such data into a floating point array RSPEC. The values in RSPEC are then scaled down by a factor such that the largest value <32767, so that the data can be converted to signed integer format and stored in ISPEC. This facility may also be required in SRED86, but has not been incorporated to date. The program then calls the header block conversion routine HEDCON, which transfers as much as possible of the information from the source spectrum header to the header array of the new format. The appropriate spectrum write routine is then called. These all write the modified target format header array and the contents of ISPEC to disk. The 860/LDOS write routine reinstates the 10 channel shift in the spectrum data which that format requires.

The main program and all the subroutines are listed on the following pages. The version listed has been used extensively for conversions from 860/LDOS format (16-bit data only) and AN10 format(16-bit and 32-bit data) to 290 format, and appears reliable for these cases. Other conversions have not been required to date, and the program has not been tested fully for such cases.

B2

```
C Option selection
        TYPE ' This program converts between spectra '
        TYPE ' of 860/LDOS, 290 and AN10000 formats. '
99      CONTINUE
        TYPE ' '
        TYPE '  '
        TYPE '          Select current format '
        TYPE ' '
        TYPE '     1.  290 '
        TYPE '     2.  860/LDOS '
        TYPE '     3.  AN10000 '
20      ACCEPT NS
        IF(NS.EQ.1) GO TO 25
        IF(NS.EQ.2) GO TO 24
        IF(NS.EQ.3) GO TO 23
        TYPE ' What? '
        GO TO 20
23      TYPE ' AN10000 format selected '
        GO TO 26
24      TYPE ' 860/LDOS format selected '
        GO TO 26
25      TYPE ' 290 format selected '
26      CONTINUE
        TYPE '    '
        TYPE '  '
        TYPE '          Select new format    '
        TYPE '     1. 290  '
        TYPE '     2. 860/LDOS  '
        TYPE '     3. AN10000  '
        TYPE '     4. No conversion / quit  '
32      ACCEPT NT
        IF(NT.EQ.NS) GO TO 37
        IF(NT.EQ.1) GO TO 35
        IF(NT.EQ.2) GO TO 34
        IF(NT.EQ.3) GO TO 33
        IF(NT.EQ.4) GO TO 999
        TYPE '  What? '
        GO TO 32
33      TYPE '   AN10000 format selected  '
        GO TO 36
34      TYPE '   860/LDOS format selected  '
        GO TO 36
35      TYPE '   290 format selected  '
        GO TO 36
37      TYPE '   That is silly-try again '
        GO TO 99
36      CONTINUE
        TYPE '  '
        TYPE '  Is this conversion direction correct? 0=Yes, 1=No'
        ACCEPT CONCHK
        IF (CONCHK.EQ.0) GO TO 30
        GO TO 99
C Read in source filename
30      TYPE ' Enter filename of source spectrum '
        READ(11,500) INSPEC
500     FORMAT(S8)
        WRITE(10,510) INSPEC
510     FORMAT(/' I am about to read ',S8,' OK? 0=Yes, 1=No')
        ITEMP=INSPEC
        ACCEPT OPT
        IF(OPT.NE.0) GO TO 30
```

```
C Read in source spectrum
          NSFLG=NS-2
          IF (NSFLG) 292,862,102
  292     CALL SRED29(INSPEC,IER)
          GO TO 293
  862     CALL SREDBE(INSPEC,IER)
          GO TO 293
  102     CALL SREDAN(INSPEC,IER)
  293     CONTINUE
C Convert header
          CONFLG(2)=NS-2
          CONFLG(1)=NT-2
          CALL HEDCON(INSPEC,IER,CONFLG)
C Choose output filename
          TYPE '    '
          TYPE ' Do you want to overwrite old spectrum? '
          TYPE ' 0=Yes, 1=No '
   70     ACCEPT M
          IF(M.EQ.1) GO TO 90
          IF(M.EQ.0) GO TO 80
          TYPE ' What? '
          GO TO 70
   80     TYPE ' I am going to overwrite spectrum. OK? 0=Yes, 1=No '
          ACCEPT OCHK
          IF(OCHK.NE.0) GO TO 90
          CALL DFILW(INSPEC,IER)
          CALL ERRMESS(IER)
          IF(IER.NE.1) GO TO 99
          OSPEC=INSPEC
          WRITE(10,530)OSPEC
  530     FORMAT(/' Overwriting spectrum ',S8)
          GO TO 100
   90     TYPE ' Enter new filename '
          READ(11,500)OSPEC
          WRITE(10,520)OSPEC
  520     FORMAT(/' New output filename is ',S8)
C Write converted spectrum to disk
  100     IF(NT.EQ.1) GO TO 290
          IF(NT.EQ.2) GO TO 860
          IF(NT.EQ.3) GO TO 1000
C 290 format
  290     CALL SWRT29(OSPEC,IER)
          IF(IER.NE.1)GO TO 99
          GO TO 110
C 860 format
  860     CONTINUE
          CALL SERTBE(OSPEC,IER)
          IF(IER.NE.1) GO TO 99
          GO TO 110
C AN10000 format
 1000     CALL SERTAN(OSPEC,IER)
          IF (IER.NE.1) GO TO 99
C Output summary
  110     WRITE(10,540)ITEMP
  540     FORMAT(/' Conversion complete for spectrum ',S8)
          IF(NT.EQ.1) GOTO 120
          IF(NT.EQ.2)GO TO 121
          IF (NT.EQ.3) GOTO 122
```

```
120      TYPE ' converted to 290 format. '
         GO TO 130
121      TYPE ' converted to 860/LDDS format '
         GO TO 130
122      TYPE ' converted to AN10000 format   '
130      WRITE(10,550)OSPEC
550      FORMAT(/' Filename of converted spectrum is ',SB)
         TYPE '  '
         TYPE '  '
         TYPE '    Any more spectra? 0=Yes, 1=No  '
         ACCEPT MORE
         IF (MORE.EQ.0) GO TO 99
999      CONTINUE
         END
```

Subroutine SRED29 - 290 format read routine

```
         SUBROUTINE SRED29(SPNAME,IER)
         DOUBLE PRECISION SPNAME
         COMMON /IARAY/ISPEC(1024) /HEAD29/IHED29(28)
C  Open file for reading (=1) on Channel 6
         CALL OPEN (6,SPNAME,1,IER)
         IF (IER .NE. 1) GOTO 90
         DO 20 I=1,28
20       READ BINARY (6) IHED29(I)
         DO 30 I=1,1013
30       READ BINARY (6) ISPEC(I)
90       CALL CLOSE (6,IER)
         CALL ERRMESS(IER)
         CONTINUE
         RETURN
         END
```

Subroutine SRED86 - 860/LDOS format read routine

```
        SUBROUTINE SRED86(SPNAME,IER)
        DOUBLE PRECISION SPNAME
        COMMON /HEAD86/IHED86(256) /IARAY/ISPEC(1024)
C  Open file for reading (=1) on CHANNEL 6
        CALL OPEN(6,SPNAME,1,IER)
        IF(IER .NE. 1) GO TO 10
C Read in 1 header block starting at block #0 on Channel 6
        CALL RDBLK(6,0,IHED86,1,IER,IBLK)
        IF (IER .NE. 1) GO TO 10
C  Read in a 4 spectrum blocks staring at block #1 on channel 6
        CALL RDBLK(6,1,ISPEC,4,IER,IBLK)
   10   CALL CLOSE(6,IER)
        CALL ERRMESS(IER)
C  Shift 860/LDOS spectrum down by offset
        NOFFS=IHED86(7)
        DO 20 J=1,1012
        K=NOFFS+1+J
   20   ISPEC(J)=ISPEC(K)
        DO 30 J=1013,1024
   30   ISPEC(J)=0
        CONTINUE
        RETURN
        END
```

Subroutine SREDAN - AN10 format read routine

```
        SUBROUTINE SREDAN(NAME,IER)
        DOUBLE PRECISION NAME
        DIMENSION RSPEC(0:1023)
        COMMON /HEADAN/ IHEDAN(0:255) /IARAY/ISPEC(0:1023)
C
C ...... READ IN 1st 7 words of HEADER ......
C word=152500K spectrum type=X-ray
C 1st =No  header words, 2nd indicates data type
C 3,4 min and max channel Nos. with non-zero data
C contain characters "keV "
        CALL OPEN(6,NAME,1,IER)
        CALL ERRMESS(IER)
        IF (IER .NE. 1) GOTO 999
        DO 10 I=0,6
   10   READ BINARY (6) IHEDAN(I)
        MHDSIZE=IHEDAN(1)
        MHDEND=MHDSIZE-1
        MHORDER=IHEDAN(2)
        MCMIN=IHEDAN(3)
        MCMAX=IHEDAN(4)
```

```
C check size  header block is actually 256
        IF (MHDSIZE .EQ. 256) GOTO 20
        WRITE (10,101) MHDSIZE
  101   FORMAT("HEADER BLOCK IS NOT 256 WORDS BUT",I4,"LONG")
        TYPE "CONTINUE (1) OR STOP (0)"
        ACCEPT NDUM
        IF (NDUM .EQ. 0) GOTO 999
C read  Gain factor GF, and Offset XO from REALS
C words 7-10. True unit Y (e.g. eV) corresponding
C to channel I is  Y=(I-XO)*GF
C
   20   READ BINARY (6) GF,XO
C
C Get approx integer equivalents. Store integer
C part. Decimal parts to 3 sig figs x 1000.
        IGF=IFIX(GF)
        IXO=IFIX(XO)
        IHEDAN(31)=IGF
        IHEDAN(32)=IFIX((GF-IGF)*1000)
        IHEDAN(33)=IXO
        IHEDAN(34)=IFIX((XO-IXO)*1000)
C Read in rest of header array. Words 11 to 17
C label,upto 32 chars + terminator zero byte
C 29,30 = Scale coeffs ISCALE,NSCALE
C Actual Val=(ISCALE * chan count filed)/NSCALE
C 31-35 not used by LINK, 36=Livetime,
C 37=Real time, 38=Time to give preset count?,
C 39,40= High and low order cps, 41=Preset time.
C If 42=1 Strobe stored in spectrum array,
C =16,(32) stored as 16,(32) bit data in header
C starting at (128) (with offset XO?)
C
        DO 25 I=11,MHDEND
   25   READ BINARY (6) IHEDAN(I)
C ----------------------------------------------
C ...... READ IN SPECTRUM DATA .......
C Zero whole of spectrum array ISPEC(1024)
        DO 30 J=0,1023
   30   ISPEC(J)=0
C
C if MHORDER =20K unsigned data 16bit,
C =420K signed 16bit   =440K signed 32bit
C i.e. 16, 262, 288 = 16 x 1,17,18 resp.
        IORDER= MHORDER/16 - 17
        IF (IORDER .GT. 0) GOTO 50
C read in 16 bit spectra, if signed and <0 set=0
C if unsigned <0, leave as analyser expects this.
        WRITE(10,102)
  102   FORMAT(' Input spectrum contains 16-bit data')
        DO 40 J=MCMIN,MCMAX
        READ BINARY (6) ISPEC(J)
X       WRITE (10,105) J,ISPEC(J)
X105    FORMAT(' Ch. ',I4,'    ',I15)
        IF (IORDER .LT. 0) GOTO 40
        IF (ISPEC(J) .LT. 0)  ISPEC(J)=0
   40   CONTINUE
        GOTO 100
C read in 32 bit signed spectra, if <0 set=0
   50   WRITE (10,103)
  103   FORMAT(' Input spectrum contains 32-bit data')
        DO 60 J=MCMIN,MCMAX
        READ BINARY (6) IHIGH,ILOW
```

```
          IF (IHIGH .GE. 0) GOTO 55
          IHIGH=0
          ILOW=0
C Convert 32-bit integer to real
 55       IF (ILOW.GE. 0)   RSPEC(J)=65536.*IHIGH +ILOW
C If l.s. byte is a negative signed integer, add 65536. to give
C equivalent real positive number
          IF(ILOW.LT.0)   RSPEC(J)=65536.*IHIGH+(ILOW+65536.)
X         WRITE(10,112) J,RSPEC(J)
X112       FORMAT ( ' Ch. ',I5,F15.4)
 60       CONTINUE
C find maximum peak value and scale factor
          RMAX=0
          DO 70 J=MCMIN,MCMAX
 70       IF (RSPEC(J) .GT. RMAX)   RMAX=RSPEC(J)
          WRITE (10,109) RMAX
 109      FORMAT( ' Max of RSPEC = ',F15.4)
C convert F.Pt. spectra to integer
          ISCALE = IFIX(RMAX/65536. + 1.)
          WRITE(10,111)ISCALE
 111      FORMAT(' Scaled down by a factor of ',I2, ' to give 16-bit data'
          DO 80 J=MCMIN,MCMAX
C If value > 32767, subtract 65536 so that resulting
C integer is correctly signed (i.e. negative)
          RSPEC(J)=RSPEC(J)/ISCALE
          IF(RSPEC(J).GT.32767.) RSPEC(J)=RSPEC(J)-65536.
          ISPEC(J)=IFIX(RSPEC(J)+.5)
X         WRITE(10,108) J,ISPEC(J)
X108       FORMAT( ' Ch. ',I4,'      ',I15)
 80       CONTINUE
C
C shift spectrum to correct place in array
C and zero top channels. Get nearest offset
 100      IXO=IFIX(XO+.5)
          I2=1023-IXO
          DO 90 I=0,I2
          J=IXO+I
 90       ISPEC(I)=ISPEC(J)
          DO 95 I=I2,1023
 95       ISPEC(I)=0
 999      CALL FCLOS(6)
          RETURN
          END
```

Subroutine HEDCON - header array conversion routine

```
          SUBROUTINE HEDCON(NAME,IER,CONFLG)
          DOUBLE PRECISION NAME
          INTEGER CONFLG(2)
          COMMON /HEADAN/ IHEDAN(0:255) /HEAD29/IHED29(0:27)
C                                                           /HEAD86/IHED86(0:255)
C Essential default values for target header are
C set up in the main prog.
C --------------------------------------------------------
C CONFLG(1) is source format CONFLG(2) is
C destination format  -1=290,  0=860,  1=AN10
C
          IF (CONFLG(2)) 290,860,1000
```

```
C Target is 290 format
 290      IF (CDNFLG(1)) 291,861,1001
C Shouldn't get here
 291      TYPE"SPECTRUM FORMAT ALREADY 290"
          GOTO 9999
C Source format is 860
 861      IHED29(0)=IHED86(27)                    ;live time
          DO 20 I=1,21
          K=I+6
 20       IHED29(I)=IHED86(K)                      ;copy label
          GOTO 9999
C Source format is AN10
 1001     IHED29(0)=IHEDAN(36)                     ;live time
          DO 30 I=1,17
          K=I+10
 30       IHED29(I)=IHEDAN(K)                      ;label
          GOTO 9999
C - - - - - - - - - - - - - - - - - - - - - - - -
C Target is 860 format
 860      IF (CDNFLG(1)) 292,862,1002
C Source format is 290
 292      IHED86(27)=IHED29(0)                     ;live time
          DO 40 I=7,27
          K=I-6
 40       IHED86(I)=IHED29(K)                      ;label
          GO TO 9999
C Shouldn't get here
 862      TYPE"SPECTRUM FORMAT ALREADY 860"
          GOTO 9999
C source format is in AN10
 1002     DO 50 I=7,26
 50       IHED86(I)=IHEDAN(I)
C 7-10 copy F.Pt. Gain and Zero, 11-26 copy label
          IHED86(27)=IHEDAN(36)                    ;live time
          IHED86(28)=IHEDAN(37)                    ;real time
          GO TO 9999
C
C- - - - - - - - - - - - - - - - - - - - - - - - - - -
C Target is AN10 format
 1000     IF(CDNFLG(1)) 293,863,1003
C Source format is 290
 293      IHEDAN(36)=IHED29(0)                     ;live time
          DO 60 I=1,16
          K=I+10
 60       IHEDAN(K)=IHED29(I)                      ;label
          GO TO 9999
C Source format is 860
 863      DO 70 I=7,26
 70       IHEDAN(I)=IHED86(I)
C 7-10 copy F.Pt. Gain and Zero, 11-26 copy label
          IHEDAN(36)=IHED86(27)                        ;live time
          IHEDAN(37)=IHED86(28)                    ;real time
          GO TO 9999
C Shouldn't get here
 1003     TYPE"FORMAT ALREADY AN10"
          GO TO 9999
C
C - - - - - - - - - - - - - - - - - - - - - - - - - -
C
 9999     RETURN
          END
```

Subroutine SWRT29 - 290 format write routine

```
        SUBROUTINE SWRT29(NAME, IER)
        DOUBLE PRECISION NAME
        COMMON /IARAY/ISPEC(0:1023) /HEAD29/IHED29(0:27)
C Open file for writing (=3) on Channel 7
        CALL OPEN(7,NAME,3,IER)
        IF (IER .NE. 1) GOTO 90
        DO 20 I=0,27
20      WRITE BINARY (7) IHED29(I)
        DO 30 I=1,1013
30      WRITE BINARY (7) ISPEC(I)
90      CALL CLOSE (7,IER)
        CALL ERRMESS(IER)
        CONTINUE
        RETURN
        END
```

Subroutine SERT86 - 860/LDOS format write routine

```
        SUBROUTINE SERT86(NAME, IER)
        DOUBLE PRECISION NAME
        COMMON /IARAY/ISPEC(0:1023) /HEAD86/IHED86(0:255)
C Shift spectrum up by offset (usually 10)
        NOFFS=IHED86(7)
        CONTINUE
        DO 25 I=0,1012
        J=1023-I
        K=J-NOFFS
25      ISPEC(J)=ISPEC(K)
        DO 30 J=0,10
30      ISPEC(J)=0
C Open file for writing (=3) on Channel 7
        CALL OPEN(7,NAME,3,IER)
        IF (IER .NE. 1) GOTO 90
        DO 20 I=0,255
20      WRITE BINARY (7) IHED86(I)
        DO 35 I=1,1023
35      WRITE BINARY (7) ISPEC(I)
90      CALL CLOSE (7,IER)
        CALL ERRMESS(IER)
        CONTINUE
        RETURN
        END
```

Subroutine SERTAN — AN10 format write routine

```
        SUBROUTINE SERTAN(NAME,IER)
        DOUBLE PRECISION NAME
        COMMON /IARAY/ISPEC(0:1023) /HEADAN/IHEDAN(0:255)
C Shift spectrum up by offset (if any)
        NOFFS=IHEDAN(7)
        DO 10 I=0,1012
        J=1023-NOFFS
        K=J-NOFFS
  10    ISPEC(J)=ISPEC(K)
        DO 20 I=0,10
  20    ISPEC(I)=0
C Open file for writing (=3) on channel 7
        CALL OPEN(7,NAME,3,IER)
        IF (IER.NE.1) GOTO 90
        DO 30 I=0,255
  30    WRITE BINARY(7) IHEDAN(I)
        DO 40 I=0,1023
  40    WRITE BINARY(7) ISPEC(I)
  90    CALL CLOSE(7,IER)
        CALL ERRMESS(IER)
        RETURN
        END
```

Subroutine ERRMESS — error message output routine

```
        SUBROUTINE ERRMESS(IER)
        IF (IER .EQ. 1) GOTO 99
        WRITE(10,100) IER
        IF(IER .EQ.  4) TYPE "ILLEGAL FILE NAME"
        IF(IER .EQ.  9) TYPE "END OF FILE"
        IF(IER .EQ. 10) TYPE "FILE IS READ PROTECTED"
        IF(IER .EQ. 11) TYPE "FILE IS WRITE PROTECTED"
        IF(IER .EQ. 12) TYPE "FILE ALREADY EXISTS"
        IF(IER .EQ. 13) TYPE "FILE DOES NOT EXIST"
        IF(IER .EQ. 16) TYPE "FILE IS NOT OPEN"
        IF(IER .EQ. 20) TYPE "CHANNEL IN USE"
        IF(IER .EQ. 26) TYPE "DISK SPACE EXHAUSTED"
        IF(IER .EQ. 27) TYPE "READ ERROR"
        IF(IER .EQ. 44) TYPE "TOO FEW DCB'S AT SYSGEN"
        IF(IER .EQ. 51) TYPE "FILE IN USE"
C       TYPE "REFER TO PAGE E-1 IN THE FORTRAN MANUAL"
 100    FORMAT(/,1X," ERROR NO. ",I3," OCCURED.",/)
C
  99    CONTINUE
        RETURN
        END
```

B2. EDX spectral analysis software – programs AN29 and CROSS

Program AN29 is a spectral analysis program which runs on the Data General Nova 3/Link Systems 290 emulator system. It is based on the program ANALYSIS, which was written to run on the Link Systems 860 by Dr. P.F. Adam, and which is described and listed in his PhD. thesis (Adam, 1985). AN29 was created by modifying the spectrum read/write routines of ANALYSIS to deal with spectra in 290 format instead of 860/LDOS format. This was done by Dr. W.A.P. Nicholson. Some of the subroutines have been modified by myself in order to fit the requirements of this work. This section briefly outlines the use of AN29, and describes the modifications which have been made.

AN29 consists of a main program which presents the user with a menu from which any of a range of subroutines may be selected. Each subroutine carries out a particular process for spectrum manipulation or analysis. Full details of these (for program ANALYSIS) may be found in the above reference. Spectra are contained in two floating point arrays. One of these, known as the A memory, generally contains the experimental spectrum of interest, while the other, the B memory, is generally used for the creation of a theoretical background shape for that spectrum. The spectrum read routine reads an integer format spectrum from disk and converts the data to floating point format, while the write routine reverses this process.

Crozier (1985) wrote a program to run on the IBM mainframe to fit a quadratic curve to the MBH form as a function of photon energy for any combination of element, T_0 and θ. An approximation to an MBH shape could then be obtained by substituting the coefficients produced for a particular case into a quadratic form. In order to do this, ANALYSIS requires to read the coefficients from a data file on disk. The file should contain a set of coefficients for all elements with $5 < Z < 92$ pertaining to a particular combination of T_0 and θ. Each file must be created on the IBM mainframe and dumped onto magnetic tape which can be read by the Nova, and transferred to the 860 if required. This procedure becomes cumbersome if many different values of T_0 and θ are considered, as was the case with the data from the JEOL TEM in this work. As a first step towards streamlining the process, the MBH generation routine MBHGEN was modified to create a version MBHDIR, incorporated in AN29,

which allowed the required set of three coefficients to be entered directly from the console. This allowed the data dump to tape to be bypassed, but was still rather time-consuming for the range of configurations under consideration. It was decided that the calculation of background shapes from the MBH equation itself would be preferable. Subroutine MBH to generate a value for σ'' for a particular combination of $h\nu$, T_0, θ and Z was translated from the version existing on the IBM to run on the Nova by Dr. Nicholson. This routine was incorporated in program CROSS, written by myself, which allows the user to specify Z, T_0 and θ, calculates MBH for the required range of photon energies, and writes the resultant theoretical spectrum to disk in 290 format. These background spectra may be read directly into the B memory of AN29.

ANALYSIS contains a routine which corrects the theoretical spectrum for the detector efficiency of a Be window detector, the Be window thickness being specified by the user. In this work, the detector efficiencies were also dependent on the thicknesses of layers of Au, Si or ice (see chapters 4 and 5). A modified version, DETLAY, of the ANALYSIS efficiency routine DETEFF was incorporated in AN29. This routine allows the theoretical spectrum to be corrected for absorption in a layer of any element. This routine makes use of the mass absorption coefficients of Springer and Nolan (197), which are calculated by subroutine MABSCO which already existed in ANALYSIS.

B3. Comparison of experimental and theoretical values for K_α/L shell x-ray production ratios – programs SIGRATIO_KRAUSE, SIGRATIO_BAMBYNEKB and SIGRATIO_BAMBYNEKCD.

These are short programs, written in SuperBasic to run on a Sinclair QL microcomputer, which carry out the necessary calculations for the analysis described in section 5.x. Each program uses the Bethe form to evaluate a theoretical prediction for the K_α/L-shell x-ray production ratio, $Q_{KL}{}^t$ for each element under consideration. The only difference between the programs is that each uses a different set of values for the L-shell fluorescence yields. The three tabulations used are referenced in section 5.x. It is assumed at this stage that $b_K = b_L$. $Q_{KL}{}^t$ is then compared with the corresponding experimentally measured value $Q_{KL}{}^e$. Any discrepancy is assumed to be due to an inequality between b_K and b_L. A value for the ratio b_K/b_L is hence deduced.

Program SIGRATIO_KRAUSE

```
110 REMark Program SIGRATIO_KRAUSE uses experimental and theoretical values
115 REMark of K alpha/L production cross section ratios to calculate values
120 REMark of the ratio of Bethe b parameters bK/bL.
140 REMark uses "effective" fluorescence yields for the L sub-shells;
150 REMark data from Krause(1979)
160 REMark
170 REMark ****************************************************************
180 PAPER 0:INK 4
190 REMark write headings to screen and printer
200 CLS
210 OPEN #3,ser1
220 PRINT #3,"RESULTS USING EFFECTIVE FLUORESCENCE YIELD VALUES FROM KRAUSE"
230 PRINT #3
240 PRINT ,"RESULTS USING EFFECTIVE FLUORESCENCE YIELD VALUES FROM KRAUSE"
250 PRINT
260 PRINT ;"element"; TO 13;"Z"; TO 26;"Expt"; TO 39;"sigmaK"; TO 52;"sigmaL";
270 PRINT TO 65;"theory";TO 78;"bK/bL"
280 PRINT
290 PRINT #3
300 LINE 0,86 TO 200,86
310 PRINT #3;"element"; TO 13;"Z"; TO 21;"Expt"; TO 34;"sigmaK"; TO 47;"sigmaL";
320 PRINT #3,TO 60;"theory";TO 73;"bK/bL"
330 REMark read data
340 REMark element (Harwell or Glasgow), Z, K-shell binding energy,
350 REMark L1,2,3 sub-shell binding energies, K-shell fluorescence
360 REMark yield, L1,2,3 sub-shell effective fluorescence yields,
370 REMark K alpha/L count ratio, K alpha line detector efficiency,
375 REMark L line detector efficiency, L line absorption factor
380 RESTORE 620
390 FOR i=1 TO 11
400 READ el$,Z,EK,EL1,EL2,EL3,wK,pK,wL1,wL2,wL3
410 READ pKL,efK,efL,aL
420 REMark calculate K alpha/L production ratio
430 expt=pKL*efL*aL/efK
440 REMark assign values to Bethe c parameters
450 cK=.85
460 cL=1
470 REMark K alpha theoretical production cross section/bK
480 sigK=LN(cK*100/EK)/EK*wK*pK
490 REMark L-shell theoretical production cross section/bL
500 sigL=(wL1*LN(cL*100/EL1))/EL1+wL2*LN(cL*100/EL2)/EL2+wL3*2*LN(cL*100/EL3)/EL3
510 REMark theoretical K alpha/L production ratio
520 theory=sigK/sigL
530 REMark comparison of experimental and theoretical production ratios
540 REMark to give experimental ratio of bK/bl
550 bKL=expt/theory
560 REMark print output
570 PRINT el$;TO 13;Z;TO 26 ;expt;TO 39 ;sigK;TO 52 ;sigL;TO 65;theory;TO 76;bKL
580 PRINT #3,el$;TO 13;Z;TO 21 ;expt;TO 34 ;sigK;TO 47 ;sigL;TO 60;theory;
590 PRINT #3,TO 71;bKL
600 END FOR i
610 REMark data lines
620 DATA "Fe(H)",26,7.11,.849,.721,.708,.339,.878,6.5E-3,6.3E-3,6.3E-3
630 DATA 1.6,1,.53,1
640 DATA "Co(H)",27,7.71,.929,.794,.779,.37,.881,7.8E-3,7.6E-3,7.8E-3
650 DATA 1.3,1,.59,1
660 DATA "Ni(H)",28,8.33,1.015,.871,.853,.39,.877,9.2E-3,8.9E-3,9.3E-3
670 DATA 1.02,1,.66,1
680 DATA "Cu(H)",29,8.98,1.1,.953,.933,.443,.879,1.1E-2,1E-2,1.1E-2
690 DATA .95,1,.71,1
700 DATA "Ge(H)",32,11.115,1.426,1.294,1.228,.554,.868,1.4E-2,1.3E-2,1.4E-2
710 DATA .57,1,.82,1
720 DATA "Mo(G)",42,20.002,2.867,2.628,2.523,.767,.837,3.6E-2,3.9E-2,3.7E-2
730 DATA .21,.97,.92,1
740 DATA "Mo(H)",42,20.002,2.867,2.628,2.523,.767,.837,3.6E-2,3.9E-2,3.7E-2
750 DATA .2,.81,.95,1
760 DATA "Ag(G)",47,25.53,3.822,3.54,3.368,.833,.825,5.3E-2,5.9E-2,5.2E-2
770 DATA .14,.84,.95,1
780 DATA "Ag(H)",47,25.53,3.822,3.54,3.368,.833,.825,5.3E-2,5.9E-2,5.2E-2
790 DATA .105,.58,.97,1
800 DATA "Sn(H)",50,29.19,4.464,4.157,3.928,.852,.818,6.7E-2,7.5E-2,6.4E-2
810 DATA 7.2E-2,.45,1,1
820 DATA "Sn(G)",50,29.19,4.464,4.157,3.928,.852,.818,6.7E-2,7.5E-2,6.4E-2
830 DATA 8E-2,.67,1,1
```

Program SIGRATIO_BAMBYNEKB data lines

```
610  REMark  data  lines
620  DATA  "Fe(H)",26,7.11,.849,.721,.708,.339,.878,5.8E-3,5.8E-3,5.6E-3
630  DATA  1.6,1,.53,1
640  DATA  "Co(H)",27,7.71,.929,.794,.779,.37,.881,7E-3,7.1E-3,6.9E-3
650  DATA  1.3,1,.59,1
660  DATA  "Ni(H)",28,8.33,1.015,.871,.853,.39,.877,8.2E-3,8.5E-3,8E-3
670  DATA  1.02,1,.66,1
680  DATA  "Cu(H)",29,8.98,1.1,.953,.933,.443,.879,1E-2,1E-2,9.5E-3
690  DATA  .95,1,.71,1
700  DATA  "Ge(H)",32,11.115,1.426,1.259,1.228,.554,.868,1.3E-2,1.4E-2,1.3E-2
710  DATA  .57,1,.82,1
720  DATA  "Mo(G)",42,20.002,2.867,2.628,2.523,.767,.837,3.8E-2,3.9E-2,3.7E-2
730  DATA  .21,.97,.92,1
740  DATA  "Mo(H)",42,20.002,2.867,2.628,2.523,.767,.837,3.8E-2,3.9E-2,3.7E-2
750  DATA  .2,.81,.95,1
760  DATA  "Ag(G)",47,25.53,3.822,3.54,3.368,.833,.825,6.1E-2,6.4E-2,6E-2
770  DATA  .14,.84,.95,1
780  DATA  "Ag(H)",47,25.53,3.822,3.54,3.368,.833,.825,6.1E-2,6.4E-2,6E-2
790  DATA  .105,58,97,1
800  DATA  "Sn(H)",50,29.19,4.464,4.157,3.928,.852,.818,7.5E-2,7.8E-2,7.4E-2
810  DATA  7.2E-2,.45,1,1
820  DATA  "Sn(G)",50,29.19,4.464,4.157,3.928,.852,.818,7.5E-2,7.8E-2,7.4E-2
830  DATA  8E-2,.67,1,1
```

Program SIGRATIO_BAMBYNEKCD data lines

```
610  REMark  data  lines
620  DATA  "Fe(H)",26,7.11,.849,.721,.708,.339,.878,1.4E-3,1.5E-3,1.5E-3
630  DATA  1.6,1,.53,1
640  DATA  "Co(H)",27,7.71,.929,.794,.779,.37,.881,2E-3,2.2E-3,2.1E-3
650  DATA  1.3,1,.59,1
660  DATA  "Ni(H)",28,8.33,1.015,.871,.853,.39,.877,2.6E-3,3E-3,2.8E-3
670  DATA  1.02,1,.66,1
680  DATA  "Cu(H)",29,8.98,1.1,.953,.933,.443,.879,3.5E-3,4E-3,3.8E-3
690  DATA  .95,1,.71,1
700  DATA  "Mo(G)",42,20.002,2.867,2.628,2.523,.767,.837,2E-2,2.8E-2,2.6E-2
710  DATA  .21,.97,.92,1
720  DATA  "Mo(H)",42,20.002,2.867,2.628,2.523,.767,.837,2E-2,2.8E-2,2.6E-2
730  DATA  .2,.81,.95,1
740  DATA  "Ag(G)",47,25.53,3.822,3.54,3.368,.833,.825,1.6E-2,4.9E-2,4.5E-3
750  DATA  .14,.84,.95,1
760  DATA  "Ag(H)",47,25.53,3.822,3.54,3.368,.833,.825,1.6E-2,4.9E-2,4.5E-3
770  DATA  .105,.58,.97,1
780  DATA  "Sn(H)",50,29.19,4.464,4.157,3.928,.852,.818,6.2E-2,6.5E-2,6.4E-2
790  DATA  7.2E-2,.45,1,1
800  DATA  "Sn(G)",50,29.19,4.464,4.157,3.928,.852,.818,6.2E-2,6.5E-2,6.4E-2
810  DATA  8E-2,.67,1,1
```

The programs require the following data for each element: I_K, $I_{L1...3}$, ω_K, $Y_{1...3}$, K_α/L count ratio and the detector efficiencies for the K_α and L-lines. These are input as DATA lines. SIGRATIO_KRAUSE is listed in full overleaf. The other two programs are similar except for the DATA lines, which are also listed for each case.

B4. EELS analysis programs on the Toltec minicomputer

These essentially fall into two categories – the analysis software supplied with the Toltec system and the user-written software developed at Glasgow University. Crozier (1985) described in detail the Toltec, the Toltec software and the user-written software to that date. The latter included the routines for EELS background fitting by extrapolation, as discussed in section 7.2. Steele (1987) detailed the additional software written by him for the constrained fitting procedure discussed in section 7.4. The routines for both fitting procedures have incorporated into the Toltec suite of analysis programs, and may be selected from the EELS menu in the analysis program XREL. Constrained fitting requires theoretical EELS edge shapes to be input from data files on disk. In order to create these, further separate programs are required. Theoretical cross sections calculated according to the hydrogenic model, as discussed in chapter 2, are calculated by programs SGK4 and SGL4. These are versions of Egerton's SIGMAKR and SIGMALR programs, adapted to run on the Toltec by Dr. P.A. Crozier. These programs ouput the calculated cross section data to disk files. The creation of Hartree-Slater cross section files is described in section 7.5. As discussed in section 7.5, it is desirable to modify the theoretical cross sections to take into account spectrometer resolution and multiple scattering. Two programs, CC and CCHS, written by myself, read in the unprocessed cross sections and carry out the necessary convolutions. The remainder of this section describes these programs. CC is listed on following pages, together with all its subroutines. CCHS, which is intended to be used for HS cross sections, is very similar, and is not listed. The only difference between the two versions lies in the number of channels of cross section data which are considered, reflecting the fact that HS cross sections are generally avaible over a shorter range of energy loss than H cross sections. The ranges of energy loss considered are 250eV (CC) and 100eV (CCHS).

B5

The main program writes information about the program to the console, calls the processing subroutine TEST, and allows the user to specify what program should be run on exit (operating system, XREL or run constrained fitting program directly). All processing is carried out within TEST. Firstly, the user is asked whether the cross section should be corrected for spin-orbit splitting. This will apply only to L-shell cross sections. If not, then subroutine DATA is called to read the cross section data from disk into array XX.

The spin-orbit splitting correction, as discussed in section 7.5, requires that the L_2 cross section should be separated from the L_3, and shifted upwards in energy loss by a particular number of channels. It is assumed that the L_3 and L_2 cross sections contribute to the combined $L_{2,3}$ cross section calculated by SGL4 in the ratio 2:1. The splitting may therefore be carried out by shifting 1/3 of the $L_{2,3}$ by the specified amount. If carried out directly on the whole cross section calculated by SGL4, however, this procedure would result in the L_1 cross section being split into two components. In order to prevent this unwanted effect, it is necessary to remove the L_1 contribution before the splitting process, and then to add it back on to give the complete cross section. SGL4 asks the user to input threshold energy loss values for the $L_{2,3}$ and L_1 edges. If a value of >250eV higher than the correct value for the L_1 threshold is specified, then over a range of 250eV the cross section produced has only the $L_{2,3}$ contribution. If spin-orbit splitting is specified, then TEST requires both a complete cross section and an $L_{2,3}$ only cross section produced in this way to be input. These are read into arrays ZZ and XX respectively. XX is then subtracted from ZZ to leave the L_1 cross section in ZZ. XX is then split into two components. The L_3 cross section is produced by multiplying XX throughout by 2/3, the result being returned to XX. The L_2 cross section is produced by multiplying this in turn by 1/2 (ie. 1/3 x the original $L_{2,3}$ cross section), the result being stored in YY. The values in YY are then shifted upwards in the array by the spin-orbit split input from the console. The complete cross section is then produced by adding XX, YY and ZZ together, the result being stored in XX.

The need to separate out the L_1 signal only applies to CC, since the range of energy loss processed by CCHS does not include the L_1 edge for the elements considered in this work. In CCHS, array ZZ is not required, and only the part of the processing involving separating the L_2 and L_3 signals is carried out.

The cross section data is at this stage in array XX, regardless of whether spin-orbit splitting has been carried out. The next step is to convolve the contents of XX with those of another array PEAK, which contains 100 channels of data which may represent either a gaussian distribution or the low-loss region of the spectrum of interest. If convolution with a gaussian is selected, subroutine GAUSS allows the user to specify a value for the FWHM, and calculates the corresponding gaussian, which is stored in PEAK, with the centre in channel number CENTRE, where CENTRE is set equal to 25. Alternatively, if convolution with the low-loss region is specified, subroutine LOWLOSS is called. This routine calls subroutine DATA to read in 100 channels of the required low loss region from a disk file into array WW. The disk file must have been previously created by using the spectrum manipulation program MNIP in the XREL user routine menu to write the required data from the spectrum display memory to disk. LOWLOSS then transfers the data to PEAK, with the centre of the zero loss peak in channel number CENTRE, and normalises so that the elements od PEAK add up to unity.

One of two routines is now called to convolve XX with PEAK. Both carry out the convolution in the same way. The convolved cross section is built up in array EDGE. The contents of PEAK are scaled according to the contents of channel i of XX, and added to channels i to i+99 of EDGE. After this process has been carried out for i=1,...,250, EDGE contains the required convolved cross section, with the edge threshold energy corresponding to channel number CENTRE. Subroutine SCONV transfers the contents of EDGE directly to XX. This produces a cross section which includes those counts which have been redistributed to below the edge threshold. Subroutine CONVOL transfers the contents of EDGE to XX shifted so that the edge threshold corresponds to the start of the array. The applications for which each version is suited are discussed in section 7.5. Finally, subroutine TEST writes the contents of XX to a disk file, and returns to the main program.

B7

Program CC

```
C******************************************************************
C This program reads in an edge cross-section from a buffered file,
C splits the L2 and L3 edges, and convolves with a gaussian or the
C low-loss region of the spectrum
C 5/6/85
        DIMENSION XX(600)
        LOGICAL IAX
        INTEGER FINCH
        IAX=.FALSE.
C Get Toltec common
        CALL BURY(IXE1,LSTOP,0)
C This was intended for future modifications
C Get user common
        CALL UBURY(ISTOP,NSTOP,0)
        CALL NEWPAGE(1)
        KXE=2
C User information
        WRITE(1,50)
 50     FORMAT(/8X,'Cross-section correction program',/
     $/,5X,'This program corrects a theoretical cross-section'
     $/,5X,'shape to take into account the spectrometer resolution'
     $/,5X,'in a spectrum with which it is to be compared. This'
     $/,5X,'x-section is convolved with either a gaussian or '
     $/,5X,'the shape of the low-loss region of the spectrum.'
     $/,5X,' For L shell x-sections, a correction can also be'
     $/,5X,'made for spin-orbit splitting of the L2 and L3 edges.'
     $/,5X,' Cross-sections are read in from buffered data files'
     $/,5X,'(if L shell splitting is required, then an L2/L3 only'
     $/,5X,'cross-section must be supplied in addition to the'
     $/,5X,'complete cross-section) and the corrected version is'
     $/,5X,'written to another buffered data file.'
     $/,5X,' For convolution with a low-loss region, the spectrum'
     $/,5X,'must be stored in a buffered file to be read in.'
     $/,5X,'      (press any key to continue)',//)
        CALL IPCH(1,KEY)
C Read in cross-section from buffered file
C and output processed cross-section to
C new buffered file
        CALL TEST(XX,M)
C Choose exit route
        CALL NEWPAGE(1)
        WRITE(1,20)
 20     FORMAT(/20X,'Select option',/
     $/,15X,'G = return to JDS user routine'
     $/,15X,'X = return to XREL'
     $/,15X,'Q = quit to CO>',//)
        CALL IPCH(1,KEY)
        IF(KEY.EQ.'Q')GO TO 300
        IF(KEY.EQ.'X')GO TO 350
        IF(KEY.EQ.'G')GO TO 400
C Execute next program
 300    CALL EXIT
 350    CALL SPRAG(' X',0,'XR','EL',' A')
 400    CALL SPRAG(' X',3,'JD','S1',' A')
        END
```

```
                 SUBROUTINE DATA(XX)
C  This routine reads in a x-section from a buffered file
C
       DIMENSION XX(600)
       WRITE(1,1)
1      FORMAT(' File name :- ')
       READ(1,2)A
2      FORMAT(A4)
       WRITE(1,20)A
       WRITE(5,20)A
20     FORMAT(' X-section data filename =',A4)
       WRITE(1,3)
3      FORMAT(' Drive number :- ')
       READ(1,4)N
4      FORMAT(I1)
       WRITE(1,21)N
       WRITE(5,21)N
21     FORMAT(' Drive number of file =',I1)
       WRITE(1,22)
       WRITE(5,22)
22     FORMAT(' Number of transfers=250')
       WRITE(99,5)N,A
5      FORMAT('R',I1,A4,' S')
       DO 10 I=1,250
       READ(4,6)E,DELTA,SIGMA,XX(I)
6      FORMAT(4E12.4)
10     CONTINUE
       RETURN
       END




                 SUBROUTINE TEST(XX,M)
  C
  C  This subroutine reads in a x-section from a buffered file,
  C  modifies it to take account of spin-orbit splitting and
  C  spectrometer resolution, and writes the new x-section
  C  to another buffered file
  C
       DIMENSION XX(600)
       DIMENSION YY(600)
       DIMENSION ZZ(600)
       DIMENSION PEAK(100)
       INTEGER N
       CALL NEWPAGE(1)
  C Choose whether to split or not to split
       WRITE(1,301)
  301  FORMAT(/10X,'Select processing to be carried out'
      $/,15X,'C = convolution only'
      $/,15X,'S = spin-orbit split and convolution'/)
       CALL IPCH(1,KEY)
       IF(KEY.EQ.'C') GO TO 800
       WRITE(1,316)
  316  FORMAT(' Spin-orbit split and convolution selected')
       WRITE(1,306)
  306  FORMAT(///'Read in complete x-section from buffered file'///)
       CALL DATA(ZZ)
       CALL NEWPAGE(1)
       WRITE(1,307)
  307  FORMAT(///'Read in L2/L3 only x-section from buffered file'///)
       CALL DATA(XX)
  C Subtract XX from ZZ to get L1 only
       DO 471 I=1,250
       ZZ(I)=ZZ(I)-XX(I)
  471  CONTINUE
```

```
C  Shift L2 edge
      CALL NEWPAGE(1)
      WRITE(1,33)
 33   FORMAT(' L edge L2/L3 shift (integer):-')
      READ(1,34) K1
 34   FORMAT(I4)
      WRITE(1,35) K1
      WRITE(5,35) K1
 35   FORMAT(' L edge L2/L3 shift=',I4)
C
C  Scale down to get L3 only
      DO 11 I=1,250
      XX(I)=XX(I)*0.6667
 11   CONTINUE
C
C  Scale and shift to get L2
      M1=250-K1
      DO 12 I=1,M1
      YY(I+K1)=XX(I)*0.5
 12   CONTINUE
      DO 1300 I=1,K1
      YY(I)=0.0
 1300 CONTINUE
C
C  Add L3 and L2 to get complete cross-section
      DO 13 I=1,250
      XX(I)=XX(I)+YY(I)
 13   CONTINUE
C Add L1 back on
      DO 472 I=1,250
      XX(I)=XX(I)+ZZ(I)
 472  CONTINUE
      GO TO 810
 800  WRITE(1,317)
 317  FORMAT('  Convolution only selected')
      WRITE(1,308)
 308  FORMAT(////'Read in x-section from buffered file'////)
      CALL DATA(XX)
 810  CONTINUE
C Convolve cross-section with a gaussian
      M=250
C Choose convolution shape
      CALL NEWPAGE(1)
      WRITE(1,730)
 730  FORMAT(/15X,'Select low-loss region model'
     $/,15X,'for resolution'
     $//,20X,'G = gaussian distribution'
     $/,20X,'L = experimental low-loss region')
      CALL IFCH(1,KEY)
      IF(KEY.EQ.'L') GO TO 740
      CALL GAUSS(PEAK)
      GO TO 750
 740  CALL LOWLOSS(PEAK)
C Choose position of new x-section
 750  CALL NEWPAGE(1)
      WRITE(1,760)
 760  FORMAT(/15X,'Select new x-section position'/
     $/,15X,'S = shifted 25 channels to the right'
     $/,15X,'     (gives complete convolved x-section)'/
     $/,15X,'N = aligned with original x-section'
     $/,15X,'     (cuts off counts redistributed to'
     $/,15X,'     below edge onset by convolution)'/)
```

```
      CALL IPCH(1,KEY)
      IF(KEY.EQ.'N') GO TO 770
      WRITE(1,771)
  771 FORMAT(////'25 channel shift selected'////)
      CALL SCONV(PEAK,XX,M,N)
      GO TO 780
  770 WRITE(1,772)
  772 FORMAT(////'Alignment with original x-section selected'////)
      CALL CONVOL(PEAK,XX,M,N)
C Output smoothed cross-section
  780 CALL NEWPAGE(1)
      WRITE(1,572)
  572 FORMAT(' Output file for smoothed X-section:-')
      READ(1,573)F5
  573 FORMAT(A4)
      WRITE(1,574)
  574 FORMAT(' Drive number:-')
      READ(1,575)IDRV
  575 FORMAT(I1)
      WRITE(99,576)IDRV,F5
  576 FORMAT('W',I1,A4,' S')
      DELTA=0.0
      SIGMA=0.0
      DO 577 I2=1,200
      E=FLOAT(I2)
      DELTA=DELTA+E
      SIGMA=SIGMA+XX(I2)
      WRITE(4,578)E,DELTA,SIGMA,XX(I2)
  578 FORMAT(4E12.4)
  577 CONTINUE
      RETURN
      END




                    SUBROUTINE SCONV
C
C  Subroutine to convolve an eels edge cross-section
C  stored in array XX with a gaussian or low loss region stored in
C  array PEAK.
C  ********************************************************
      SUBROUTINE SCONV(PEAK,XX,M,N)
      COMMON /BFIT/ XDATA(1024),YDATA(1024),A(10)
      DIMENSION PEAK(100)
      DIMENSION EDGE(600)
      DIMENSION XX(600)
      INTEGER START,END,CENTRE
C
C  Print warning about shift
      WRITE(5,78)
      WRITE(5,79)
  78  FORMAT(' Note that new x-section is shifted')
  79  FORMAT(' 25 channels to the right')
C  Define centre of array PEAK
      CENTRE=25
C  Set accumulation array to zero
      DO 940 I=1,600
      EDGE(I)=0
  940 CONTINUE
```

```
C  Loop to process each channel
C
       DO 600 I=1,250
C Spread out current channel counts and add
C to accumulation array
       DO 605 J=1,99
C Note that cross-section is shifted by CENTRE channels
       K=I-1+J
       EDGE(K)=EDGE(K)+(XX(I)*PEAK(J))
  605    CONTINUE
  600    CONTINUE
C
C  Put convolved cross-section in XX
       N=75
       DO 610 L=1,250
       XX(L)=EDGE(L)
  610    CONTINUE
       RETURN
       END


                        SUBROUTINE CONVOL
C
C  Subroutine to convolve an eels edge cross-section
C  stored in array XX with a gaussian or low loss region stored in
C  array PEAK.
C  **************************************************
       SUBROUTINE CONVOL(PEAK,XX,M,N)
       COMMON /BFIT/ XDATA(1024),YDATA(1024),A(10)
       DIMENSION PEAK(100)
       DIMENSION EDGE(600)
       DIMENSION XX(600)
       INTEGER START,END,CENTRE
C
C  Define centre of array PEAK
       CENTRE=25
C  Set accumulation array to zero
       DO 940 I=1,600
       EDGE(I)=0
  940    CONTINUE
C  Loop to process each channel
C
       DO 600 I=1,250
C Spread out current channel counts and add
C to accumulation array
       DO 605 J=1,99
C Note that cross-section is shifted by CENTRE channels
       K=I-1+J
       EDGE(K)=EDGE(K)+(XX(I)*PEAK(J))
  605    CONTINUE
  600    CONTINUE
C Shift cross-section back
       DO 945 I=1,225
       EDGE(I)=EDGE(I+25)
  945    CONTINUE
C
C  Put convolved cross-section in XX
       N=75
       DO 610 L=1,250
       XX(L)=EDGE(L)
  610    CONTINUE
       RETURN
       END
```

```
C
C   This subroutine creates a gaussian distribution
C   in array PEAK, the width parameter sigma being
C   specified by the user
C   ***********************************************
        SUBROUTINE GAUSS(PEAK)
        COMMON /BFIT/ XDATA(1024),YDATA(1024),A(10)
        DIMENSION PEAK(100)
        INTEGER CENTRE
        REAL NORM
C
C   Define centre of gaussian
        CENTRE=25
C   Input width parameter of gaussian
        CALL NEWPAGE(1)
        WRITE(1,500)
 500    FORMAT(' Input FWHM of gaussian (real):-')
        READ(1,505) WIDTH
 505    FORMAT(F10.3)
        WRITE(1,506)WIDTH
        WRITE(5,506) WIDTH
 506    FORMAT(' FWHM of gaussian=',F10.3,/)
C   Convert from FWHM to sigma
        WIDTH=WIDTH/2.35
C   Calculate normalisation constant
        AY=SQRT(6.283)
        NORM=WIDTH*AY
C
C   Loop to calculate values of gaussian
        DO 510 I=1,49
        B=(I-CENTRE)*(I-CENTRE)
        C=-2.0*(WIDTH**2)
        D=B/C
        E=EXP(D)
        PEAK(I)=E/NORM
 510    CONTINUE
        DO 511 I=50,100
        PEAK(I)=0.0
 511    CONTINUE
        RETURN
        END
```

```
                    SUBROUTINE LOWLOSS(PEAK)
C This subroutine reads in from a buffered file the low-loss
C region of a spectrum, and stores it in array PEAK
C
       DIMENSION WW(600)
       DIMENSION PEAK(100)
       CALL NEWPAGE(1)
C Read in low-loss region
       WRITE(1,601)
 601   FORMAT('Input the number of channels in the buffered file'
      $/,'before the zero-loss peak value (integer)   :-')
       READ(1,602)IZL
 602   FORMAT(I3)
       WRITE(1,603) IZL
       WRITE(5,603) IZL
 603   FORMAT(I3,' channels before peak in data file')
       WRITE(1,600)
 600   FORMAT(///'Read in low-loss region from buffered file'///)
       CALL DATA(WW)
       TOTAL=0.0
       DO 604 I=1,100
       ISH=IZL-25+I
       IF(ISH.LE.0)GO TO 606
       PEAK(I)=WW(ISH)
       GO TO 607
 606   PEAK(I)=0.0
 607   TOTAL=TOTAL+PEAK(I)
 604   CONTINUE
       DO 605 I=1,100
 608   FORMAT(F10.3)
       PEAK(I)=PEAK(I)/TOTAL
 605   CONTINUE
       RETURN
       END
```

Appendix C

Preparation of holey backing films on single-hole mounts

The EDX analysis described in chapters 4 and 5 required spectra in which any contribution from outwith the area of specimen illuminated by the beam was minimised. Bulk contributions can arise due to stray scattering on to parts of the microscope, the specimen holder or the grid on which the specimen is supported. The latter contribution can be minimised by using a specimen grid with the largest possible clear area of specimen on which the grid does not encroach. The most suitable type of grid for this work is therefore the single-hole mount (SHM).

In both EDX and EELS analysis, it was desirable to minimise the specimen thickness. In EDX this limits the extent of specimen self-absorption. The evaporated metal films used here, which are <500A thick, are not self-supporting on a SHM, and so must be supported on a backing film. The backing film will, however, add to the specimen thickness. It is desirable that the backing should be holey, so that there are areas of thin metal film alone over the holes. Commercially available holey carbon films are usually supported on fine mesh grids, and are not suitable for the EDX aanalysis required here. Such films are, however, suitable for EELS analysis, and were used for the boride specimens discussed in chapter 8. This appendix outlines the process used to prepare holey formvar and formvar/carbon films on SHMs for EDX analysis.

The formvar film is initially formed on a glass microscope slide using the apparatus illustrated in figure C1. The solution in the draining tube is prepared by dissolving 1g of formvar powder in 100ml of chloroform, and adding ~1ml of glycerine. The glycerine breaks down into droplets which are in suspension, and lead to the presence of holes in the formvar film. If the glycerine is omitted, then a solid formvar film results. The microscope slide is polished with a Selvyt and placed in the tube as shown. The tap is then opened, allowing the solution to drain out of the tube into the receptacle below. A formvar fim is formed on the slide by the vapour left as the level of the solution falls. The

slower the level drops, the more time there is for the film to form, and so a thicker film forms. The speed of draining, and hence the film thickness, is controlled by the tap. The thickness may be varied upwards from ~200A.

The formvar film must now be transferred to the specimen grids. The edge of the film is separated from the slide by running a moistened finger around the edge of the top surface. The film is then carefully floated off onto the surface of a container of distilled water. The grids can be placed on the floating film, and picked up by placing a piece of paper on the surface over them. The grids adhere to the paper when it is lifted off and can then be left to dry. Finally, any remaining glycerine must be removed from the films. This is done by holding each grid in a jet of steam for ~30sec.

The size and number of the holes depends on the particular combination of the proportion of glycerine in the solution, film thickness and steaming time. The most suitable combination for a particular application should be found by trial and error. If it is required that the backing film should be conducting to prevent charging under the beam, as will be the case if the specimen material itself is non-conducting, a carbon film may be evaporated on top of the formvar. Such formvar/carbon films were used to support the crystals of MoO_3 for the specimen of that material described in chapter 4. In principle it is possible to dissolve the formvar in chloroform to leave a holey carbon film. This was not considered to be necessary here since it appeared that the holes completely penetrated the formvar/carbon combination.
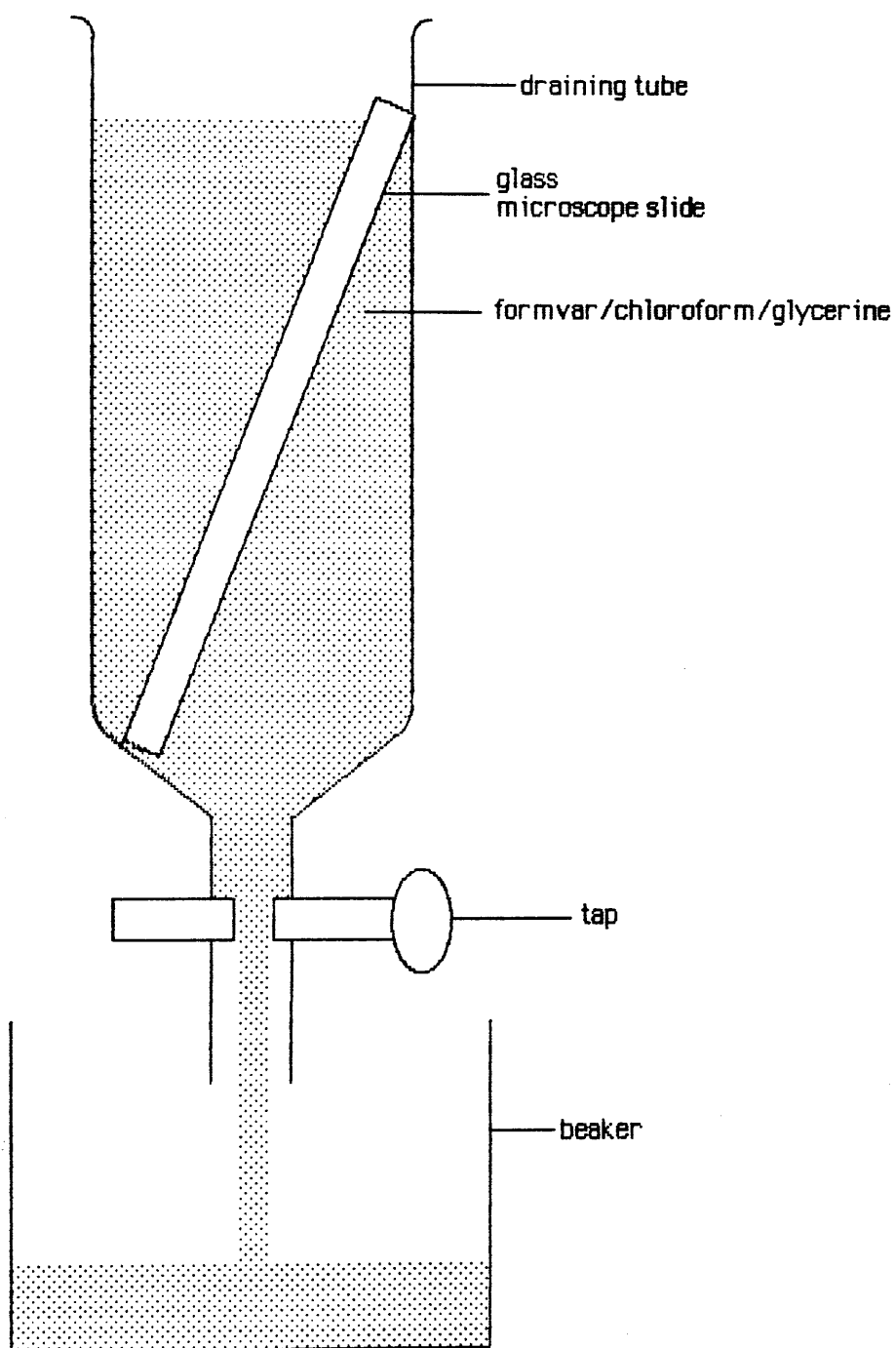
Figure C1. Apparatus for the preparation of holey formvar films.

Appendix D

On the relationship between fluorescence yield ω and effective fluorescence yield v

In the evaluation of L-shell cross sections, account should be taken of the fact that the L-shell is split into three sub-shells, and that there is a definite possibility of radiationless Coster-Kronig transitions taking place within the shell, as described in chapter 5. The resultant cross sections ϕ_{Li} for the individual sub-shells are given by

$$\phi_{L3} = \sigma_{L3} + (f_{13} + f_{12}f_{23})\phi_{L1} + f_{23}\phi_{L2}$$

$$\phi_{L2} = \sigma_{L2} + f_{12}\phi_{L1} \qquad\qquad \textbf{D1}$$

$$\phi_{L1} = \sigma_{L1}$$

where σ_{Li} is the total ionisation cross section for electron excitation of the L_i sub-shell, and f_{iJ} is the Coster-Kronig yield for transitions from the L_i to the L_J sub-shells.

The x-ray production cross section for the L_i sub-shell is given in terms of the fluorescence yield ω by

$$I_{Li} = \phi_{Li}\omega_{Li} \qquad\qquad \textbf{D2}$$

In the sources used here for data (see chapter 5 for references), the L-shell fluorescence yields are expressed in terms of the effective fluorescence yields v, defined by

D1

$$Y_1 = \omega_{L1} + \omega_{L2}f_{12} + \omega_{L3}(f_{13} + f_{12}f_{23})$$

$$Y_2 = \omega_{L2} + \omega_{L3}f_{23} \qquad\qquad \textbf{D3}$$

$$Y_3 = \omega_{L3}$$

In these terms the L_i sub-shell x-ray production cross section is given by

$$I_{Li} = \sigma_{Li}Y_i \qquad\qquad \textbf{D4}$$

The effective fluorescence yield values used are therefore appropriate for use directly with the ionisation cross sections predicted by the Bethe model.

Appendix E

A simplified model for incomplete charge collection (ICC) at the back face of an x-ray detector crystal

It was noted in chapter 5 that there was a "bump" in the background on the low energy side of the K_α peak in spectra recorded on the VG HB501 from Mo, Ag and Sn. It appears that up to ~10% of the K_α counts in these cases are redistributed over a range of channels corresponding to energies less than the K_α line energy. This effect is only apparent for photons, of energy $h\nu >$~15keV. It is clearly observed for Mo, but cannot be detected for Ge. The effect is analogous to the ICC found for photons of energy <5.9keV studied in detail by Craven et al. (1985, 1987). ICC effects considered to date appear to be due to the presence of an inefficient layer of Si at the front face of the detector crystal (see chapter 3). This appendix outlines a very simple model which shows how a similar inefficient layer at the back face of the crystal might give rise to an effect similar to that observed in the spectra from the VG HB501. No attempt is made here to model the shape of the bump. It is merely suggested that there might be a layer at the back face of the crystal in which some of the energy of the of a photon absorbed there is not collected.

For the purposes of this model it is assumed that the crystal is a uniform block of Si, a layer at the back face of which is less efficient than the bulk in collecting carriers produced by an incident photon. The situation is illustrated in figure E1. The crystal thickness is T, while the thickness of the inefficient layer is L. If n_0 photons of a particular energy $h\nu$ are incident upon the front surface, then the number n which have been detected within a depth x in the crystal is given by

$$n = n_0(1-\exp(-\mu/\rho(h\nu).\rho.x)) \qquad E1$$

where $\mu/\rho(h\nu)$ is the mass absorption coefficient for a photon of energy $h\nu$ in SI. We are interested in the proportion P of the total number of photons which are detected, ie. the number detected in depth T, are detected in the inefficient layer. We must therefore evaluate the difference between the number of photons
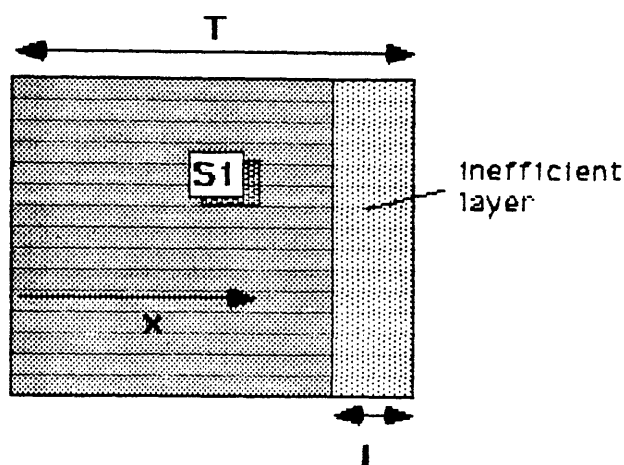
Figure E1. Illustration of parameters for back face ICC model.

detected within depth T and the number detected within depth T-L, and divide by the former to give the required proportion. This leads to the expression for P

$$P = \frac{\exp(-\mu/\rho(h\nu).\rho.T) \, [\exp(\mu/\rho(h\nu).\rho.L) - 1]}{1 - \exp(-\mu/\rho(h\nu).\rho.T)} \qquad E2$$

This expression was evaluated for the cases of Mo, where $\mu/\rho(h\nu)=5.7$ (Heinrich, 1987), and Ge, where $\mu/\rho(h\nu)=36$. T was taken to be 0.1cm which was the value deduced for the effective crystal thickness by comparison of the high energy background with MBH, for the early spectra for which the bump effect appeared most significant. If L=0.01cm, then P~5% for Mo, and ~0.03% for Ge. If the inefficient layer is an order of magnitude thinner, ie. L=0.001cm, then P~0.5% for Mo, and ~0.002% for Ge. According to this, 0.01cm thick inefficient layer of Si would produce an effect of similar magnitude to that found in the spectra considered here. This thickness is, however, very much larger than the thickness of `0.1μm typically assumed for the thickness of the Si "dead" layer at the front face of the crystal(eg. Thomas, 1984). The "bump" was not found in any spectra recorded on the VG HB5. The effective thickness deduced for the crystal of the detector on that microscope was 0.21. Repeating the calculation of P for this value of T, with L again =0.01cm, gives P~1% for Mo, and ~3×10^{-6}% for Ge.

The model discussed here predicts trends similar to those found in practice.

It predicts that back face ICC will be of much greater significance for elements such as Mo, Ag and Sn than for elements of medium Z such as Cu and Ge . This is supported by the fact that a bump is only observed for the heavier elements studied. It is not clear how realistic the value of the thickness of the inefficient layer required to predict the magnitude of the effect correctly is. It is,however, likely that the magnitude of ICC at the back face of the crystal in the detector on the HB501 is greater than at the front face. Much work has been done by the manufacturer to reduce the effects of ICC at the front faces of its crystals. It is probable that less attention has been paid to date to the back face.

References

P F Adam (1986), PhD. Thesis, University of Glasgow.

C C Ahn, O L Krivanek (1983), EELS Atlas, available from HREM facility, Centre for Solid State Science, Arizona State University, Tempe Az, USA.

C C Ahn, P Rez (1985), Ultramicroscopy **17**, 105.

W Bambynek, B Crasemann, R W Fink, H-U Freund, H Mark, C D Swift, R E Price, P V Rao (1972), Rev. Mod. Phys. **44**, 716.

J Bentley , G L Lehman, P S Sklad (1982) ,in Proc. 10th International Congress on Electron Microscopy, Hamburg, vol. 2, 191.

H A Bethe (1930), Ann. der Phys. **5**, 325.

R E Burge, D L Misell (1968), Phil. Mag. **18**, 251.

E H S Burhop, W N Asaad (1972), Adv. in Atomic and Molecular Phys. **8**, 163.

J N Chapman, C C Gray, B W Robertson, W A P Nicholson (1983), X-ray Spectrom. **12**, 153

G Cliff, G W Lorimer (1975), J. Microsc. **103**, 203.

C Colliex, C Mory (1984), in Quantitative Electron Microscopy, eds. J N Chapman and A J Craven, Scottish Universities Summer Schools in Physics, 1983, p 149.

A J Craven (1979), Proc. EMAG 1979, in Inst. Phys. Conf. Series no. 52, ed. T Mulvey, 47.

A J Craven, T W Buggy (1981), Ultramicroscopy **7**, 27.

A J Craven, T W Buggy (1984), J. Microsc. **136** (2), 227.

A J Craven, P F Adam, R Howe (1985), in Proc. EMAG 1985, Inst. Phys. Conf. Series no. 78, ed. G J Tatlock, 189.

A J Craven, C P McHardy, W A P Nicholson (1987) Proc. EMAG 1987.

A Y Crewe (1971), 'High Intensity Electron Sources and Scanning Electron Microscopy', in Electron Microscopy and Material Science, ed. U Valdre, p 162.

P A Crozier, J N Chapman, A J Craven, J M Titchmarsh (1983), in Proc. EMAG 1983, Inst. Phys. Conf. Series no. 68, ed. P Doig, 107.

P A Crozier, J N Chapman, A J Craven, J M Titchmarsh (1984), in AnalyticalElectron Microscopy 1984, eds. D B Williams and D C Joy, San Francisco Press Inc., p 79

P A Crozier (1985), PhD. Thesis, University of Glasgow.

P Duncumb (1968), J. de Microsc. **7**, 581.

N A Dyson (1973), X-Rays in Atomic and Nuclear Physics, Longmans.

R F Egerton (1979), Ultramicroscopy **4**, 169.

R F Egerton (1984a), J. Electron Microscopy Technique **1**, 37.

R F Egerton (1984b), in Quantitative Electron Microscopy, eds. J N Chapman and A J Craven, Scottish Universities Summer Schools in Physics, 1983, p 273.

R F Egerton (1984c), Scanning Electron Microscopy 1984 (II), 505.

R F Egerton (1984d), in Analytical Electron Microscopy 1984, eds. D B
        Williams and D C Joy, San Francisco Press Inc., p 263.

R Eisberg, R Resnick (1974), Quantum Physics of Atoms, Molecules,
        Solids, Nucleii and Particles, J Wiley and Son.

G Elwert (1939), Ann. Phys. 11, 257.

R W Fink, P V Rao (1974), in Handbook of Spectroscopy, ed. J W Robinson,
        CRC Press, Cleveland, Ohio, p 219.

R L Gluckstern, M H Hull Jr. (1953), Phys. Rev. 90, 1030.

J I Goldstein, D B Williams (1977), Scanning Electron Microscopy 1977
        (I), 651.

P J Goodhew, J E Castle (1983), in Proc. EMAG 1983, Inst. Phys. Conf.
        Series no. 68, ed. P Doig, 515.

P J Goodhew (1985), Proc. EMAG 1985, in Inst. Phys. Conf. Series no. 78,
        ed. G J Tatlock, 183.

C C Gray, J N Chapman, W A P Nicholson, B W Robertson, R P
        Ferrier (1983), X-ray Spectrom. 12, 163.

K F J Heinrich (1987), from National Bureau of Standards, Gaithersburg,
        Md 20899.

M Inokuti (1971), Rev. Mod. Phys. 43, 297.

D C Joy, D M Maher, R G Farrow (1980), Microbeam Analysis, 154.

P Kirkpatrick, L Weidmann (1945), Phys. Rev. 67, 321.

H W Koch, J W Motz (1959), Rev. Mod. Phys. **31**, 920.

H A Kramers (1923), Phil. Mag. **46**, 836.

M O Krause (1979), J. Phys. Chem. Ref. Data **8** (2), 307.

A Langenberg, J van Eck (1979), J. Phys. B **12**, 1331.

R D Leapman, P Rez, D F Mayer (1980), J. Chem. Phys. **72** (2), 1232.

M A Listengarten (1960), Bull. Acad. Science, USSR, Phys. **24**, 1050.

N F Mott, H S W Massey (1965), Theory of Atomic Collisions, 3rd. edition, Clarendon Press.

W A P Nicholson, B W Robertson, J N Chapman (1977), in Proc. EMAG 1977, Inst. Phys. Conf. Series no. 36, ed. D L Misell, 373.

K M Ostyn, C B Carter (1982), in Proc. 10th International Congress on Electron Microscopy, Hamburg, vol. 2, 191.

C J Powell (1976), Rev. Mod. Phys. **48**, 33.

R H Pratt, H K Tseng, C M Lee, L Kissel, C MacCallum, M Riley (1977), A. Data Nucl. Data Tables **20**, 175.

P Rez (1984), X-ray Spectrom. **13** (2), 55.

B W Robertson (1979), PhD. Thesis, University of Glasgow.

E Rutherford (1911), Phil. Mag. **21**, 669.

T P Schreiber, A M Wims (1981), Ultramicroscopy **7**, 27.

J H Scofield (1974), A. Data Nucl. Data Tables **14** (2), 122.

P S Sklad, J Bentley, P Angelini, G L Lehman (1984), in Analytical

Electron Microscopy 1984, eds. D B Williams and D C Joy, San
Francisco Press Inc., p 285.

A Sommerfeld (1931), Ann. Phys. **11**, 257.

G Springer, B Nolan (1976), Canadian J. Spectrosc. **21**, 134.

J D Steele, J N Chapman, P F Adam (1984), in Electron Microscopy
1984, Proc. 8th European Congress on Electron Microscopy,
Budapest, eds. A Csanady, P Rohlich and D Szabo, p 373.

J D Steele, J M Titchmarsh, J N Chapman, J H Paterson (1985),
Ultramicroscopy **17**, 273.

J D Steele (1987), PhD. Thesis, University of Glasgow.

L E Thomas (1984), in Analytical Electron Microscopy 1984, eds. D B
Williams and D C Joy, San Francisco Press Inc., p 358.

P Trebbia (1987), submitted for publication in Ultramicroscopy.

J B Vandersande, W A Furdanowicz, M R Libera (1987), in Proc. 11th
International Congress on X-ray Optics and Microanalysis, 1986,
London, Ontario, eds. J D Brown and R H Packard, Graphic
Services, University of West Ontario, p 403.

J A Venables (1981), in Qunatitative Microanalysis with High Spatial
Resolution, eds. G W Lorimer, M H Jacobs, P Doig, Metals
Society, p 205.

G Wirmark, H Nordén (1984), in Analytical Electron Microscopy 1984,
eds.   D B Williams and D C Joy, San Francisco Press Inc., p 269.

N J Zaluzec (1984),in Analytical Electron Microscopy 1984, eds. D B
Williams and D C Joy, San Francisco Press Inc., p 279.

C Zener (1930), Phys. Rev. **36**, 51.